Programming Self-assembly: Formation of Discrete Perylene Bisimide Aggregates

Dissertation zur Erlangung des

naturwissenschaftlichen Doktorgrades

der Julius-Maximilians-Universität Würzburg

vorgelegt von

Changzhun Shao

aus Liaoning

Würzburg 2012

Eingereicht am 15.10.2012

bei der Fakultät für Chemie und Pharmazie

1. Gutachter: Prof. Dr. Frank Würthner

2. Gutachter: Prof. Dr. Christoph Lambert

der Dissertation

1. Prüfer: Prof. Dr. Frank Würthner

2. Prüfer: Prof. Dr. Christoph Lambert

3. Prüfer: Prof. Dr. Ingo Fischer

des Öffentlichen Promotionskolloquiums

Tag des Öffentlichen Promotionskolloquiums:

14.12.2012

Doktorurkunde ausgehändigt am:

for my wife and family

List of Abbreviations

AFM	atomic force microscopy
CD	circular dichroism
COSY	correlated spectroscopy
DLS	dynamic light scattering
ESI-MS	electrospray mass spectrometry
ESI-TOF	electrospray ionization time-of-flight
EXSY	exchange spectroscopy
FRET	fluorescence resonance energy-transfer
HPLC	high performance liquid chromatography
HRMS	high resolution mass spectrometry
MALDI-TOF	matrix-assisted laser desorption injection time-of-flight
M.p.	melting point
NMR	nuclear magnetic resonance
NOE	nuclear Overhauser effect
DOSY	diffusion ordered spectroscopy
PBI	perylene bisimide
ppm	parts per million
ROESY	rotating-frame Overhauser enhancement spectroscopy
r.t.	room temperature
THF	tetrahydrofuran
TMS	tetramethylsilane
UV/Vis	ultraviolet/visible

Table of Contents

Chapter 1

Introduction and Aim of this Thesis

Self-assembly,[1] the organization of molecules based on non-covalent interactions, is crucial in nature to create complex and functional biological structures, such as base pairing in double helical DNA, organization of phospholipid bilayers in membranes and the folding of proteins to form quaternary structures. In materials science, self-assembly is emerging as an efficient "bottom-up" strategy to fabricate materials with unique properties unattainable by conventional synthetic routes. During the last decades, chemists have taken advantage of molecular self-assembly by using weak interactions, i.e. hydrogen bonding,[2] π-π-stacking,[3] metal ion coordination[4] and solvophobic effects[5] to build supramolecular architectures as nano- and soft materials[6] or molecular devices and machines.[7] The rapid development of this field is remarkable on account of the successful constructions of many spectacular supramolecular aggregates with increasing complexity.

As one of the important non-covalent forces relevant to self-assembly, aromatic π-π-interactions[3] exert significant influence on determining the structure and properties of supramolecular assemblies in many key biological processes.[8] Inspired by the light harvesting apparatus of purple bacteria that efficiently concentrates solar energy using an array of self-assembled chlorophyll dyes,[9] self-assembly of artificial functional dye molecules has attracted great attention in biological and materials sciences.[10] A large number of self-assembled π-conjugated systems featuring charge and/or energy transport properties have been employed as effective electronic and photonic molecular devices, such as organic field effect transistors[11] and solar cells.[12] However, the production of artificial dye assemblies that mimic the sophisticated function of biomolecules has not yet been demonstrated. In a majority of cases, the improvement of their functional properties is based on the "trial-and-error" procedure. Strategies for precise control of multi-chromophore aggregates have rarely been explored at the nanoscopic scale.[13] To this end, programing discrete π-stacks is desirable to facilitate the investigation of optical and electronic interactions between artificial functional dyes. Investigation of such assemblies could potentially provide profound insights into the structure-property relationships of aggregated dyes.[14] Additionally, it has been recognized that the achievement of more complex assemblies demands not only a detailed investigation of thermodynamics involved in the characterization of ground-state energies, but also the kinetic and mechanistic studies related to the ground-state and transition-state energies.[15]

Among the most important industrial dyes and pigments, perylene bisimides (PBIs) are excellent photofunctional building blocks for light harvesting[16] and the most promising candidates for organic n-type semiconductor materials.[17] In solution, PBI compounds are capable of self-assembling into one-dimensional infinite columnar aggregates by means of strong solvophobic and π-π-interactions. Upon self-assembly these aggregates display distinct optical and electronic properties.[18] The degree of aggregation is governed primarily by three factors, i.e. concentration, temperature and solvent.[18b] However, more detailed elucidation of the structure-property relationships are difficult because of the random aggregate sizes, i.e. they exist as a polydisperse mixture of aggregates such as dimers, trimers and higher oligomers under thermodynamic equilibrium.

The aim of this thesis is to program the self-assembly of PBIs to form discrete aggregates (Figure 1). The strategies employed to precisely control the aggregation behavior of PBIs relies on prescient molecular design and subsequent successful synthesis of the proper PBI building blocks. Modification of the target PBIs is limited to the two imide positions, as introduction of bay-substituents distorts the PBI core and therefore, alters the optical properties as well as the aggregation strength of parent PBIs.[19] By means of conventional spectroscopic methods like NMR and UV/Vis measurements, the structural and optical features of discrete PBI aggregates can be elucidated to reveal their structure-property relationships. Associated with quantum-chemical calculations, general concepts for effective production of artificial dye assemblies with desired optical and electronic properties would be expected.

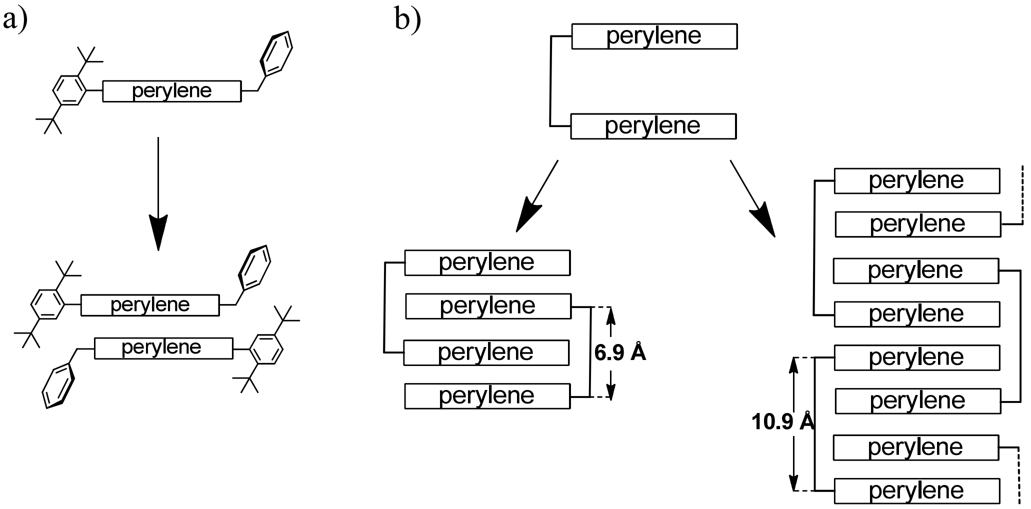

Figure 1. Schematic representation of the strategies for discrete PBI aggregate formation by modification of imide substituents.

Chapter 2 gives a literature overview of self-assembly kinetics. Three aspects including experimental methods, kinetic versus thermodynamic control and mechanistic studies of self-assembly processes are exemplified and discussed.

Chapter 3 is focused on the discrete dimer formation of parent PBIs realized by means of delicate steric control (Figure 1a). As the most basic assembly, dimer aggregates of PBIs are the most used model for theoretical investigations. Despite their obvious importance in understanding dye-dye interactions, discrete PBI dimers are very difficult to observe experimentally due to the inherent aggregation propensity of large π-conjugated scaffolds.[20] This chapter describes fundamental insights into dimerization thermodynamics of PBIs probed by NMR and UV/Vis spectroscopy with reference to solvent effects and ^{1}H NMR linewidth analysis upon PBI π-π-interactions.

In **Chapter 4**, the dimerization study is extended to include exclusively formed PBI quadruple stacks, i.e. interdigitated dimer aggregates of tweezer-like PBI dyads (on the left of Figure 1b). Such backbone-supported PBI stacks assembled via multiple π-π-interactions exhibit high kinetic stability. The enhanced kinetic stability enables straightforward investigation of the distinct optical properties of PBI quadruple stacks. Time-dependent absorption measurements are performed to assess the rates and activation energy of the disassembly process.

By extending the backbone length the tweezer may accommodate two PBI units. As a consequence, oligomeric stacking of the extended PBI dyad (on the right of Figure 1b) was observed which will be in **Chapter 5**. With great effort, both thermodynamic and kinetic investigations are performed to depict a full energy landscape of the cooperative process of the backbone-directed PBI self-assembly.

A summary of this thesis is presented in **Chapter 6** in English and German.

References

[1] a) G. Whitesides, J. Mathias, C. Seto, *Science* **1991**, *254*, 1312-1319; b) G. M. Whitesides, B. Grzybowski, *Science* **2002**, *295*, 2418-2421; c) D. Philp, J. F. Stoddart, *Angew. Chem. Int. Ed.* **1996**, *35*, 1154-1196; d) J.-M. Lehn, *Supramolecular Chemistry*, VCH, Weinheim, **1995**.

[2] a) J. Bernstein, M. C. Etter, L. Leiserowitz, *The Role of Hydrogen Bonding in Molecular Assemblies (Chapter 11 in Structure Correlation)*, Wiley-VCH Weinheim, **2008**; b) L. J. Prins, D. N. Reinhoudt, P. Timmerman, *Angew. Chem. Int. Ed.* **2001**, *40*, 2382-2426.

[3] a) C. A. Hunter, *Angew. Chem. Int. Ed.* **1993**, *32*, 1584-1586; b) C. A. Hunter, *Chem. Soc. Rev.* **1994**, *23*, 101-109; c) C. A. Hunter, K. R. Lawson, J. Perkins, C. J. Urch, *J. Chem. Soc., Perkin Trans. 2* **2001**, 651-669; d) C. A. Hunter, J. K. M. Sanders, *J. Am. Chem. Soc.* **1990**, *112*, 5525-5534.

[4] a) B. J. Holliday, C. A. Mirkin, *Angew. Chem. Int. Ed.* **2001**, *40*, 2022-2043; b) R. Chakrabarty, P. S. Mukherjee, P. J. Stang, *Chem. Rev.* **2011**, *111*, 6810-6918; c) B. Linton, A. D. Hamilton, *Chem. Rev.* **1997**, *97*, 1669-1680.

[5] a) Z. Chen, B. Fimmel, F. Würthner, *Org. Biomol. Chem.* **2012**, DOI: 10.1039/C1032OB07131B; b) M. S. Cubberley, B. L. Iverson, *J. Am. Chem. Soc.* **2001**, *123*, 7560-7563; c) J. C. Nelson, J. G. Saven, J. S. Moore, P. G. Wolynes, *Science* **1997**, *277*, 1793-1796; d) C. Reichardt, *Solvents and Solvent Effects in Organic Chemistry*, Wiley-VCH, Weinheim, **2003**.

[6] a) I. W. Hamley, *Angew. Chem. Int. Ed.* **2003**, *42*, 1692-1712; b) E. Katz, I. Willner, *Angew. Chem. Int. Ed.* **2004**, *43*, 6042-6108; c) J. C. Love, L. A. Estroff, J. K. Kriebel, R. G. Nuzzo, G. M. Whitesides, *Chem. Rev.* **2005**, *105*, 1103-1170; d) P. K. Vemula, G. John, *Accounts. Chem. Res.* **2008**, *41*, 769-782.

[7] a) V. Balzani, A. Credi, F. M. Raymo, J. F. Stoddart, *Angew. Chem. Int. Ed.* **2000**, *39*,

3348-3391; b) V. Balzani, A. Credi, M. Venturi, *Molecular Devices and Machines*, Wiley-VCH Weinheim, **2004**; c) B. L. Feringa, R. A. van Delden, M. K. J. ter Wiel, *Molecular Switches*, Wiley-VCH Weinheim, **2001**; d) F. Hof, S. L. Craig, C. Nuckolls, J. J. Rebek, *Angew. Chem. Int. Ed.* **2002**, *41*, 1488-1508; e) E. R. Kay, D. A. Leigh, F. Zerbetto, *Angew. Chem. Int. Ed.* **2007**, *46*, 72-191.

[8] a) E. A. Meyer, R. K. Castellano, F. Diederich, *Angew. Chem. Int. Ed.* **2003**, *42*, 1210-1250; b) L. M. Salonen, M. Ellermann, F. Diederich, *Angew. Chem. Int. Ed.* **2011**, *50*, 4808-4842.

[9] a) T. Pullerits, V. Sundström, *Accounts. Chem. Res.* **1996**, *29*, 381-389; b) X. Hu, T. Ritz, A. Damjanovic, F. Autenrieth, K. Schulten, *Q. Rev. Biophys.* **2002**, *35*, 1-62; c) T. S. Balaban, H. Tamiaki, A. R. Holzwarth, *Top. Curr. Chem.* **2005**, *258*, 1-38; d) G. McDermott, S. M. Prince, A. A. Freer, A. M. Hawthornthwaite-Lawless, M. Z. Papiz, R. J. Cogdell, N. W. Isaacs, *Nature* **1995**, *374*, 517-521.

[10] a) F. J. M. Hoeben, P. Jonkheijm, E. W. Meijer, A. P. H. J. Schenning, *Chem. Rev.* **2005**, *105*, 1491-1546; b) L. Brunsveld, B. J. B. Folmer, E. W. Meijer, R. P. Sijbesma, *Chem. Rev.* **2001**, *101*, 4071-4098; c) A. C. Grimsdale, K. Müllen, *Angew. Chem. Int. Ed.* **2005**, *44*, 5592-5629; d) F. Würthner, in *Supramolecular Dye Chemistry (Topics in Current Chemistry), Vol. 258*, Springer, Berlin, **2005**.

[11] C. Wang, H. Dong, W. Hu, Y. Liu, D. Zhu, *Chem. Rev.* **2012**, DOI: 10.1021/cr100380z.

[12] a) A. Mishra, P. Bäuerle, *Angew. Chem. Int. Ed.* **2012**, *51*, 2020-2067; b) T. M. Clarke, J. R. Durrant, *Chem. Rev.* **2010**, *110*, 6736-6767.

[13] J. K. Klosterman, Y. Yamauchi, M. Fujita, *Chem. Soc. Rev.* **2009**, *38*, 1714-1725.

[14] a) F. Würthner, K. Meerholz, *Chem.-Eur. J.* **2010**, *16*, 9366-9373; b) V. Dehm, M. Buchner, J. Seibt, V. Engel, F. Würthner, *Chem. Sci.* **2011**, *2*, 2094-2100.

[15] a) J. J. Hopfield, *PNAS* **1974**, *71*, 4135-4139; b) T. Yamane, J. J. Hopfield, *PNAS* **1977**, *74*, 2246-2250.

[16] a) M. R. Wasielewski, *Acc. Chem. Res.* **2009**, *42*, 1910-1921; b) F. Wuerthner, *Chem. Commun.* **2004**, 1564-1579.

[17] a) F. Würthner, M. Stolte, *Chem. Commun.* **2011**, *47*, 5109-5115; b) J. E. Anthony, A. Facchetti, M. Heeney, S. R. Marder, X. Zhan, *Adv. Mater.* **2010**, *22*, 3876-3892.

[18] a) F. Würthner, Z. Chen, V. Dehm, V. Stepanenko, *Chem. Commun.* **2006**, 1188-1190; b) Z. Chen, V. Stepanenko, V. Dehm, P. Prins, L. D. A. Siebbeles, J. Seibt, P. Marquetand, V. Engel, F. Würthner, *Chem.-Eur. J.* **2007**, *13*, 436-449; c) V. Dehm, Z. Chen, U. Baumeister, P. Prins, L. D. A. Siebbeles, F. Würthner, *Org. Lett.* **2007**, *9*, 1085-1088.

[19] Z. Chen, U. Baumeister, C. Tschierske, F. Würthner, *Chem.-Eur. J.* **2007**, *13*, 450-465.

[20] Z. Chen, A. Lohr, C. R. Saha-Möller, F. Würthner, *Chem. Soc. Rev.* **2009**, *38*, 564-584.

Chapter 2

Kinetics of Self-assembly

Abstract: Recent advances in the study of self-assembly kinetics are reviewed. In the first part of this chapter, the methodologies applied to investigate the kinetics of supramolecular self-assembly, including traditional ^{1}H NMR, UV/Vis and fluorescence spectroscopic experiments, as well as specific methods like two-dimensional exchange spectroscopy and magnetic birefringence are demonstrated and discussed. Secondly, kinetic and thermodynamic control over supramolecular chirality inversion, metal coordination and hydrogen-bonded assemblies, as well as molecular threading and recognition are exemplified. Finally, two eminent examples that explore the mechanisms of complex self-assembly processes are presented.

2.1 Introduction

Chemical kinetics is the area of science encompassing the measurement of reaction rates and the study of reaction mechanisms.[1] It has found wide applications ranging from the understanding of kinetic control in biological systems to industrial chemical synthesis that involve the use of catalyst and the optimization of reaction conditions.

In the field of supramolecular chemistry,[2] kinetics of self-assembly has recently captured more and more interest. Self-assembly is clearly a time-dependent process, and it may thus display kinetic control with the increase of assembly complexity. Indeed, kinetic self-assembly products trapped in local energy minima have been detected for many systems in recent years. In 1998, Lehn and coworkers reported the sequential formation of linear and circular helicates upon mixing the same ligands and metal ions.[3] Moreover, notable examples of kinetic control in assembly processes were illustrated in supramolecular chirality inversion,[4] molecular threading,[5] host-guest complexation,[6] metal coordination[3, 7] and hydrogen-bonded assemblies.[8] Specifically, a “molecular catalyst” for the formation of rosette-shaped assembly was presented by Reinhoudt et al. in 2002.[8a] Although a number of kinetically controlled self-assembling systems have been reported, well-developed theoretical discription of the construction of assemblies under kinetic control has yet to be established. It requires a mechanistic understanding of self-assembly processes and the energy differences of all transient species in the processes. However, it is still difficult to fully discribe the mechnism of a self-assembly process on account of its complexity.[9] Several pioneering works related to mechanistic investigations showed that self-assembly processes may mostly involve complex intra- or intermolecular catalysis by the coexisting species in a system.[9a-c]

2.2 Experimental Methods for Kinetic Studies of Self-assembly

Two principle factors must be considered when determining the proper approach to study self-assembly kinetics: 1) which spectroscopic methods provide a useful handle to probe the self-assembly process; and 2) how fast the self-assembly process takes place to ensure that the instrument is capable of functioning on the relevant time scale.

In general, all the conventional measurements applied for thermodynamic studies, i.e., ^{1}H NMR, UV/Vis, fluorescence and circular dichroism spectroscopies can also be employed to investigate the kinetics of self-assembly. Unusually, electrospray mass spectrometry and high-performance liquid chromatography are also applicable in kinetic experiments when performed in the time course of self-assembly process. Some other methods, for instance, two-dimensional exchange spectroscopy for (pseudo-)first-order slow exchange processes on NMR time scale and magnetic birefringence for probing morphology variations in solution, have been applied in specific kinetic studies. Additionally, applications of instrumentation like mixed-flow microreactors and stopped-flow equipment facilitate the investigation of very fast self-assembly processes.

2.2.1 ^{1}H NMR Spectroscopy

^{1}H NMR spectroscopy is a powerful tool to analyze the thermodynamics as well as kinetics of self-assembly. When an aggregation process exhibits rapid exchange between monomers and aggregates on the NMR time scale, a simple pattern of averaged resonances will be observed. Nonlinear regression analysis of the shifted averaged resonances in response to concentration variations can provide details of the thermodynamics of the aggregation process. In addition, given that the exchange process is kinetically slow, a ^{1}H NMR spectrum can distinguish individual species in a multi-component system.

By means of this primary analytical method, Isaacs and coworkers have explored the kinetic self-sorting of a four-component system comprising two cucurbit[*n*]uril molecules (CB[*n*]; $n = 6, 7$), cyclohexane diammonium **1** and two-faced alkyl-adamantyl-ammonium **2** (Figure 1).[6a] Both host molecules CB[6] and CB[7] can accommodate the cyclohexane ring of guest **1** and form tight 1:1 complexes. Due to steric influence, CB[7] with wider carbonyl-lined portals complexes the two-faced guest **2** preferentially, binding the adamantyl moiety inside the cavity, while CB[6] with smaller portals can only bind the alkyl moiety of guest **2**. Thus, upon mixing the four components in equivalent amounts together, there are two combinations of host-guest complexes. One combination is CB[6]·**2** and CB[7]·**1** which were immediately observed in the NMR spectrum after mixing the components. The second is

CB[6]·**1** and CB[7]·**2** that formed exclusively after 56 days. Accordingly, the former combination can be described as the kinetic product, while the latter is the thermodynamic product.

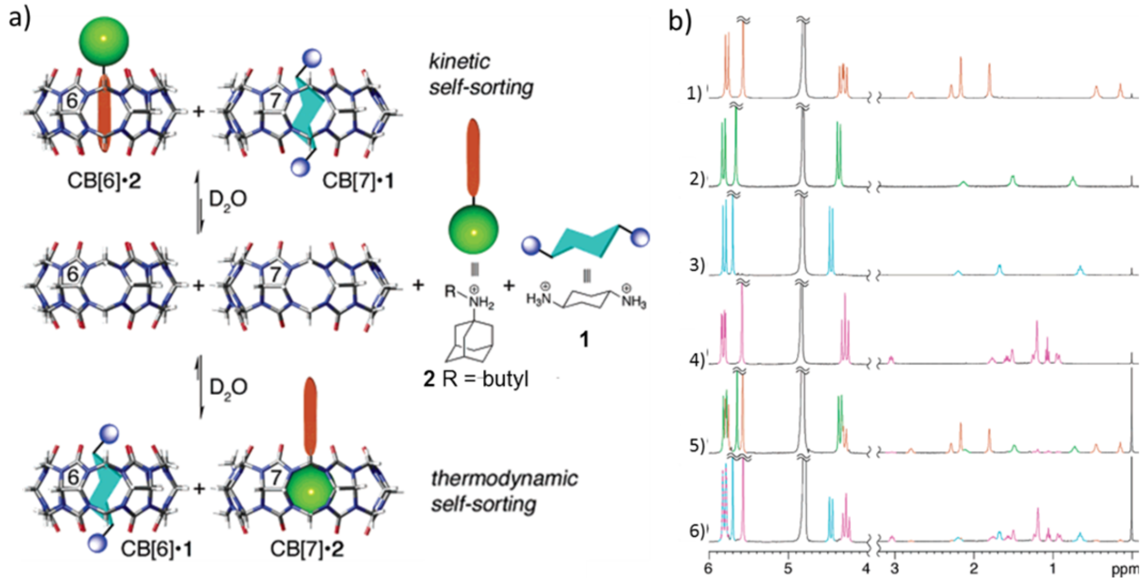

Figure 1. a) Schematic representation of kinetic versus thermodynamic self-sorting of a four-component system containing two host molecules CB[6] and CB[7] as well as two guest molecules **1** and **2**; b) ^{1}H NMR spectra (400 MHz, 298 K, 5 mM Na_2SO_4 in D_2O, pH = 7.0) of 1) CB[6]·**2**, 2) CB[7]·**1**, 3) CB[6]·**1**, 4) CB[7]·**2**, 5) a mixture of CB[6]·**2** and CB[7]·**1** recorded after 6 min and 6) a mixture of CB[6]·**1** and CB[7]·**2a** recorded after 56 days after mixing the components. Reproduced with permission from *J. Am. Chem. Soc.* **2006**, *128*, 14093-14102. Copyright 2012 American Chemical Society.

Time-dependent proton NMR measurements can quantitatively determine the kinetic rate constants since the integral of NMR signals reveals the relative amounts of the individual species in the system. The authors followed the formation (at room temperature) and dissociation (at 80–96 °C temperature) of complex CB[6]·**1** at a certain concentration by means of NMR monitoring. In this way, the association rate k_{in} and dissociation rate k_{out} for complex CB[6]·**1** were deduced to be 1.2×10^{-3} M^{-1} s^{-1} and 8.5×10^{-10} s^{-1}, respectively.

This study on kinetic self-sorting by host-guest complexation[6a] effectively illustrates the power of ^{1}H NMR spectroscopy as a general approach for probing kinetically and thermodynamically controlled assemblies[3, 5a-d, 7-8] and for providing accurate data for investigating the mechanisms of self-assembly processes.[9a, b]

2.2.2 UV/Vis Spectroscopy

UV/Vis spectroscopy is especially suited to explore the kinetics of chromophore self-assembly.[10] Pasternack et al. investigated the kinetics of porphyrin assembly on a DNA template by fitting the kinetic profiles at absorption peaks of reactant and product with an alternative and non-conventional approach that they developed for application on systems involving the growth of supramolecular assemblies.[10a] The authors analyzed additionally the kinetics of disassembly of the DNA bound porphyrin array, and incorporated time-dependent rate constants to precisely fit the kinetic data.[10b] In another work, they extended their kinetic studies to the self-assembly of two different J-aggregates: one a porphyrin without a template and the other a pseudoisocyanine on polyvinylsulfonate.[10c]

More recently, Arduini and coworkers studied the kinetics of the threading process of axle compound **3** into wheel-type host **4** from its upper rim (Figure 2).[10d] Upon the formation of pseudo-rotaxane $[\mathbf{4}\supset\mathbf{3}]_{\mathrm{up}}$, a new absorption band at 261 nm appeared. In order to follow the fast self-assembly process, a stopped-flow technique was applied and facilitated the recording of rapid kinetics in the millisecond time range.[6b, 10a, 10d] The kinetic absorbance curves were analyzed for $t \geq 2$ ms in terms of a second-order rate equation and gave the threading rate constant of 2.9×10^{7} M^{-1} s^{-1}. Furthermore, temperature-dependent kinetic experiments were carried out in the range of 277-303 K to evaluate the activation enthalpy $\Delta H^{\neq} = -8$ kJ mol^{-1} and activation entropy $\Delta S^{\neq} = 126$ J K^{-1} mol^{-1} according to the Eyring plot.

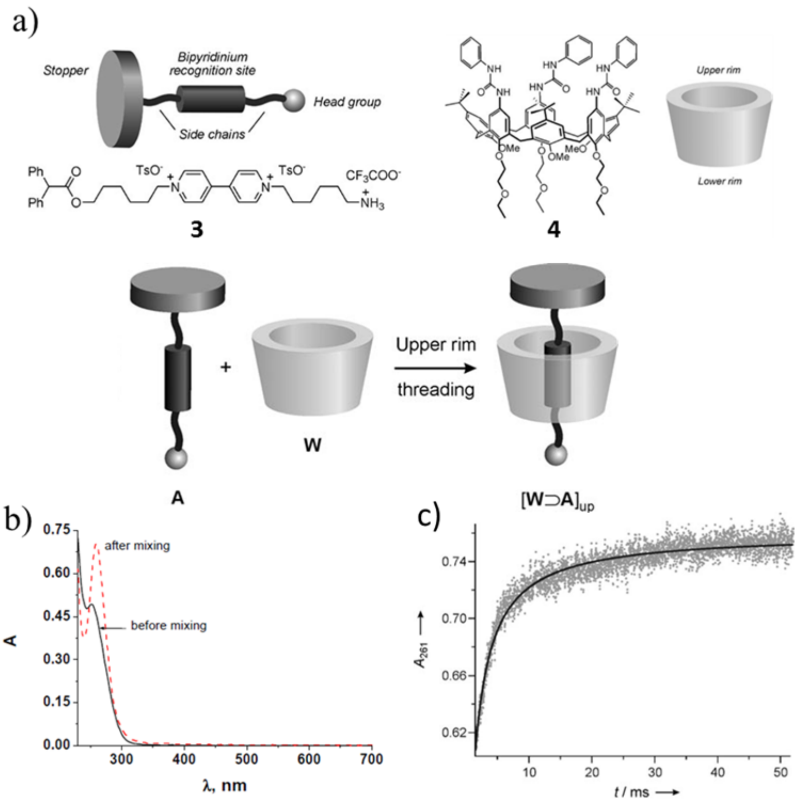

Figure 2. a) Schematic representation of pseudo-rotaxane formation of axle-type guest **3** and wheel-type host **4**. b) Absorption spectra recorded before (solid line) and after (dashed line) mixing **3** and **4** at a concentration of 1×10^{-5} M^{-1} in CH_2Cl_2 at ambient temperature. c) Stopped-flow kinetic trace monitored at 261 nm upon mixing **3** and **4** in equimolar amounts (1×10^{-5} M^{-1} in CH_2Cl_2) at 293 K. The solid line represents the data fitting according to a second-order rate equation. Reproduced with permission from *Chem. Eur. J.* **2009**, *15*, 3230-3242. Copyright 2012 John Wiley and Sons.

2.2.3 Circular Dichroism (CD)

In addition to UV/Vis spectroscopy, CD spectroscopy is also particularly useful to gain insight into the formation and packing properties of dye aggregates. With regard to chiral and/or helical supramolecular assemblies, CD spectroscopy is an especially powerful tool. Therefore, CD spectroscopy may be applied to measure the kinetic processes involved in the organization of chiral supramolecular assemblies.[4, 9a, 11] Würthner and coworkers synthesized both achiral and chiral bis(merocyanine) **5** and **6**, shown in Figure 3**.**[4a] The achiral dye **5** self-assembled into highly defined nanorods via supramolecular polymerization, but no sign of helicity was observed. Chiral derivative **6**, bearing two *R*-2-octyl side chains at the imide positions, self-assembled into nanorods that showed strong CD signals, thereby revealing their helicity.

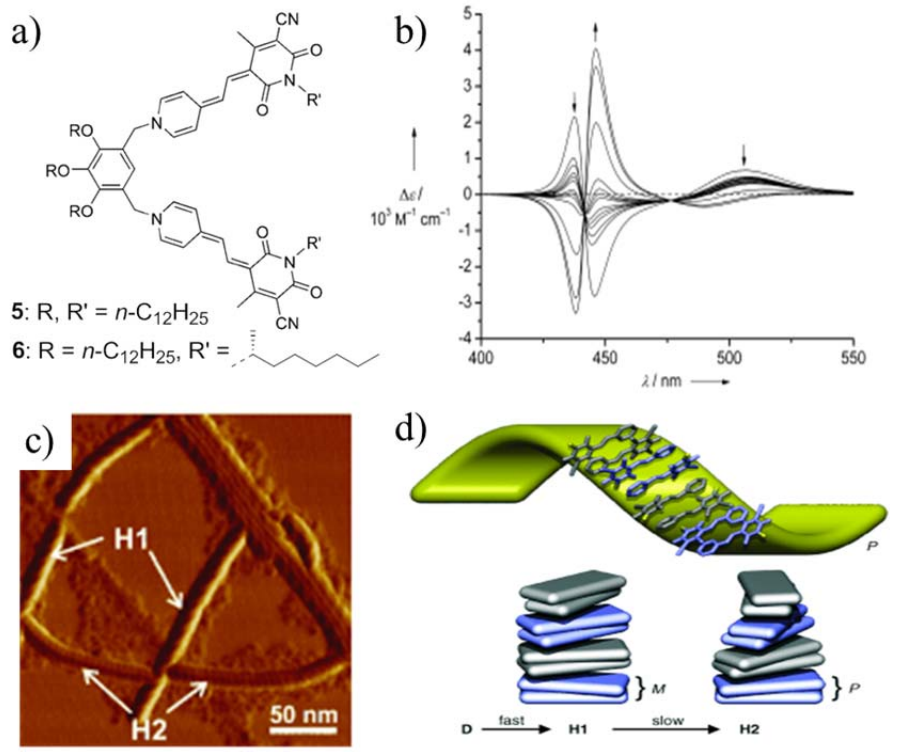

Figure 3. a) Chemical structure of bis(merocyanine) **5** and **6**; b) time-dependent CD spectra (96-7050 min) showing the transition from the initially formed H-aggregated species **H1** into the thermodynamically more stable H-aggregated species **H2** for dye **6** at 10^{-5} M in a mixture of THF/MCH (*v*:*v* = 3:7) recorded at ambient temperature; c) AFM phase images of the samples prepared by spin-coating of solutions of dye **6** (10^{-5} M in a solvent mixture of THF/MCH (*v*:*v* = 3:7)) onto HOPG at 11 hours after initiation of self-assembly; d) schematic representation of the proposed self-assembly process of dye **6**. Reproduced with permission from *Angew. Chem. Int. Ed.* **2005**, *44*, 5071-5074. Copyright 2012 John Wiley and Sons.

Upon addition of non-polar MCH solvent into a THF stock solution of chiral bis(merocyanine) **6**, time-dependent CD and UV/vis spectral changes were recorded over the course of one hour to follow the transition from instantaneously formed dimer **D** to the H-aggregated species **H1**. The formation of the **H1** aggregate obeys first-order kinetics, and the corresponding rate constant is $k = 0.42$ min^{-1}. To the authors' surprise, a total inversion of the CD spectra was observed during the following time (96–7050 min), while the UV/Vis spectra remained almost unchanged. In comparison with the kinetically controlled intermediate **H1**, the thermodynamic self-assembled product that displayed the identical H-aggregate absorption spectrum but inversed CD spectrum was denoted as **H2**. By taking AFM images, the difference of the **H1** and **H2**-aggregated nanorods were visually recognized. Both aggregates exhibit right-handed helical structures, but the thermodynamically favored **H2** assembly is more compact. Accordingly, it was proposed that the *M* to *P* change of the helical twist between the closest neighboring chromophores in the hierarchically wound stacks induced the H1 to H2 transition. In a similar manner to changing solvent ratios to alter the binding constants of self-assembly in thermodynamic experiments, the rate constant can be modulated by the volume ratio of a two-solvent system. In the present case, supramolecular stereomutation was detected on convenient time scales upon mixing the good solvating THF and non-polar MCH solvents in a volume ratio of 30:70.

2.2.4 Fluorescence Spectroscopy

Fluorescence spectroscopy can be used to investigate dynamic processes at very low concentration, as the sensitivity of this technique enables detection of fluorescent species even at nanomolar concentrations. The limit of this method is that the assembled species must be[6b, 9c, 12] or be outfitted with[13] fluorophores.

By observing fluorescence resonance energy transfer (FRET) processes, Rebek and coworkers investigated the kinetics of hetero-dimerization of calix[4]arenes **7** and **8** functionalized with sulfonyl urea and aryl urea on their wider rims, respectively (Figure 4).[13] By tagging one calixarene component with a donor fluorophore and the other with an acceptor one, hetero-dimerization brings the two chromophores within 20 Å, a distance suitable for efficient energy transfer to occur between donor and acceptor. Thus, FRET could be monitored at the emission maxima of both donor and acceptor fluorophores. After mixing calixarene **7** and **8**, the enhancement of acceptor emission and the reduction of donor emission indicated the occurrence of FRET, thus reflecting the hetero-dimerization process. Quantitatively, the association rate constant was derived from the time-dependent fluorescence measurements by using an excess of **7**. In this way, the second-order assembly was simplified by means of pseudo-first-order approximation to yield the k_{ass} of 3000 M^{-1} s^{-1} in benzene at 25 °C.

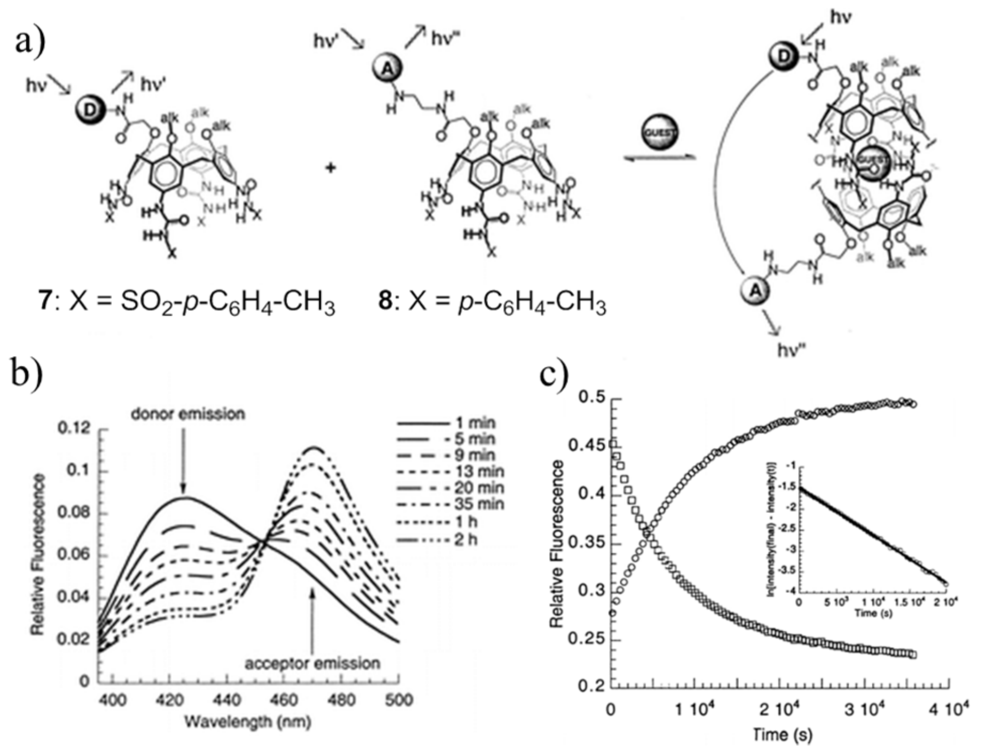

Figure 4. a) Schematic representation of dimerization of **7** and **8** and the FRET process observed in the dimeric state. b) time-dependent fluorescence measurements upon a combination of **7** and **8** at 100 nM in chloroform. c) Time-dependent changes in fluorescence intensity of the donor emission maximum (415 nm, squares) and acceptor intensity maximum (455 nm, circles) upon a combination of **7** (250 nM) and **8** (100 nM) in benzene at 25 °C. Inset shows the pseudo-first-order kinetic treatment of the data. Reproduced with permission from *J. Am. Chem. Soc.* **2000**, *122*, 7876-7882. Copyright 2012 American Chemical Society.

2.2.5 Electrospray Mass Spectrometry (ESI-MS)

On account of the severe superposition of signals in a multi-component system, NMR spectroscopy is suitable only when relatively simple and uniform aggregates are generated. To this end, mass spectrometry may be a better choice for a complicated system as each species corresponds to a single mass peak, distinguishable from others in a majority of cases.[14]

Very recently, Schalley and coworkers unitized the ESI-MS to probe the kinetics of formation of intermediates and error-correction during the self-sorting[15] of multiply threaded pseudo-rotaxanes (Figure 5).[5e] For a 3-component mixture consisting of a divalent ammonium receptor axle **9**-2H·2PF$_6$ and two crown ethers C7 and C8 present in an equimolar ratio, the thermodynamic properties control the formation of the final self-sorted product **13**-2H·2PF$_6$ since C7 and C8 create the most stable complex at the respective blue and green ammonium position of receptor axle **9**-2H·2PF$_6$.[14, 16] On the other hand, if C7 binds at the green ammonium position earlier than C8, the complexation of C8 at the blue ammonium position is blocked owing to steric hindrance of both approaching sites. Allowing for the sequence-specific assembly and the potential mismatch of kinetic and thermodynamic order, the self-sorting route to final product **13**-2H·2PF$_6$ cannot be straightforward. To monitor the intermediates and wrongly assembled structures, time-dependent ESI-MS measurements proved effective to elucidate the complexation kinetics of **13**-2H·2PF$_6$ self-sorting as demonstrated in Figure 5.

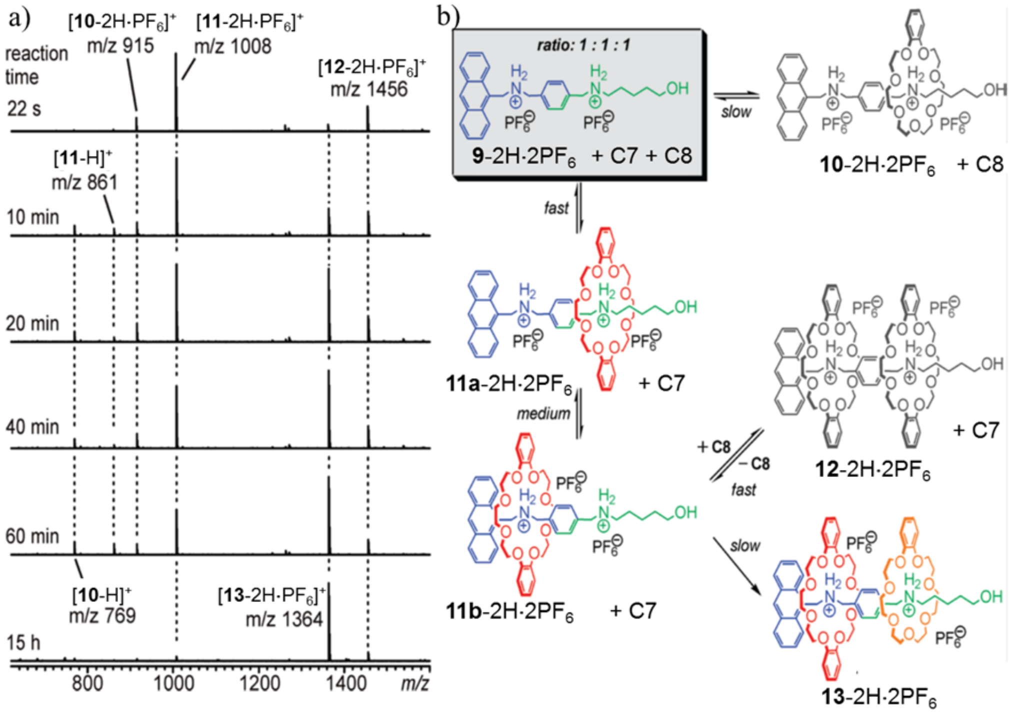

Figure 5. a) ESI mass spectra of an equimolar mixture of C7, C8 and 3-2H2PF6 recorded after different reaction times (295 K, CH_2Cl_2: CHCN = 8:1, 250 µM). b) Formation pathways of 10-2H2PF6 as identified from the MS results. Reproduced with permission from *J. Am. Chem. Soc.* **2010**, *132*, 2309-2320. Copyright 2012 American Chemical Society.

In this study a mixed-flow microreactor (Figure 6) was coupled to an ESI mass spectrometer. With this set-up the authors achieved ESI-MS detection in the time window of a second or less. Despite the high resolution and high sensitivity, ESI-MS can only be employed as a qualitative or semi-quantitative method since the peak intensities in mass spectra do not necessarily indicate the concentration of detected species in solution.[17] Additionally, care has to be taken when assigning the MS signals due to the existence of ionization artifacts and the dissociation of non-covalent complexes during ionization.[5e]

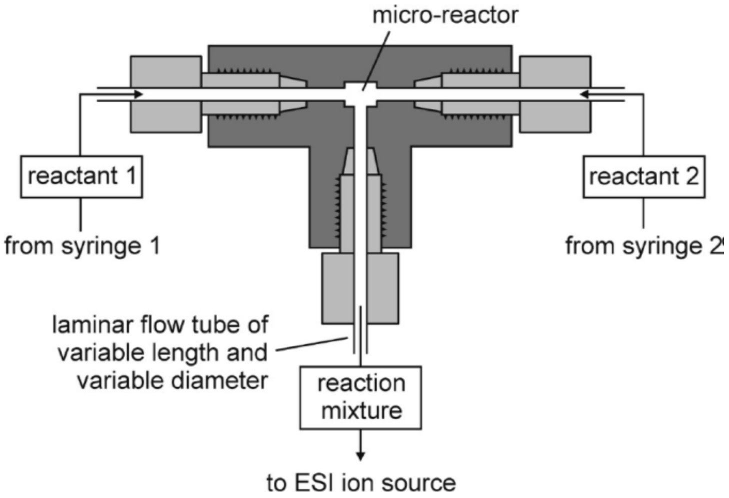

Figure 6. Schematic representation of the ESI-MS-coupled mixed-flow microreactor for studying short-time kinetics. Reproduced with permission from *J. Am. Chem. Soc.* **2010**, *132*, 2309-2320. Copyright 2012 American Chemical Society.

2.2.6 High-performance Liquid Chromatography (HPLC)

Generally applied as a chromatographic technique used to separate a mixture of compounds, HPLC can also be employed for kinetic studies of self-assembly. In Li's group, this separation method was used to probe the synthesis of perylene bisimide (PBI) catenane **16** starting from PBI monomer **14** as outlined in Figure 7.[18] Three possible routes based on molecular self-assembly of PBI driven by π-π-interactions were proposed. The catenane **16** can feasibly originate from the reaction of linear monomer **14** and cyclic dimer **15** (k_2), or two cyclic dimers **15** (k_3), or four linear monomers **14** (k_4).

To shed light on the kinetics and mechanistic analysis, the authors performed HPLC monitoring at various reaction times (Figure 7b). With regard to the decrease of monomer **14**, the reaction coordinate could be divided into an initial period (0–25min) and a steady-state period (more than 25 min), both of which followed second-order (or pseudo-second-order) reaction kinetics (Figure 7c). As demonstrated by the variation of concentration as a function of reaction time (Figure 7d), the major product was monocyclic dimer **15** and there was no appreciable formation of catenane **16** in the initial period. Conversely, in the steady-state period the concentration of dimer **15** remained constant and the major new product was catenane **16**. Accordingly, the experimental observation could only be rationalized by the first proposal (k_1 + k_2), suggesting the mostly possible pathway to catenane **16** from linear monomer **14** and cyclic dimer **15**.

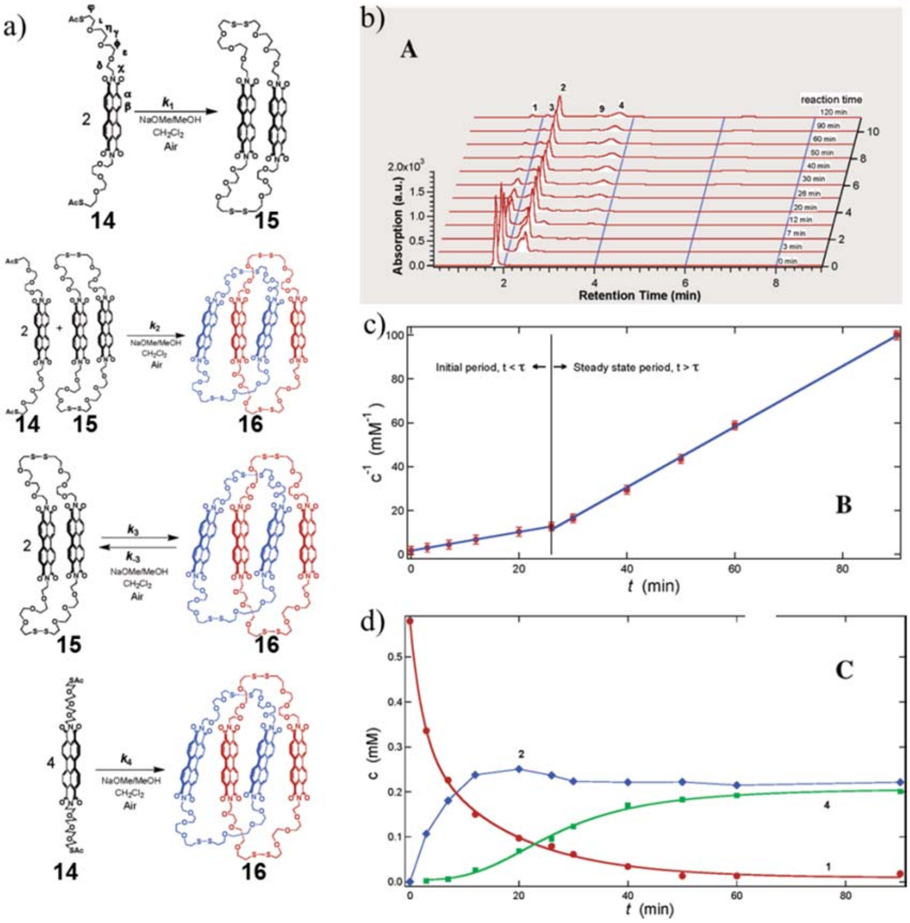

Figure 7. a) Three possible routes to form PBI catenane **16** starting with monomer **14**. b) HPLC monitoring of reaction mixture at various reaction time (monomer 1 at 0.58 mM). c) Linear relationships of $c(\mathbf{14})^{-1}$ versus t indicating second-order (or pseudo-second-order) reaction with respect to monomer **14** in both initial period and steady-state period. d) Plots of concentration changes of monomer **14** (red), dimer **15** (blue) and catenane **16** (green) with time. Reproduced with permission from *J. Am. Chem. Soc.* **2006**, *128*, 11150-11159. Copyright 2012 American Chemical Society.

2.2.7 *Two-dimensional Exchange Spectroscopy (2D EXSY)*

2D EXSY is an advanced technique for studying the kinetics of chemical or conformational exchange processes.[19] The unique ability to resolve and assign the separate signals owing to nuclei in different chemical environments makes it especially powerful for kinetic studies. This method is based on selective irradiation (saturation or inversion) of one or more resonances of an exchanging system, followed by examination of the effect of that perturbation on the remaining sites.[20] If the exchange process proceeds at a detectable rate (between 10^{-2} and 10^{2} s^{-1}), 2D EXSY can make use of the additional NMR spectral changes to offer site to site exchange rate constants.[20]

The 2D NMR cross-peaks provide a clear picture of the exchange process. The essential feature of a quantitative 2D EXSY experiment is the relationship between the cross peak intensities (volume integrals) and the rate constant for chemical or conformational exchange.[20] The pulse sequence for a 2D EXSY experiment is shown in Figure 8a. The labeling time t_1 (sometimes called evolution time) is variable. The mixing time t_m is the time during which chemical exchange occurs and is monitored by the 2D experiment. The acquisition time t_2 is also variable and the same as the acquisition time t in 1D NMR.

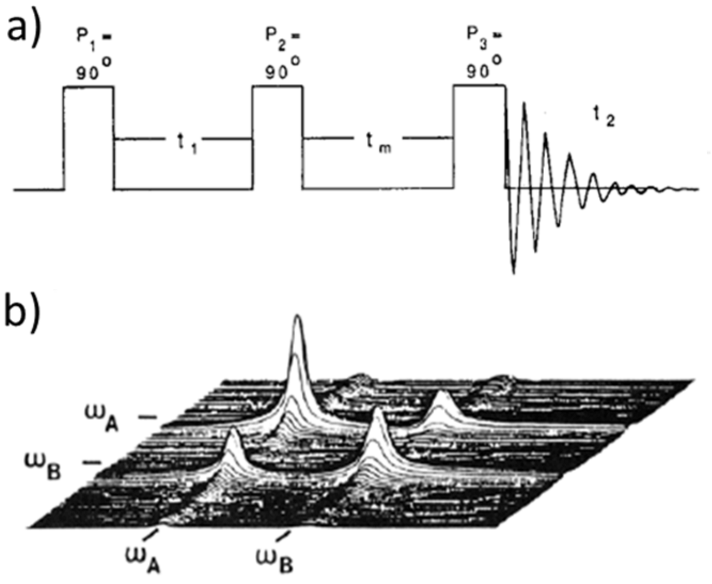

Figure 8. a) Pulse sequence used in a 2D EXSY experiment. This sequence is repeated for a number of incremented t_1 periods and constant t_m. b) A typical 2D exchange spectrum between species A and B. Reproduced with permission from *Chem. Rev.* **1990**, *90*, 935-967. Copyright 2012 American Chemical Society.

For an exchange process between species A and B,

$$\mathrm{A} \underset{k_b}{\overset{k_a}{\rightleftharpoons}} \mathrm{B}$$

the exchange rate constant can be expressed as

$$k_{ex} = k_a + k_b = t_m^{-1} \ln\frac{r+1}{r-1}$$

where r is related to the intensity ratio between the cross peaks by

$$r = 4X_\mathrm{a}X_\mathrm{b}\frac{I_{aa}+I_{bb}}{I_{ab}+I_{ba}} - (X_\mathrm{a} - X_\mathrm{b})^2$$

(I is the volume integrals of cross peaks, X_a and X_b are the mole fractions of populations A and B, respectively.) If the 2D EXSY measurement is recorded under the condition of $X_a = X_b = 0.5$, the r value can be simplified as

$$r = \frac{I_{aa}+I_{bb}}{I_{ab}+I_{ba}}$$

Thus, the rate constant can be expressed in terms of cross peak intensities, which is experimentally obtainable. The slope in a plot of $\varphi = \ln\frac{r+1}{r-1}$ as a function of t_m gives the exchange rate constant k_ex.

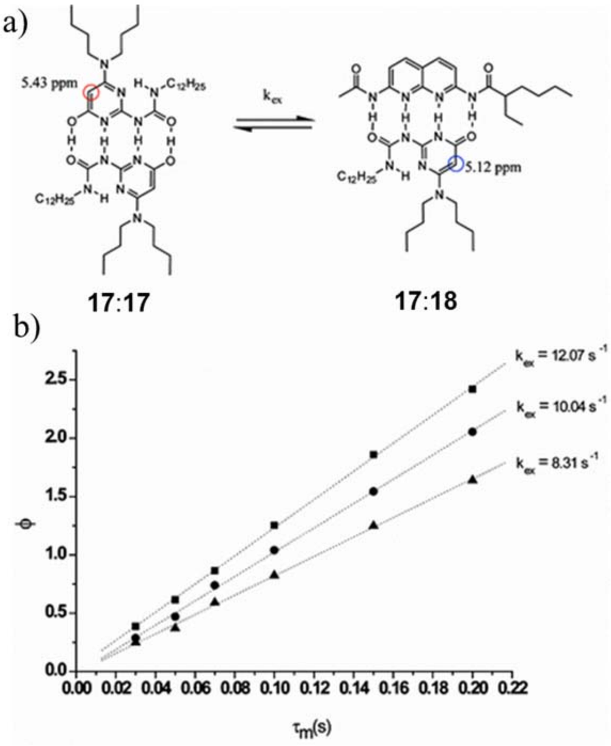

Figure 9. a) Pseudo-first-order exchange process of homocomplex **17**:**17** and heterocomplex **17**:**18**. b) Plot of φ versus mixing time t_m for 1:2 mixtures of **18** and **17** at three different concentrations (triangle: 5mM **18** and 10 mM **17**; circle: 10 mM **18** and 20 mM **17**, rectangle: 20 mM **18** and 40 mM **17**). The dotted lines represents the linear fitting according to the equation $\varphi = k_\mathrm{ex}\ t_\mathrm{m}$. Reproduced with permission from *J. Am. Chem. Soc.* **2008**, *130*, 5479-5486. Copyright 2012 American Chemical Society.

To study the exchange kinetics of 2-ureido-pyrimidinone **17** and 2,7-diamido-1,8-naphthyridine **18**, 2D EXSY experiments were conducted by Sijbesma, Meijer and coworkers in solutions containing **18** and **17** in a molar ratio of 1:2, in which case homodimer **17**:**17** and the heterodimer **17**:**18** exist in approximately equimolar amounts.[9b] At three concentrations, the φ value calculated from the volume integrals of the alkylidene protons of homodimer **17**:**17** and heterodimer **17**:**18** at respective 5.43 and 5.12 ppm were linearly fitted with the variations of mixing time t_m, resulting in the pseudo-first-order rate constant k_{ex} from 8.31 to 12.07 s^{-1} for exchange process upon increasing concentration.

In addition, the 2D EXSY experiments have been utilized to determine the axle exchange rate in pseudo-rotaxanes,[5e] guest exchange kinetics in molecular baskets[9g] and the rate constant for dissociation/dimerization of calix[4]arene derivative.[21]

2.2.8 Magnetic Birefringence

Magnetic birefringence is a newly developed method for determining the structure of aggregates in solution.[22] Unlike atomic force microscopy (AFM) that is performed on a substrate in the solid state, the measurement of magnetic-field-induced birefringence can be achieved in solution in a contact-free way; and therefore, the effects of solvent evaporation and molecule-substrate interactions on the aggregate structure may be avoided. This technique is sensitive to the degree of molecular order of an entire aggregate rather than the short-range order as probed by methods like UV/Vis and CD spectroscopy.[22a] In an experimentally available magnetic field, only ordered aggregates of sufficient size can overcome the thermal randomization and alignment, while disordered aggregates or small molecules cannot.[23] The induced alignment can be detected optically as magnetic birefringence Δn, which depends on size, order and density of aggregates. As a result, ordered and disordered aggregates can be distinguished in a quantitative manner.[22a] However, this measurement needs normally a known model for comparison or the assistance of other techniques to validate the observations.[22]

Christianen, De Feyter and coworkers investigated the kinetics of temperature-induced aggregation of macrocyclic molecule **19** in solution by using magnetic-field-induced birefringence (Figure 10).[22a] The magnetic birefringence of a solution of macrocycle **19** (at 10^{-4} M in cyclohexane) was measured over 400 hours at different temperatures T_f. As illustrated by the measurement at T_f = 14 °C (Figure 10c), three different time regimes were recognized. At the initiation of the experiment, no birefringence was observed; however, light scattering experiments indicated the presence of large objects. These findings are attributed to the formation of disordered aggregates (regime I). During a period of 50 hours, birefringence and aggregate absorption increased with time. AFM and small-angle X-ray scattering verified the transformation of random aggregates into ordered fibers within this period. By fitting the shapes of Δn curve, the molecular number in aggregates was estimated to be 5000 on average (regime II). After 50 hours, Δn value began to reduce due to the formation of a fiber network (regime III).

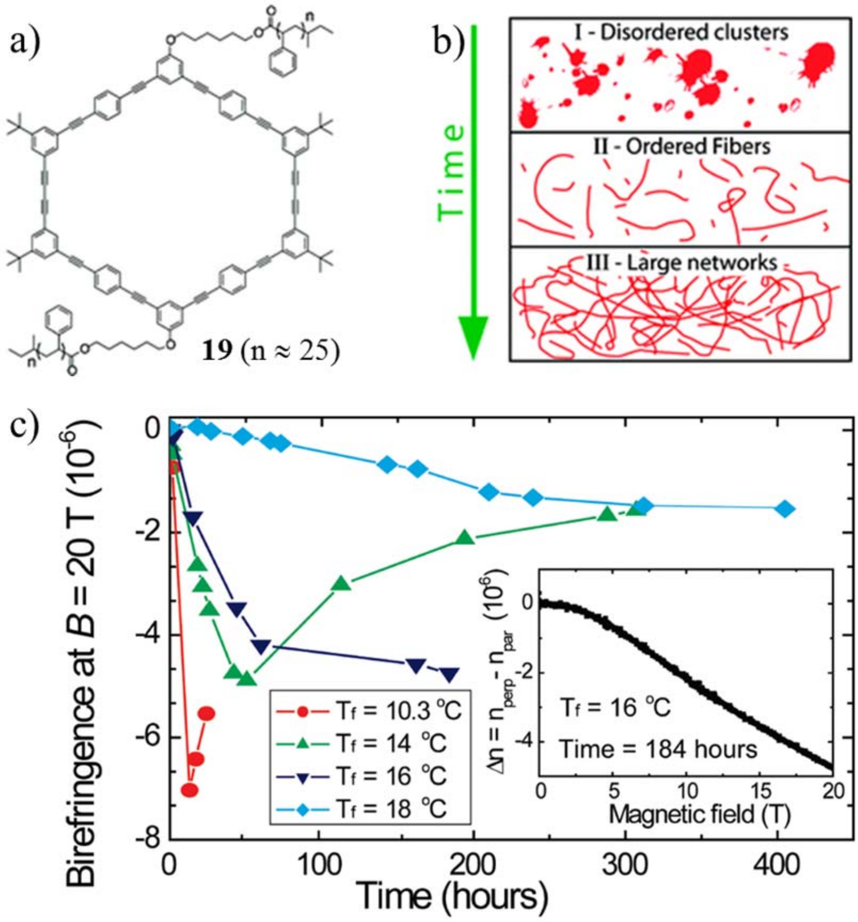

Figure 10. a) Chemical structure of macrocyclic molecule **19**. b) Schematic representation of the situation at T_f = 14 °C, showing the transition from disordered objects (I) to ordered fibers (II) to a large network of fibers (III). c) Solution birefringence at B = 20 T as a function of time for different temperature T_f. The inset shows a full birefringence curve. Reproduced with permission from *J. Am. Chem. Soc.* **2009**, *131*, 14134-14135. Copyright 2012 American Chemical Society.

2.3 Kinetic versus Thermodynamic Control

In nature, biological systems exist inherently in a non-equilibrium state in both time and space. Nature uses various strategies to maintain control over the temporal and spatial distribution of significant biological species such as proteins, nucleic acids and ions.[24] Many biological processes that are essential in gene expression, such as chromatin remodeling and transcriptional control, are mostly regulated by kinetic control.[25] Recent thermodynamic measurements showed that the most stable structural form of a number of proteins under cellular conditions is fibrillar.[26] Thus, this finding implies that the folding and presumably function of many proteins may only be under kinetic control.[27]

Long ago, chemists realized the importance of kinetic versus thermodynamic control in organic synthesis.[28] In nearly all chemical reactions multiple products can be formed, and the distribution of these products is governed by a delicate balance of thermodynamics and kinetics. The thermodynamic product is the final product corresponding to the overall energy minimum, while the kinetic product is unstable or metastable and trapped in a local energy minimum. Whilst a kinetic product can be an intermediate on the pathway to the thermodynamic product, it is also possible that a kinetic product is not on the pathway and has an entirely different conformational structure than the thermodynamic product.[1a, 1c] By altering reaction conditions the course of a reaction may be steered towards a desired product, either by thermodynamics or by kinetics.

In supramolecular systems, such as those involving supramolecular chirality inversion,[4] metal coordination,[3, 7] hydrogen-bonded assemblies,[8] or molecular threading and recognition,[5-6] both kinetic and thermodynamic products have been observed.

2.3.1 Supramolecular Chirality Inversion

Supramolecular chirality is the expression of absolute molecular chirality at the macromolecular level and originates from the self-assembly of multiple copies of one or more chiral components or from the self-organization of chiral oligomeric systems.[4b] Upon the formation of long nanotubes self-assembled from small molecules, supramolecular chirality detected by means of CD spectroscopy exhibits in some cases chirality inversion in response to the time, solvent, temperature and/or concentration.[4]

Fenniri et al. studied helical rosette nanotubes (RNT), shown in Figure 11, obtained through the self-assembly of guanine-cytosine derivative **20** in methanol (referred to as M-chiromer).[4b] Unexpectedly, they observed mirror image supramolecular chirality inversion (referred to as W-chiromer) upon the addition of very small amounts of water (less than 1 vol%). Both M- and W-chiromers exhibit the same hierarchical organization, dimensions and shape confirmed by NOESY NMR experiments, UV/Vis spectra and AFM/TEM/SEM imaging. The formation of M-chiromer is under kinetic control, while the W-chiromer is attributed to the thermodynamic product on the basis of following findings: 1) time-dependent dynamic light scattering (DLS) and SEM studies established that the growth of M-chiromer is faster than that of W-chiromer. 2) upon heating the M-chiromer sample adopted the opposite supramolecular chirality, while the heated W-chiromer sample exhibited no changes in CD profile over 336 hours. 3) with catalytic amounts of W-chiromer (10 mol%), M-chiromer underwent complete chirality inversion as monitored by time-dependent CD spectra. Assisted by computational studies, a mechanism for chiromer formation was proposed. Dissolution of compound **20** in water or methanol should most likely lead to the formation of both left- and right-handed short rosette nanotubes. Because there is no energy barrier to the formation of left-handed RNTs in methanol, the population of M-chiromer will grow faster (kinetic pathway) and take over the supramolecular chirality of the system. On the contrary, the RNT growth is significantly slower and the initial energy barriers to form left- and right-handed RNTs are similar in water, the W-chiromer with lower energy will form preferentially as a thermodynamic product.

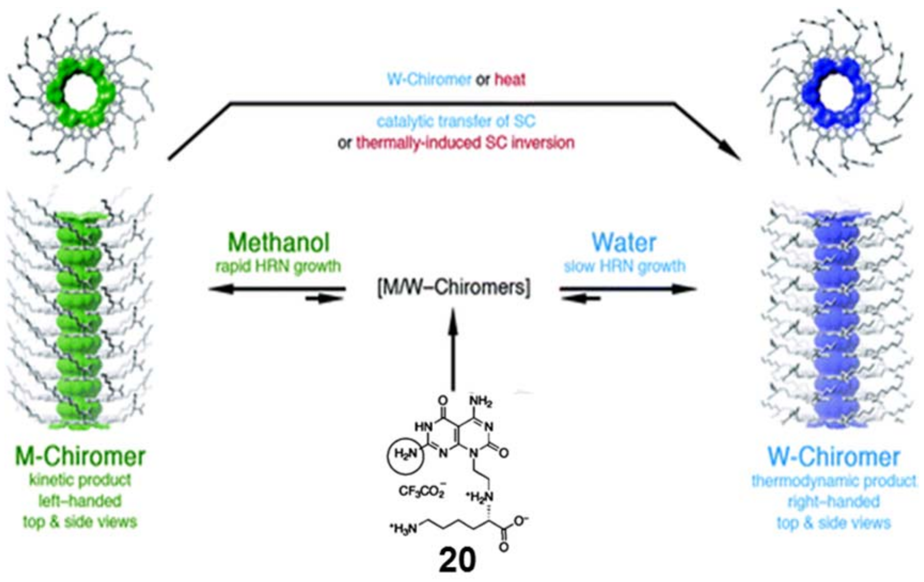

Figure 11. Kinetic and thermodynamic pathways for chiromer formation and interconversion in methanol (left) and water (right). Reproduced with permission from *J. Am. Chem. Soc.* **2007**, *129*, 5735-5743. Copyright 2012 American Chemical Society.

In another study, Ramaiah et al. investigated helical fibers self-assembled by cholesterol-appended squaraine dye **21** (Figure 12).[4c] Squaraine dye **21** forms two H-type chiral assemblies with opposite chirality in different solvent compositions of good ($CHCl_3$) and poor (CH_3CN). The CD spectra recorded in a solvent mixture of $CHCl_3/CH_3CN$ (v:v = 1:1) showed a bisignate CD signal with a negative Cotton effect, reflecting the formation of aggregates in a left-handed helical pattern. Increasing the fraction of CH_3CN switches the CD signal from a negative to a positive Cotton effect due to a left-handed (*M*) to right-handed (*P*) transformation of the two aggregates. Temperature- and concentration-dependent experiments indicate that the aggregate observed at the lower fraction of poor solvent can be assigned to the thermodynamically stable form, whereas the self-assembly is under kinetic control at higher fractions of poor solvent. By considering the solvent-induced chirality inversion, it was believed that solvent effects (solvation and solvent polarity) surrounding the aggregate may hold the key to determining the handedness of the resultant assembly.[4b] Since the AFM images showed the presence of both *M*- and *P*-helical structures without either helicity dominating, the macroscopic helicity of the aggregates of **21** is not necessarily related to the microscopic helicity observed by CD spectroscopy. Similar observations were also reported by Würthner et al. in the study of supramolecular stereomutation of merocyanine dye nanorods.[4a, 11a, b]

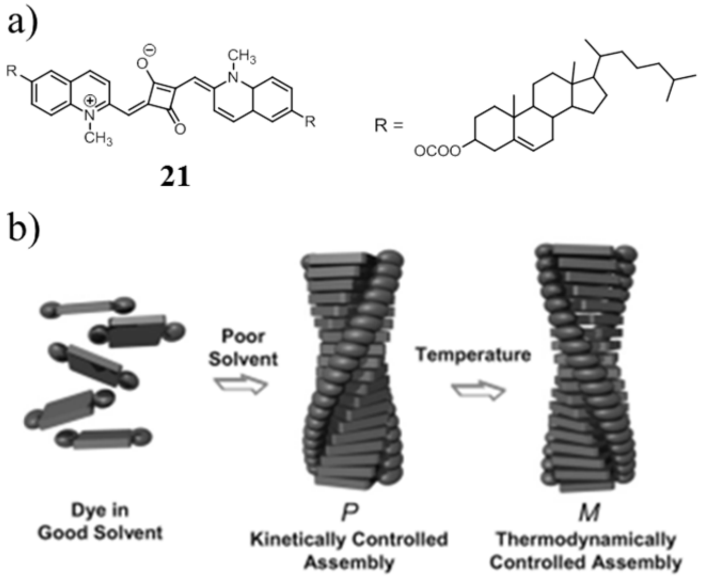

Figure 12. a) Chemical structure of cholesterol-appended squaraine dye **21**. b) Schematic representation of kinetically and thermodynamically controlled self-assembly of dye **21**. Reproduced with permission from *Chem. Eur. J.* **2007**, *13*, 5944-5951. Copyright 2012 John Wiley and Sons.

2.3.2 Metal-ion Driven Self-assembly

Self-assembly of polynuclear metal coordination compounds can result in a variety of complex architectures in which a number of kinetic products may appear before generation of the thermodynamic products.[3, 7] Depending on the heights of related energy barriers, a given process may display kinetic and/or thermodynamic control under a certain set of conditions.

Lehn et al. explored the self-assembly of a linear tris-bipyridine ligand **22** with Fe^{2+} or Ni^{2+}, metal ions that adopt an octahedral coordination geometry with tris-bipyridine ligands (Figure 13).[29] To their surprise, the same ligand coordinated to the same metal ions can yield two different supramolecular architectures, i.e. linear **23** and circular **24** helicates. By means of ^{1}H NMR spectroscopy and ESI-MS, the self-assembly course of ligand **22** and Fe^{2+} was monitored as a function of time.[3] It was found that an equimolar mixture of ligand **22** and Fe^{2+} yielded the linear helicate **23** after a relatively short reaction time. The initially formed trinuclear **23** gradually disassembled after prolonged heating, accompanied by the appearance of pentanuclear **24**. Hence, the linear helicate **23** is ascribed to the kinetic product, which progressively converts into the thermodynamic product **24**. Since the disappearance of **23** follows a double-exponential decay, the authors suggested that multiple mechanistic pathways for the conversion of **23** to **24** are likely.

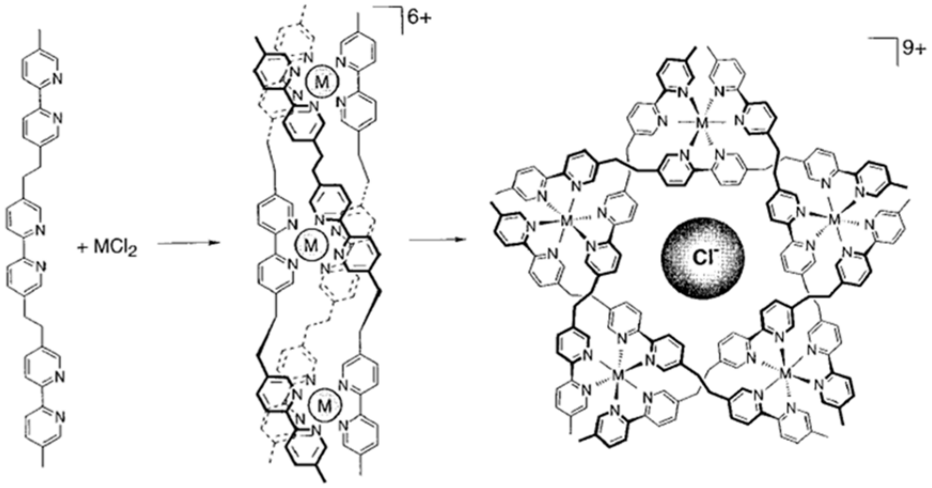

22 **23** **24**

Figure 13. The chronological (but not necessarily mechanistic) sequence of self-assembly processes of tris-bipyridine ligand L and metal ions M (M = Fe^{II} or Ni^{II}). Reproduced with permission from *Angew. Chem. Int. Ed.* **1998**, *37*, 3265-3268. Copyright 2012 John Wiley and Sons.

In the above-mentioned example, the kinetic product **23** is metastable and forms reversibly from the components. When kinetic structure has a cavity suitable for recognizing a guest, an appropriate guest may remarkably stabilize the kinetic product.[30] Fujita and coworkers studied the dynamic assembly of a dodecapyridine ligand **25** and Pd^{II} ions (Figure 14).[7b] In the absence of an appropriate guest, the complexation of ligand **25** with $[(en)Pd(NO_3)_2]$ **26** in D_2O gave rise to a complicated mixture as was evident from the ^1H NMR spectrum. However, quantitative assembly of **25** into mono-end-capped tube $\mathbf{27}^{12+}$ was accomplished by the addition of rodlike guests such as 4,4'-dimethylbiphenyl. In addition to the expected structure $\mathbf{27}^{12+}$, the coordination of **25** and **26** also resulted in the double open tube $\mathbf{28}^{24+}$, in which ligand **25** adopts an extended conformation. This open tube was only observed at higher concentrations as a minor product, but could be purified through slow crystallization. Interestingly, once isolated, $\mathbf{28}^{24+}$ could not be converted into $\mathbf{27}^{12+}$ at a lower concentration. Accordingly, both structures were not in a rapid equilibrium and are thus kinetically trapped.

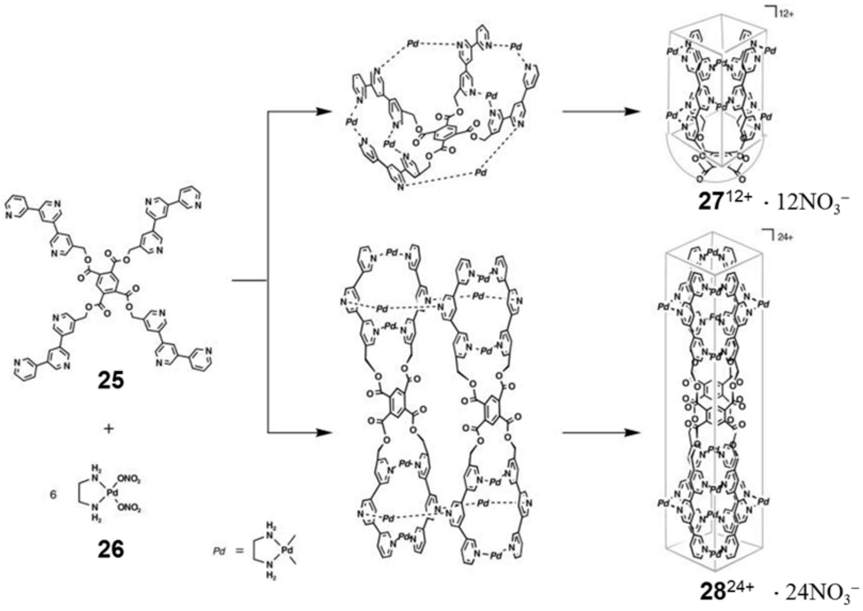

Figure 14. Self-assembly of dodecapyridine ligand **25** and [(en)Pd$(NO_3)_2$] **26** into mono-end-capped tube **27**$^{12+}$ and double open tube **28**$^{24+}$. The template molecule necessary for the formation of **27**$^{12+}$ and **28**$^{24+}$ were omitted for clarity. Reproduced with permission from *Angew. Chem. Int. Ed.* **2003**, *42*, 3267-3270. Copyright 2012 John Wiley and Sons.

2.3.3 Hydrogen-bond Driven Self-assembly

The formation of self-assembled hydrogen-bonded structures is typically a fast and reversible process that occurs instantaneously upon mixing the individual components in solution.[31] Under thermodynamic control, initially mis-formed aggregates can dissociate and recombine to quantitatively produce the correct assembly. However, in the presence of a great number of individual interactions, kinetic control plays an essential role in hydrogen-bond directed self-assembly and seriously restricts the potential formation of H-bonded architectures of more than 3 nm.[8a, 9a, 32]

In nature, the use of so-called “chaperones” provides a solution to this problem.[33] Molecular chaperones are small protein-like molecules that assist in the protein folding process by stabilizing metastable structures on the way to their bioactive conformation. Reinhoudt et al. reported the first example of small molecules acting as molecular chaperones in the formation of synthetic hydrogen-bonded assemblies.[8a] In a former study, the authors found that the self-assembly of multicomponent rosette assemblies like $\mathbf{29}_3\cdot(\mathrm{DEB})_{12}$ are quantitatively achieved within seconds after mixing a 1:4 ratio of calix[4]arene tetramelamine

29 and 5,5-diethylbarbituric acid (DEB) together at ambient temperature (Figure 15).[34] In place of DEB, the assembly of **29** with *N*-butyl cyanuric acid (BuCYA) in a 1:4 ratio, however, does not produce the expected $\mathbf{29}_3$·(BuCYA)$_{12}$, even though it is based on the same assembly motif. ^{1}H NMR spectroscopy and gel permeation chromatography (GPC) showed the formation of a mixture of oligomeric assemblies. Remarkably, the spontaneous formation of $\mathbf{29}_3$·(BuCYA)$_{12}$ occurs cleanly upon mixing a 1:4 ratio of **29** and BuCYA in the presence of equimolar DEB (BuCYA: DEB = 1:1) at room temperature. It is worth noting that the assembly $\mathbf{29}_3$·(BuCYA)$_{12}$ could only be accomplished when DEB is added into the system with free tetramelanine **29** before the addition of BuCYA. Hence, the DEB molecules serve as a "self-assembly catalyst" to guide the formation of target assemblies.

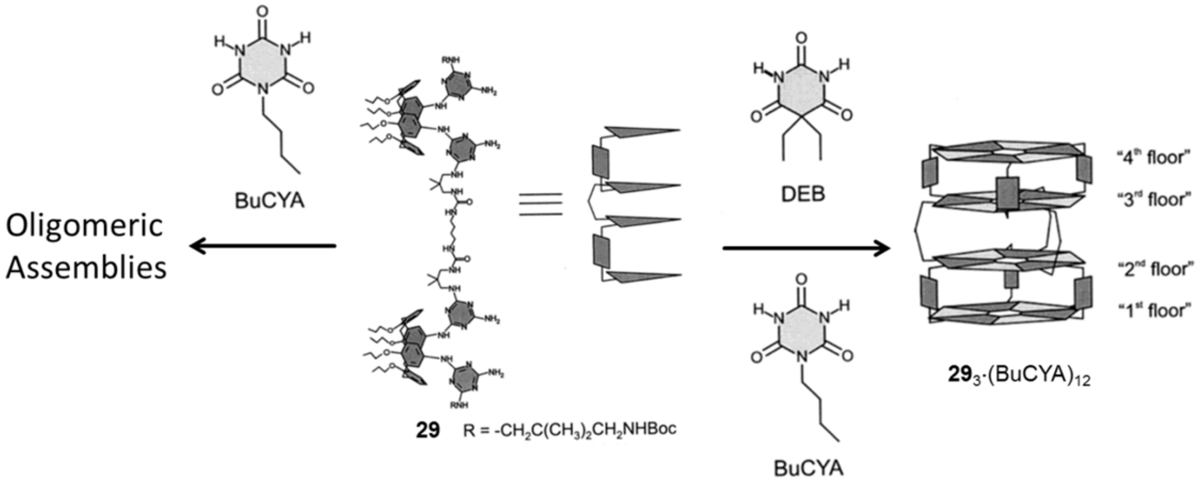

Figure 15. Schematic representation of the self-assembly of calix[4]arene tetramelamine **29** and *N*-butyl cyanuric acid (BuCYA) in the absence or presence of 5,5-diethylbarbituric acid (DEB). Reproduced with permission from *J. Am. Chem. Soc.* **2002**, *124*, 7638-7639. Copyright 2012 American Chemical Society.

2.3.4 Molecular Threading and Recognition

During the process of pseudo-rotaxane threading,[5a-c, 5e] the self-correction of initially formed, kinetically labile intermediates serves as an important mechanistic process.[5e] Upon self-sorting of multiple host-gest complexes, kinetic and thermodynamic controls play an important role in the time-dependent observation of different products (*vide supra, see 2.2.1*).[6a] In one paper, Stoddart and coworkers proposed the question, "can multivalency be expressed kinetically" and said, "the answer is yes".[5b] The authors studied the strict self-assembly of a triply threaded two-component superbundle 3in-[**29**$\supset$**30**][PF$_6$]$_6$ shown in Figure 16. When a ^{1}H NMR spectrum was recorded immediately after mixing equimolar trifurcated trisbipyridinium salt [**29**][PF$_6$]$_6$ and tritopic triscrown ether **30**, the spectrum revealed the rapid formation of doubly threaded supermolecule 2in-[**29**$\supset$**30**][PF$_6$]$_6$ with two complexed arms and one uncomplexed arm. After 235 hours, a new set of resonances indicated the quantitative formation of thermodynamically stable assembly 3in-[**29**$\supset$**30**][PF$_6$]$_6$. By detailed time-dependent ^{1}H NMR measurements, the data points were fitted to the model for a reversible first-order reaction between 2in-[**29**$\supset$**30**][PF$_6$]$_6$ and 3in-[**29**$\supset$**30**][PF$_6$]$_6$, giving the rate constants k_1 and k_2 of 4.7×10^{-6} and 1.4×10^{-6} s^{-1}, respectively. Furthermore, the energy barriers of $\Delta G_1^{\neq}$ and $\Delta G_2^{\neq}$ were calculated to be 20.9±0.3 and 21.5±0.3 kcal mol^{-1}, suggestive of the difficulty in both the formation and the dissociation of superbundle 3in-[**29**$\supset$**30**][PF$_6$]$_6$.

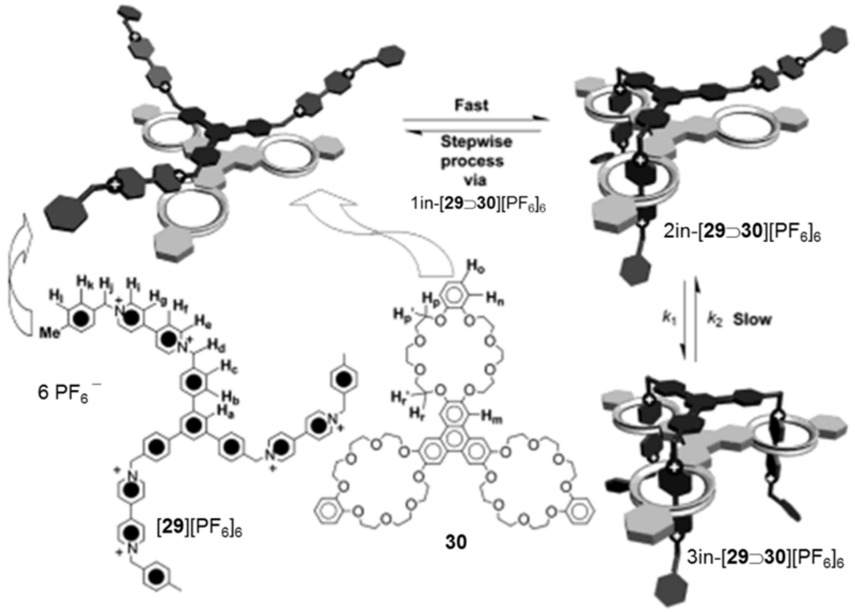

Figure 16. Schematic representation of the stepwise self-assembly of the triply threaded two-component superbundle 3in-[**29**$\supset$**30**][PF$_6$]$_6$. Reproduced with permission from *J. Am. Chem. Soc.* **2004**, *126*, 2288-2289. Copyright 2012 American Chemical Society.

2.4 Mechanistic Studies of Self-assembly Processes

Every chemical process may be described in terms of both kinetic and thermodynamic aspects. While thermodynamics involve the energy difference between products and reactants described as the free energy ΔG, kinetics relate to the rates of chemical processes, and are measured in terms of the rate constant k associated with the activation energy. Proper interpretation of reaction rates and activation energy barriers provides insight into the mechanism of a chemical process. For rational design of a complicated supramolecular self-assembly, it is an important task to determine the rate constants of an assembly process and further understand the complexation mechanism. However, there are only a few papers referred to profound interpretation of self-assembly mechanisms to date.[9]

For the mechanistic studies of self-assembly, it should be noted that "…*Given the initial and final states of an elementary reaction, and therefore a thermodynamic description of the system, there exist a priori an infinite number of paths (i.e. mechanisms) from the initial to the final states. The essential role of kinetics is to eliminate most of these possibilities and suggest the most likely path. It is often stated that it is only possible to disprove a postulated mechanism; it is not possible to prove that a suggested mechanism is correct. The meaning of this statement is that if a proposed mechanism is inconsistent with the kinetic data, the mechanism must be incorrect; whereas if it is consistent with the data, it may be correct. Other mechanisms, as yet unimagined, may also be consistent with the data, or later experimental data may rule out the provisionally correct mechanism. We must accept this somewhat discouraging conclusion; let us view it as a challenge...*"[1c]

2.4.1 Rosette Racemization

Supramolecular chirality of non-covalent assemblies is mostly induced by the introduction of chiral centers (*R* or *S*) in the components.[4a, b, 35]. Reinhoudt et al. presented a strategy to build enantiomerically pure hydrogen-bonded assembly composed of only achiral components.[9a] The enantiomerically pure assembly $\mathbf{31}_3$·$(\mathrm{BuCYA})_6$ could be obtained via chiral induction using calix[4]arene dimelamine **31** and chiral barbiturates, followed by exchange of the chiral components with achiral *N*-butyl cyanurates (BuCYA) while maintaining the previously induced chirality. Impressively, the quantitative barbiturate–cyanurate exchange process preserves the *M*- or *P*-chirality earlier induced by the chiral barbiturates. At room temperature, the resultant enantioselective assembly (*P*)- or (*M*)-$\mathbf{31}_3$·$(\mathrm{BuCYA})_6$ is kinetically stable enough to be isolated in optically pure form (the half-life of racemization is approximately 4.5 d).

Furthermore, Reinhoudt and coworkers investigated the mechanism of racemization process between (P)-$\mathbf{31}_3$·(BuCYA)$_6$ and (M)-$\mathbf{31}_3$·(BuCYA)$_6$. Three possible courses for racemization were envisioned, that is intramolecular racemization, an uncatalyzed dissociative mechanism and a catalyzed dissociative mechanism by liberated chiral barbiturates in the system as illustrated in Figure 17. The intramolecular racemization could be eliminated since exchange of dimelamine was detected upon mixing $\mathbf{1}_3$·(BuCYA)$_6$ and a similar assembly containing a calix[4]arene dimelamine derivative. By determining the order in (P)-$\mathbf{1}_3$·(BuCYA)$_6$ and chiral barbiturate, the initial rate of racemization was expressed in terms of the equation:

$$R_{t=0} = \frac{\mathrm{d}[(P){-}\mathbf{31}_3\cdot(\mathrm{BuCYA})_6]}{\mathrm{d}t} = (k_{\mathrm{cat}}[(S){-}\mathrm{BAR}] + k_{\mathrm{uncat}})[(P){-}\mathbf{31}_3\cdot(\mathrm{BuCYA})_6]_0$$

with k_{cat} = 7.4×10^{-3} M^{-1} s^{-1} and k_{cat} = 1.1×10^{-5} s^{-1} (50 °C). Therefore, the racemization might occur via a dissociative mechanism that is either uncatalyzed or catalyzed. The rate-limiting step should involve the dissociation of calix[4]arene dimelamine **31** from the intact assembly, followed by rapid racemization and formation of the opposite enantiomer.

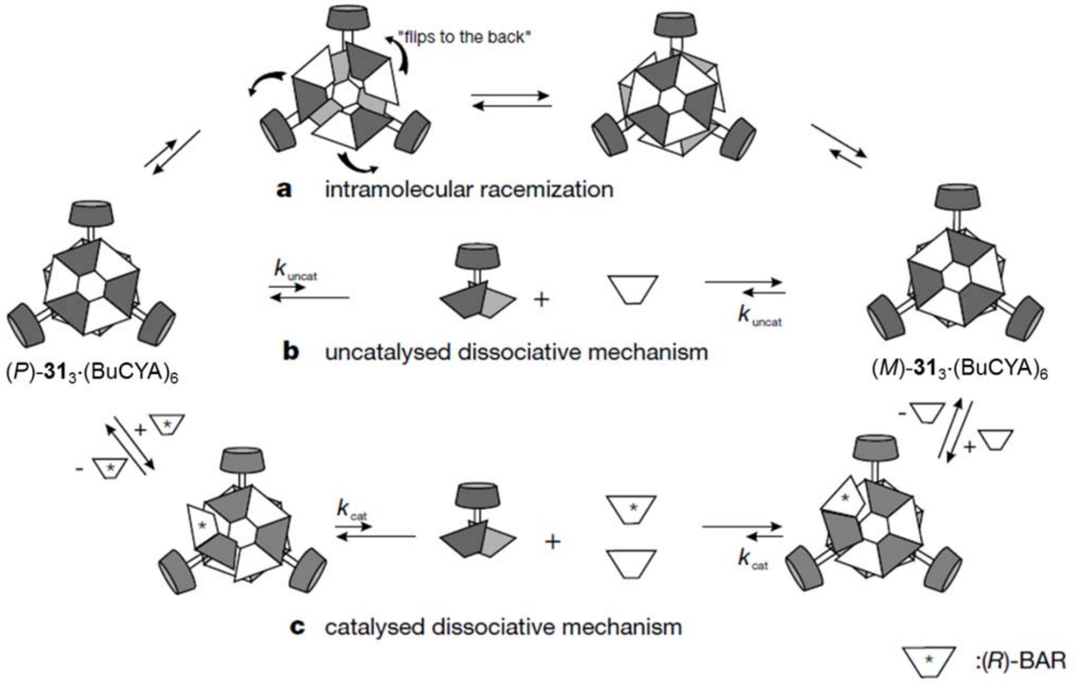

Figure 17. Schematic representation of the different racemization pathways: a) intramolecular mechanism; b) an uncatalyzed and c) a catalyzed dissociative mechanism. Reproduced with permission from *Nature* **2000**, *408*, 181-184. Copyright 2012 Nature Publishing Group.

2.4.2 Ureido-Pyrimidinone:2,7-Diamido-Naphthyridine Complexation

The compound ureido-pyrimidinone (U) exhibits distinct conformations upon self-assembly.[36] In a D_8-toluene solution, U exists as dimerized tautomers of 2-ureido-4[1*H*]-pyrimidinone (U_g) and 2-ureido-pyrimidin-4-ol with the keto dimers as the predominate species (90%), as shown in Figure 18. The [1,3] prototropic shift of this compound results in the formation of the 2-ureido-6[1*H*]-pyrimidinone (U_h) monomer, which can associate with 2,7-diamido-1,8-naphthyridine (N) to generate U:N heterodimers based on strong complementary hydrogen-bonding interactions.[37] This dual complexation motif in combination with the high selectivity for heterodimerization makes the U:N system particularly suitable for formation of supramolecular block and graft copolymers.[38]

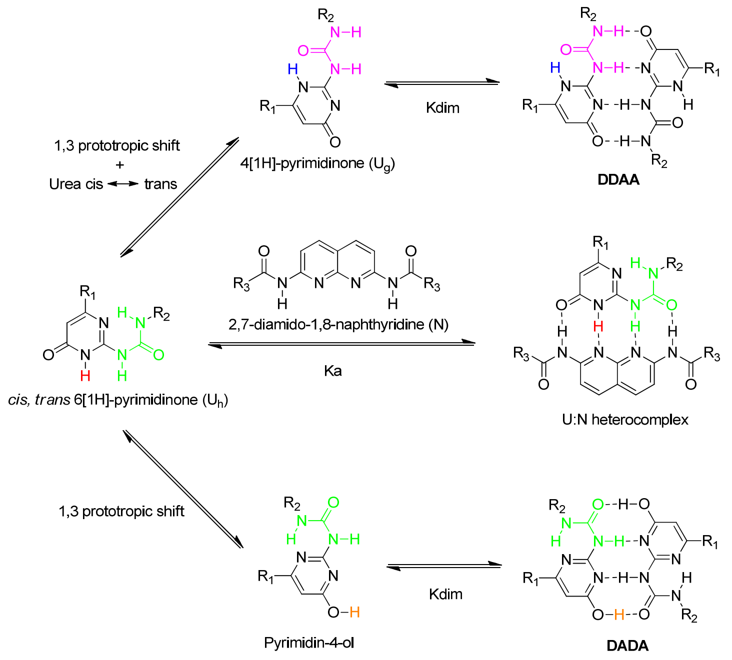

Figure 18. Proposed intermediates in the exchange of the different tautomer form of ureido-pyrimidinone dimers with 2,7-diamindo-1,8-naphthyridine (the substituents R_1, R_2 and R_3 can be any functional groups). Reproduced with permission from *J. Am. Chem. Soc.* **2008**, *130*, 5479-5486. Copyright 2012 American Chemical Society.

Meijer, Sijbesma and coworkers investigated the association kinetics and proposed a reasonable pathway for the formation of the U:N heterocomplex from the U:U keto homodimers (Figure 19).[9b] Experimentally, time-dependent ^{1}H NMR and UV/Vis spectroscopic measurements demonstrated an increase in the initial conversion rate upon increasing the total concentration of equimolar **32** and **33** in a D_8-toluene solution. They considered a simple three-step dissociative mechanism whereby the tautomerization from U_g to U_h monomer form is a unimolecular event, and kinetic simulation using the program Gepasi[39] revealed that the initial conversion rate decreases at higher concentration, in sharp contrast with the experimental results. Since theoretical studies have shown that tautomerization of similar compounds via intermolecular proton transfer has a lower energy barrier compared to a stepwise intramolecular proton transfer,[40] a bimolecular state for the tautomerization from U_g to U_h monomer form was considered. Simulation of the conversion-time plots using this mechanism displayed independent initial rate upon the total concentration. Thus, this kinetic model was also inappropriate to explain the experimental data. Finally, by considering the catalytic role of free N in the tautomerization of U_g monomer form an acceptable kinetic model simulation was obtained that showed the initial conversion rate of U_2 to U:N increased with concentration, in agreement with the experimental observation. As a consequence, both U and N should contribute significantly to the catalysis of ureido-pyrimidinone tautomerizaiton as reflected by the plausible mechanism.

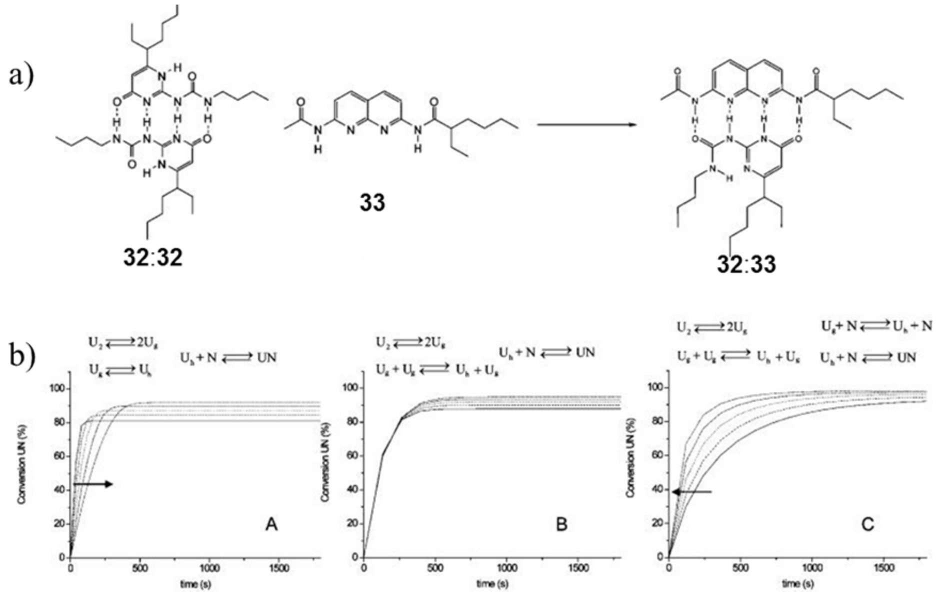

Figure 19. a) Conversion from U:U keto homodimers **32**:**32** to U:N heterocomplex **32**:**33**. b) simulated plots of U:N heterocomplex conversion versus time at different concentrations for 1:1 mixture of **32** and **33** for (A) unimolecular tautomerization model, (B) bimolecular U assisted tautomerization and (C) N and U assisted bimolecular tautomerization. The arrows indicate the increase with the total concentration of **32** and **33**. Reproduced with permission from *J. Am. Chem. Soc.* **2008**, *130*, 5479-5486. Copyright 2012 American Chemical Society.

2.5 Conclusions

The development of new methodologies and techniques to monitor both rapid and slow dynamic processes is a prerequisite for systematic kinetic studies of self-assembly processes. Considering the importance of kinetic control in biological system, the kinetics of self-assembly may attract considerably more attention in the future. To date, kinetic control of self-assembly has not yet been achieved by rational design but rather serendipity. One difficulty often encountered by chemists when exploring the mechanisms of complex self-assembly processes, as encountered in the history of chemical kinetics, is a lack of sufficient mathematical preparation. As exemplified in the text, intra- and/or intermolecular catalysis are often involved, making the simulation of experimental data significantly complicated. In this sense, interdisciplinary cooperation would surely help facilitate the development of systematic kinetic investigations in the field of supramolecular self-assembly.

2.6 References and Notes

[1] a) L. G. Arnaut, S. J. Formosinho, H. Burrows, *Chemical Kinetics: From Molecular Structure to Chemical Reactivity*, 1st ed., Elsevier, Amsterdam, **2007**; b) A. A. Frost, R. G. Pearson, *Kinetics and Mechanism*, 2nd ed., Wiley, New York, **1961**; c) K. A. Connors, *Chemical Kinetics: The Study of Reaction Rates in Solution*, New ed., John Wiley & Sons, New York, **1990**.

[2] a) J. Lehn, *Science* **1993**, *260*, 1762-1763; b) J.-M. Lehn, *Supramolecular Chemistry*, VCH, Weinheim, **1995**.

[3] B. Hasenknopf, J.-M. Lehn, N. Boumediene, E. Leize, A. Van Dorsselaer, *Angew. Chem. Int. Ed.* **1998**, *37*, 3265-3268.

[4] a) A. Lohr, M. Lysetska, F. Würthner, *Angew. Chem. Int. Ed.* **2005**, *44*, 5071-5074; b) R. S. Johnson, T. Yamazaki, A. Kovalenko, H. Fenniri, *J. Am. Chem. Soc.* **2007**, *129*, 5735-5743; c) K. Jyothish, M. Hariharan, D. Ramaiah, *Chem. Eur. J.* **2007**, *13*, 5944-5951.

[5] a) T. Oshikiri, Y. Takashima, H. Yamaguchi, A. Harada, *J. Am. Chem. Soc.* **2005**, *127*, 12186-12187; b) J. D. Badjić, S. J. Cantrill, J. F. Stoddart, *J. Am. Chem. Soc.* **2004**, *126*, 2288-2289; c) T. Oshikiri, Y. Takashima, H. Yamaguchi, A. Harada, *Chem. Eur. J.* **2007**, *13*, 7091-7098; d) E. Masson, X. Lu, X. Ling, D. L. Patchell, *Org. Lett.* **2009**, *11*, 3798-3801; e) W. Jiang, A. Schäfer, P. C. Mohr, C. A. Schalley, *J. Am. Chem. Soc.* **2010**, *132*, 2309-2320.

[6] a) P. Mukhopadhyay, P. Y. Zavalij, L. Isaacs, *J. Am. Chem. Soc.* **2006**, *128*, 14093-

14102; b) A. S. M. Dyck, U. Kisiel, C. Bohne, *J. Phys. Chem. B* **2003**, *107*, 11652-11659.

[7] a) A. Hori, K.-i. Yamashita, M. Fujita, *Angew. Chem. Int. Ed.* **2004**, *43*, 5016-5019; b) S. Tashiro, M. Tominaga, T. Kusukawa, M. Kawano, S. Sakamoto, K. Yamaguchi, M. Fujita, *Angew. Chem. Int. Ed.* **2003**, *42*, 3267-3270; c) M. Yamanaka, Y. Yamada, Y. Sei, K. Yamaguchi, K. Kobayashi, *J. Am. Chem. Soc.* **2006**, *128*, 1531-1539; d) C. G. Claessens, M. J. Vicente-Arana, T. Torres, *Chem. Commun.* **2008**, 6378-6380; e) V. M. Cangelosi, T. G. Carter, L. N. Zakharov, D. W. Johnson, *Chem. Commun.* **2009**, 5606-5608; f) O. Chepelin, J. Ujma, P. E. Barran, P. J. Lusby, *Angew. Chem.* **2012**, *124*, 4270-4273.

[8] a) V. Paraschiv, M. Crego-Calama, T. Ishi-i, C. J. Padberg, P. Timmerman, D. N. Reinhoudt, *J. Am. Chem. Soc.* **2002**, *124*, 7638-7639; b) J. T. Davis, M. S. Kaucher, F. W. Kotch, M. A. Iezzi, B. C. Clover, K. M. Mullaugh, *Org. Lett.* **2004**, *6*, 4265-4268.

[9] a) L. J. Prins, F. De Jong, P. Timmerman, D. N. Reinhoudt, *Nature* **2000**, *408*, 181-184; b) T. F. A. de Greef, G. B. W. L. Ligthart, M. Lutz, A. L. Spek, E. W. Meijer, R. P. Sijbesma, *J. Am. Chem. Soc.* **2008**, *130*, 5479-5486; c) P. Nordell, P. Lincoln, *J. Am. Chem. Soc.* **2005**, *127*, 9670-9671; d) B. J. Holliday, Y.-M. Jeon, C. A. Mirkin, C. L. Stern, C. D. Incarvito, L. N. Zakharov, R. D. Sommer, A. L. Rheingold, *Organometallics* **2002**, *21*, 5713-5725; e) N. Fatin-Rouge, S. Blanc, A. Pfeil, A. Rigault, A.-M. Albrecht-Gary, J.-M. Lehn, *Helv. Chim. Acta* **2001**, *84*, 1694-1711; f) N. Fatin-Rouge, S. Blanc, E. Leize, A. Van Dorsselaer, P. Baret, J.-L. Pierre, A.-M. Albrecht-Gary, *Inorg. Chem.* **2000**, *39*, 5771-5778; g) C. L. D. Gibb, X. Li, B. C. Gibb, *PNAS* **2002**, *99*, 4857-4862.

[10] a) R. F. Pasternack, E. J. Gibbs, P. J. Collings, J. C. dePaula, L. C. Turzo, A. Terracina, *J. Am. Chem. Soc.* **1998**, *120*, 5873-5878; b) R. F. Pasternack, E. J. Gibbs, D. Bruzewicz, D. Stewart, K. S. Engstrom, *J. Am. Chem. Soc.* **2002**, *124*, 3533-3539; c) R. F. Pasternack, C. Fleming, S. Herring, P. J. Collings, J. dePaula, G. DeCastro, E. J. Gibbs, *Biophys. J.* **2000**, *79*, 550-560; d) A. Arduini, R. Bussolati, A. Credi, G. Faimani, S. Garaudée, A. Pochini, A. Secchi, M. Semeraro, S. Silvi, M. Venturi, *Chem. Eur. J.* **2009**, *15*, 3230-3242; e) M. Baroncini, S. Silvi, M. Venturi, A. Credi, *Chem. Eur. J.* **2010**, *16*, 11580-11587.

[11] a) A. Lohr, F. Würthner, *Chem. Commun.* **2008**, 2227-2229; b) A. Lohr, F. Würthner, *Angew. Chem. Int. Ed.* **2008**, *47*, 1232-1236; c) A. Lohr, F. Würthner, *Isr. J. Chem.* **2011**, *51*, 1052–1066.

[12] a) P. Nordell, F. Westerlund, L. M. Wilhelmsson, B. Nordén, P. Lincoln, *Angew. Chem. Int. Ed.* **2007**, *46*, 2203-2206; b) B. Önfelt, P. Lincoln, B. Nordén, *J. Am. Chem. Soc.* **2001**, *123*, 3630-3637.

[13] R. K. Castellano, S. L. Craig, C. Nuckolls, J. Rebek, *J. Am. Chem. Soc.* **2000**, *122*,

7876-7882.

[14] W. Jiang, C. A. Schalley, *PNAS* **2009**, *106*, 10425-10429.

[15] a) M. M. Safont-Sempere, G. Fernández, F. Würthner, *Chem. Rev.* **2011**, *111*, 5784-5814; b) A. Wu, L. Isaacs, *J. Am. Chem. Soc.* **2003**, *125*, 4831-4835.

[16] W. Jiang, H. D. F. Winkler, C. A. Schalley, *J. Am. Chem. Soc.* **2008**, *130*, 13852-13853.

[17] E. Leize, A. Jaffrezic, A. Van Dorsselaer, *J. Mass. Spectrom.* **1996**, *31*, 537-544.

[18] W. Wang, L. Wang, B. J. Palmer, G. J. Exarhos, A. D. Q. Li, *J. Am. Chem. Soc.* **2006**, *128*, 11150-11159.

[19] J. Jeener, B. H. Meier, P. Bachmann, R. R. Ernst, *J. Chem. Phys* **1979**, *71*, 4546-4553.

[20] C. L. Perrin, T. J. Dwyer, *Chem. Rev.* **1990**, *90*, 935-967.

[21] O. Mogck, M. Pons, V. Böhmer, W. Vogt, *J. Am. Chem. Soc.* **1997**, *119*, 5706-5712.

[22] a) J. C. Gielen, A. Ver Heyen, S. Klyatskaya, W. Vanderlinden, S. Höger, J. C. Maan, S. De Feyter, P. C. M. Christianen, *J. Am. Chem. Soc.* **2009**, *131*, 14134-14135; b) C. G. Jeroen, O. S. Igor, P. H. J. S. Albertus, C. M. C. Peter, J. C. Maan, *Sci. Technol. Adv. Mater.* **2009**, *10*, 014601.

[23] P. C. M. Christianen, I. O. Shklyarevskiy, M. I. Boamfa, J. C. Maan, *Physica B: Condensed Matter* **2004**, *346–347*, 255-261.

[24] L. Stryer, *Biochemistry*, 4th ed., W. H. Freeman and Co., New York, **1995**.

[25] Y. Xue, J.-q. Liu, K.-w. Zheng, Z.-y. Kan, Y.-h. Hao, Z. Tan, *Angew. Chem. Int. Ed.* **2011**, *50*, 8046-8050.

[26] a) A. J. Baldwin, T. P. J. Knowles, G. G. Tartaglia, A. W. Fitzpatrick, G. L. Devlin, S. L. Shammas, C. A. Waudby, M. F. Mossuto, S. Meehan, S. L. Gras, J. Christodoulou, S. J. Anthony-Cahill, P. D. Barker, M. Vendruscolo, C. M. Dobson, *J. Am. Chem. Soc.* **2011**, *133*, 14160-14163; b) D. Thirumalai, G. Reddy, *Nat. Chem.* **2011**, *3*, 910-911.

[27] a) P. Jennings, P. Wright, *Science* **1993**, *262*, 892-896; b) R. Pellarin, P. Schuetz, E. Guarnera, A. Caflisch, *J. Am. Chem. Soc.* **2010**, *132*, 14960-14970.

[28] a) A. G. Catchpole, E. D. Hughes, C. K. Ingold, *J. Chem. Soc.* **1948**, 8-17; b) R. B. Woodward, H. Baer, *J. Am. Chem. Soc.* **1944**, *66*, 645-649.

[29] a) B. Hasenknopf, J.-M. Lehn, B. O. Kneisel, G. Baum, D. Fenske, *Angew. Chem. Int. Ed.* **1996**, *35*, 1838-1840; b) R. Krämer, J.-M. Lehn, A. De Cian, J. Fischer, *Angew. Chem. Int. Ed.* **1993**, *32*, 703-706; c) B. Hasenknopf, J.-M. Lehn, N. Boumediene, A. Dupont-Gervais, A. Van Dorsselaer, B. Kneisel, D. Fenske, *J. Am. Chem. Soc.* **1997**, *119*, 10956-10962.

[30] a) M. Fujita, S. Nagao, K. Ogura, *J. Am. Chem. Soc.* **1995**, *117*, 1649-1650; b) S. Hiraoka, M. Fujita, *J. Am. Chem. Soc.* **1999**, *121*, 10239-10240; c) M. Albrecht, O. Blau, R. Fröhlich, *Chem. Eur. J.* **1999**, *5*, 48-56; d) Y. Kubota, S. Sakamoto, K. Yamaguchi, M. Fujita, *PNAS* **2002**, *99*, 4854-4856; e) T. Yamaguchi, S. Tashiro, M.

Tominaga, M. Kawano, T. Ozeki, M. Fujita, *J. Am. Chem. Soc.* **2004**, *126*, 10818-10819.

[31] L. J. Prins, D. N. Reinhoudt, P. Timmerman, *Angew. Chem. Int. Ed.* **2001**, *40*, 2382-2426.

[32] a) J. P. Mathias, E. E. Simanek, C. T. Seto, G. M. Whitesides, *Angew. Chem. Int. Ed.* **1993**, *32*, 1766-1769; b) L. J. Prins, E. E. Neuteboom, V. Paraschiv, M. Crego-Calama, P. Timmerman, D. N. Reinhoudt, *J. Org. Chem.* **2002**, *67*, 4808-4820.

[33] a) R. A. Laskey, B. M. Honda, A. D. Mills, J. T. Finch, *Nature* **1978**, *275*, 416-420; b) R. J. Ellis, *Trends Biochem. Sci.* **2006**, *31*, 395-401.

[34] K. A. Jolliffe, P. Timmerman, D. N. Reinhoudt, *Angew. Chem. Int. Ed.* **1999**, *38*, 933-937.

[35] L. J. Prins, J. Huskens, F. de Jong, P. Timmerman, D. N. Reinhoudt, *Nature* **1999**, *398*, 498-502.

[36] a) F. H. Beijer, R. P. Sijbesma, H. Kooijman, A. L. Spek, E. W. Meijer, *J. Am. Chem. Soc.* **1998**, *120*, 6761-6769; b) S. H. M. Söntjens, R. P. Sijbesma, M. H. P. van Genderen, E. W. Meijer, *J. Am. Chem. Soc.* **2000**, *122*, 7487-7493.

[37] a) G. B. W. L. Ligthart, H. Ohkawa, R. P. Sijbesma, E. W. Meijer, *J. Am. Chem. Soc.* **2004**, *127*, 810-811; b) T. Park, E. M. Todd, S. Nakashima, S. C. Zimmerman, *J. Am. Chem. Soc.* **2005**, *127*, 18133-18142; c) P. S. Corbin, S. C. Zimmerman, *J. Am. Chem. Soc.* **1998**, *120*, 9710-9711; d) X.-Z. Wang, X.-Q. Li, X.-B. Shao, X. Zhao, P. Deng, X.-K. Jiang, Z.-T. Li, Y.-Q. Chen, *Chem. Eur. J.* **2003**, *9*, 2904-2913.

[38] a) T. Park, S. C. Zimmerman, S. Nakashima, *J. Am. Chem. Soc.* **2005**, *127*, 6520-6521; b) T. Park, S. C. Zimmerman, *J. Am. Chem. Soc.* **2006**, *128*, 13986-13987; c) O. A. Scherman, G. B. W. L. Ligthart, H. Ohkawa, R. P. Sijbesma, E. W. Meijer, *PNAS* **2006**, *103*, 11850-11855; d) T. Park, S. C. Zimmerman, *J. Am. Chem. Soc.* **2006**, *128*, 14236-14237; e) H. Ohkawa, G. B. W. L. Ligthart, R. P. Sijbesma, E. W. Meijer, *Macromolecules* **2007**, *40*, 1453-1459.

[39] P. Mendes, *Trends Biochem. Sci.* **1997**, *22*, 361-363.

[40] a) P. I. Nagy, F. R. Tejada, W. S. Messer, *J. Phys. Chem. B* **2005**, *109*, 22588-22602; b) P.-T. Chou, C.-Y. Wei, F.-T. Hung, *J. Phys. Chem. B* **1997**, *101*, 9119-9126; c) F. Freeman, H. N. Po, *J. Phys. Chem. A* **2006**, *110*, 7904-7912; d) Z. Yang, M. T. Rodgers, *Phys. Chem. Chem. Phys.* **2004**, *6*, 2749-2757; e) A. Padermshoke, Y. Katsumoto, M. Aida, *J. Phys. Chem. B* **2006**, *110*, 26388-26395.

Chapter 3

Perylene Bisimide Dimer Aggregates:

Fundamental Insights into Self-assembly by NMR and UV/Vis Spectroscopy

Abstract: A novel perylene bisimide (PBI) dye bearing one solubilizing dialkoxybenzyl and one bulky 2,5-di-*tert*-butyl phenyl substituent was synthesized and its aggregation behavior was analyzed by NMR and UV/Vis spectroscopy in various chloroform/methylcyclohexane (MCH) solvent mixtures. In the presence of no less than 10 vol% chloroform, exclusive self-assembly of this PBI dye into π-stacked dimers was unambiguously confirmed by means of both concentration-dependent ^{1}H NMR and UV/Vis spectroscopic experiments. Based on ROESY NMR, a well-defined π-stacked dimer structure was determined and further corroborated by molecular modeling studies. By varying the solvent composition of chloroform and MCH the solvent effects on the Gibbs free energy of PBI dimerization were elucidated, which showed a pronounced nonlinearity between lower and higher MCH contents. This observation could be related to a further growth process of dimers into larger aggregates that occurs in the absence of chloroform, which is required to solvate the aromatic π-surfaces. With the help of a single crystal structure analysis for a related PBI dye, a structural model could be derived for the extended aggregates that are still composed of defined π-π-stacked PBI dimer entities.

3.1 Introduction

Aromatic π-π-interactions[1] are one of the important non-covalent forces and exert significant influence on determining the structure and properties of supramolecular assemblies in many key biological processes.[2] To mimic functional biological structures, aromatic stacks have recently received appreciable attention as futuristic functional nanosystems.[3] Likewise, in thin films a great number of π-π-stacked organic materials have been employed as effective electronic and photonic molecular devices such as organic field effect transistors[4] and solar cells[5]. Among the various synthetic π-conjugated molecules, perylene bisimides (PBIs) have been shown to be excellent photofunctional building blocks for light harvesting[6] and the most promising candidates for n-type semiconductor materials[7] because of their high photostability, excellent optical properties and electron affinity.

Our group is particularly interested in controlling PBI self-assembly and elucidating the relationship between supramolecular structure and emergent optoelectronic properties.[8, 9] In solution, PBI compounds with solubilizing alkyl and alkoxy chains at the imide positions form one-dimensional infinite columnar aggregates by means of π-π-interaction.[8] The aggregation degrees may be governed primarily by three factors, i.e. concentration, temperature and solvent.[8b] However, more detailed elucidation of the structure-property relationships are made difficult on account of their random aggregate sizes, that is they exist as a polydisperse mixture of aggregates such as dimers, trimers and higher oligomers. In this sense, discrete PBI dimers which are self-assembled by single π-π-interaction are strongly in demand to provide in-depth appreciation of PBI aggregation behavior. To date, it is still a challenge to trap PBI aggregation at the stage of dimer formation. Alternatively, PBI dimer aggregates have been produced in the presence of additional constraints such as covalent linkages or hydrogen bonds.[10] The Wasielewski group synthesized a PBI dimer where two PBI units are covalently fixed to a rigid backbone.[10a] In this way, the PBI dimer arrangement is restricted to a reduced conformational space that facilitates good agreements between theoretical calculation and spectroscopic data.[11] Nevertheless, the backbone-directed parallel orientation and a π-π-distance of 4.5 Å are obviously not the favored arrangement of non-covalent PBI aggregates in solution or the solid state. A similar situation is encountered for calixarene-tethered PBIs synthesized by our group.[10b] Even though the two perylene planes are restricted in a small space, their intramolecular folding process is dynamic and the spectroscopic features are strongly influenced by the electron-rich calixarene units. The first self-assembled PBI dimers were described by Schenning and Meijer.[10c] In this case, the PBI π-π-stacking appears not to be the dominant driving force for the dimer formation; instead, discrete dimerization is achieved with the aid of four-fold hydrogen bonding.

Very recently, our group reported discrete dimer formation of bay-substituted core-twisted PBIs comprising oligo(ethylene glycol) bridges that surround one side of the perylene plane and therefore prevent aggregation beyond dimers.[12] In this article, we present an alternative strategy for the uniform dimer formation of bay-unsubstituted PBIs. The discrete dimerization behavior of PBIs is realized on the basis of delicate steric control. A new PBI derivative with both rigid and flexible substituents, one at each imide position, has been designed and synthesized. Notably, Matile and coworkers have lately applied the same concept for naphthalene bisimides (NBIs). However, owing to the smaller π-surface of NBIs the π-π-stacking forces are significantly reduced and no in-depth elucidation of the thermodynamics of dimerization was achieved.[13] For our PBI systems, systematic NMR spectroscopic studies paired with molecular modeling illustrate in detail the self-assembled dimer formation process and the well-defined dimer structure. The thermodynamics of PBI dimerization were determined by variable-concentration ^{1}H NMR and UV/Vis spectroscopic experiments in a solvent mixture of $CDCl_3/D_{14}$-MCH (*v*:*v* = 1:5). Finally, the solvent effect on the Gibbs free dimerization energy is investigated by altering the solvent composition and a most interesting further self-assembly process into larger aggregates is observed upon depletion of the good solubilizing solvent chloroform.

3.2 Molecular Design of the PBI Building Block

In order to confine the self-assembly of PBI to dimers in solution, elaborate design of the PBI substituents is a prerequisite since parent PBIs as well as many other π-systems[14] have a strong propensity to form infinite aggregates. In the absence of bay-substituents that exert additional distortion effects,[12] only modifications at the two imide positions may be taken into account.

In this work we chose the 2,5-di-*tert*-butyl phenyl group as one of the imide substituents, because the *ortho*-positioned *tert*-butyl fragment is so bulky that rotation around the C–N bond is essentially impossible (rotational barrier more than 180 kJ mol^{-1}).[15] This feature has been exploited for the design of NBI receptors for adenines[16] and NBI oligomers with ‘‘locked-in’’ conformations.[17] Since the 2,5-di-*tert*-butyl phenyl group is fixed and unsymmetrical the perylene plane may be distinguished into two facets. For the purpose of this discussion, the *m*- and *o*-perylene-facets are defined as being on the same side as the *m*- and *o*-*tert*-butyl groups, respectively (Figure 1a). At the second imide nitrogen, a benzyl group was installed that may freely rotate around the C–N bond at the methylene linker. Steric repulsion between the imide carbonyls and the benzyl group drives the benzyl ring to be preferentially located above or below the perylene plane. When the benzyl ring is bent away from the *o*-perylene-facet, this conformation is assigned the open-*o*-facet conformation; if the benzyl ring rotates away from *m*-perylene-facet, it is called the open-*m*-facet conformation. As demonstrated in Figure 1a, both open-*m*-facet and open-*o*-facet conformations possess only one accessible perylene facet for π-π-interaction as the other facet is blocked by both the imide substituents. The open-*o*-facet conformation has a half-opened *o*-perylene-facet, whereas *m*-perylene-facet is fully accessible in open-*m*-facet conformation. In the molecularly dissolved state (non-aggregated), rotation of the benzyl group around the C–N bond serves like a “rotating door” making this molecule conformationally switchable between open-*o*-facet and open-*m*-facet conformation. Both conformations can make use of the accessible perylene facet to form π-π-stacked PBI dimers, ideally in a head-to-tail manner to compensate for the spatial demands of the *tert*-butyl moieties. Upon dimerization, the benzyl groups will effectively be locked in a single conformation away from the aggregating facet, preventing further aggregation of the self-assembled PBI dimers.

On account of the different monomer conformations, three kinds of π-π-stacked dimers may be envisioned, namely *m*-*m*-dimer (*m*-perylene-facet versus *m*-perylene-facet stacking of two open-*m*-facet conformations), *m*-*o*-dimer (*m*-perylene-facet in open-*m*-facet conformation versus *o*-perylene-facet in open-*o*-facet conformation) and *o*-*o*-dimer (*o*-perylene-facet versus *o*-perylene-facet stacking of two open-*o*-facet conformations) as shown in Figure 1b. While the *o*-*tert*-butyl moiety points towards the π-surface of the *o*-perylene-facet, the *m*-*tert*-butyl group extends outside the *m*-perylene-facet. Therefore, *m*-*m*-dimers should exhibit enhanced face-to-face contact when compared to *m*-*o*- and *o*-*o*-dimers. Owing to the potentially larger π-π-overlap, we anticipated that the designed PBI building block would prefer *m*-*m*-dimer formation to *m*-*o*- and/or *o*-*o*-dimers under a thermodynamically controlled self-assembly process.

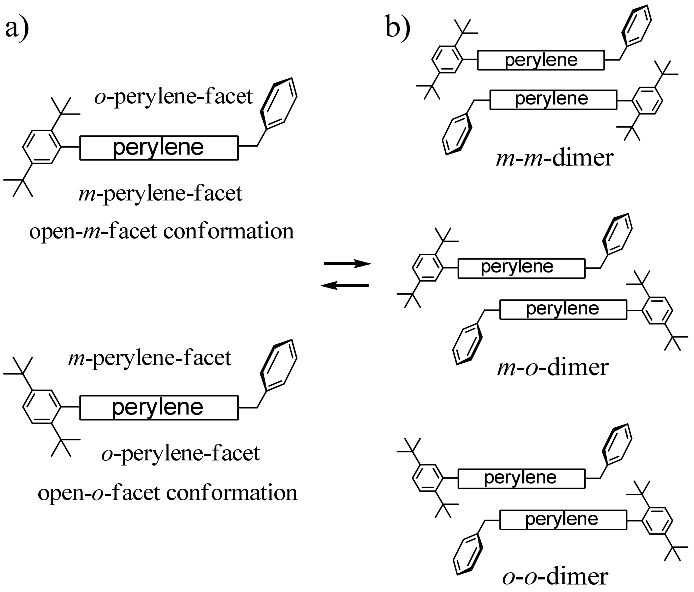

Figure 1. Possible equilibrium between a) open-*m*-/*o*-facet monomer conformations and b) *m*-*m*-, *m*-*o*- and *o*-*o*-dimer combinations.

3.3 Results and Discussion

3.3.1 Synthesis of the Desired PBI Building Block

The desired PBI derivative was obtained according to the synthetic route outlined in Scheme 1. Benzyl alcohol **1**[18] was converted to benzyl bromide **2** with an Appel reaction in high yield (87%). Subsequently, the bromide compound **2** was treated with sodium azide to quantitatively afford benzyl azide **3** that was reduced to benzyl amine **4** in a Staudinger reaction over two steps. Condensation of perylene mono-imide **5**[19] with benzyl amine **4** furnished the target molecule PBI **6** in a reasonable yield of 50%. In a similar way, a reference

PBI **7** was synthesized by condensation of perylene mono-imide **5** with commercially available 4-iodobenzyl amine in a reasonable yield of 64%.

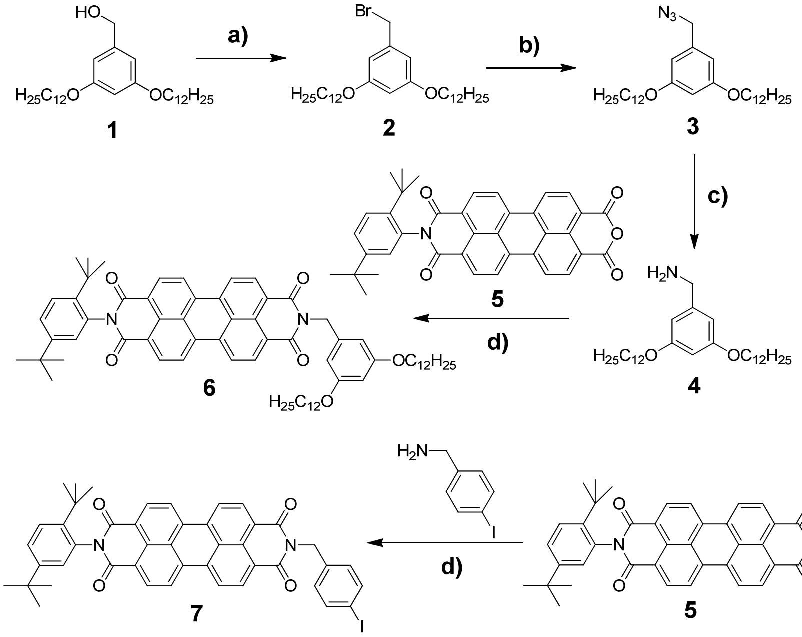

Scheme 1. Synthesis of PBI **6** and PBI **7**: a) CBr_4, PPh_3, dry THF, under argon, r.t., 18 h, 87%. b) NaN_3, DMF, 105 °C, 3 h, 99%. c) PPh_3, dry THF, r.t., 2 h; H_2O, 3 h, 75%. d) imidazole, 140 °C, 4 h, 50% for PBI **6** and 64% for PBI **7**.

PBI **6** and PBI **7** were purified using recycling HPLC and fully characterized by ^{1}H NMR, ^{13}C NMR spectroscopy and ESI-TOF mass spectrometry. Although the *tert*-butyl groups provide satisfying dissolution of these PBIs in chlorinated organic solvents like CH_2Cl_2 or $CHCl_3$,[20] additional long alkoxy chains on the benzyl ring of PBI **6** were introduced simply to raise its solubility in non-polar solvents such as MCH that facilitate aggregation.[21]

3.3.2 Concentration-dependent ^{1}H NMR Spectroscopic Studies

NMR spectroscopy is the preeminent method to monitor and quantify the formation of supramolecular architectures.[22] In dilution experiments, it has been commonly observed that the proton resonance signals are shifted to a higher field upon π-π-stacking[23] and to a lower field upon hydrogen bonding[24]. Due to the sensitivity of each proton to its magnetic environment, observation of resonance shifts provides a wealth of structural information about the self-assembled aggregates. Nevertheless, this powerful tool has been rarely employed to follow the process of PBI π-π-stacking.[12b,25] The intrinsic obstacle is the fact that PBI aggregates often suffer from extremely broadened NMR signals.[26]

To shed light into the aggregation behavior of PBI **6**, the concentration-dependent ^{1}H NMR spectra were recorded at ambient temperature ranging from 0.02 to 40 mM in a solvent mixture of $CDCl_3$/D_{14}-MCH (v:v = 1:5). This solvent composition was selected after a series of variations to be the most suitable one to cover the major range of the aggregation process. Upon increasing concentration, the chemical shifts of perylene protons P1–4 undergo a pronounced high-field shift as illustrated in Figure 2, reflecting the intermolecular association of PBI chromophores via π-π-interaction. It is worthwhile to mention that the two different imide substituents and their pronounced impact on the aggregate structure differentiate the perylene protons into four signals P1, P2, P3 and P4, and they exhibit distinct concentration-dependent changes in chemical shift. Of these protons, P3 experiences the largest up-field shift ($\Delta\delta = -1.38$ ppm), followed by P4 ($\Delta\delta = -1.10$ ppm) and then P2 ($\Delta\delta = -0.99$ ppm), while the P1 resonance moves to high field only by −0.40 ppm. This phenomenon indicates that the π-π-stacking center of PBI **6** is not located at the center of the perylene unit, but displaced towards the P3 and P4 protons. It can be attributed to the steric demand of bulky *tert*-butyl unit which shifts the aggregation center in the direction to the benzyl imide side.

Besides the high-field shift of perylene protons, a significant down-field movement of aromatic A6 signal occurred concomitantly, indicative of hydrogen bond formation.[27] In this case, it is ascribed to the weak [C–H···O] hydrogen bond[28] between the aromatic A6 proton and carbonyl oxygen atom. However, the A6 proton resides outside the perylene plane and cannot interact with the carbonyl oxygen atoms of its own molecule. Accordingly, because of π-π-dimer formation the A6 proton may approach the carbonyl oxygen of the neighboring PBI molecule. It is surprising and unexpected to detect the weak [C–H···O] interaction in solution, despite the existence of chloroform co-solvent in the system that may also act as a comparable hydrogen bond donor.[29] Thus, the weak [C–H···O] interaction cannot be regarded as a major driving force for PBI **6** self-assembly. As shown in molecular modeling studies (*vide infra*), the close intermolecular proximity of the A6 proton and the carbonyl oxygen is only a result of PBI **6** π-π-stacking. From a structural point of view, however, the observation of a

[C–H···O] interaction provides further evidence for tightly stacked PBI chromophores in solution (as close as 3.2–3.4 Å)[6b] with a preferential rotational angle of approximately 30°, in accordance with the intrinsic electrostatic attraction of PBI units.[9] Because proton A6 is positioned over the *m*-perylene-facet, it can approach the intermolecular carbonyl oxygen only when PBI **6** is organized into *m*-*m*-type dimers.

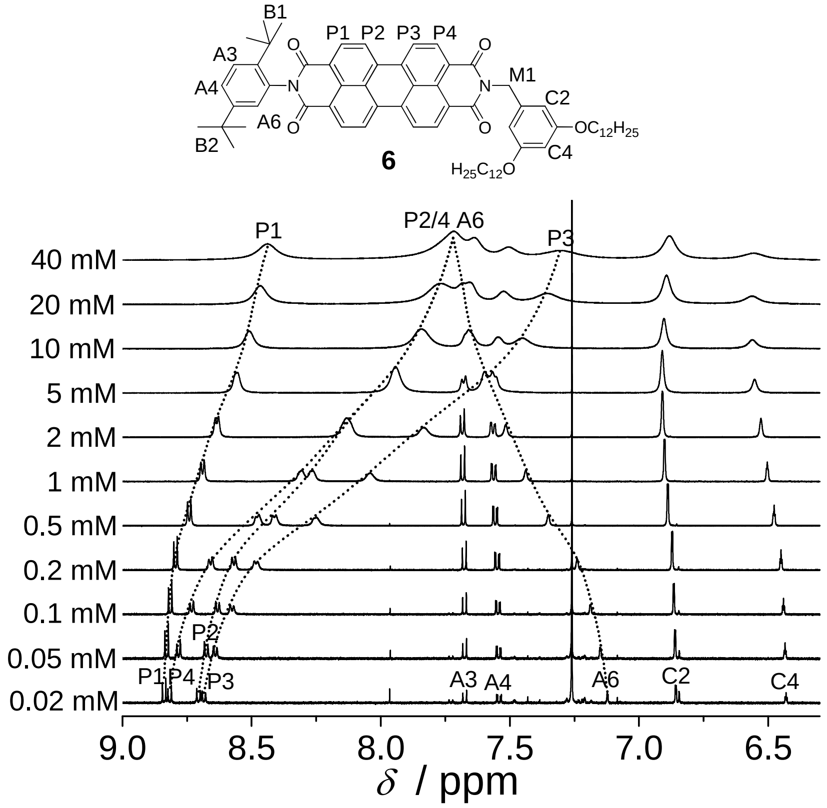

Figure 2. Top: Molecular structure of PBI **6** with designation of its protons. Bottom: Aromatic range of concentration-dependent ^{1}H NMR spectra of PBI **6** from 2×10^{-5} to 4×10^{-2} M in $CDCl_3$/D_{14}-MCH (*v*:*v* = 1:5) conducted with 600 MHz NMR at 293 K. The dotted lines follow the resonance shifts of protons P1, P2, P3, P4 and A6 with the concentration changes.

The most striking feature revealed in Figure 2, however, is the clean transition from monomers to dimer aggregates without further π-π-stacking into extended oligomers, even at higher concentration. During the entire NMR dilution experiments of PBI **6**, only a simple pattern of proton resonances is observed that exhibit significant broadening upon increasing concentration. This can be perceived in terms of rapid exchange between monomers and aggregates on the NMR time scale. In principle, at lower temperature the dimer species should become trapped in either *M*- or *P*-helical arrangements with concomitant splitting of each of the P1, P2, P3 and P4 signals into two signals. Unfortunately, even at 204 K we could not observe such separated resonances (Figure S1). Because in a fast exchange regime the observed chemical shift of a specific proton is the weighted average of chemical shifts in the native (non-exchanging) states, nonlinear least-squares analysis of the concentration-dependent chemical shift variations was performed to probe the thermodynamics of the aggregation process (Figure 3).[14,30] All of the resonance variations of the perylene and A6 protons fit well to a model that assumes only dimer formation.[14]

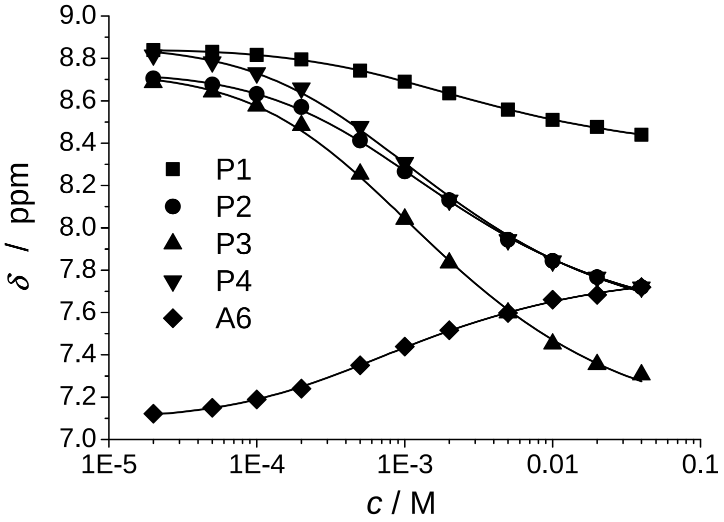

Figure 3. Fitting of the concentration-dependent chemical shift (δ) variations of perylene protons P1–P4 and aromatic proton A6 (see Figure 2) to a dimer model by means of nonlinear least-squares analysis (correlation coefficient more than 0.998).

For a two-state equilibrium between monomer (M) and dimer (D) species,

$$2\,\mathrm{M} \xrightleftharpoons{K_\mathrm{D}} \mathrm{D} \tag{1}$$

the equilibrium constant K_D can be characterized by the equation

$$K_\mathrm{D} = c_\mathrm{D} / (c_\mathrm{M})^2 \tag{2}$$

Herein, both c_D and c_M can be expressed by a function of the overall concentration c_T and the molar fraction of aggregated molecules α_agg as shown in the following equations:

$$c_\mathrm{D} = c_\mathrm{T}\,\alpha_\mathrm{agg} / 2 \tag{3}$$

$$c_\mathrm{M} = c_\mathrm{T}\,(1 - \alpha_\mathrm{agg}) \tag{4}$$

Since the α_agg values at a certain concentration c_T can be extracted from the nonlinear least-squares analysis, both c_D and c_M are obtainable. The aggregation degree α_{agg} of PBI **6** at a concentration of 40 mM reaches nearly 90%, indicating almost complete PBI **6** dimer formation. From the fitting procedure of perylene protons, the dimerization constant K_D is generated to be 340–600 M^{-1}, whereas the best fit of A6 proton gives a somewhat higher value of 900±50 M^{-1}. In spite of these deviations, all the values are in the same order of magnitude and of high reliability (correlation coefficients more than 0.998).

3.3.3 Concentration-dependent UV/Vis Spectroscopic Studies

UV/Vis spectroscopy is an alternative means applicable over a large concentration range to elucidate the thermodynamics for dyes with characteristic absorption bands in the UV/Vis range. The same PBI **6** solutions used for the NMR dilution experiments in the concentration range of 0.02 and 40 mM in $CDCl_3/D_{14}$-MCH (*v*:*v* = 1:5) were subjected to concentration-dependent UV/Vis measurements using cuvettes with path lengths of 0.01–5 mm at ambient temperature (Figure 4). At low concentration, the absorption spectra show well-resolved vibronic bands between 400 and 550 nm for the S_0–S_1 transition of the single PBI chromophores that can be attributed to the breathing vibration of the perylene skeleton polarized along the long molecular axis. The absorption maximum resides at 521 nm, followed by a second band at 485 nm and a third at 454 nm. The value of $A^{0\rightarrow0}/A^{0\rightarrow1}$ at the lowest concentration is greater than 1.6, characteristic of the molecularly dissolved (non-aggregated) state of bay-unsubstituted PBIs.[25a,26a]

Upon increasing concentration, the absorption bands gradually transform, revealing strong electronic coupling between PBI chromophores due to aggregation. A new absorption maximum with a substantially smaller ε value arises at 494 nm, hypsochromically shifted by 27 nm. Such a hypsochromic shift is typical for H-type π-π-stacking of parent PBIs. Simultaneously, the prominent monomer absorption at 521 nm flattens at higher concentration.

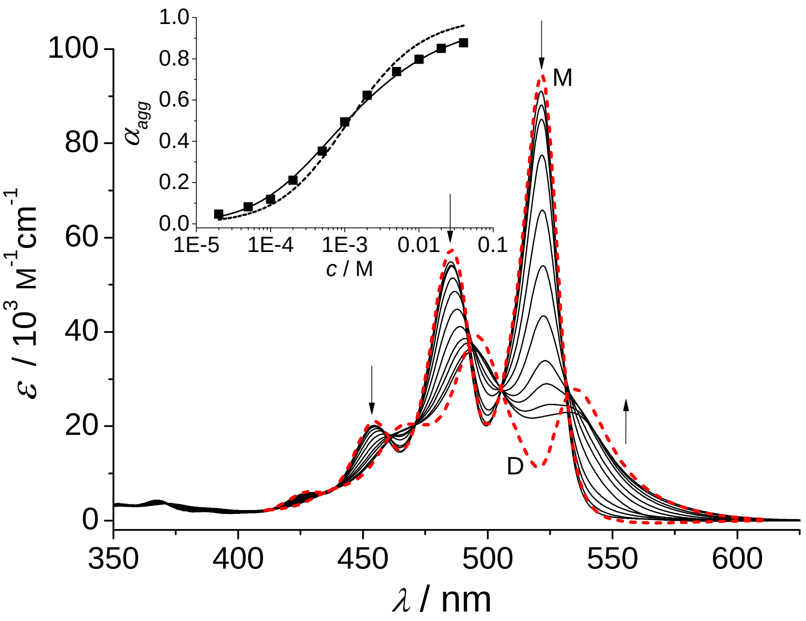

Figure 4. Concentration-dependent absorption spectra of PBI **6** from 2×10^{-5} to 4×10^{-2} M in $CDCl_3/D_{14}$-MCH (*v*:*v* = 1:5) recorded at 293 K. The red dotted lines are the calculated monomer (M) and dimer (D) absorptions from available data in terms of the dimer model. Arrows indicate the spectral changes upon increasing concentration. Notably, the spectrum labeled as D shows the absorbance of one PBI **6** dye within the dimer aggregates and the dimer spectrum therefore has a twofold intensity. Inset: Fitting of the concentration-dependent absorbance at 521 nm to a dimer model by means of nonlinear least-squares analysis (correlation coefficient 0.997). For comparison, fitting to the isodesmic model is also shown (dashed line).

The whole set of concentration-dependent absorption spectra share several isosbestic points at 532, 505, 471, 460 and 438 nm, implying an aggregation equilibrium between only two explicit species in the system, monomer and dimer of PBI **6**. Nonlinear least-square analysis of the concentration-dependent UV/Vis data exhibited a good fit to the dimerization model (inset of Figure 4). The resultant dimerization constant K_D calculated from the monomer absorption maximum at 521 nm is 910±110 M^{-1}, in close agreement with the values from our NMR analysis.[31] Based on the recorded absorptions (α_{agg} from 5% up to 90%), the spectra of the pure monomer and dimer species are calculated and shown as dotted lines in Figure 4. The calculated monomer spectrum exhibits an extinction coefficient of 94500 $M^{-1}cm^{-1}$ at 521 nm and the calculated dimer spectrum is characterized by two main bands at 496 nm (ε = 39000 $M^{-1}cm^{-1}$) and 535 nm (ε = 27800 $M^{-1}cm^{-1}$). The presence of two allowed optical transitions in the dimer spectrum that are displaced to longer and shorter wavelengths with regard to the main transition of the monomer complies with a rotational displacement of the dyes in the π-stack.[8b,32] Remarkably, owing to the very high intensity of the PBI monomer 0→0 transition, the important lower energy absorption band of the dimer could not be experimentally obtained (solid lines), but was only revealed by our mathematical analysis of the monomer-dimer equilibrium.

To the best of our knowledge, this study is the first example where the aggregation behavior of a PBI dye has been fully elucidated by means of both concentration-dependent NMR and UV/Vis experiments. As the same samples prepared in the deuterated solvent mixture of $CDCl_3$/D_{14}-MCH (*v:v* = 1:5) were used, non-systematic errors were avoided. According to our general understanding, the spectral changes in dilution experiments are attributed to the excitonic coupling[32] of the dyes' transition dipole moments for the case of UV/Vis absorption measurements, and to ring-current effects and hydrogen bond formation in proton NMR spectra. Herein, the spectral changes due to the three distinct interactions could be followed simultaneously by using the two spectroscopic techniques. As demonstrated in Figures 3 and 4, the concentration-dependent NMR and UV/Vis spectra exhibit spectral changes that are attributed unambiguously to PBI **6** dimerization.

3.3.4 DOSY and ROESY NMR Studies

To further corroborate exclusive PBI **6** dimer formation, diffusion ordered spectroscopy (DOSY) NMR experiments were carried out with the sample at a concentration of 40 mM to evaluate the aggregate size in solution.[33] Although the aggregation degree reaches nearly 90% at this concentration, analysis of the DOSY spectrum demonstrates a relatively large value of 2.11×10^{-10} m^2 s^{-1} for the translational diffusion coefficient D (Figure S2), indicating small-sized assemblies.[8b] By assuming a spherical shape, the hydrodynamic radius of the small PBI **6** stacks is evaluated based on the Stokes-Einstein equation: $D = k_B T / (6 \pi \eta R)$, where k_B is the Boltzmann constant, T is the experimental temperature, η is the viscosity of the solvent mixture[34] and R is the hydrodynamic radius of the species. According to this equation, the hydrodynamic diameter of PBI **6** aggregates was derived to be 3.2 nm. Taking into account the intramolecular distance of 2.4 nm between B2 and C4 protons in open-*m*-facet conformation of PBI **6** and the alkoxy chain extended length of 1 nm, the detected dimension from DOSY NMR experiment confirms the absence of assemblies larger than dimers of PBI **6**.

For PBI **6** dimers, there are three potential combinations, *m*-*m*-dimer, *m*-*o*-dimer and *o*-*o*-dimer as outlined in Figure 1b. To determine if all three dimer conformations coexist or if one of them is preferred, the spatial proximity of individual protons was probed by the nuclear Overhauser effect (NOE). Cross peaks in such two-dimensional NMR spectra indicate through-space interactions at proximities of 5 Å or less and are particularly useful for determining the structure of aggregates in solution.[35] Because the mass of dimers of PBI **6** (2074 g/mol) lies in a range where NOESY signal intensity may be fairly low, a ROESY technique was employed instead.

The ROESY NMR experiment was carried out with a degassed sample of PBI **6** in $CDCl_3/D_{14}$-MCH (*v*:*v* = 1:2) at a concentration of 10 mM.[36] Since the fixed di-*tert*-butyl phenyl group distinguishes the perylene plane into *o*- and *m*-perylene-facets, the two distinct *tert*-butyl protons B1 and B2 residing above and below the perylene plane can be regarded as "probing protons" to detect the stacked PBI counterpart located over the *o*- or *m*-perylene-facet in the dimer structure. As shown in Figure 5a, protons B2 have spatial cross correlation with protons C2 and M1 from the other imide side. Because the rigid perylene skeleton separates the two imide positions intramolecularly far away from each other, the cross signals between protons from different imide sides can be safely assigned to the dimer structure of PBI **6**. The presence of cross peaks for B2 with C2 and M1 is a strong evidence for the exclusive formation of head-to-tail *m*-*m*-dimers. In this manner, the benzyl group is oriented away from the *m*-perylene-facet and its methylene protons become spatially adjacent to the *m*-*tert*-butyl moiety of the nearby PBI molecule. Additionally, the cross peak between protons A6 and M1 validates the unique *m*-*m*-dimeric arrangement and also provides further evidence for the weak [C–H···O] hydrogen bonding between the A6 proton and carbonyl oxygen as observed in NMR dilution experiments. Only in *m*-*m*-dimers, the A6 protons can intermolecularly approach both M1 protons and carbonyl oxygen atoms.

Furthermore, it should be especially noted that unlike protons B2 and A6 there is no cross peak that could demonstrate spatial approach between B1 and remote protons from the benzyl imide substituent or perylene core. This finding precludes not only the existence of *m*-*o*- and *o*-*o*-dimers, but also the possibility of further cofacial π-stacking of *m*-*m*-dimers. For PBI **6** *m*-*m*-dimers, the outside facing *o*-perylene-facets are blocked by the *o*-*tert*-butyl and benzyl groups, sterically shielding the dimer from further π-π-stacking beyond dimer species.

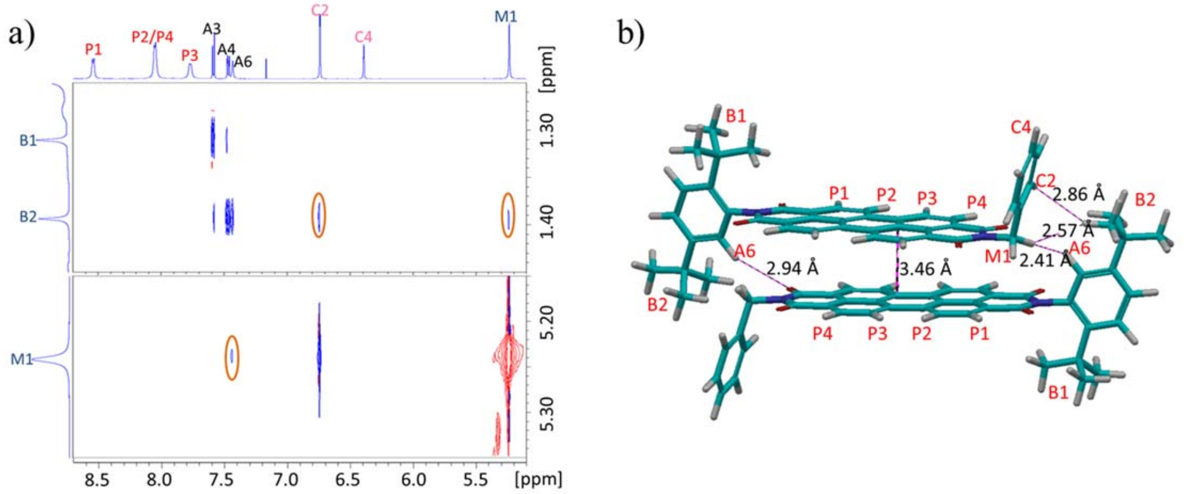

Figure 5. a) Part of the ROESY NMR spectrum of PBI **6** at a concentration of 10 mM in $CDCl_3$/D_{14}-MCH (*v*:*v* = 1:2) conducted with 600 MHz NMR at 293 K. Positive and negative signals are represented by blue and red contours, respectively. b) MM3* geometry-optimized *m*-*m*-dimer structure of the designed PBI building block with selected intermolecular distances and red labeled protons discussed in the text.

3.3.5 Molecular Modeling of PBI Dimer Structure

To help visualize the structure of the PBI **6** dimer we have performed molecular modeling studies on the basis of our NMR and UV/Vis measurements. The molecular modeling studies were accomplished with MacroModel using MM3* force field calculations on the dimer with surrounding chloroform molecules.[37] We began the calculation with a simple monomeric PBI building block (PBI **6** without the solubilizing long alkoxy chains) and performed an energy minimization until full convergence in search of the optimal conformation. Irrespective of the rotation of the benzyl ring along the C–C bond, only two kinds of optimized geometries bear the lowest calculated potential energy of -25 kJ mol^{-1}, corresponding to the open-*m*-facet and open-*o*-facet conformations (Figure 1a). The steric repulsion between the benzyl and the carbonyl groups should be the reason why the benzyl group is prone to lie outside the perylene plane. After these two conformations were confirmed as the lowest energy states, two PBI molecules were placed in a parallel face-to-face stacked *m*-*m*-dimeric arrangement and energy minimized. The dimer conformational search found a global minimum for the calculated potential energy of −125 kJ mol^{-1} that corresponds to the *m-m*-dimeric structure with a certain rotational angle, in accord with experimental observations. For comparison, the calculated energies of *m-o-* and *o-o*-dimers according to the same procedure were −117 and −114 kJ mol^{-1}, respectively. These values are approximately 10 kJ mol^{-1} higher than that of the minimized *m-m*-dimer. The main energy difference arises from the van der Waals term, which is attractive for π-π-stacking and roughly proportional to the area of π-overlap.[1b]

In the geometry-optimized *m-m*-dimer structure illustrated in Figure 5b, the face-to-face stacked PBIs have a π-π-distance of 3.46 Å and a rotational angle of 26°. The spatial distance between B2 and C2, B2 and M1 as well as A6 and M1 are within 3 Å, accounting for the through-space correlation detected in the ROESY NMR spectrum. Since there was zero contribution of hydrogen bonds for the potential energy, the weak [C–H···O] hydrogen bonding was not included in the calculation. In spite of this fact, the A6 protons are directly facing the carbonyl oxygen atoms of the adjacent PBI. There is a 2.94 Å intermolecular H···O distance and the C–H···O bending angle is 152°. As observed in crystal structures and biological systems,[28b,e] these findings corroborate the existence of the weak [C–H···O] hydrogen bonds in PBI **6** *m-m*-dimer. It is worth noting that although a starting geometry with initially parallel aligned PBI units was applied, the geometry-optimized PBI dimers display a certain rotational angle and a slight longitudinal shift, with the best π-overlap area close to the benzyl imide side of the unsymmetrical PBI building block. This complies with the observation in NMR dilution experiments that perylene protons P3 and P4 exhibit the largest high-field shift, followed by protons P2 and then P1. Overall, the dimer structure obtained from the molecular modeling studies is strongly consistent with our robust experimental results.

3.3.6 Aggregation Studies in Pure MCH Solvent

In the previous variable-concentration NMR and UV/Vis spectroscopic experiments we have employed a solvent mixture of $CDCl_3$/D_{14}-MCH (*v*:*v* = 1:5) to cover the largest possible range of the binding isotherm (α_{agg} from 5% up to 90%). Chloroform is a “good” solvent for

PBIs, in which PBI **6** has a high solubility but quite weak aggregation property (Figure S3/4).[21] On the contrary, MCH is a “bad” solvent in which PBIs bear a low solubility but very strong aggregation tendency.[21] Indeed, unlike in the presence of no less than 10 vol% chloroform (*vide infra*, see Figure 9) a complex pattern of proton NMR spectrum appears in pure MCH solvent at higher concentration and the corresponding DOSY NMR indicate the formation of large aggregates beyond dimers (Figure 6a and S6). Although these spectra show a number of reasonably defined resonances, a reliable assignment was impossible.

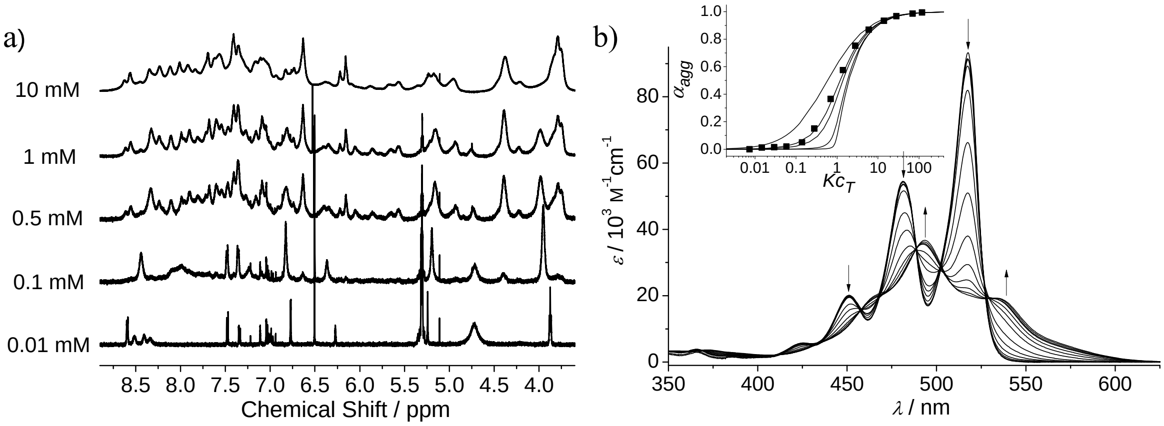

Figure 6. a) Concentration-dependent ^{1}H NMR spectra of PBI **6** from 10^{-5} to 10^{-2} M in pure D$_{14}$-MCH conducted with 600 MHz NMR at 293 K. b) Concentration-dependent absorption spectra of PBI **6** from 10^{-6} to 10^{-2} M in pure undeuterated MCH recorded at 293 K. Arrows indicate the spectral changes upon increasing concentration. Inset: Fraction of aggregated molecules α_{agg} plotted as a function of Kc_{T} with different $\sigma = K_2/K$ values according to the cooperative model (lines from left to right: σ = 1, 0.2, 0.1, 0.01 and 0.001), and plot of experimental absorption data of PBI **6** in MCH at 517 nm.

Accordingly, the aggregation behavior of PBI **6** in MCH was investigated by means of concentration-dependent UV/Vis spectroscopy. Unlike the aggregation process in the solvent mixture, the self-assembly of PBI **6** in pure MCH upon increasing concentration suggests the involvement of some cooperativity.[38] By applying the simple K_2–K model,[39] two equilibrium constants of K_2 = 2800 M^{-1} for dimerization and K = 14000 M^{-1} for subsequent growth were estimated (inset of Figure 6b). From the K_2 value of 2800 M^{-1}, the Gibbs dimerization energy for PBI **6** in MCH was assessed to be –19.3 kJ mol^{-1} that agrees with the extrapolated $\Delta_{\mathrm{D}}G°_{\mathrm{MCH}}$ value (*vide infra*). However, the further cooperative aggregation process is puzzling if we take into account the fact that extended PBI π-π-stacking beyond *m*-

m-dimers is sterically prevented and that the UV/Vis spectra of aggregate solutions in MCH (Figure 6b) show a close resemblance to those observed for the dimer aggregates in the presence of chloroform (Figure 4). Furthermore, several isosbestic points in Figure 6b corroborate the presence of only two types of spectroscopically distinguished species, i.e. monomer and dimer of PBI **6**, over the whole concentration range in MCH.

Inspired by the crystal structure of the reference PBI building block **7** (Figure 7b; for further details see Supporting Information and CCDC 876014 at Cambridge Crystallographic Data Centre), we realize that the di-*tert*-butyl phenyl group may occupy the free *o*-perylene-facets of PBI **6** *m*-*m*-dimer. Such binding process might be strongly favored owing to a proper rigidification of the benzyl substituent in an ideal conformation for accommodation of the di-*tert*-butyl phenyl subunit of another PBI **6** dimer. Thus, we propose a further growth process for PBI **6** self-assembly in MCH as shown in Figure 7c. In this kind of packing arrangement, the solvophobic effect[21] and the [C–H···π] interaction[40] should play a significant role.[41] In the absence of chloroform that favorably solvates the PBI π-surface, PBI **6** dimers need to find a way to exclude the badly solubilizing MCH molecules on top of their "naked" *o*-perylene-facets, and the accommodation of the di-*tert*-butyl phenyl groups just meets this demand. This obviously leads to a rather spectacular change of the self-assembly process from anti-cooperative (in the presence of "good" solvent chloroform) to cooperative (in pure MCH) upon variation of the solvent composition.

A noticeable feature of this further growth process is that it is not readily identifiable by the UV/Vis spectral changes because they are still governed by excitonic coupling within the PBI dimer stacks, whereas excitonic coupling to neighboring PBIs is negligible owing to a large distance and improper angular relationship[32] between the dyes' transition dipole moments.[42] Thus, from the self-assembly process proposed in Figure 7c we are able to rationalize why the UV/Vis spectra in Figure 6b only indicate the existence of π-π-stacked PBI dimer aggregates. In many aggregation studies, similar concentration- and temperature-dependent changes in the UV/Vis spectra with isosbestic points are taken as evidence for a simple dimerization equilibrium. Herein, we have shown by an in-depth analysis of the binding isotherm with the cooperative K_2–K model and additional concentration-dependent NMR experiments that such interpretations are not necessarily correct. Indeed, we believe that many dye aggregates, if not the majority, grow into more extended aggregates in solvents with poor solubilizing capabilities for aromatic π-surfaces (e.g., aliphatic solvents, protic solvents and water), although the UV/Vis spectra in these solvents are still in accordance with the presence of excitonically coupled dimers.[9] This is explained by the pronounced distance-dependence of the excitonic coupling[32] prohibiting further insight into the location of additional neighboring molecules whose transition dipole moments are not as proximate as those within the π-stacked dimer units.

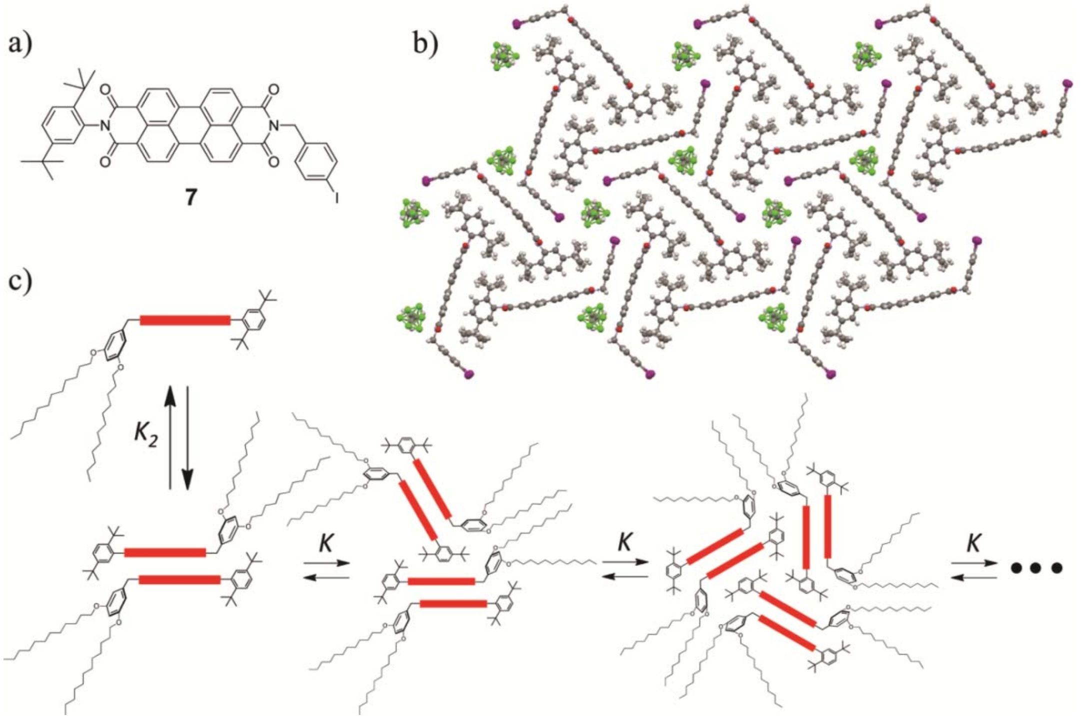

Figure 7. a) Molecular structure of PBI **7**. b) Packing of PBI **7** crystal structure (view along *c*-axis). The co-crystallized $CHCl_3$ molecules are also shown. c) Schematic representation of the proposed aggregation behavior of PBI **6** in MCH.

3.3.7 Solvent-dependent Aggregation Studies

Solvation is an important factor in controlling the self-assembly of aromatic π-stacks.[21,43] Due to the complexity of the nature of π-π-interactions,[44] the relationship between the solvent polarity and the strength of aromatic interaction is not simple.[1,2] In recent work, we have examined the magnitude of PBI π-π-interaction in water and 16 organic solvents covering the whole polarity range.[21] In this study, the Gibbs free binding energies were correlated with different solvent polarity scales including relative permittivity ε_r, Kirkwood-Onsager function $(\varepsilon_r - 1)/(2\varepsilon_r + 1)$, $E_T(30)$, π^* as well as χ_R. The primary conclusion from this study was that the aromatic π-π-interaction is the strongest in both non-polar aliphatic and most-polar protic solvents, and the weakest in chloroaliphatic solvents of intermediate polarity such as dichloromethane and chloroform.[21,43d] In a variety of cases, however, it is better to employ a binary solvent mixture to achieve the desired binding strength, particularly in studies of the folding process of oligomers and macromolecules.[26a,43a,43d,45] By mixing a 'good' and 'bad' solvent, the folding degree could be modulated and a straight-line relationship between the Gibbs folding energy and solvent composition was found in the transition region.[46]

While keeping in mind the special situation in pure MCH solvent (*vide supra*), we have further examined the solvent effect on the Gibbs dimerization energies of PBI **6** by using solvent titration experiments in a similar way as studied for solvent denaturation of foldamers.[26a,45] The solvent-dependent UV/Vis absorptions with $CHCl_3$/MCH compositions from 100:0 to 10:90 were acquired at a fixed concentration of 10 mM and ambient temperature. Accordingly, the absorption changes shown in Figure 8a can only be attributed to the solvent effect. Such absorption changes resemble those of the concentration-dependent measurements. With increasing MCH content, the monomer bands decrease gradually and the dimer bands become apparent. The aggregation degree α_{agg}, dimerization constant K_D and Gibbs dimerization energy $\Delta_D G°$ were calculated for each solvent composition according to Equations (5), (6) and (7), respectively.

$$\alpha_{agg} = \frac{(\varepsilon_{A0-0})_{max} - \varepsilon_{A0-0}}{(\varepsilon_{A0-0})_{max} - (\varepsilon_{A0-0})_{min}} \qquad (5)$$

$$K_D = \frac{[D]}{[M]^2} = \frac{\alpha_{agg}}{2(1-\alpha_{agg})^2 c_T} \qquad (6)$$

$$\Delta_D G° = -RT \ln K_D \qquad (7)$$

If we neglect the possibilities of preferential solvation, the Gibbs free dimerization energies at the respective solvent composition should be proportional to their component in the solvent mixture:

$$\Delta_D G° = m\Delta_D G°_{MCH} + (1-m)\Delta_D G°_{CHCl_3} \qquad (8)$$

$$\Delta_{\mathrm{D}}G^{\circ} = m\left(\Delta_{\mathrm{D}}G^{\circ}{}_{\mathrm{MCH}} - \Delta_{\mathrm{D}}G^{\circ}{}_{\mathrm{CHCl_3}}\right) + \Delta_{\mathrm{D}}G^{\circ}{}_{\mathrm{CHCl_3}} \qquad (9)$$

where m is the volume fraction of MCH in the solvent mixture, $\Delta_{\mathrm{D}}G^{\circ}{}_{\mathrm{CHCl_3}}$ and $\Delta_{\mathrm{D}}G^{\circ}{}_{\mathrm{MCH}}$ represent the Gibbs free energy contribution for the PBI **6** dimerization in pure $CHCl_3$ and MCH, respectively. In Figure 8b, the $\Delta_{\mathrm{D}}G^{\circ}$ values were plotted against the MCH content m in the range of m = 0 and 0.9. The points can be fitted to two linear relationships with the intersection at m = 0.6. At low MCH contents (from m = 0 to 0.6), the linear fitting can be interpreted in terms of Equation (9), giving rise to an extrapolated $\Delta_{\mathrm{D}}G^{\circ}{}_{\mathrm{MCH}}$ value of −16.0±0.2 kJ mol^{-1}. In contrast, upon utilization of the data points for higher MCH contents (from m = 0.6 to 0.9), the dotted fitting line crosses the Y-axis at m = 1.0 for an ideal $\Delta_{\mathrm{D}}G^{\circ}{}_{\mathrm{MCH}}$ value of −19.8±0.1 kJ mol^{-1}. In our opinion, this discrepancy points to a selective solvation phenomenon. In the presence of up to 60 vol% MCH in $CHCl_3$, PBI π-faces are preferentially solvated by $CHCl_3$ molecules. At higher MCH contents, however, preferential solvation by the decreasing fraction of $CHCl_3$ molecules becomes disfavored for entropic reason (i.e. $CHCl_3$ molecules have to be considered like guest molecules dissolved in MCH) and PBI dimerization involving the m-perylene-facets becomes strongly triggered by the solvophobic effect of the MCH solvent.

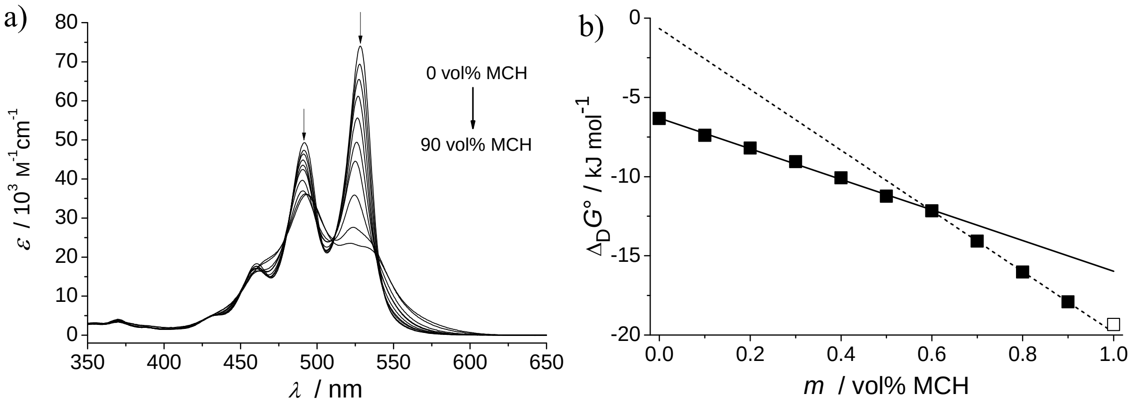

Figure 8. a) Solvent-dependent UV/Vis absorption changes of PBI **6** at a concentration of 10 mM recorded at 293 K, starting in pure $CHCl_3$ and increasing the volume fraction of undeuterated MCH in 10 vol% steps. Arrows indicate the spectral changes upon increasing the volume fraction of MCH. b) Plot of the $\Delta_{\mathrm{D}}G^{\circ}$ values versus the MCH volume fraction m. The solid and dotted lines are the best linear fitting results of the points from m = 0 to 0.6 and from m = 0.6 to 0.9. The data point of $\Delta_{\mathrm{D}}G^{\circ}$ = 19.3 kJ mol^{-1} at m = 1 was deduced from the K_2 value of 2800 M^{-1} in terms of K_2-K model.

3.3.8 ^{1}H NMR Linewidths

Further fundamental insights into PBI aggregation can be derived from the signal broadening in NMR spectra. The widths of the ^{1}H NMR signals of PBI **6** exhibit a pronounced dependence on $CDCl_3/D_{14}$-MCH ratio (Figure 9), concentration (Figure 6a) and temperature (Figure S1). For a high chloroform fraction, a small PBI **6** concentration and the ambient temperature sharp signals are observed corresponding to a weighted average of monomer and dimer resonances with fast exchange between each other. For the opposite extreme (pure MCH and high PBI **6** concentration) a large number of individual ^{1}H NMR signals with moderate linewidths appear which can be attributed to coexisting dimers and oligomers with slow exchange resulting in individual resonances for each species. The broad NMR signals in the intermediate region can thus be interpreted by coalescence effects as the crossover from slow to fast exchange processes. All three types of discussed spectra (fast, intermediate and slow exchange) can be observed by varying the solvent from pure chloroform to pure MCH at a fixed PBI **6** concentration (Figure 9). The spectral changes (chemical shifts, linewidths) upon increasing the MCH fraction from 0 to 90 vol% strongly resemble those monitored for rising concentration of PBI **6** at a constant $CDCl_3/D_{14}$-MCH ratio (Figure 2).

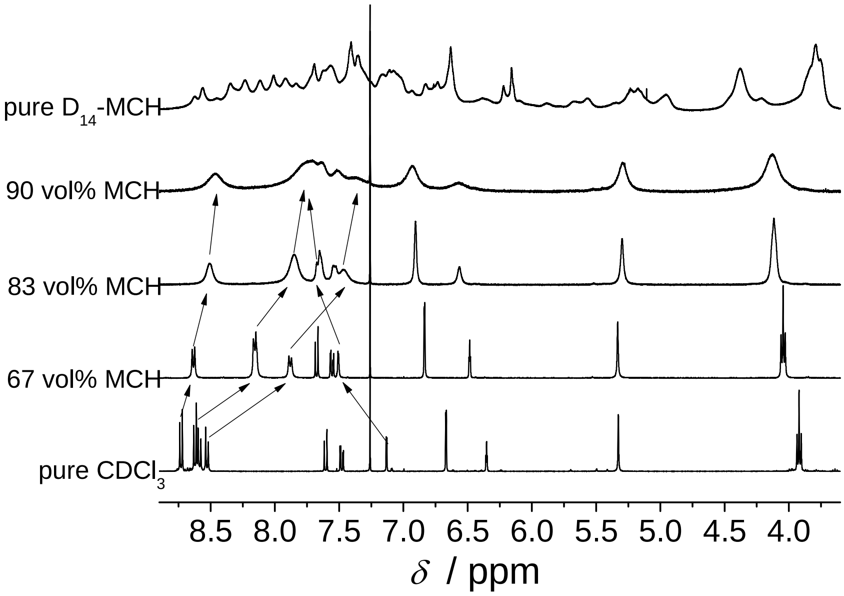

Figure 9. Partial ^{1}H NMR spectra of PBI **6** recorded with 600 MHz NMR at a concentration of 10 mM in pure $CDCl_3$ and D_{14}-MCH solvents as well as in solvent mixtures of $CDCl_3/D_{14}$-MCH.

In additional investigations, we kept the dimerization degree α_{agg} constant (around 50%) and compared the ^{1}H linewidths under different experimental conditions, starting with a PBI **6** concentration of 2 mM in a $CDCl_3$/D_{14}-MCH (v:v = 1:5) mixture at 25 °C. Upon increasing the concentration of PBI **6** either the chloroform content (Figure 10) or the temperature (Figure 11) have to be augmented to ensure a constant α_{agg}. The narrowing of NMR signals observed for both cases can be attributed to kinetically less stable dimers at larger chloroform content or higher temperature, resulting in faster exchange rates.

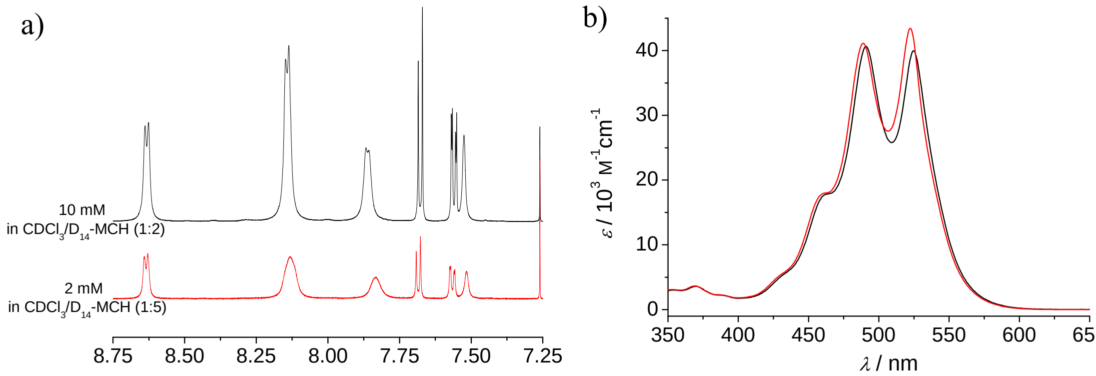

Figure 10. a) Partial 600 MHz ^{1}H NMR and b) absorption spectra of PBI **6** samples in $CDCl_3$/D_{14}-MCH (1:2) at 10 mM (black line) and in $CDCl_3$/D_{14}-MCH (1:5) at 2 mM (red line) recorded at 25 °C.

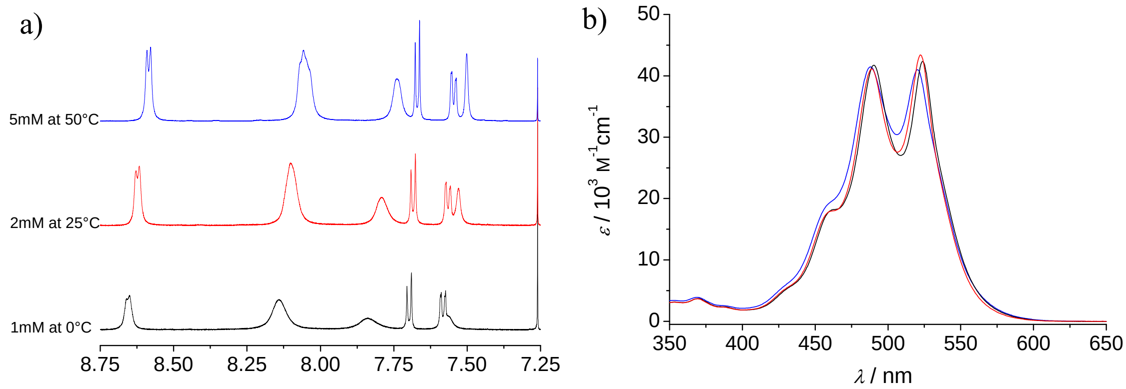

Figure 11. a) Partial 600 MHz ^{1}H NMR and b) absorption spectra of PBI **6** samples in $CDCl_3$/D_{14}-MCH (1:5) at 1 mM (black line, recorded at 0 °C), at 2 mM (red line, recorded at 25 °C) and at 5 mM (blue line, recorded at 50 °C).

These results suggest that the onset of NMR signal broadening with increasing MCH content and/or PBI **6** concentration correlates with the selective solvation phenomenon discussed in the previous paragraph. For a sufficient amount of chloroform, the PBI π-faces are preferentially solvated by chloroform molecules connected with a fast exchange between monomers and dimers due to the "weakening" of π-π-interactions by the "good" solvent chloroform. Below a critical chloroform content (which increases with PBI **6** concentration) the exchange rate between monomers and dimers slows down due to the solvophobic effect of MCH. In addition, dimers start to assemble into larger oligomers resulting in a further decrease of exchange frequencies in pure MCH solvent.

3.4 Conclusions

In this chapter, we reported a novel PBI building block featuring one rigid and one flexible substituent at the two imide positions. By virtue of the steric demand of these substituents, the designed PBI is prone to form discrete π-π-stacked dimers rather than extended oligomeric π-stacks. The dimerization process of PBI **6** has been elucidated by means of nonlinear least-squares analysis of the concentration-dependent ^{1}H NMR and UV/Vis spectra in terms of a dimer model. DOSY NMR spectroscopy further confirmed the absence of aggregates larger than dimer. The observed shifts of proton resonances in NMR dilution experiments indicate the formation of a head-to-tail π-stack composed of two PBIs with a certain rotational displacement. Detailed elucidation of the head-to-tail *m*-*m*-dimer structure with a rotational angle of about 30° is corroborated by means of ROESY NMR spectra associated with molecular modeling studies. Consequently, we have not only programmed PBI dimer formation driven solely by π-π-interaction, but also fully described the well-defined dimer structure in solution.

Furthermore, the π-π-stacking of PBI **6** was investigated in different $CHCl_3$/MCH solvent mixtures. Two regimes with a linear relationship of the Gibbs free energy versus the solvent composition are found between 0 and 60 vol% MCH and between 60 and 90 vol% MCH in $CHCl_3$ (for PBI **6** at a concentration of 10 mM), suggesting a selective solvation effect. Accordingly, preferential solvation of the π-surfaces by chloroform molecules weakens the PBI π-π-interaction in solvent mixtures as long as the $CHCl_3$ content is of sufficient magnitude (≥ 40%). In pure MCH solvent, the free π-face suffers from bad solvation which triggers the formation of larger aggregates according to complex ^{1}H NMR spectra, DOSY NMR studies and UV/Vis dilution experiments. The latter indeed revealed a cooperative self-assembly process that cannot be explained by a simple PBI dimerization process. Based on the single crystal structure of a similar PBI building block, a packing model was elaborated for the extended aggregation that does not involve additional contacts between PBI π-faces beyond those given in the dimer units, in compliance with the UV/Vis spectra of the aggregates. To the best of our knowledge, this is the first time that often observed apparent equilibriums between two spectroscopically distinguished species with well-defined isosbestic points in concentration- or temperature-dependent UV/Vis experiments were analyzed not only in terms of a simple dimerization (monomer-dimer) or an isodesmic growth (monomer-oligomer). Instead, we have provided experimental evidence for the formation of larger aggregates composed of π-dimeric units. The formation of such aggregates by various types of complex self-assembly pathways[47] might indeed be very common, but has been widely overlooked in the past.

3.5 Experimental Section

All solvents and reagents were purchased from commercial sources and used as received without further purification, unless otherwise stated. Dry solvents were purified according to literature procedures.[48] Benzyl alcohol **1** and perylene monoimide **5** were synthesized as described in literature.[18,19] Thin layer chromatography (TLC) was conducted on aluminum plates coated with silica gel (60 F_{254}, Merck). Column chromatography was performed using silica gel (Geduran Si 60 from Merck, particle size 0.040–0.063 mm) as stationary phase. Recycling preparative HPLC was performed on a system (JAI LC-9105) equipped with a photodiode array UV/Vis detector (JAI 3702) and an RI detector (JAI RI-7s) by use of a semi-preparative NUCLEOSIL 100–5 NO_2 column (Macherey&Nagel). For HPLC separation, HPLC grade solvents ($CHCl_3$ and MeOH) from VWR (Darmstadt, Germany) were used. High resolution electrospray ionisation (ESI) mass spectra were measured on a MicroTOF Focus instrument (Bruker Daltronik GmbH) and MALDI-TOF measurements were carried out on a

Bruker Autoflex II. The melting points were measured by using Olympus BX-41 polarization microscope equipped with a Linkam THMS 600 hot stage and a temperature controller unit.

UV/Vis Absorption Studies. The UV/Vis absorption measurements were performed on a Perkin Elmer Lambda 35 spectrometer making use of conventional quartz cells with 0.01−10 mm path length to cover a large concentration range. The slit width and the scan speed were set to be 1.0 nm and 120 nm/min, respectively. The temperature was controlled with a PTP-1+1 Peltier Temperature Programmer (PerkinElmer). In order to avoid non-systematic error, all the samples having a concentration of more than 0.5 mM were individually prepared by carefully dissolving the precisely weighed compound in solvents, assuming that the volume of the compound is negligible after dissolution. The samples with a concentration less than 0.5 mM were diluted ten times from a corresponding stock solution. For a comparative study with NMR spectra, UV/Vis dilution experiments were conducted in the deuterated solvents.

NMR Spectroscopic Studies. ^{1}H, ^{13}C, DEPT, COSY, HSQC and HMBC NMR spectra were recorded in standard 5 mm NMR tubes on a Bruker Avance 400 and/or a Bruker DMX 600 spectrometer with TMS or residual undeuterated solvents as internal standard (7.26 ppm for $C\mathit{H}Cl_3$ and 77.00 ppm for $\mathit{C}DCl_3$). The 2D ROESY and DOSY data were acquired with the 600 MHz instrument which is equipped with a 5 mm ^{13}C/^{1}H cryoprobe with z axis gradient coil capable of producing pulsed magnetic field gradients of 55 G/cm. For low-temperature NMR measurements, the temperature was calibrated using NMR samples of 4% CH_3OH in D_4-methanol and 80% ethylene glycol in D_6-DMSO, respectively. Prior to 2D ROESY NMR measurements, the deuterated solvents and the NMR tubes used were degassed by bubbling with dry argon gas. Alternating-phase 180° pulses were applied during the mixing time of 200 ms for the ROESY spectra to suppress unwanted TOCSY contributions.[49] In the DOSY experiments, the suppression of flow effects owing to temperature gradients in the coil of the cryoprobe was achieved in two different ways: (i) using the stimulated echo BPP-LED pulse sequence[50] (longitudinal eddy current delay sequence with bipolar gradient pulse pairs for diffusion and additional spoil gradients after the second and fourth 90° pulse) in which convection in the z direction was suppressed by sample rotation[51] and (ii) by the corresponding double stimulated echo pulse sequence[52] (without sample rotation and with spoil gradients after the second, fourth and sixth 90° pulse) in which the double stimulated echo results in a compensation of the flow effects. The following acquisition parameters were used for both methods: duration δ of a bipolar gradient pulse 4 or 6 ms, diffusion time Δ 50 ms, eddy current delay 5 ms. The diffusion time Δ was kept constant in each DOSY experiment while the sinusoidal diffusion gradients were incremented from 2% to 95% of maximum gradient strength in 32 linear steps.

3,5-Bis(dodecyloxy)benzyl bromide (2): A mixture of 3,5-bis(dodecyloxy)benzyl alcohol **1** (1.52 g, 3.2 mmol), carbon tetrabromide (1.60 g, 4.8 mmol, 1.5 equiv.) and triphenylphosphine (1.26 g, 4.8 mmol, 1.5 equiv.) in anhydrous THF (16 mL) was stirred under an argon atmosphere at room temperature overnight (~ 16 h). The solvent was removed under reduced pressure and the residue was washed with MeOH (3×10 mL). After that, the crude product was purified by column chromatography on silica gel with CH_2Cl_2/*n*-hexane (*v*/*v* = 1:1) as eluent. Yield: 1.49 g (2.76 mmol, 87%) as a white solid. TLC (CH_2Cl_2/*n*-hexane = 1:1): $R_f = 0.83$. M.p.: 48–49 °C. ^{1}H NMR (400 MHz, $CDCl_3$): δ 6.51 (d, $J = 2.0$ Hz, 2H, Ph-*H*), 6.38 (t, $J = 2.0$ Hz, 1H, Ph-*H*), 4.40 (s, 2H, PhCH_2Br), 3.93 (t, $J = 6.8$ Hz, 4H, OCH_2CH$_2$), 1.76 (quin, $J = 6.8$ Hz, 4H, OCH$_2$CH_2), 1.41–1.48 (m, 4H, OCH$_2$CH$_2$CH_2), 1.27 (br-s, 32H, alkoxy-*H*), 0.89 (t, $J = 7.0$ Hz, 6H, CH$_2$CH_3). HRMS (ESI-TOF, pos. mode): calcd for $C_{31}H_{56}BrO_2$ ($[M+H]^+$) 539.34582; found 539.34587. Anal. calcd for $C_{31}H_{55}BrO_2$: C, 68.99; H, 10.27; found: C, 68.72; H, 10.42.

3,5-Bis(dodecyloxy)benzyl azide (3): A mixture of 3,5-bis(dodecyloxy)benzyl bromide **2** (1.08 g, 2.0 mmol) and sodium azide (390 mg, 6.0 mmol, 3.0 equiv.) in anhydrous DMF (20 mL) was heated to 105 °C for 3 h. After cooling, the DMF solvent was removed under reduced pressure. The residue was dissolved in ethyl ether (20 mL) and washed with H_2O and brine (3×20 mL). The aqueous layer was extracted with ethyl ether (3×20 mL) and the combined organic layers were concentrated in vacuum and purified by column chromatography on silica gel with CH_2Cl_2/*n*-hexane (*v*/*v* = 1:1) as eluent. Yield: 0.99 g (2.0 mmol, 99%) as a white solid. TLC (CH_2Cl_2/*n*-hexane = 1:1): $R_f = 0.76$. M.p.: 36–37 °C.

^{1}H NMR (400 MHz, $CDCl_3$): δ 6.43 (d, J = 2.4 Hz, 2H, Ph-*H*), 6.41 (t, J = 2.4 Hz, 1H, Ph-*H*), 4.25 (s, 2H, $PhCH_2N_3$), 3.94 (t, J = 6.4 Hz, 4H, OCH_2CH_2), 1.77 (quin, J = 6.4 Hz, 4H, OCH_2CH_2), 1.41−1.48 (m, 4H, $OCH_2CH_2CH_2$), 1.27 (br-s, 32H, alkoxy-*H*), 0.88 (t, J = 6.8 Hz, 6H, CH_2CH_3). HRMS (ESI-TOF, pos. mode): calcd for $C_{31}H_{56}N_3O_2$ ($[M+H]^+$) 502.43670; found. 502.43631. Anal. calcd for $C_{31}H_{55}N_3O_2$: C, 74.20; H, 11.05; N, 8.37; found: C, 74.26; H, 11.21; N, 8.35.

3,5-Bis(dodecyloxy)benzyl amine (4): To a solution of 3,5-bis(dodecyloxy)benzyl azide **3** (0.61 g, 1.2 mmol) in THF (10 mL) was added triphenylphosphine (0.65 g, 2.5 mmol). After the reaction mixture was stirred for 2 h at room temperature, distilled H_2O (0.2 mL, 11.1 mmol) was added and it was stirred for another 3 h. After reaction, the solvent was removed under reduced pressure. The residue was dissolved in CH_2Cl_2 (20 mL) and washed with 5% NaOH solution (3×20 mL). The aqueous layer was extracted with CH_2Cl_2 (3×20 mL) and the combined organic layers were concentrated in vacuum and purified by a short column chromatography on silica gel with CH_2Cl_2/MeOH (*v*/*v* = 97:3) as eluent. The ^{1}H NMR and MS indicate a mixture of benzyl amine product and triphenylphosphine oxide byproduct (molar ratio about 1:1), which was used for next step without further purification. Yield: 0.43 g (0.9 mmol, 75%) as a white solid. TLC (CH_2Cl_2/MeOH = 9:1): R_f = 0.47. ^{1}H NMR (400 MHz, $CDCl_3$): δ 6.45 (d, J = 2.4 Hz, 2H, Ph-*H*), 6.34 (t, J = 2.4 Hz, 1H, Ph-*H*), 3.92 (t, J = 6.6 Hz, 4H, OCH_2CH_2), 3.80 (s, 2H, $PhCH_2NH_2$), 1.77 (quin, J = 6.6 Hz, 4H, OCH_2CH_2), 1.40–1.47 (m, 4H, $OCH_2CH_2CH_2$), 1.27 (br-s, 32H, alkoxy-*H*), 0.88 (t, J = 6.8 Hz, 6H, CH_2CH_3). HRMS (ESI-TOF, pos. mode): calcd for $C_{31}H_{58}N_1O_2$ ($[M+H]^+$) 476.44621; found 476.44612.

***N*-(3,5-Bis(dodecyloxy)benzyl)-*N’*-(2,5-di-*tert*-butylphenyl)perylene-3,4:9,10-tetracarboxylic acid bisimide (6):** A mixture of *N*-(2,5-di-*tert*-butylphenyl)perylene-3,4:9,10-tetracarboxy-3,4-anhydride-9,10-imide **5** (116 mg, 0.20 mmol), 3,5-bis(dodecyloxy)-benzyl amine **4** (240 mg, 0.75 mmol) and imidazole (10 g) was stirred under an argon atmosphere at 140 °C for 4 h. Before cooling, the reaction was directly quenched with 2.0 M HCl (50 mL) and stirred for another 1 h. The resulting precipitate was separated by filtration and washed with MeOH (3×10 mL). After drying in vacuum, the crude product was purified first by silica gel chromatography (CH_2Cl_2 as eluent) and then by using recycling HPLC ($CHCl_3$ as eluent). Yield: 102 mg (0.10 mmol, 50%) as a deep red solid. TLC (CH_2Cl_2): R_f = 0.34. M.p.: 168–169 °C. ^{1}H NMR (400 MHz, $CDCl_3$): δ 8.24–8.68 (m, 8H, perylene protons), 7.61 (d, J = 8.8 Hz, 1H, Ph-*H*), 7.49 (dd, J_1 = 8.8 Hz, J_2 = 2.4 Hz, 1H, Ph-*H*), 7.30 (t, J = 2.4 Hz, 1H, Ph-*H*), 6.66 (d, J = 2.4 Hz, 2H, Bn-*H*), 6.36 (t, J = 2.4 Hz, 1H, Bn-*H*), 5.29 (s, 2H, NCH_2), 3.93 (t, J = 6.4 Hz, 4H, OCH_2CH_2), 1.74 (quin, J = 6.4 Hz, 4H, OCH_2CH_2), 1.40–1.45 (m, 4H, $OCH_2CH_2CH_2$), 1.37 (s, 9H, *t*-bu-*H*), 1.31 (s, 9H, *t*-bu-*H*), 1.24 (br-s, 32H, alkoxy-*H*), 0.87 (t, J = 6.8 Hz, 6H, CH_2CH_3). ^{13}C NMR (100 MHz, $CDCl_3$): δ 164.2, 162.9, 160.3, 150.3, 143.7, 139.0, 134.4, 134.1, 132.6, 131.5, 131.1, 129.6, 128.9, 128.7, 128.0, 126.3, 126.2, 125.9, 123.7, 123.0, 122.9, 122.8, 107.3, 100.3, 68.0, 43.7, 35.5, 34.3, 31.9, 31.7, 31.3, 29.8, 29.7, 29.6, 29.5, 29.4, 29.3, 29.2, 26.0, 22.7, 14.1. HRMS (ESI-TOF, pos. mode): calcd for $C_{69}H_{85}N_2O_6$ $[M+H]^+$ 1037.64021; found 1037.64073. Anal. calcd for $C_{69}H_{84}N_2O_6$: C, 79.88; H, 8.16; N, 2.70; found: C, 79.39; H, 8.13; N, 2.90.

***N*-(4-Iodobenzyl)-*N'*-(2,5-di-*tert*-butylphenyl)perylene-3,4:9,10-tetracarboxylic acid bisimide (7):** A mixture of *N*-(2,5-di-*tert*-butylphenyl)perylene-3,4:9,10-tetracarboxy-3,4-anhydride-9,10-imide **5** (100 mg, 0.17 mmol), 4-iodobenzyl amine (100 mg, 0.43 mmol) and imidazole (10 g) was stirred under an argon atmosphere at 140 °C for 4 h. Before cooling, the reaction was directly quenched with 2.0 M HCl (50 mL) and stirred for another 1 h. The resulting precipitate was separated by filtration and washed with MeOH (3×10 mL). After drying in vacuum, the crude product was purified by silica gel chromatography (CH_2Cl_2 as eluent) and then by using recycling HPLC ($CHCl_3$ as eluent). Yield: 90 mg (0.11 mmol, 64%) as a red solid. TLC (CH_2Cl_2): R_f = 0.10. M.p.: 388–389 °C. ^{1}H NMR (400 MHz, $CDCl_3$): δ 8.54–8.74 (m, 8H, perylene protons), 7.65 (dt, J_1 = 8.8 Hz, J_2 = 2.0 Hz, 2H, Bn-*H*), 7.61 (d, J = 8.8 Hz, 1H, Ph-*H*), 7.48 (dd, J_1 = 8.8 Hz, J_2 = 2.4 Hz, 1H, Ph-*H*), 7.33 (dt, J_1 = 8.8 Hz, J_2 = 2.0 Hz, 2H, Bn-*H*), 7.13 (d, J = 2.4 Hz, 1H, Ph-*H*), 5.34 (s, 2H, NCH_2), 1.35 (s, 9H, *t*-bu-*H*), 1.29 (s, 9H, *t*-bu-*H*). ^{13}C NMR (100 MHz, $CDCl_3$): δ 164.3, 163.3, 150.2, 143.7, 137.6, 136.7, 134.8, 134.7, 132.6, 131.8, 131.6, 131.2, 129.8, 129.3, 128.8, 127.8, 126.6, 126.4, 126.3, 123.8, 123.2, 123.1, 123.0, 93.3, 43.3, 35.5, 34.3, 31.7, 31.2. HRMS (ESI-TOF, pos. mode):

calcd for $C_{45}H_{36}IN_2O_4$ $[M+H]^+$ 795.17143; found. 795.17179. Anal. calcd for $C_{45}H_{35}IN_2O_4$: C, 68.01; H, 4.44; N, 3.53; found: C, 68.00; H, 4.52; N, 3.58.

3.6 References and Notes

[1] a) C. A. Hunter, K. R. Lawson, J. Perkins, C. J. Urch, *J. Chem. Soc., Perkin Trans. 2* **2001**, 651–669; b) C. A. Hunter, J. K. M. Sanders, *J. Am. Chem. Soc.* **1990**, *112*, 5525–5534; c) C. R. Martinez, B. L. Iverson, *Chem. Sci.* **2012**, *3*, 2191–2201.

[2] a) E. A. Meyer, R. K. Castellano, F. Diederich, *Angew. Chem. Int. Ed.* **2003**, *42*, 1210–1250; b) L. M. Salonen, M. Ellermann, F. Diederich, *Angew. Chem. Int. Ed.* **2011**, *50*, 4808–4842.

[3] a) F. J. M. Hoeben, P. Jonkheijm, E. W. Meijer, A. P. H. J. Schenning, *Chem. Rev.* **2005**, *105*, 1491–1546; b) R. Bhosale, J. Misek, N. Sakai, S. Matile, *Chem. Soc. Rev.* **2010**, *39*, 138–149.

[4] C. Wang, H. Dong, W. Hu, Y. Liu, D. Zhu, *Chem. Rev.* **2012**, *112*, 2208–2267.

[5] a) A. Mishra, P. Bäuerle, *Angew. Chem. Int. Ed.* **2012**, *51*, 2020–2067; b) T. M. Clarke, J. R. Durrant, *Chem. Rev.* **2010**, *110*, 6736–6767.

[6] a) M. R. Wasielewski, *Acc. Chem. Res.* **2009**, *42*, 1910–1921; b) F. Würthner, *Chem. Commun.* **2004**, 1564–1579.

[7] a) F. Würthner, M. Stolte, *Chem. Commun.* **2011**, *47*, 5109–5115; b) J. E. Anthony, A. Facchetti, M. Heeney, S. R. Marder, X. Zhan, *Adv. Mater.* **2010**, *22*, 3876–3892.

[8] a) F. Würthner, Z. Chen, V. Dehm, V. Stepanenko, *Chem. Commun.* **2006**, 1188–1190; b) Z. Chen, V. Stepanenko, V. Dehm, P. Prins, L. D. A. Siebbeles, J. Seibt, P. Marquetand, V. Engel, F. Würthner, *Chem. Eur. J.* **2007**, *13*, 436–449; c) V. Dehm, Z. Chen, U. Baumeister, P. Prins, L. D. A. Siebbeles, F. Würthner, *Org. Lett.* **2007**, *9*, 1085–1088.

[9] a) R. F. Fink, J. Seibt, V. Engel, M. Renz, M. Kaupp, S. Lochbrunner, H.-M. Zhao, J. Pfister, F. Würthner, B. Engels, *J. Am. Chem. Soc.* **2008**, *130*, 12858–12859; b) H.-M. Zhao, J. Pfister, V. Settels, M. Renz, M. Kaupp, V. C. Dehm, F. Würthner, R. F. Fink, B. Engels, *J. Am. Chem. Soc.* **2009**, *131*, 15660–15668; c) J. Seibt, T. Winkler, K. Renziehausen, V. Dehm, F. Würthner, H. D. Meyer, V. Engel, *J. Phys. Chem. A* **2009**, *113*, 13475–13482.

[10] a) J. M. Giaimo, J. V. Lockard, L. E. Sinks, A. M. Scott, T. M. Wilson, M. R. Wasielewski, *J. Phys. Chem. A* **2008**, *112*, 2322–2330; b) C. Hippius, I. H. M. van Stokkum, E. Zangrando, R. M. Williams, M. Wykes, D. Beljonne, F. Würthner, *J. Phys. Chem. C* **2008**, *112*, 14626–14638; c) A. Syamakumari, A. P. H. J. Schenning, E. W. Meijer, *Chem. Eur. J.* **2002**, *8*, 3353–3361.

[11] a) D. Veldman, S. M. A. Chopin, S. C. J. Meskers, M. M. Groeneveld, R. M. Williams,

R. A. J. Janssen, *J. Phys. Chem. A* **2008**, *112*, 5846–5857; b) H. Yoo, J. Yang, A. Yousef, M. R. Wasielewski, D. Kim, *J. Am. Chem. Soc.* **2010**, *132*, 3939–3944; c) F. Gao, Y. Zhao, W. Liang, *J. Phys. Chem. B* **2011**, *115*, 2699–2708.

[12] a) M. M. Safont-Sempere, P. Osswald, K. Radacki, F. Würthner, *Chem. Eur. J.* **2010**, *16*, 7380–7384; b) M. M. Safont-Sempere, P. Osswald, M. Stolte, M. Grüne, M. Renz, M. Kaupp, K. Radacki, H. Braunschweig, F. Würthner, *J. Am. Chem. Soc.* **2011**, *133*, 9580–9591.

[13] N.-T. Lin, A. Vargas Jentzsch, L. Guenee, J.-M. Neudorfl, S. Aziz, A. Berkessel, E. Orentas, N. Sakai, S. Matile, *Chem. Sci.* **2012**, *3*, 1121–1127.

[14] Z. Chen, A. Lohr, C. R. Saha-Möller, F. Würthner, *Chem. Soc. Rev.* **2009**, *38*, 564–584.

[15] H. Langhals, S. Demmig, H. Huber, *Spectrochim. Acta A* **1988**, *44*, 1189–1193.

[16] J. M. Lavin, K. D. Shimizu, *Chem. Commun.* **2007**, 228–230.

[17] D.-S. Choi, Y. S. Chong, D. Whitehead, K. D. Shimizu, *Org. Lett.* **2001**, *3*, 3757–3760.

[18] I. Bury, B. Heinrich, C. Bourgogne, D. Guillon, B. Donnio, *Chem. Eur. J.* **2006**, *12*, 8396–8413.

[19] H. Kaiser, J. Lindner, H. Langhals, *Chem. Ber.* **1991**, *124*, 529–535.

[20] H. Langhals, *Chem. Ber.* **1985**, *118*, 4641–4645.

[21] Z. Chen, B. Fimmel, F. Würthner, *Org. Biomol. Chem.* **2012**, *10*, 5845−5855.

[22] a) S. P. Brown, H. W. Spiess, *Chem. Rev.* **2001**, *101*, 4125–4156; b) J. Hu, T. Xu, Y. Cheng, *Chem. Rev.* **2012**, *112*, 3856−3891; c) H.-J. Schneider, F. Hacket, V. Rüdiger, H. Ikeda, *Chem. Rev.* **1998**, *98*, 1755–1786.

[23] a) J. Wu, A. Fechtenkötter, J. Gauss, M. D. Watson, M. Kastler, C. Fechtenkötter, M. Wagner, K. Müllen, *J. Am. Chem. Soc.* **2004**, *126*, 11311–11321; b) J. A. A. W. Elemans, A. E. Rowan, R. J. M. Nolte, *J. Am. Chem. Soc.* **2002**, *124*, 1532–1540; c) D. Zhao, J. S. Moore, *J. Org. Chem.* **2002**, *67*, 3548–3554.

[24] a) F. H. Beijer, H. Kooijman, A. L. Spek, R. P. Sijbesma, E. W. Meijer, *Angew. Chem. Int. Ed.* **1998**, *37*, 75–78; b) C. Rether, E. Verheggen, C. Schmuck, *Chem. Commun.* **2011**, *47*, 9078–9079; c) R. Wyler, J. de Mendoza, J. Rebek, *Angew. Chem. Int. Ed.* **1993**, *32*, 1699–1701.

[25] a) A. D. Q. Li, W. Wang, L.-Q. Wang, *Chem. Eur. J.* **2003**, *9*, 4594–4601; b) W. Wang, L.-S. Li, G. Helms, H.-H. Zhou, A. D. Q. Li, *J. Am. Chem. Soc.* **2003**, *125*, 1120–1121.

[26] a) V. Dehm, M. Büchner, J. Seibt, V. Engel, F. Würthner, *Chem. Sci.* **2011**, *2*, 2094–2100; b) M. J. Ahrens, L. E. Sinks, B. Rybtchinski, W. Liu, B. A. Jones, J. M. Giaimo, A. V. Gusev, A. J. Goshe, D. M. Tiede, M. R. Wasielewski, *J. Am. Chem. Soc.* **2004**, *126*, 8284–8294; c) B. Rybtchinski, L. E. Sinks, M. R. Wasielewski, *J. Phys. Chem. A* **2004**, *108*, 7497–7505; d) M. J. Ahrens, R. F. Kelley, Z. E. X. Dance, M. R. Wasielewski, *Phys. Chem. Chem. Phys.* **2007**, *9*, 1469–1478.

[27] E. Arunan, G. R. Desiraju, R. A. Klein, J. Sadlej, S. Scheiner, I. Alkorta, D. C. Clary,

R. H. Crabtree, J. J. Dannenberg, P. Hobza, H. G. Kjaergaard, A. C. Legon, B. Mennucci, D. J. Nesbitt, *Pure Appl. Chem.* **2011**, *83*, 1619–1636.

[28] a) J. D. Badjić, S. J. Cantrill, J. F. Stoddart, *J. Am. Chem. Soc.* **2004**, *126*, 2288–2289; b) G. R. Desiraju, *Acc. Chem. Res.* **1991**, *24*, 290–296; c) F. M. Raymo, M. D. Bartberger, K. N. Houk, J. F. Stoddart, *J. Am. Chem. Soc.* **2001**, *123*, 9264–9267; d) T. Steiner, *Angew. Chem. Int. Ed.* **2002**, *41*, 48–76; e) A. Senes, *PNAS* **2001**, *98*, 9056–9061.

[29] a) J. L. Cook, C. A. Hunter, C. M. R. Low, A. Perez-Velasco, J. G. Vinter, *Angew. Chem. Int. Ed.* **2007**, *46*, 3706–3709; b) S. L. Cockroft, C. A. Hunter, *Chem. Commun.* **2006**, 3806–3808.

[30] R. B. Martin, *Chem. Rev.* **1996**, *96*, 3043–3064.

[31] In accordance with the values obtained by NMR analysis for different protons, also here slightly different K_D values were obtained at different wavelengths: 410±50 M^{-1} at 454 nm and 520±70 M^{-1} at 485 nm.

[32] a) M. Kasha, H. R. Rawls, M. A. El-Bayoumi, *Pure Appl. Chem.* **1965**, *11*, 371–392; b) M. Kasha, *Radiat. Res.* **1963**, *20*, 55–70.

[33] Y. Cohen, L. Avram, L. Frish, *Angew. Chem. Int. Ed.* **2005**, *44*, 520–554.

[34] In the strict sense, the viscosity of the sample solution rather than that of the solvent should be used to calculate the hydrodynamic radius. With higher concentration, the viscosity of the medium becomes larger, leading to slightly exaggerated value for hydrodynamic radius. The measurement of a precise viscosity value for the 40 mM solution could not be performed due to the considerable amount of compound needed.

[35] H. Mo, T. C. Pochapsky, *Prog. Nucl. Mag. Res. Sp.* **1997**, *30*, 1–38.

[36] Owing to the signal broadening, the ROESY NMR spectrum of PBI **6** was first recorded with the sample in $CDCl_3/D_{14}$-MCH (v:v = 1:5) at 1 mM. A more clear ROESY spectrum was obtained with the sample in $CDCl_3/D_{14}$-MCH (v:v = 1:2) at 10 mM. In addition, the sample in $CDCl_3$ at 50 mM has also been measured (Figure S5). All of the three ROESY spectra exhibit the same and reproducible cross signals.

[37] *Maestro, version 9.1, MacroModel, version 9.8,* Schrödinger, LLC, New York, NY, **2011**.

[38] C. A. Hunter, H. L. Anderson, *Angew. Chem. Int. Ed.* **2009**, *48*, 7488–7499.

[39] T. E. Kaiser, V. Stepanenko, F. Würthner, *J. Am. Chem. Soc.* **2009**, *131*, 6719–6732.

[40] a) C. A. Hunter, *J. Chem. Soc., Chem. Commun.* **1991**, 749–751; b) W. B. Jennings, B. M. Farrell, J. F. Malone, *Acc. Chem. Res.* **2001**, *34*, 885–894; c) O. Takahashi, Y. Kohno, M. Nishio, *Chem. Rev.* **2010**, *110*, 6049–6076.

[41] J. N. H. Reek, A. H. Priem, H. Engelkamp, A. E. Rowan, J. A. A. W. Elemans, R. J. M. Nolte, *J. Am. Chem. Soc.* **1997**, *119*, 9956–9964.

[42] It is worth to note that the K value of 14000 M^{-1} is more than one order of magnitude

smaller than the binding constant observed for extended PBI aggregation in the absence of bulky substituents at the imide positions (see reference 21). Accordingly, the proposed packing arrangement only accounts for the special situation where extended PBI π-π-interaction is impossible.

[43] a) M. S. Cubberley, B. L. Iverson, *J. Am. Chem. Soc.* **2001**, *123*, 7560–7563; b) S. Lahiri, J. L. Thompson, J. S. Moore, *J. Am. Chem. Soc.* **2000**, *122*, 11315–11319; c) F. Würthner, S. Yao, T. Debaerdemaeker, R. Wortmann, *J. Am. Chem. Soc.* **2002**, *124*, 9431–9447; d) G. A. Breault, C. A. Hunter, P. C. Mayers, *J. Am. Chem. Soc.* **1998**, *120*, 3402–3410.

[44] S. Grimme, *Angew. Chem. Int. Ed.* **2008**, *47*, 3430–3434.

[45] C. R. Ray, J. S. Moore, *Adv. Polym. Sci.* **2005**, *177*, 91–149.

[46] R. B. Prince, J. G. Saven, P. G. Wolynes, J. S. Moore, *J. Am. Chem. Soc.* **1999**, *121*, 3114–3121.

[47] a) P. A. Korevaar, S. J. George, A. J. Markvoort, M. M. J. Smulders, P. A. J. Hilbers, A. P. H. J. Schenning, T. F. A. de Greef, E. W. Meijer, *Nature* **2012**, *481*, 492–496; b) A. Lohr, F. Würthner, *Isr. J. Chem.* **2011**, *51*, 1052–1066; c) Y. Tidhar, H. Weissman, S. G. Wolf, A. Gulino, B. Rybtchinski, *Chem. Eur. J.* **2011**, *17*, 6068–6075.

[48] D. D. Perrin, W. L. F. Armarego, *Purification of Laboratory Chemicals*, Pergamon Press: Oxford, 1980.

[49] a) T. L. Hwang, A. J. Shaka, *J. Am. Chem. Soc.* **1992**, *114*, 3157–3159; b) T.-L. Hwang, M. Kadkhodaei, A. Mohebbi, A. J. Shaka, *Magn. Reson. Chem.* **1992**, *30*, 24–34.

[50] D. H. Wu, A. D. Chen, C. S. Johnson, *J. Magn. Reson. A* **1995**, *115*, 260–264.

[51] a) J. Lounila, K. Oikarinen, P. Ingman, J. Jokisaari, *J. Magn. Reson. A* **1996**, *118*, 50–54; b) N. Esturau, F. Sánchez-Ferrando, J. A. Gavin, C. Roumestand, M.-A. Delsuc, T. Parella, *J. Magn. Reson.* **2001**, *153*, 48–55.

[52] A. Jerschow, N. Müller, *J. Magn. Reson.* **1997**, *125*, 372–375.

3.7 Supporting Information

Low-temperature ^{1}H NMR measurements

Low-temperature NMR measurements for the PBI **6** sample in $CDCl_3/D_{14}$-MCH (*v*:*v* = 1:5) was performed. Even at a temperature of 204 K, the separation of the single pattern of proton resonance signals could not be observed.

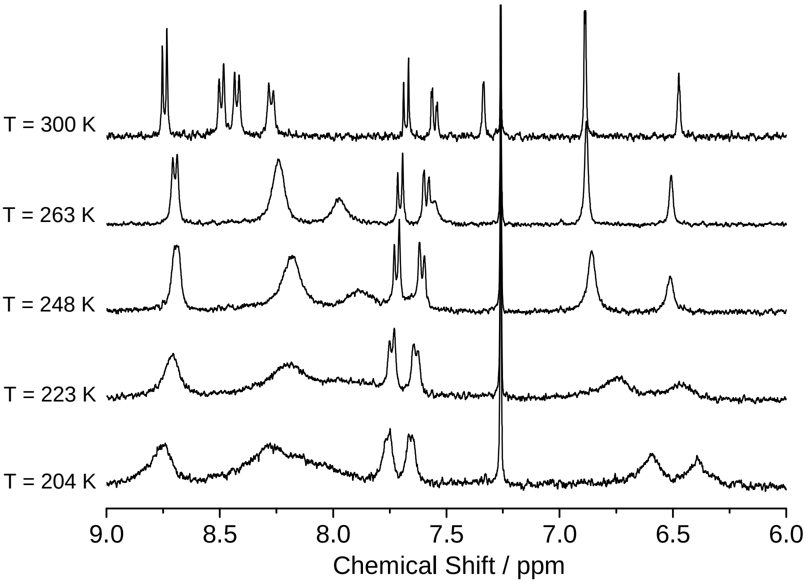

Figure S1. Aromatic range of temperature-dependent ^{1}H NMR spectra of PBI **6** at a concentration of 0.5 mM in $CDCl_3/D_{14}$-MCH (*v*:*v* = 1:5) recorded with 400 MHz NMR.

*DOSY NMR of PBI **6** at 40 mM in $CDCl_3/D_{14}$-MCH (v:v = 1:5)*

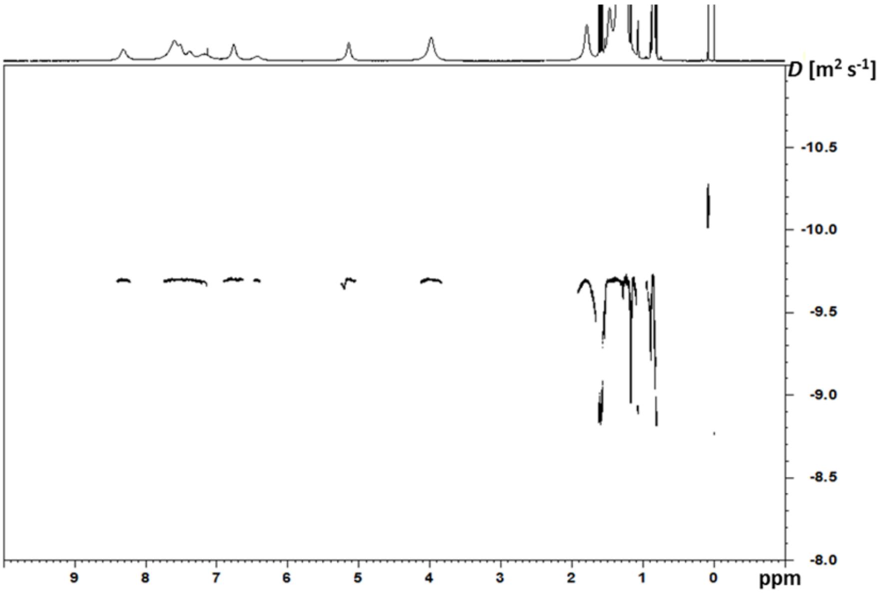

Figure S2. DOSY NMR spectrum of PBI **6** (40 mM in $CDCl_3/D_{14}$-MCH (*v*:*v* = 1:5), 600 MHz NMR, at 293 K). The diffusion coefficients *D* [m^2 s^{-1}] are plotted in a logarithmic scale against chemical shift *δ* [ppm].

Aggregation studies of PBI **6** *in chloroform*

The aggregation behavior of PBI **6** in pure chloroform was elucidated by ^{1}H NMR spectroscopy (Figure S3). Upon increasing concentration, the proton resonances of PBI **6** in $CDCl_3$ exhibit similar shifts as recorded in $CDCl_3/D_{14}$-MCH (*v*:*v* = 1:5). The perylene proton resonances are shifted to high-field due to the shielding effect, while the aromatic proton A6 is shifted to down-field as a result of the weak [C–H···O] hydrogen bond interaction. The chemical shift variations of all the perylene and A6 protons fit very well to a dimer model, suggesting discrete dimerization of PBI **6** in chloroform (Figure S4). The head-to-tail *m*-*m*-dimer motive was verified by through-space correlations detected in the ROESY NMR spectrum (Figure S5).

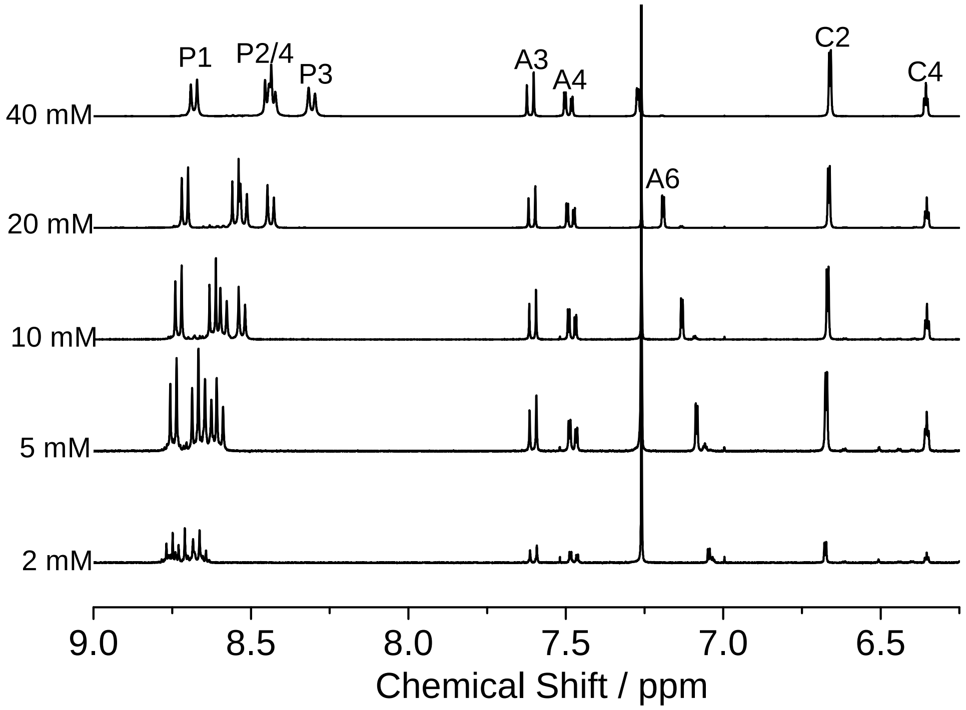

Figure S3. Aromatic range of concentration-dependent ^{1}H NMR spectra of PBI **6** from 2×10^{-3} to 4×10^{-2} M in pure $CDCl_3$ conducted with 400 MHz NMR at 293 K.

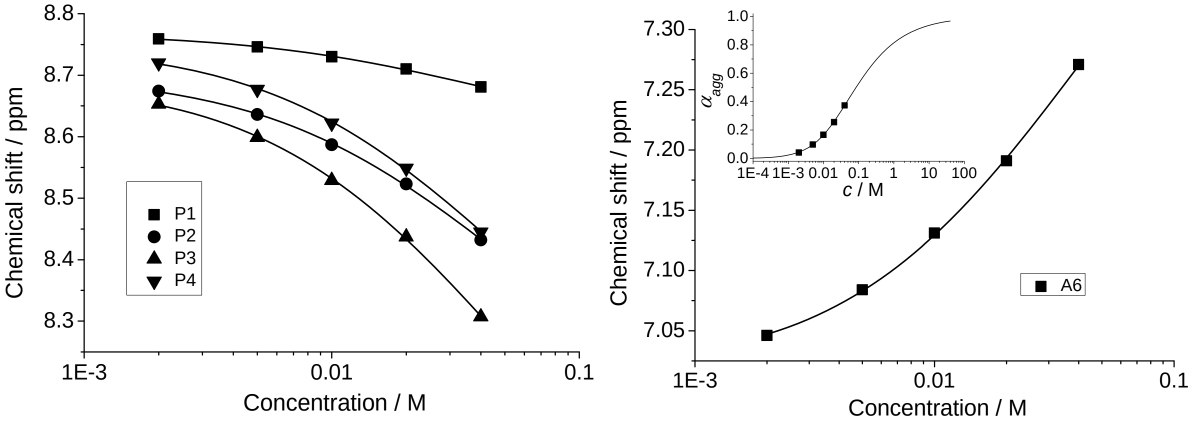

Protons	P1	P2	P3	P4	A6
R^2	0.99827	0.99904	0.99916	0.99907	0.99929
K_D (M^{-1})	10.4±2.0	9.3±1.4	9.3±1.3	9.0±1.3	11.8±1.4

Figure S4. Top: Fitting of chemical shift variations of perylene protons (left) and A6 proton (right) to a dimer model. Inset shows the changes of aggregation degree α_{agg} in response to the concentration increase. Bottom: List of the correlation coefficient R^2 and association constant K_{D} values obtained from the best fitting.

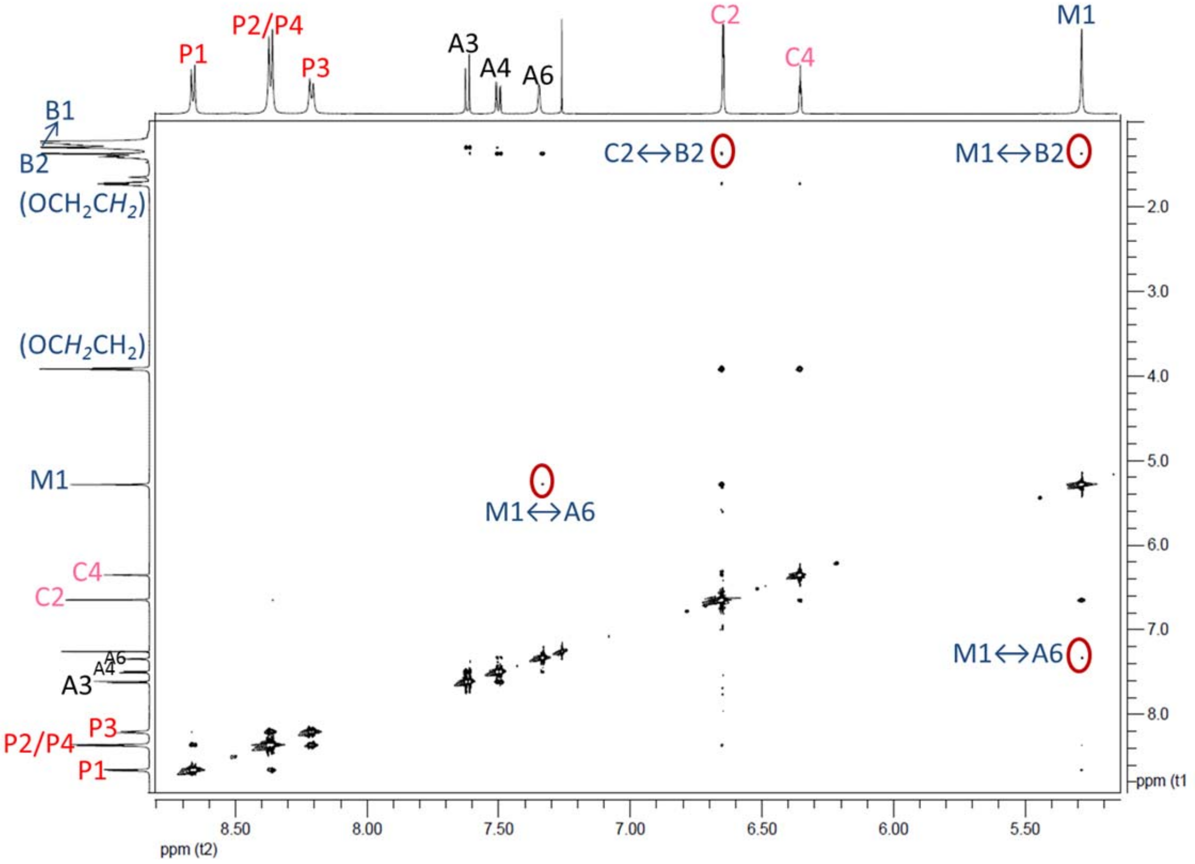

Figure S5. ROESY NMR spectrum of PBI **6** at a concentration of 50 mM in pure $CDCl_3$ conducted with 600 MHz NMR at 293 K.

DOSY NMR of PBI **6** *at 10 mM in* D_{14}*-MCH*

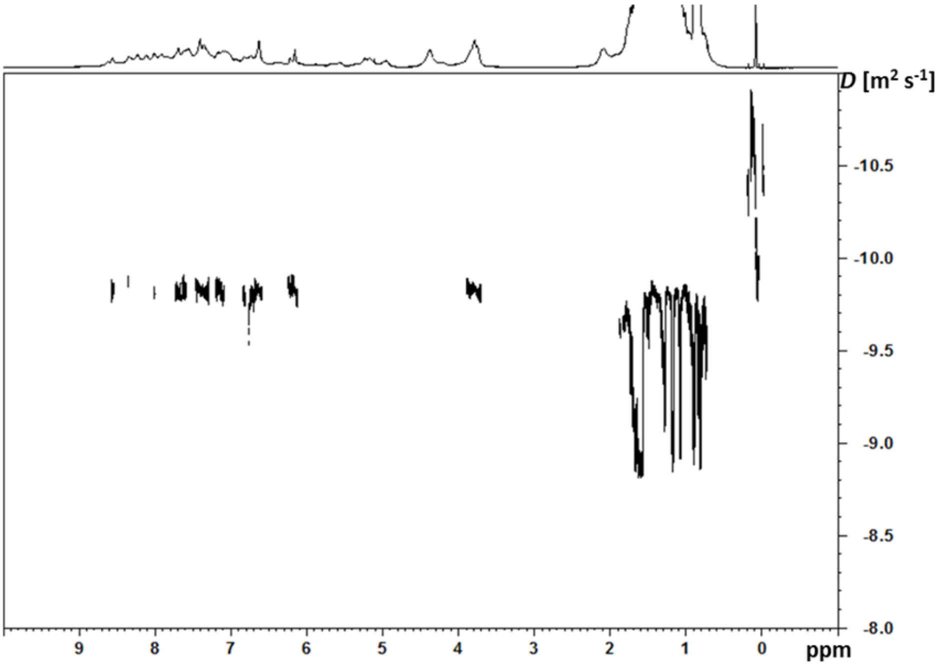

Figure S6. DOSY NMR spectrum of PBI **6** (10 mM in pure D_{14}-MCH, 600 MHz NMR, at 293 K). The diffusion coefficients D [m^2 s^{-1}] are plotted in a logarithmic scale against chemical shift δ [ppm].

Crystal Structure of PBI **7**

The crystals of PBI **7** were grown from chloroform/ethanol mixture and include co-crystallized $CHCl_3$ molecules. The crystal data were collected on a Bruker Kappa Apex2 diffractometer with a CCD area detector and Montel multi-layer mirror monochromated MoKα radiation. The structure was solved using direct methods, refined with the ShelX software package (Sheldrick, G., *Acta Cryst.* **2008**, *A64*, 112–122.) and expanded using Fourier techniques. All non-hydrogen atoms were refined anisotropically. Hydrogen atoms were included in structure factors calculations. All hydrogen atoms were assigned to idealized geometric positions.

Crystal data for PBI **7**: $C_{45.67}H_{35.67}Cl_2IN_2O_4$, $M_r = 874.23$, clear orange prism, 0.05 × 0.06 × 0.17 mm^3, hexagonal space group P63/m, a = 23.1988(10) Å, b = 23.1988(10) Å, c = 12.4904(5) Å, $a = b = 90°$, $g = 120°$, V = 2130.9(6) Å^3, $Z = 6$, $r_{\text{calcd}} = 1.496$ g cm^{-3}, $m = 1.010$ mm^{-1}, $F(000) = 2656$, T = 100(2) K, $R_1 = 0.0385$, $wR_2 = 0.0976$, 3891 independent reflections [$2q \leq 51.4°$] and 325 parameters. CCDC 876014 contains the supplementary crystallographic data for this paper. These data can be obtained free of charge from The Cambridge Crystallographic Data Centre via www.ccdc.cam.ac.uk/data_request/cif.

The crystal structure of PBI **7** exhibits a unique two-dimensional PBI packing without any PBI-PBI π-π-interaction (Figure 7b and S7), which is obviously not the situation for PBI **6** derivative in solution according to our ^{1}H NMR and UV/Vis measurements. Even with the free rotation around the methylene linker, only the open-*m*-facet conformation is observed in the crystal structure, consistent with the monomer conformation for PBI **6** *m*-*m*-dimer formation in solution. As illustrated in Figure 7b, the blocked *o*-perylene-facet is perfectly occupied by a 2,5-di-*tert*-butyl phenyl group of a neighboring molecule. When the solvophobic effect plays an important role in the PBI stacking, i.e. in aliphatic solvents, such packing arrangement may be a choice for further growth of the dimer aggregates of PBI **6**. For PBI **7** in crystal structure, the open *m*-perylene-facet is stacked with the benzyl ring, although the π-π-interaction between benzyl ring and perylene facet should be much weaker than that of PBI-PBI π-π-interactions.

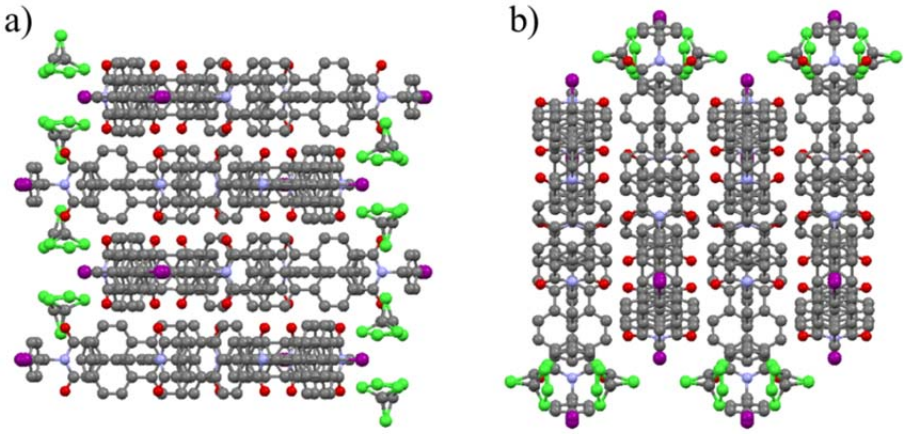

Figure S7. Packing of PBI **7** in crystal structure. View along the *a*-axis (a) and *b*-axis (b). The co-crystallized $CHCl_3$ molecules are also shown.

Chapter 4

Perylene Bisimide Quadruple Stacks:

Kinetically Stable Dimer Aggregates of Tweezer-like PBI Dyad Compound

Abstract: A tweezer-like perylene bisimide (PBI) dyad appending two PBI units at the respective *o*- and *m*'-position of a diphenylacetylene (DPA) backbone has been synthesized. In this manner the intramolecular distance of two PBI units can be precisely controlled to be around 6.9 Å, which is exactly twice the π-π-interaction spacing of PBIs. Therefore, the interdigitated dimerization of this molecule can create the desired PBI quadruple π-stacks. The self-assembled dimer formation was verified by MALDI-TOF mass spectrometry and dynamic light scattering (DLS) measurements. The structured absorption and sharp fluorescence of dimers of the PBI dyad can be interpreted in terms of Kasha's exciton theory. Accompanied with the PBI aggregation, the DPA absorption exhibited a red shift which can be attributed to a DPA planarization process. This observation corroborates the interdigitated dimer structure of the PBI dyad. Allowing for the unsymmetrical chemical structure, we have made a comparison study to elucidate the potential dimer conformation. Furthermore, time-dependent absorption measurements were designed to assess the activation energy of the dimer dissociation in the good solvent chloroform to be as high as 83.8±0.8 kJ mol^{-1}, thus explaining the experimentally observed high kinetic stability of the dimer aggregates.

4.1 Introduction

Self-assembled π-conjugated systems featuring charge and energy transport properties are intensively investigated in biological and material sciences.[1] Inspired by the light harvesting system of purple bacteria relying on self-assembled chlorophyll dyes,[2] enormous efforts have been paid to the rational control of the self-assembly process of artificial functional dyes, in particular with respect to applications in organic electronics.[3] As one of the most important industrial dyes and pigments, perylene bisimides (PBIs) are of great interest for futuristic functional nanosystems due to their high photostability, excellent optical properties and electron affinity.[4]

PBIs possessing large, electron-deficient π-systems exhibit strong π-π-interactions[5] and variable optical properties upon one-dimensional π-π-stacking due to exciton coupling of the dyes.[6] However, as the aggregation behavior of PBIs is dynamic and different mutual arrangements of the dyes are energetically not very distinct,[7] detailed interpretation of the effects determining the self-assembly process and the optical properties is impossible. As such, there has been considerable attention to control the size and stability of PBI π-stacks, since stable discrete aggregates are crucial to examine the parameters governing PBI π-π-interactions and exciton couplings.[8] In Chapter 3, we built self-assembled PBI dimer aggregates by virtue of elaborate steric control at the imide positions. Absorption spectra of PBI pure dimer aggregates could, however, not be obtained experimentally due to the dynamic equilibrium and the presence of residual amounts of monomers, but only revealed by our mathematical analysis on the monomer-dimer equilibrium. In this sense, kinetically stable and defined PBI π-stacks are more desirable to elucidate the optoelectronic properties of PBI self-assembly. In the present work, we report our efforts to produce discrete PBI quadruple π-stacks (dimer aggregates of PBI dyad compound) that are self-assembled by means of multiple PBI π-π-interaction and realize therefore kinetic stability. In this way, we can interpret the optical features of PBI quadruple stacks straightforwardly from steady-state absorption and fluorescence measurements.

4.2 Molecular Design of the PBI Building Block

In order to build discrete and stable PBI quadruple stacks, we need the assistance of a rigid backbone serving as a pillar to direct and maintain the aggregation.[9] The backbone selected is diphenylacetylene, in short DPA. It features a combination of linearity, rigidity and rotatability.[10] When one PBI unit is attached to the *ortho*-position of one phenyl ring, and another to the *meta*-position of the second phenyl ring, the linear and rigid DPA can control a parallel separation of the two PBI units at a distance of 6.9 Å as revealed by molecular modeling study with MacroModel using MM3* force field calculation.[11] Notably, this distance is precisely twice the π-π-distance observed for PBI aggregates in solid state (Figure 1).[4a, 12] Accordingly, we can anticipate the tweezer-like PBI dyads can self-assemble to form interdigitated dimer aggregates[13] based on PBI quadruple π-stacking. Notably, Matile and coworkers have recently utilized this kind of backbone to govern surface "zipper" architectures for the smaller naphthalene bisimides (NBIs).[14] In contrast to their work based on rather flexible linkers between the oligophenylethynyl backbone and NBIs, we chose a methylene linking group between the PBI units and DPA backbone to ensure the proper alignment of PBI π-systems, while being short enough to preserve rigidity and spacing constraints of a zipper architecture.

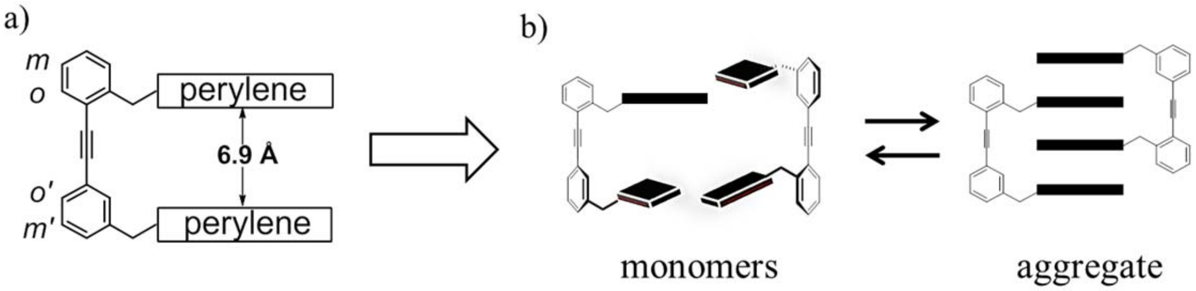

Figure 1. Schematic representation of a) the designed PBI dyad building block and b) its self-assembly process.

4.3 Results and Discussion

4.3.1 Synthesis and Isolation

The desired PBI dyad building block was synthesized according to the synthetic route outlined in Scheme 1. To obtain the *meta*- and *ortho*-iodo-benzyl amines **2** and **3**, different reducing agents were tested. The Pd/C-catalyzed hydrogenation and sodium borohydride proved insufficient to reduce the benzonitrile. On the contrary, lithium aluminium hydride was such a strong reducing agent that the iodo-functionalities were also partially removed. A suitable reducing agent in this case was eventually found to be $BH_3 \cdot THF$ complex in THF which rendered the desired amines **2** and **3** in a reasonable isolated yield of around 50%. Subsequently, benzyl amines **2** and **3** were each condensed with perylene monoimide **1**[15] to produce unsymmetrical PBI precursors **4** and **5**, respectively. PBI **4** was then modified by the Pd/Cu-catalyzed coupling reaction with trimethylsilylacetylene and the following desilylation using tetra-*n*-butylammonium fluoride to convert the iodo-functionality into an acetylene group.[16] In the final step, Sonogashira cross-coupling[17] of iodo-functionalized PBI **5** and acetylene-functionalized PBI **6** furnished the desired PBI dyad **7** in a moderate yield of 57%. The long “swallow-tail” alkyl chains attached at the imide terminals of PBI units[18] provide sufficient solubility for PBI dyad **7** in chlorinated solvents such as $CHCl_3$ and CCl_4.

Similarly, reference PBI dyads **8** and **9** were synthesized to help elucidate the aggregate conformation of the unsymmetrical PBI dyad **7**. These reference dyads feature a 2,5-di-*tert*-butyl phenyl group, which was utilized to program the PBI dimerization,[19] in place of one of the alkyl imide substituents of dyad **7**. The *tert*-butyl groups provide also satisfying dissolution of PBIs in organic solvents.[20]

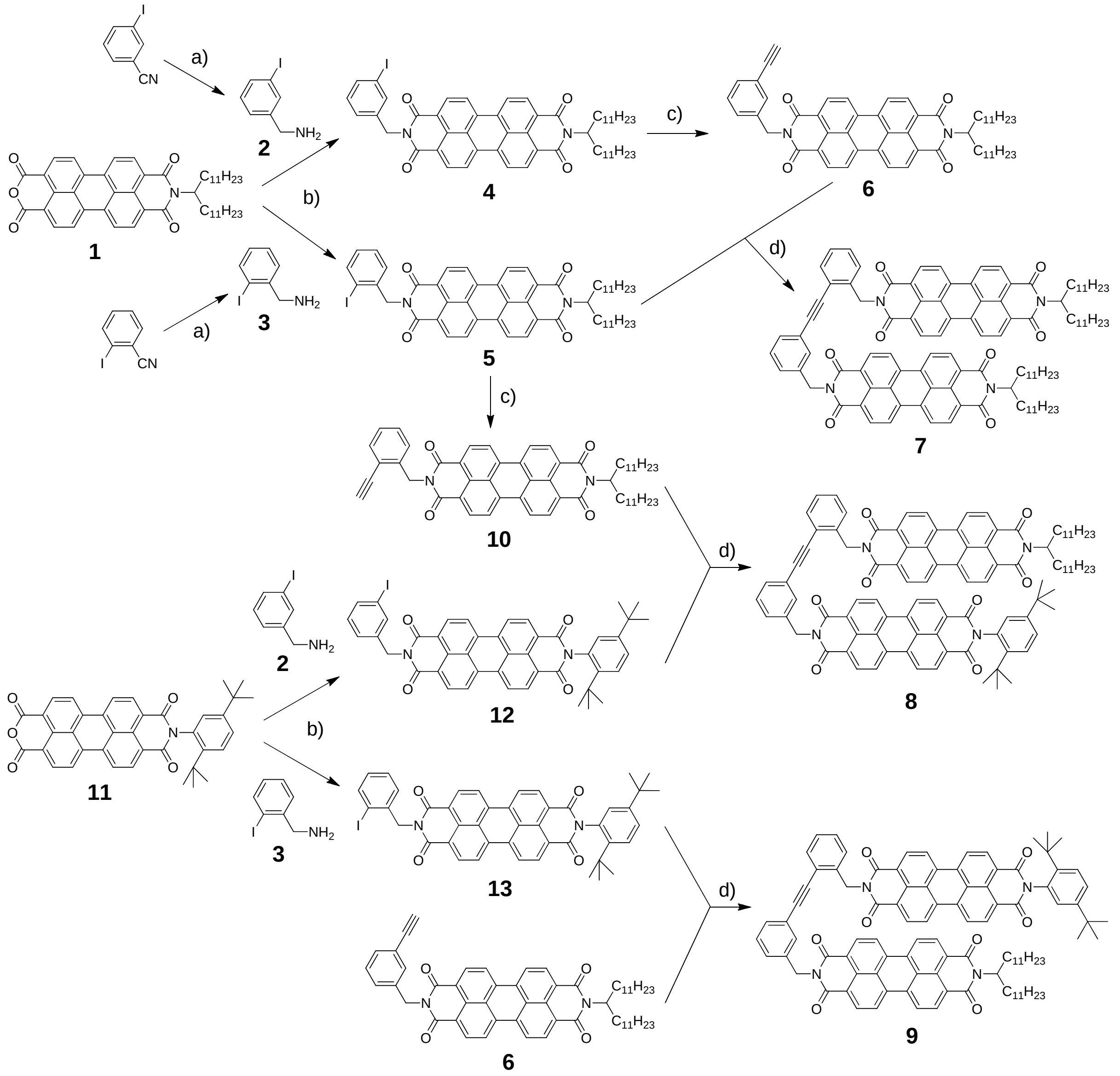

Scheme 1. Synthesis of PBI dyads **7**, **8** and **9:** a) $BH_3 \cdot THF$, dry THF, 0 °C, 24 h, 58% for **2** and 45% for **3**. b) imidazole, 140 °C, 4 h, 65% for **4**, 61% for **5**, 44% for **12** and 47% for **13**. c) Trimethylsilylacetylene, $Pd(PPh_3)_2Cl_2$, CuI, CH_2Cl_2/NEt_3 (v:v = 3:1), 40 °C, 3 h; tetra-*n*-butylammonium fluoride, THF, r.t., 10 min, 89% for **6** and 77% for **10** over two steps. d) $Pd(PPh_3)_2Cl_2$, CuI, THF/NH(iPr)$_2$ (v:v = 5:1), 40 °C, 18 h, 57% for **7**, 55% for **8** and 49% for **9**.

Due to unavoidable homo-coupling of PBI **6**,[21] it was not possible to isolate the pure PBI dyad **7** by conventional column chromatography. The crude product isolated after two-fold chromatography on a silica column with chloroform as eluent still contained significant amounts (15%) of the homo-coupling byproduct of PBI **6**. Complete purification of dyad **7** could, however, be achieved by means of semi-preparative HPLC (Figure 2) by setting the highest flow speed of 9.9 mL min^{-1} from a concentrated stock solution of the reaction mixture in $CHCl_3$. Under these conditions dyad **7** prevails in a kinetically trapped aggregated state whilst the impurities exist as monomer or in dynamic equilibrium with respective aggregates. Accordingly, the first fraction with a retention time of 4.5−6 min was collected and fully characterized by ^{1}H NMR, ^{13}C NMR spectroscopy, MALDI-TOF mass spectrometry and elemental analysis to be pure dyad **7**. The freshly eluted solution of this fraction has a red color which gradually turns bright yellow. Such color changes of the solution are typical for a dissociation of PBI aggregates into PBI monomers.[6a, b] Analytical HPLC studies with diode array detection corroborate that this fraction indeed shows the characteristic absorption profile of dyad **7** aggregates (inset of Figure 2, see also Figure S1). This finding points to the presence of dyad **7** in the form of its kinetically trapped aggregates after isolation of the crude product by conventional column chromatography. The long tail of this fraction can, therefore, be attributed to the partial disassembly of dyad **7** aggregates through the HPLC column. It is worth to mention that by using a slow flow speed (less than 6 mL min^{-1}) and/or a diluted stock solution the first fraction did not appear and dyad **7** was thus chromatographically inseparable from the homo-coupling byproduct.

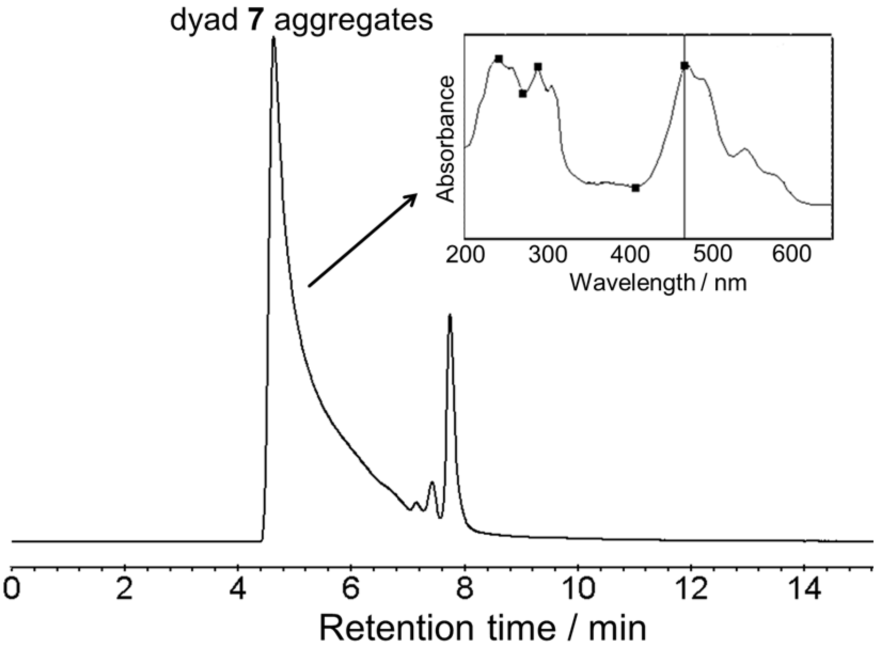

Figure 2. Semi-preparative HPLC separation of the reaction mixture containing PBI dyad **7** and homo-coupling byproduct. The stock solution was concentrated in chloroform and the eluent used is a solvent mixture of $CHCl_3$/MeOH (*v*:*v* = 100:1). Inset shows the in-situ absorption of the first fraction.

4.3.2 Determination of the Aggregate Size

During the last ten years, mass spectrometry has progressed a long way in the field of supramolecular chemistry.[22] Among the different methods in mass spectrometry, matrix-assisted laser desorption/ionization (MALDI) is one of the relatively soft ionisation methods that has been widely applied to monitor non-covalent self-assemblies and in particular π-π-stacked species.[13d, 23] The impressive finding that aggregates of PBI dyad **7** survive HPLC separation with eluent of 1 vol% MeOH in $CHCl_3$ is suggestive of strong and uniform aggregate formation of dyad **7**.[8f] On account of the high stability, mass spectrometric experiments were accomplished to precisely determine the aggregate size of dyad **7**.

The MALDI-TOF mass spectrum was recorded from a sample of dyad **7** (10^{-4} M in CCl_4) using 2-[(2*E*)-3-(4-*tert*-butylphenyl)-2-methylprop-2-enylidene]malononitrile (DCTB) as the matrix. As demonstrated in Figure 3, besides the first peak with an *m/z* value of 1627 confirming the molecular mass of dyad **7** molecule, there is an apparent signal at *m/z* = 3254 corresponding to the dimer of dyad **7**. It is noteworthy that no further peak at multiples of the *m/z* = 1627 parent ion value assignable to larger aggregates can be perceived, implying that dimers are the only present aggregates of dyad **7**. [13d, 23][24]

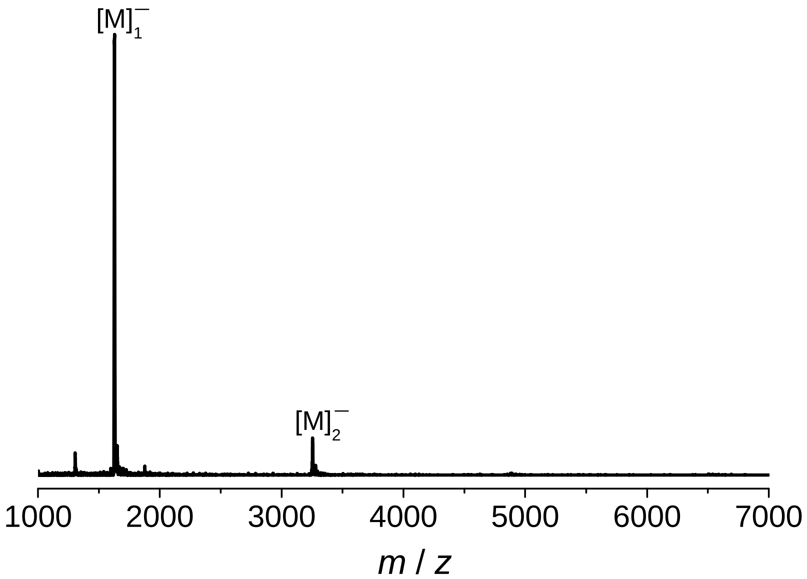

Figure 3. MALDI-TOF mass spectrum (linear mode) of PBI dyad **7**. The peaks corresponding to monomer and dimer species are marked with $[M]_1^-$ and $[M]_2^-$, respectively. 2-[(2*E*)-3-(4-*tert*-butylphenyl)-2-methylprop-2-enylidene]malononitrile (DCTB) was used as the matrix.

For the same solution as utilized for MALDI-TOF studies, i.e. 10^{-4} M in CCl_4, dynamic light scattering (DLS) measurements were performed. The observed signal also corroborates small nanoparticles with a diameter less than the 3 nm, which is in the range of the measurement limit of light scattering instrument (Figure 4).[25] Such a dimension clearly confirms the absence of large aggregate formation of dyad **7** beyond dimers.

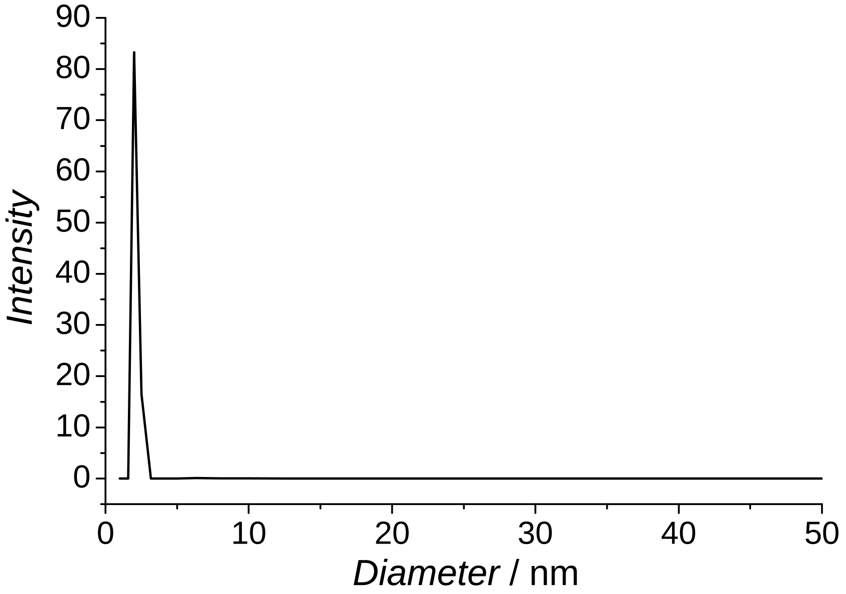

Figure 4. Dynamic light scattering (DLS) measurement for self-assembled dyad **7** at a concentration of 10^{-4} M in CCl_4 measured at an angle of 90° and at 293 K.

4.3.3 Determination of the Aggregate Structure

Structural elucidation of PBI cofacial aggregates in solution presents a significant challenge by means of NMR spectroscopic methods due to the extremely broadened proton NMR spectra even for defined PBI aggregates.[8d, 25b, c, 26] It can be interpreted by coalescence effects as the crossover from slow to fast exchange processes.[19] Additionally, many imide substituents including those based on swallow-tails exert also certain influence on the NMR signal broadening.[27] Further possibility may be attributed to the fluctuation in mutual orientation of the dyes in the π-stacks.[28] Very recently, the lowest-energy π-π-stacking geometry of PBI dimer aggregates has been theoretically[7] and experimentally[6] described to a cofacial stacking at a π-π-distance of around 3.4 Å and a rotational angle of around 30°. More exact structural determination seems impossible as the energy barriers related to the rotational angle as well with regard to translational offsets are quite modest.[7] Indeed, it has been found that even in liquid crystalline and frozen states, PBI dyes in H-type columnar aggregates exhibit rotational fluctuations.[29] Single-molecule fluorescence spectroscopy unveiled photoexcitation-induced self-assembly dynamics of flexibly folded PBI π-π-stackings.[30] Also for self-assembled and for covalently fixed cofacial PBI π-stacks, the structural reorganization in response to the excited state formation has been noted by time-resolved fluorescence spectroscopy.[6, 31]

On the other hand, PBI-based systems have the advantage that the π-π-stacking results in distinct UV/Vis spectral changes due to exciton coupling between the transition dipoles of adjacent chromophores.[4a, 6] Quantum chemical calculations revealed that the absorption spectra of PBI aggregates depend not only on the aggregate size[32] but in particular on the geometry and distance of the π-π-stacks.[7, 33] In the case of dyad **7** dimers, despite the appearance of an extremely broadened proton NMR spectrum (Figure S2), the interdigitated dimer structure can be elucidated by analyzing the PBI and DPA absorption changes between non-aggregated and aggregated states of dyad **7** (*vide infra*).

As a result of the non-symmetry of dyad **7**, the interdigitated dimer structure may possess three different conformations. If the *m*-appended PBI unit is designated to be M and the *o*-positioned one to be O, the three possible dimer patterns can be depicted as MOOM, MMOO (or OOMM) and OMMO (Figure 5). In spite of the presence of PBI quadruple stacking, slightly different PBI π-π-overlap may be envisioned for these three structures by considering the distinct flexibility of *m*- and *o*-appended PBI units (at the outside and inside of the DPA backbone, respectively) and the steric influence of rigid DPA backbone upon PBI aggregation. Of the three conformations, MOOM and OMMO motifs are structurally symmetric and therefore more likely to be the form that dyad **7** dimers adopt.

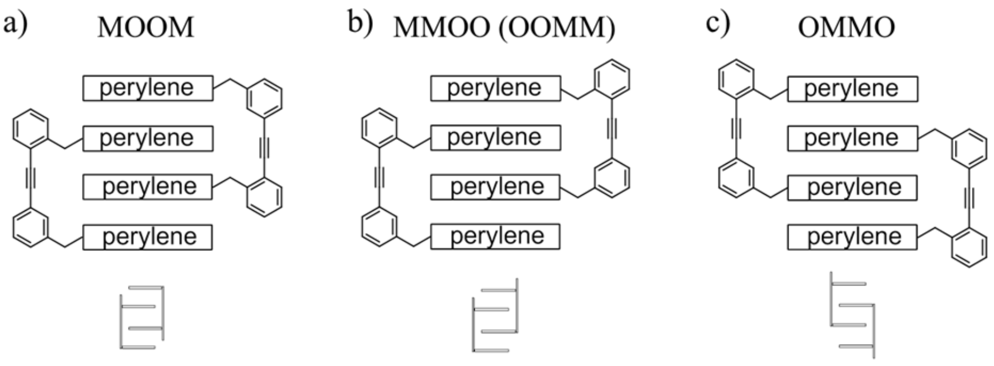

Figure 5. Schematic representation of the three possible dimer conformations a) MOOM, b) MMOO (or OOMM) and c) OMMO of dyad **7** due to the unsymmetrically appended PBI units on the DPA backbone. Bottom shows the simplified representation of the three dimer conformations.

To explore the potential dimer conformation(s) of dyad **7**, we have made a comparison study with two reference PBI dyads **8** and **9**. The dimer formation of both derivatives **8** and **9** was confirmed by means of MALDI-TOF mass spectra (Figure S3 and S4). On the basis of our former studies,[19] one of the four PBI facets in dyads **8** and **9** is shielded and thus does not involve in π-π-interaction owing to the pronounced steric demand of *o*-*tert*-butyl group. As a consequence, dyad **8** will selectively dimerize toward MOOM-type conformation, whereas dyad **9** will form OMMO-type array (Figure 6).

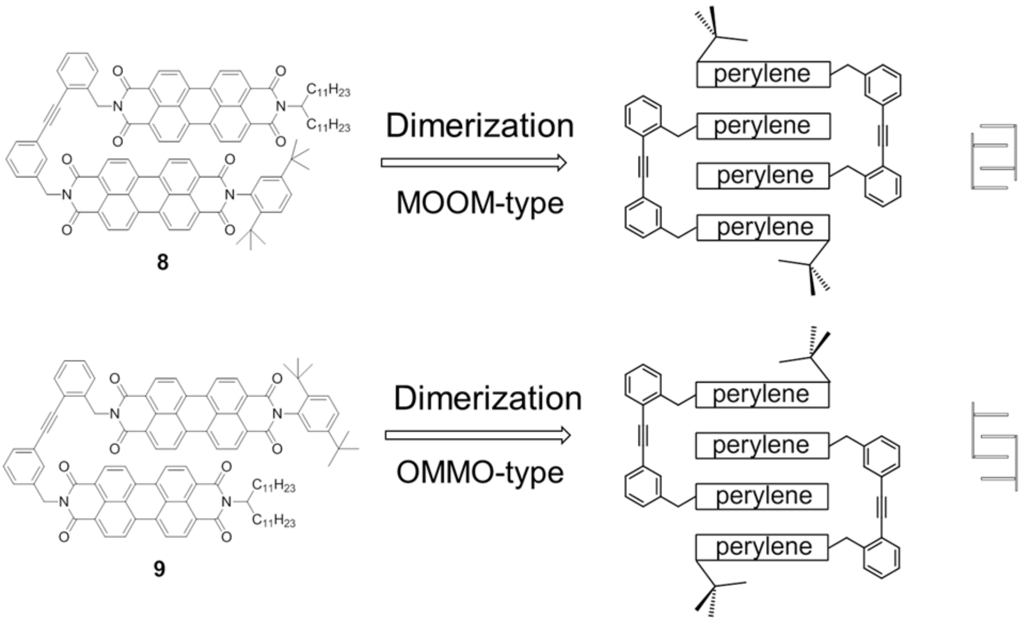

Figure 6. Schematic representation of the only likely dimer conformation of reference PBI dyads **8** and **9**, respectievely.

Since the color of PBI dyes is sensitive to the slight offsets of their π-π-stacking,[4a] UV/Vis and fluorescence spectroscopy are particularly suited to probe the packing properties of dyad **7** dimers. Figure 7 exhibits the dimer absorption and fluorescence of dyads **7**, **8** and **9** recorded at a concentration of 10^{-5} M in CCl_4. The absorption profile of dyad **7** dimer is highly comparable to that of dyad **8** dimer with absorption maximum at 470 nm. In contrast, the absorption maximum of dyad **9** dimer resides at 493 nm, which is the second absorption band for dyad **7** and **8** dimers. Examination of their absorption profiles reveals that each of the dyads **7**–**9** is composed of four absorption bands (two red-shifted and two blue-shifted ones), reflecting the same four excited states (*vide infra*). In the case of dyad **9** dimer, the first band at 470 nm is degraded into an absorption shoulder while the second absorption at 493 nm becomes pronounced. The pronounced similarity of excited states for all the dyads **7**, **8** and **9** dimers can also be realized from the almost identical fluorescence spectra with a single band at 602 nm (the emission bands between 500 and 550 nm are ascribed to the coexistence of traces of strongly fluorescent monomers in the system).

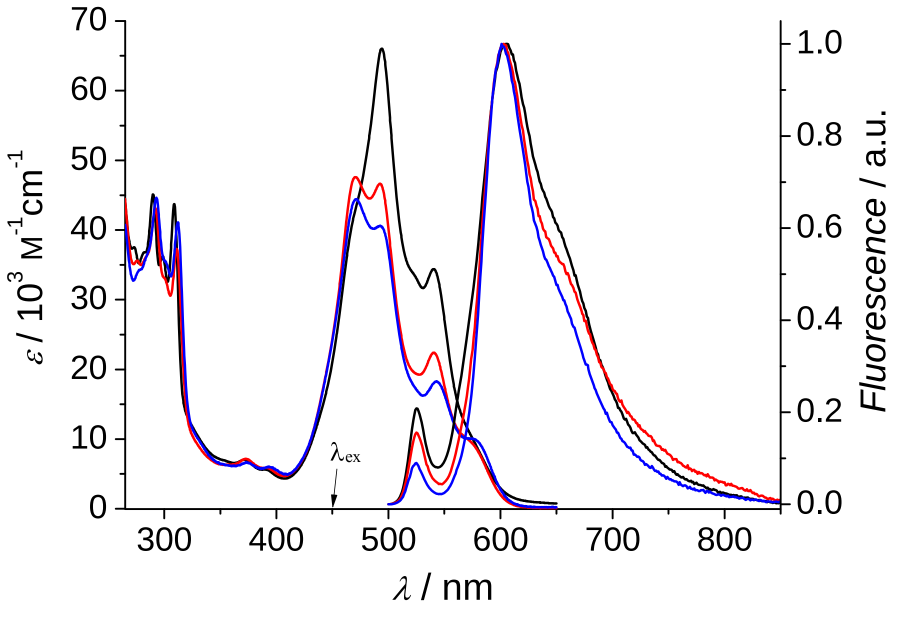

Figure 7. Absorption and fluorescence (excited at 450 nm) spectra of dyad **7** (blue), **8** (red) and **9** (black) at 10^{-5} M in CCl_4 recorded at 293 K**.**

From these experimental observations we can assume that dyad **7** dimer adopts the MOOM-type conformation similar to that of dyad **8** dimer. Although the PBI quadruple stacking generates the identical four excited states according to the Kasha's exciton theory,[34] the slight stacking offset of different dimer conformations may influence the selection rules for the two highest excited states. Our molecular modeling studies reflect that the OMMO-type conformation of dyad **9** dimer has a more pronounced central displacement than the MOOM-type conformation of dyad **7** and **8** dimers (Figure S5). The conformational difference can also be recognized from the blue shift of DPA absorption of dyad **9** dimer relative to those of dyad **7** and **8** dimers (*vide infra*). This indicates that in the OMMO-type conformation, the PBI may achieve the optimal π-π-contact at the expense of more DPA backbone distortion. Accordingly, the preference of MOOM-type dimer conformation of dyad **7** may be attributed to the more flexible *m*-PBI-units standing outside with the two stiff *o*-PBI-units inside, thus optimizing the PBI π-π-overlap in the quadruple stacks.

4.3.4 UV/Vis Spectroscopic Studies

Although the dimer of dyad **7** exhibits extraordinary stability, it is created by means of non-covalent PBI π-π-interactions via self-assembly in solution. According to thermodynamic considerations, altering the solvent polarity, concentration and/or temperature should lead to variations in the UV/Vis absorption spectra of dyad **7** due to the different ratio of monomers and dimers in a system. Figure 8 shows two extreme cases where dyad **7** is found to be molecularly dissolved at a concentration of less than 10^{-5} M in chloroform and almost quantitatively in a dimeric state at a concentration of more than 10^{-5} M in CCl_4.

As shown in Figure 8, both UV/Vis absorption spectra of dyad **7** dimer and monomer consist of two parts: in the visible range the bands between 400 and 600 nm are ascribed to the absorption of PBI units,[4a] whereas the DPA backbone displays bands in the UV range from 275 to 320 nm.[35][36] Since there is no overlap of these bands and the methylene linker interrupts the electronic communication between the two kinds of chromophores, it facilitates the individual observation of their absorption variations upon dimerization of dyad **7**.

The PBI-related absorption band of dyad **7** monomer shares the common properties as that of molecularly dissolved parent PBIs.[4a] It has a well-resolved vibronic structure between 400 and 550 nm for the $S_0 \rightarrow S_1$ transition of the single PBI chromophores that can be related to the breathing vibration along the long axis of the perylene skeleton.[6] The band maximum resides at 528 nm, followed by a second band at 491 nm and a third at 460 nm. Considering the high value of $A^{0\rightarrow0}/A^{0\rightarrow1} = 1.56$[8d, 37] and the extinction coefficient value of 1.60×10^5 M^{-1} cm^{-1} (corresponding to two PBI units as given in dyad **7** molecule),[38] there is no evidence for electronic coupling between inter- as well as intramolecular PBI units of dyad **7** in this case. Hence, the rigid and rotatable DPA backbone enables sufficient separation of the two intramolecular PBI units.

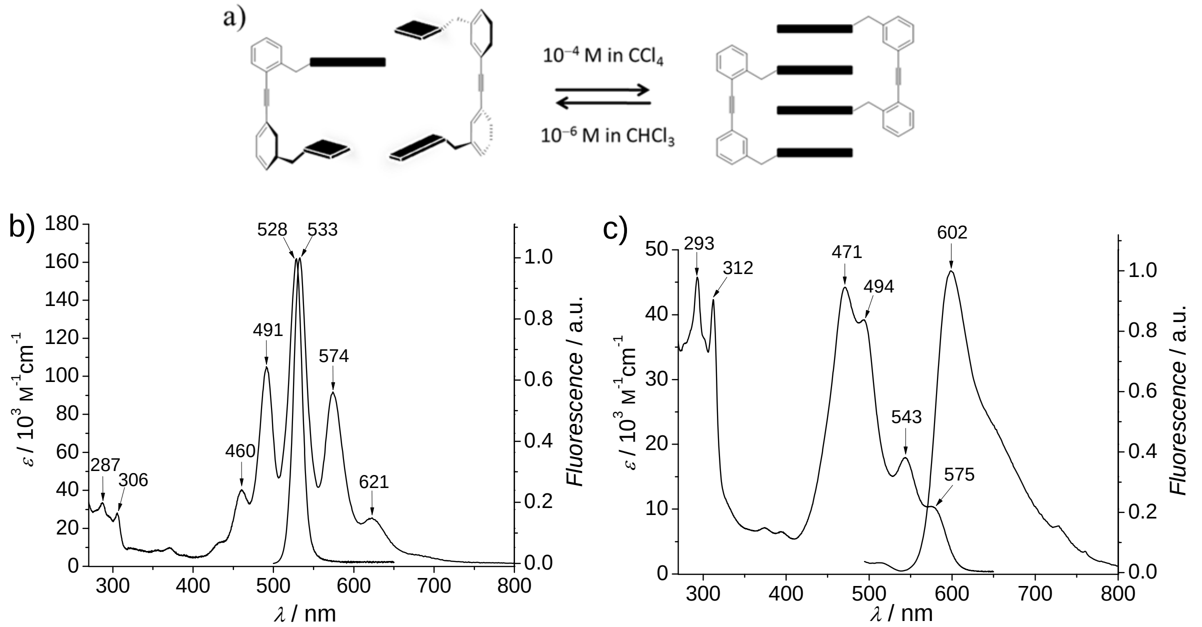

Figure 8. a) Schematic representation of the equilibrium between monomer and dimer of dyad **7** in solution. The UV/Vis absorption and normalized fluorescence (excited at 450 nm) spectra of b) dyad **7** monomer (at 10^{-6} M in $CHCl_3$) and c) dyad **7** dimer (at 10^{-4} M in CCl_4) recorded at 293 K.

In striking contrast, the PBI absorption of dyad **7** dimer obviously differs from that of the monomer. Remarkably, the progression of the four peaks is almost a mirror-image with the absorption maximum blue-shifted to 471 nm ($\Delta\lambda$ = 57 nm), accompanied by a substantially decreased extinction coefficient value of only 4.50×10^4 M^{-1} cm^{-1}.[39] To the best of our knowledge, a hypsochromic shift of 57 nm is the highest value ever observed for PBI aggregation. In addition, the structured absorption shows another blue-shifted band at 494 nm and a red-shifted band at 543 nm, as well as a red-shifted shoulder around 575 nm. Such spectral features strongly suggest the one-dimensional H-type stacking of PBI units in dyad **7** dimers.[4a, 6b]

In general, the absorption spectra of PBI aggregates can be interpreted in terms of Kasha's exciton theory.[34] As predicted by the theory, the energies of the excited states are split and the number of joint energy states is equal to the number of coupled molecules. In the case of dyad **7** dimer, the four absorption maxima (three bands and a shoulder) can therefore be related to the PBI quadruple stacking, indicative of the interdigitated dimer structure of dyad **7**. The face-to-face PBI π-stacking in dimers of dyad **7** enables the higher energy transitions at 471 nm (2.63 eV) and 494 nm (2.51 eV). The most blue-shifted band at 471 nm shows the strongest absorption intensity, reflecting the most favored selection rule for H-aggregates. Meanwhile, the H-type PBI aggregation exhibits also a certain rotational displacement of the transition dipole moments, which makes the lower energy transitions partially allowed.[4a] They correspond to the weaker absorption at 543 nm (2.28 eV) and around 575 nm (2.16 eV).

Experimentally, structured PBI aggregate absorption with four distinct bands is observed for the first time. If the wavelengths are converted into energy units, we can gain the energy levels of the four excited states. As depicted in Figure 9, they bear the same second-order energy splitting of 0.12 eV. Furthermore, the first-order energy splitting of 0.35 eV and the van-der-Waals energy difference of –0.05 eV between the uncoupled and coupled excited states can be derived. These splitting values fit well to the theoretically calculated magnitude for PBI excitonic coupling.[7, 32, 33b]

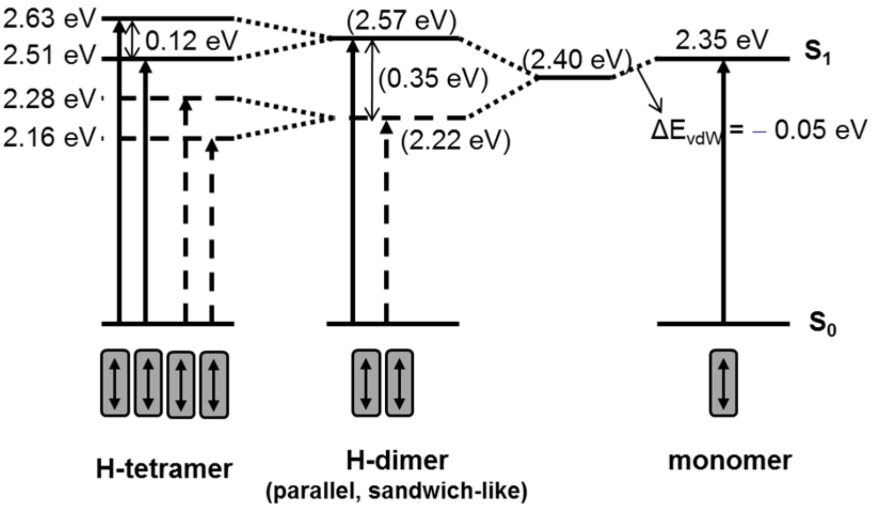

Figure 9. Energy splitting of excited states of H-type PBI quadruple stacking according to the exciton theory. The values without bracket are converted from the wavelength values in dyad **7** dimer and monomer absorptions. The values with bracket are the average deduced from the observed ones.

Interestingly, the DPA absorption in dyad **7** dimeric state has a red shift of 6 nm and an absorbance increase in comparison with that in the monomeric state. This phenomenon is more noticable when upon recording of the kinetic absorption changes from dimer to monomer (*vide infra*, see Figure 14). While the PBI absorption changes are dependent on the electronic coupling, the wavelengths of DPA absorption maxima are sensitive to its rotation along the triple C-C-bond that leads to the planarization and deplanarization of the two phenyl rings (Figure 10).[10, 40] Accordingly, the DPA absorption changes can be explained by planarization of DPA backbone in dyad **7** dimeric states. As the rotational barrier for the phenyl rings is only 3.60 kJ mol^{-1},[10b] DPA chromophores tend to be freely rotating and non-conjugated under ambient conditions as in the dyad **7** monomeric state. However, in the dimeric state, the aggregation of PBI units imposes extra forces to freeze the rotation of DPA backbone, making it more conjugated and planarized. As a result, the planarization of DPA configuration lowers its excitation energy and enhances its absorbance. Since the DPA (de)planarization is synchronous to the PBI (dis)aggregation process,[14b] the observation of the DPA absorption variations provides further evidence for interdigitated dimer structure of dyad **7**.

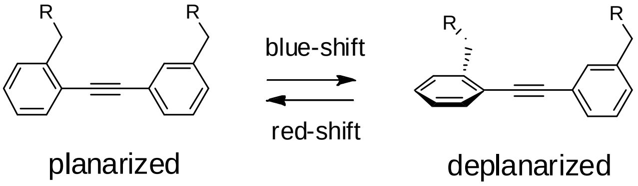

Figure 10. Schematic representation of the planarized and deplanarized DPA conformations.

4.3.5 Fluorescence Spectroscopic Studies

As shown in Figure 8, the emission of dyad **7** monomer has a well-resolved structure and exhibits a mirror-image relationship with the PBI $S_0 \rightarrow S_1$ absorption band. On the contrary, the fluorescence spectrum of dyad **7** dimer is structureless and bears a single band at 602 nm, along with an underlying shoulder at about 640 nm. Such relatively sharp and short-wavelength fluorescence band for PBI aggregates is rarely observed and only reported in the single-molecule fluorescence spectroscopic investigation of foldable linear PBI tetramer.[30b] In this study, the authors have observed five representative spectral types, one of which is a single band at 600 nm. The spectral switching is explained by the excited state dynamics due to the photoexcitation-induced unfolding and refolding process of the linear PBI tetramer. In the case of dyad **7** dimer, dynamic dissociation of the PBI stacking can be excluded by the fact that the emission of PBI monomer (at 530 nm) could hardly be detected. Accordingly, the single band at 602 nm can be assigned to the four densely π-stacked PBI units and interpreted in terms of the emission energy from lowest excited state to ground state.

To further elucidate the fluorescence properties of the dyad **7** dimer, the sample of dyad **7** at a lower concentration of 10^{-5} M in CCl_4 was used. At this concentration, the dimer band still dominates in the emission and traces of monomer fluorescence below 550 nm can also be recognized, while the absorption shows subtle changes relative to that at a concentration of 10^{-4} M in CCl_4 (Figure 11). After proper assignment of the monomer and dimer emission based on the excitation spectra detected at 530 and 602 nm, respectively (Figure 12), the fluorescence quantum yield of dyad **7** dimer could be derived to be 17% (the area integration of the emission band has been done from 550 nm to exclude most of the monomer emission), whereas that of dyad **7** monomer measured at a concentration of 10^{-6} M in $CHCl_3$ is 80%. Accordingly, face-to-face PBI π-π-stacking is responsible for the fluorescence quenching phenomenon as expected for a H-aggregate.[4a]

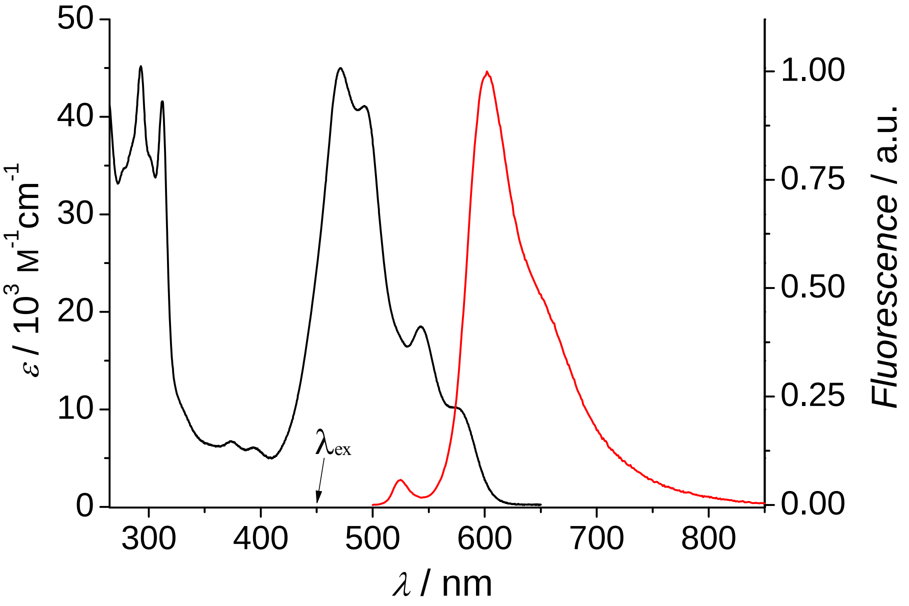

Figure 11. UV/Vis absorption and normalized fluorescence (excited at 450 nm) spectra of dyad **7** at a concentration of 10^{-5} M in CCl_4 recorded at 293 K.

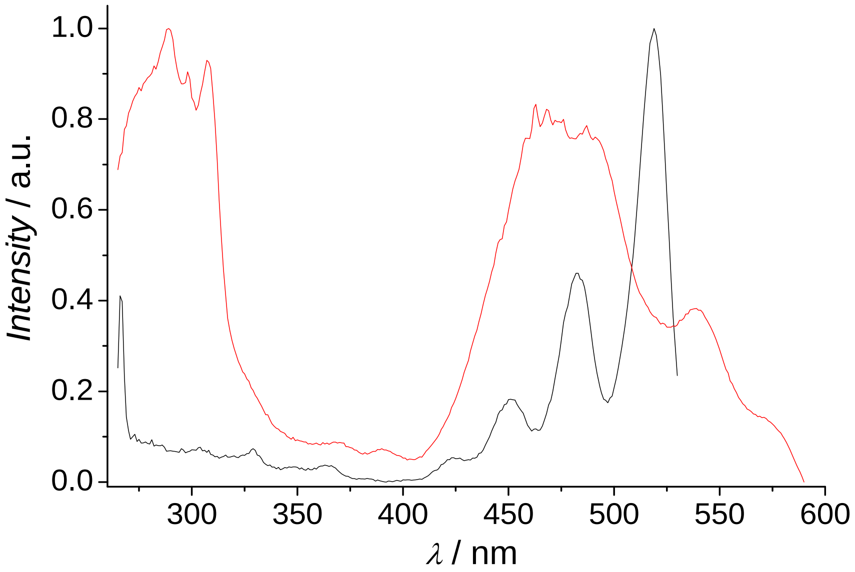

Figure 12. Fluorescence excitation spectra of dyad **7** at a concentration of 10^{-5} M in CCl_4, detected at 530 nm (black line) and 600 nm (red line) recorded at 293 K.

For the fluorescence life time measurements (Figure 13), the monomer emission at 530 nm fits well to a single exponential, yielding a lifetime of 3.8 ns, while the dimer decay obtained at 602 nm fits well to a biexponential to produce two lifetimes: one is a faster 3.9 ns component attributed to the monomer state, the other is a slower 24.3 ns component corresponding to the dimer emission. The dimer lifetime is approximately six times higher than that of the monomer. On account of the relatively longer life time for emission of extended PBI aggregates (32.7 ns) which relax into excimers,[6b] we attribute the value of 24.3 ns to the emission from an excitonic state delocalized over PBI quadruple stacks that does not relax into an excimer state.

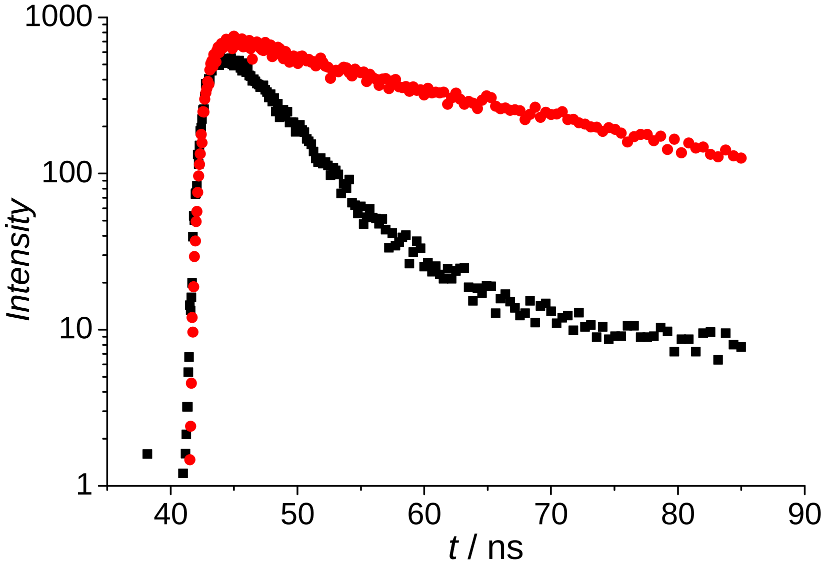

Figure 13. Fluorescence decay curves of the monomer (black points, detected at 530 nm) and dimer (red points, detected at 600 nm) bands of dyad **7** at a concentration of 10^{-5} M in CCl_4 recorded at 293 K.

4.3.6 Kinetic Studies

It is uncommon that π-π-stacked PBI species can survive the HPLC separation and mass spectrometry measurements. This reflects that the non-covalently self-assembled dyad **7** dimer features a steadiness of high degree comparable to the strength of a covalent bond. To quantitatively assess the activation energy for the dissociation of dyad **7** dimer in solution, we designed kinetic experiments to monitor the time-dependent absorption changes when a small amount of concentrated solution containing dyad **7** dimers[41] was dispersed into a thousand times larger volume of pure chloroform (Figure 14). At a final concentration of 10^{-5} M, dyad **7** molecules have a strong propensity to be molecularly dissolved in the good solvating solvent $CHCl_3$, which is recognized from the well-resolved bands of the final absorption spectra. The absorption variations recorded in a time interval of 15 min share several well-defined isosbestic points at 545, 477, 463, 450 and 266 nm, indicative of the disassembly process between only two explicit species, the dimer and monomer of dyad **7**.[42]

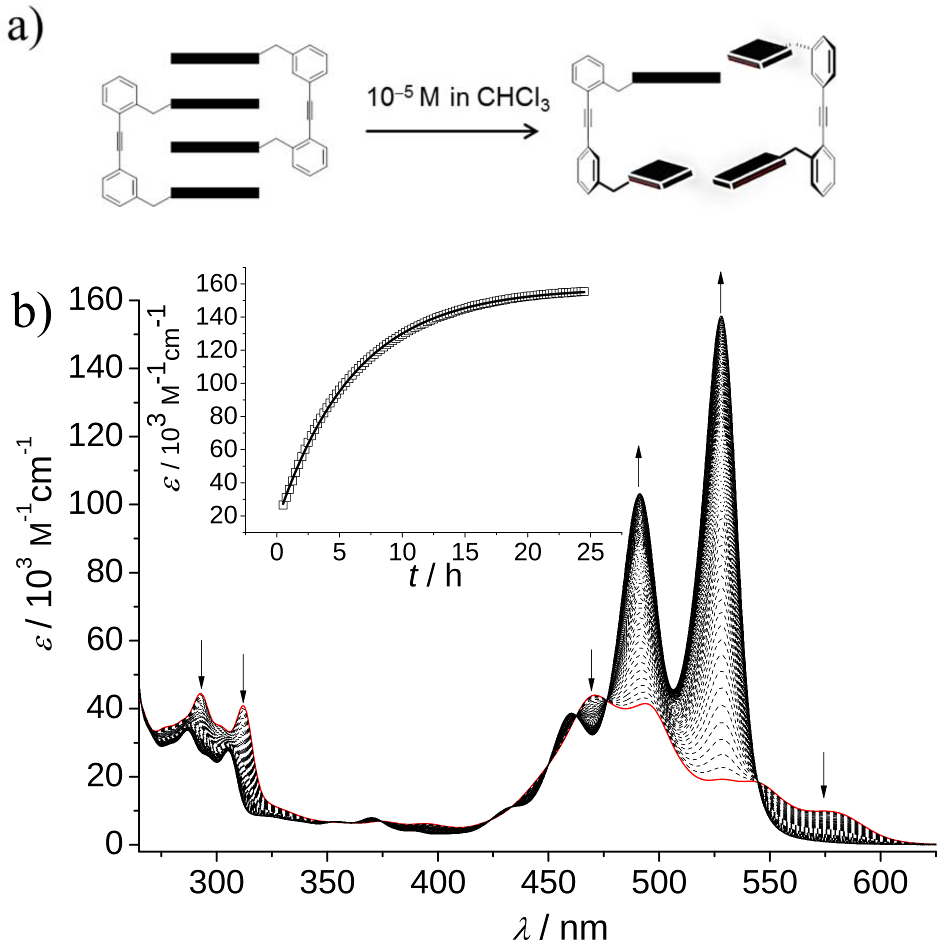

Figure 14. a) Schematic representation of the disassembly course in kinetic experiments. b) Recorded absorption spectral variations at a time interval of 15 min for 24 h when 3 μL of dyad **7** stock solution at 10^{-2} M in $CHCl_3$ was added into 3 mL of pure $CHCl_3$ solvent at 293 K. Arrows indicate the absorption changes with time. Inset: A plot of the absorbance at 521 nm versus time and the best fitting to a simple mono-exponential equation.

The same kinetic process has also been monitored by ^{1}H NMR spectra (Figure S7). Since the aromatic ^{1}H NMR signals for the dimer of dyad **7** are so broad at a concentration of 10^{-5} M, they become effectively negligible against the monomer signals. In the first six hours, the enhancement of monomer signals is appreciable, while they do not exhibit an obvious increase for the further 18 hours. Such observation implies the exponential development of dyad **7** monomers in the system with time, in accordance with the consideration that the dimer dissociation process can be regarded as a first-order reaction.

If we assume that at time t = 0 hours, the dimer concentration $c_{\mathrm{M_2}}(0)$ is equal to a, and after a time interval of t hours, the dimer concentration $c_{\mathrm{M_2}}(t)$ changes to $(a - x)$ and the monomer concentration will be accordingly $c_{\mathrm{M}}(t) = 2x$, the following equations apply:

$$\mathrm{M_2} \xrightarrow{k_1} \mathrm{2M}$$

$$t = 0 \qquad c_{\mathrm{M_2}}(0) = a \qquad c_{\mathrm{M}}(0) = 0$$

$$t = t \qquad c_{\mathrm{M_2}}(t) = a - x \qquad c_{\mathrm{M}}(t) = 2x$$

During this set of absorption experiments, the ensemble absorption $A(t)$ measured at time t is the summation of the dimer and monomer absorption of dyad **7** in the system and can therefore be expressed as a single function of the x value, where the $\varepsilon_{\mathrm{M_2}}$ and ε_{M} are the extinction coefficients of dimer and monomer, d is the cuvette length of 1 cm.

$$A(t) = \varepsilon_{\mathrm{M_2}} \cdot d \cdot (a - x) + \varepsilon_{\mathrm{M}} \cdot d \cdot 2x \qquad (1)$$

According to the rate law for the first-order reaction, the concentration variation x can be expressed as an exponential function of time t, where k_1 is the disassembly rate constant from dyad **7** dimer to monomer.

$$x = a - ae^{-k_1 t} \qquad (2)$$

Taking equation (2) into equation (1), the ensemble absorption $A(t)$ and the ensemble extinction coefficient $\varepsilon(t)$ can be written as an exponential function of time t:

$$A(t) = \varepsilon_{\mathrm{M_2}} \cdot d \cdot a \cdot e^{-k_1 t} + \varepsilon_{\mathrm{M}} \cdot d \cdot 2 \cdot (a - ae^{-k_1 t}) \qquad (3)$$

$$A(t) = 2\varepsilon_{\mathrm{M}} da + (\varepsilon_{\mathrm{M_2}} da - 2\varepsilon_{\mathrm{M}} da) e^{-k_1 t} \qquad (4)$$

$$\varepsilon(t) = \frac{A^t}{d \cdot 2a} = \varepsilon_{\mathrm{M}} + \left(\frac{\varepsilon_{\mathrm{M_2}}}{2} - \varepsilon_{\mathrm{M}}\right) e^{-k_1 t} \qquad (5)$$

Considering a dead time of $t^0 = t - t'$ between the ideal time t and recorded time t' and setting a constant value $C = \left(\frac{\varepsilon_{\mathrm{M_2}}}{2} - \varepsilon_{\mathrm{M}}\right) e^{-k_1 t^0}$, we can get:

$$\varepsilon(t') = \varepsilon_{\mathrm{M}} + \left(\frac{\varepsilon_{\mathrm{M_2}}}{2} - \varepsilon_{\mathrm{M}}\right) e^{-k_1 t^0} \cdot e^{-k_1 t'} = \varepsilon_{\mathrm{M}} + C \cdot e^{-k_1 t'} \qquad (6)$$

Fitting the measured absorption coefficient $\varepsilon(t')$ values at 528 nm against the measured time t' gives exactly an exponential function, from which the kinetic constant k_1 can be acquired (inset of Figure 14). Besides at the monomer maximum, the measured $\varepsilon(t')$ values at different wavelengths fit very well into the equation (6) with correlation coefficient better than 0.999 (Table S1). From the fitting curves, reasonable ε_{M} and *C* values can be directly obtained. The ε_{M} values correspond well to the monomer absorption, whereas the *C* values show the correct positive or negative signs with regard to the absorption relationship of $\varepsilon_{\mathrm{M_2}}/2$ and ε_{M} at different wavelengths. More importantly, all the fittings generate quite similar k_1

values that was averaged to offer a rate constant value of 0.16 h^{-1} for the dissociation process of dyad **7** dimer and a corresponding half time of $t_{1/2}$ = 4.31 h.

For most chemical reactions, the reaction rate increases with temperature and the Eyring–Polanyi equation describes a quantitative dependence of the rate constant k on the absolute temperature T:

$$\ln\frac{k}{T} = -\frac{\Delta H^{\neq}}{R}\cdot\frac{1}{T} + (\ln\frac{k_B}{h} + \frac{\Delta S^{\neq}}{R}) \qquad (7)$$

where R is the gas constant, k_{B} is Boltzmann constant and h is Planck's constant.

At different temperatures from 25 to 50 °C, the same kinetic experiments were repeated and thus a series of k_1 values can be acquired (Table S2). Fitting the $\ln(k_1/T)$ values against $1/T$ generates a linear relationship in agreement with the Eyring equation (7) (Figure 15). From this linear fitting, the Gibbs disassembly energy of activation $\Delta G^{\neq}$ = 77.6±0.8 kJ mol^{-1} and disassembly activation energy E_{a} = 83.8±0.8 kJ mol^{-1} of dyad **7** dimer in chloroform at ambient temperature results according to equations (8) and (9), respectively.

$$\Delta G^{\neq} = \Delta H^{\neq} - T\Delta S^{\neq} \qquad (8)$$

$$E_{\mathrm{a}} = \Delta H^{\neq} + RT \qquad (9)$$

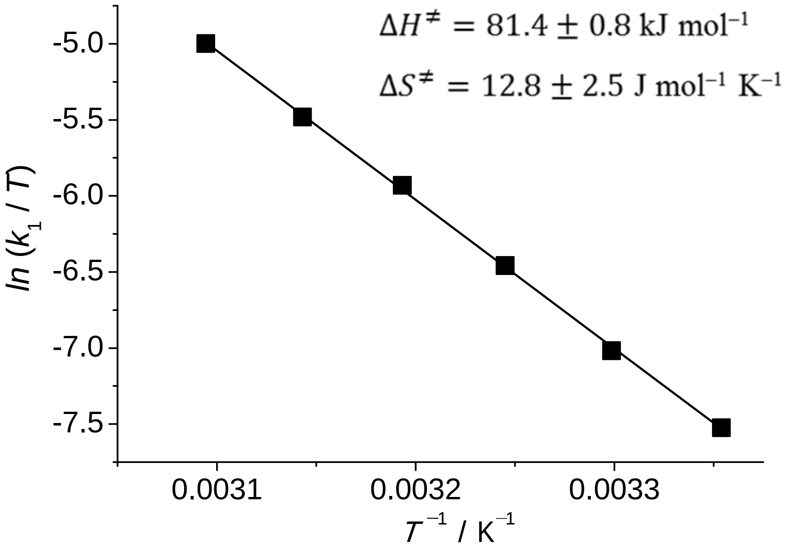

Figure 15. Eyring plot for the temperature dependence of the disassembly rate constant k_1 of dyad **7** dimer in $CHCl_3$.

For comparison, the activation energy E_a of quadruply hydrogen-bonded 2-ureido-4[1H]-pyrimidinone dimers in $CHCl_3$ is 70±2 kJ mol^{-1}.[43] Dyad **7** dimer stabilized by triple PBI π-π-interaction has accordingly a higher activation energy in the same solvent, in line with thermodynamic view that π-π-interaction and hydrogen bonding exhibit comparable strength. Accordingly, the interlocked self-assembly of tweezer-like dyad **7** provides a method to produce kinetically stable π-stacks, presumably resulting from the multiple cooperative π-π-interactions, a concept analogous to the multiple cooperative hydrogen bonds that was applied for non-covalent synthesis of kinetically stable hydrogen-bonded complex assemblies.[44]

4.4 Conclusions

In this chapter, we have introduced discrete PBI quadruple π-stacks by DPA backbone-supported dimerization of PBI dyad **7**. Interestingly, our comparison study demonstrated that PBI dyad **7** has a propensity to form exclusively a MOOM-type dimer conformation allowing for the non-symmetry of its molecular structure. As predicted by Kasha's exciton theory,[34] the structured absorption and sharp fluorescence for the PBI quadruple π-stacks could be observed experimentally for the first time. The interdigitated dimer aggregates of dyad **7** "survived" HPLC separation and could be detected by mass spectrometry measurements, demonstrating very high kinetic stability. By means of time-dependent UV/Vis absorption measurement the activation energy of dimer dissociation of dyad **7** in good solvating solvent chloroform could be determined to be 83.8±0.8 kJ mol^{-1}. This value is even higher than that of quadruple hydrogen bonding.[43] Therefore, our studies indicate that by appropriate space control, the DPA-type backbone can guide the formation of π-π-interacted self-assembly with unexpected high kinetic stabilities, which facilitate the optical and electronic examination of π-π-stacked organic materials.

4.5 Experimental Section

All solvents and reagents were purchased from commercial sources and used as received without further purification, unless otherwise stated. Dry solvents were obtained according to literature procedures.[45] Perylene monoimides **1** and **11** were synthesized according to the literature.[15, 18, 46] Thin layer chromatography (TLC) was conducted on aluminum plates coated with silica gel (60 F_{254}, Merck). Column chromatography was performed using silica gel (Geduran Si 60 from Merck, particle size 0.040–0.063 mm) as the stationary phase. Semi-preparative HPLC was performed on a JASCO system (PU 2080 PLUS) equipped with a photodiode array UV/Vis detector (UV 2077 PLUS) by use of a semi-preparative NUCLEOSIL 100-5 NO_2 column (Macherey&Nagel). Analytical HPLC was performed on a system (PU 2080 PLUS) with a photodiode array detector (MD 2015) from JASCO equipped with a ternary gradient unit (LG 2080–02) and line degasser (DG-2080-533) by use of an analytical NUCLEOSIL 100-5 NO_2 column (Macherey&Nagel). For HPLC separation, HPLC grade solvents ($CHCl_3$ and MeOH) from VWR (Darmstadt, Germany) were used. Dynamic light scattering (DLS) measurements were performed at 25 °C on a N5 Submicron Particle Size Analyzer, Beckman Coulter, using a 25 mW helium-neon laser (632.8 nm). Sample solutions were filtered into a dust-free vial through a 0.45 mm hydrophobic polytetrafluoroethylene (PTFE) filter. Data were collected at scattering angles of 90^o and analyzed with a PCS control software. The melting points were measured by using Olympus BX-41 polarization microscope equipped with a Linkam THMS 600 hot stage and a temperature controller unit.

^1H, ^{13}C and 2D NMR spectra were recorded in standard 5 mm NMR tubes on a Bruker Avance 400 and/or a Bruker DMX 600 spectrometer with TMS or residual undeuterated solvents as internal standard (7.26 ppm for $C\mathit{H}Cl_3$ and 77.00 ppm for $\mathit{C}DCl_3$). High resolution electron spray ionisation (ESI) mass spectra was measured on a MicroTOF Focus instrument (Bruker Daltronik GmbH) and MALDI-TOF measurements were carried out on a Bruker Autoflex II by using a nitrogen laser (337.1 nm).

The UV/Vis absorption measurements were performed on a Perkin Elmer Lambda 40 spectrometer. The slit width and the scan speed were set to be 1.0 nm and 240 nm/min, respectively. In the case of temperature-dependent measurements, the temperature was controlled with a PTP-1+1 Peltier Temperature Programmer (PerkinElmer). The fluorescence studies were conducted on a PTI QM-4/2003 spectrofluorometer. The fluorescence spectra are corrected against photomultiplier and lamp intensity. The solvents for spectroscopic measurements were of spectroscopic grade und used as received. The fluorescence yield was measured according to the literature procedure with the *N*,*N'*-bis(2,5-di-*tert*-butylphenyl)-3,4:9,10- tetracarboxylic acid bisimide (Φ_{fl} = 0.99 in chloroform) as standard.[47]

Procedure 1 (general procedure for the reduction of iodinated benzonitriles by a solution of BH_3·THF): To a solution of the respective iodinated benzonitrile (5.0 mmol) in anhydrous THF (10 mL), a solution of BH_3·THF complex (10.0 mmol) in THF was added slowly under an argon atmosphere at 0 °C. The reaction mixture was stirred at room temperature for 24 hrs. The reaction was then quenched with water (20 mL) and the THF solvent was removed under reduced pressure. The aqueous solution was made alkaline (pH value of ≈ 10) by adding 10% sodium hydroxide solution. The crude product was extracted with Et_2O (3×15 mL) and purified by column chromatography on silica gel using CH_2Cl_2/MeOH (*v*:*v* = 19:1) as eluent.

Procedure 2 (general procedure for the imidization of perylene monoimide with iodobenzylamines): A mixture of perylene monoimide (0.10 mmol), the respective iodobenzylamine (0.10–0.15 mmol) and imidazole (10 g) was heated to 140 °C and stirred for 4 hrs under an argon atmosphere. The reaction was quenched with 2 M hydrochloric acid (30 mL) and stirred for 1 h. The precipitate was filtered and washed sequentially with 2.0 M HCl, H_2O and MeOH (each 20 mL). The crude product was dried under vacuum overnight and purified by column chromatography on silica gel.

Procedure 3 (general procedure for the coupling of trimethylsilylacetylene with an aryl iodide by using the palladium-copper cross-coupling reaction): To a Schlenk flask containing a magnetic stirring bar was added the aryl iodide compound (0.10 mmol), bis(triphenylphosphine)palladium(II) dichloride (3−5 mol%) and copper iodide (5−10 mol%). The vessel was then sealed, evacuated and backfilled with argon (three times). A solvent mixture of CH_2Cl_2/NEt_3 (*v*:*v* = 3:1, 4 mL) was added followed by the trimethylsilylacetylene (0.14 mmol). The successful start of the coupling reaction can be monitored by the increase of turbidity of the reaction mixture, which was stirred at 40°C for 3 hrs. The solution was diluted with CH_2Cl_2 (10 mL) and washed with 2 M hydrochloric acid (3×15 mL). The aqueous layer was extracted with CH_2Cl_2 (3×15 mL). The combined organic layers were dried over Na_2SO_4, concentrated under reduced pressure and purified by column chromatography on silica gel.

Procedure 4 (general procedure for the desilylation of trimethylsilylalkynes): To a solution of the trimethylsilyl-protected alkyne compound (0.10 mmol) in anhydrous THF, 1.0 M tetra-*n*-butylammonium fluoride (TBAF) solution (0.12 mmol) was slowly added. The successful start of the deprotection reaction can be realized by the change in solution color from red to black. The reaction mixture was stirred at room temperature for 10 min. The solvents were then removed under reduced pressure. The resulting crude product was purified by column chromatography on silica gel.

Procedure 5 (general procedure for the Sonogashira cross-coupling reaction of iodo-functionalized PBI with acetylene-functionalized PBI): To a Schlenk flask containing a magnetic stirring bar was added the respective iodo-PBI (10 μmol), acetylene-PBI (10.5 μmol), $PdCl_2(PPh_3)_2$ (1 mg) and CuI (1 mg). The vessel was then sealed, carefully evacuated and backfilled with argon (three times). A degassed solvent mixture of THF/NH(*i*Pr)$_2$ (v:v = 5:1, 3 mL) was added under an argon atmosphere, followed by stirring at 40 °C for 18 hrs. The reaction was quenched with 15 mL of distilled water, and the resultant precipitate was filtered and washed with MeOH (3×10 mL). The crude product was purified twice by a silica gel column with $CHCl_3$ as eluent and subsequently by means of semi-preparative HPLC (flow speed of 10 mL/min) with $CHCl_3$/MeOH (v:v = 100:1) as eluent. The first fraction between 4.5 and 5.5 min was collected and characterized to be the pure PBI dyads.

3-Iodobenzylamine 2: It was prepared by general procedure 1, using 3-iodobenzonitrile (1.15 g, 5.0 mmol), a solution of $BH_3 \cdot THF$ in THF(1.0 M, 10.0 mL, 10.0 mmol), anhydrous THF (10 mL). Yield: 0.67 g (2.9 mmol, 58%) as an oily liquid. TLC (CH_2Cl_2/MeOH = 9:1): R_f= 0.40. ^{1}H NMR (400 MHz, $CDCl_3$): δ 7.69 (s, 1H, ph-*H*), 7.58 (d, J = 7.8 Hz, 1H, ph-*H*), 7.27 (dd, J_1 = 7.7 Hz, J_2 = 0.6 Hz, 1H, ph-*H*), 7.07 (t, J = 7.7 Hz, 1H, ph-*H*), 3.83 (s, 2H, CH_2NH$_2$). HRMS(EI): calcd for C_7H_8IN 232.97014; found 232. 96941.

2-Iodobenzylamine 3: It was prepared by general procedure 1, using 2-iodobenzonitrile (1.15 g, 5.0 mmol), a solution of $BH_3 \cdot THF$ in THF (1.0 M, 10.0 mL, 10.0 mmol), anhydrous THF (10 mL). Yield: 0.52 g (2.2 mmol, 45%) as an oily liquid. TLC (CH_2Cl_2/MeOH = 9:1): R_f = 0.36. ^{1}H NMR (400 MHz, $CDCl_3$): δ 7.82 (dd, J_1 = 7.8 Hz, J_2 = 1.0 Hz, 1H, ph-*H*), 7.31-7.39 (m, 2H, ph-*H*), 6.95 (td, J_1 = 7.4 Hz, J_2 = 1.9 Hz, 1H, ph-*H*), 3.87 (s, 2H, CCH_2NH_2). HRMS(EI): calcd for C_7H_8IN 232.97014; found 232.96956.

***N*-(3-Iodobenzyl)-*N'*-(12-tricosanyl)perylene-3,4:9,10-tetracarboxylic acid bisimide 4:** It was prepared by general procedure 2, using *N*-(12-tricosanyl)perylene-3,4:9,10-tetracarboxy-3,4-anhydride-9,10-imide **1** (71 mg, 0.10 mmol), 3-iodobenzylamine **2** (23 mg, 0.10 mmol) and imidazole (10.0 g). The crude product was purified by column chromatography on silica gel with CH_2Cl_2/*n*-hexane (*v*/*v* = 9:1) as eluent. Yield: 60 mg (0.06 mmol, 65%) as a deep-red solid. TLC (CH_2Cl_2): R_f = 0.53. M.p. 247–248 °C. ^{1}H NMR (400 MHz, $CDCl_3$): δ 8.57–8.68 (m, 8H, perylene protons), 7.92 (s, 1H, ph-*H*), 7.61 (d, *J* = 7.8 Hz, 1H, ph-*H*), 7.55 (d, *J* = 8.1 Hz, 1H, ph-*H*), 7.07 (t, *J* = 7.8 Hz, 1H, ph-*H*), 5.33 (s, 2H, NCH_2), 5.14–5.22 (m, 1H, $NCH(CH_2)_2$), 2.22–2.28 (m, 2H, $NCH(CH_2)_2$), 1.84–1.89 (m, 2H, $NCH(CH_2)_2$), 1.19 (br s, 36H, alkyl-*H*), 0.84 (t, *J* = 6.9 Hz, 6H, CH_2CH_3). ^{13}C NMR (150 MHz, $CDCl_3$): δ 164.53, 163.45, 163.21, 139.26, 137.88, 136.84, 134.87, 134.11, 131.82, 131.62, 131.05, 130.21, 129.46, 129.34, 128.53, 126.36, 126.23, 124.14, 123.40, 123.19, 122.87, 122.82, 94.38, 54.83, 43.00, 32.35, 31.88, 29.60, 29.59, 29.57, 29.54, 29.31, 26.97, 22.65, 14.09. HRMS (ESI-TOF, pos. mode): calcd for $C_{54}H_{62}IN_2O_4$ $[M+H]^+$ 929.37488; found 929.37488. Anal. calcd for $C_{54}H_{61}IN_2O_4$: C, 69.82; H, 6.62; N, 3.02; found: C, 69.79; H, 6.65; N, 3.14.

***N*-(2-Iodobenzyl)-*N'*-(12-tricosanyl)perylene-3,4:9,10-tetracarboxylic acid bisimide 5:** It was prepared by general procedure 2, using *N*-(12-tricosanyl)perylene-3,4:9,10-tetracarboxy-3,4-anhydride-9,10-imide **1** (71 mg, 0.10 mmol), 3-iodobenzylamine **3** (23 mg, 0.10 mmol) and imidazole (10.0 g). The crude product was purified by column chromatography on silica gel with CH_2Cl_2/*n*-hexane (*v*/*v* = 9:1) as eluent. Yield: 57 mg (0.06 mmol, 61%) as a deep-red solid. TLC (CH_2Cl_2): R_f = 0.63. M.p. 296–297 °C. ^{1}H NMR (400 MHz, $CDCl_3$): δ 8.61–8.71 (m, 8H, perylene protons), 7.90 (dd, J_1 = 7.8 Hz, J_2 = 1.2 Hz, 1H, ph-*H*), 7.20 (td, J_1 = 7.6 Hz,

J_2 = 1.2 Hz, 1H, ph-*H*), 6.92–6.98 (m, 2H, ph-*H*), 5.40 (s, 2H, NCH_2), 5.12–5.22 (m, 1H, NC*H*(CH_2)$_2$), 2.21–2.30 (m, 2H, NCH(CH_2)$_2$), 1.83–1.90 (m, 2H, NCH(CH_2)$_2$), 1.20 (br-s, 36H, alkyl-*H*), 0.84 (t, *J* = 6.9 Hz, 6H, CH_2CH_3). ^{13}C NMR (150 MHz, $CDCl_3$): δ 164.56, 163.47, 163.27, 139.63, 138.37, 135.12, 134.18, 131.86, 131.13, 129.57, 129.53, 128.79, 128.37, 126.58, 126.33, 126.10, 124.22, 123.48, 123.31, 123.02, 122.78, 98.09, 54.83, 49.10, 32.35, 31.89, 29.60, 29.59, 29.56, 29.53, 29.31, 26.96, 22.65, 14.09. HRMS (ESI-TOF, pos. mode): calcd for $C_{54}H_{62}IN_2O_4$ $[M+H]^+$ 929.37488; found 929.37488. Anal. calcd for $C_{54}H_{61}IN_2O_4$: C, 69.82; H, 6.62; N, 3.02; found: C, 69.84; H, 6.68; N, 3.23.

***N*-(3-Ethynylbenzyl)-*N'*-(12-tricosanyl)perylene-3,4:9,10-tetracarboxylic acid bisimide 6:** It was prepared by general procedures 3 and 4, using *N*-(3-iodo-benzyl)-*N'*-(12-tricosanyl)-perylene-3,4:9,10-tetracarboxylic acid bisimide **4** (93 mg, 0.10 mmol), trimethylsilylacetylene (14 mg, 0.14 mmol), $Pd(PPh_3)_2Cl_2$ (2 mg) and CuI (1 mg). The quantitative intermediate was subject to the desilylation procedure in the presence of 1.0 M TBAF (0.12 mL, 0.12 mmol). The crude product was purified by column chromatography on silica gel with CH_2Cl_2 as eluent. Yield: 74 mg (0.09 mmol, 89%) as a red solid. TLC (CH_2Cl_2): R_f = 0.59. M.p. 246–247 °C. ^{1}H NMR (400 MHz, $CDCl_3$): δ 8.41–8.63 (m, 8H, perylene protons), 7.70 (t, *J* = 1.3 Hz, 1H, ph-*H*), 7.58 (td, J_1 = 8.0 Hz, J_2 = 1.4 Hz, 1H, ph-*H*), 7.40 (td, J_1 = 7.7 Hz, J_2 = 1.4 Hz, 1H, ph-*H*), 7.30 (t, *J* = 7.8 Hz, 1H, ph-*H*), 5.35 (s, 2H, NCH_2), 5.15–5.22 (m, 1H, NC*H*(CH_2)$_2$), 3.05 (s, 1H, CC*H*), 2.21–2.30 (m, 2H, NCH(CH_2)$_2$), 1.85–1.91 (m, 2H, NCH(CH_2)$_2$), 1.20 (br s, 36H, alkyl-*H*), 0.83 (t, *J* = 6.9 Hz, 6H, CH_2CH_3). ^{13}C NMR (150 MHz, $CDCl_3$): δ 164.54, 163.46, 163.22, 137.28, 134.81, 134.13, 132.61, 131.82, 131.57, 131.44, 131.05, 129.74, 129.46, 129.32, 128.51, 126.34, 126.23, 124.12, 123.38, 123.16, 122.86, 122.33, 83.46, 83.02, 54.83, 43.28, 32.35, 31.88, 29.60, 29.59, 29.57, 29.53, 29.31, 26.97, 22.65, 14.08. HRMS (ESI-TOF, pos. mode): calcd for $C_{56}H_{63}N_2O_4$ $[M+H]^+$ 827.47823; found 827.47821. Anal. calcd for $C_{56}H_{62}N_2O_4$: C, 81.32; H, 7.56; N, 3.39; found: C, 81.05; H, 7.63; N, 3.64.

PBI Dyad 7: It was prepared by general procedure 5, using *N*-(2-iodobenzyl)-*N'*-(12-tricosanyl)-perylene-3,4:9,10-tetracarboxylic acid bisimide **5** (9.3 mg, 10 µmol) and *N*-(3-

ethynylbenzyl)-*N'*-(12-tricosanyl)perylene-3,4:9,10-tetracarboxylic acid bisimide **6** (8.7 mg, 10.5 μmol). Yield: 9.3 mg (5.7 μmol, 57%) as a deep-red solid. M.p. > 400 °C. ^{1}H NMR (600 MHz, $CDCl_3/CF_3COOD$ (*v*:*v* = 4:3)): δ 8.80–8.88 (m, 16H, perylene protons), 7.63 (s, 1H, ph-*H*), 7.56–7.68 (m, 1H, ph-*H*), 7.45 (d, *J* = 8.4 Hz, 1H, ph-*H*), 7.41 (d, *J* = 8.4 Hz, 1H, ph-*H*), 7.30 (t, *J* = 8.4 Hz, 1H, ph-*H*), 7.24–7.28 (m, 2H, ph-*H*), 7.15–7.16 (m, 1H, ph-*H*), 5.76 (s, 2H, NCH_2), 5.49 (s, 2H, NCH_2), 5.23–5.29 (m, 2H, $NCH(CH_2)_2$), 2.22–2.29 (m, 4H, $NCH(CH_2)_2$), 1.93–2.00 (m, 2H, $NCH(CH_2)_2$), 1.23 (br-s, 72H, alkyl-*H*), 0.84 (t, *J* = 7.2 Hz, 12H, CH_2CH_3). ^{13}C NMR (150 MHz, $CDCl_3/CF_3COOD$ (*v*:*v* = 4:3)): δ 167.18, 166.20, 166.00, 165.93, 157.84, 157.55, 152.58, 150.69, 150.37, 150.05, 149.73, 136.66, 136.50, 136,46, 136.14, 133.74, 133.69, 133.31, 131.57, 131.45, 129.93, 129.91, 129.86, 129.84, 129.12, 129.07, 128.80, 127.88, 126.92, 126.87, 126.72, 126.71, 126.19, 125.25, 124.78, 124.76, 124.53, 123.98, 122.54, 122.48, 122.12, 94.76, 87.31, 57.19, 57.18, 44.65, 44.18, 32.58, 32.57, 32.17, 29.85, 29.79, 29.78, 29.73, 29.66, 29.65, 29.58, 27.20, 22.84, 13.79. MS (MALDI-TOF, Matrix DCTB): calcd for $C_{110}H_{122}N_4O_8$ $[M]^-$ 1627.930; found 1628.053 (Monomer), 3256.441 (Dimer) (Due to its bad solubility in acetonitrile, no ESI-HRMS could be acquired). Anal. calcd for $C_{110}H_{122}N_4O_8$: C, 81.15; H, 7.55; N, 3.44; found: C, 80.80; H, 7.66; N, 3.40.

PBI Dyad 8: It was prepared by general procedure 5, using *N*-(3-iodobenzyl)-*N'*-(2,5-di-*tert*-butylphenyl)-perylene-3,4:9,10-tetracarboxylic acid bisimide **12** (7.9 mg, 10 μmol) and *N*-(2-ethynylbenzyl)-*N'*-(12-tricosanyl)perylene-3,4:9,10-tetracarboxylic acid bisimide **10** (8.7 mg, 10.5 μmol). Yield: 8.2 mg (5.5 μmol, 55%) as a deep-red solid. M.p. 386–387 °C. ^{1}H NMR (600 MHz, $CDCl_3/CF_3COOD$ (*v*:*v* = 1:1)): δ 8.83–8.97 (m, 16H, perylene protons), 7.70 (d, *J* = 8.4 Hz, 1H, ph-*H*), 7.65 (s, 1H, ph-*H*), 7.58–7.61 (m, 2H, ph-*H*), 7.48 (d, *J* = 8.4 Hz, 1H, ph-*H*), 7.43 (d, *J* = 8.4 Hz, 1H, ph-*H*), 7.31 (t, *J* = 8.4 Hz, 1H, ph-*H*), 7.27–7.29 (m, 2H, ph-*H*), 7.17–7.19 (m, 1H, ph-*H*), 7.09 (d, *J* = 2.4 Hz, 1H, ph-*H*), 5.79 (s, 2H, NCH_2), 5.52 (s, 2H, NCH_2), 5.26–5.32 (m, 1H, $NCH(CH_2)_2$), 2.25–2.31 (m, 2H, $NCH(CH_2)_2$), 1.95–2.01 (m, 2H, $NCH(CH_2)_2$), 1.32 (s, 9H, *t*-butyl-*H*), 1.30 (s, 9H, *t*-butyl-*H*), 1.24 (br-s, 36H, alkyl-*H*), 0.85 (t, *J* = 7.2 Hz, 6H, CH_2CH_3). ^{13}C NMR (150 MHz, $CDCl_3/CF_3COOD$ (*v*:*v* = 1:1)): δ 167.38, 166.24, 166.08, 152.58, 150.85, 150.52, 150.20, 149.88, 144,29, 136.98, 136.68, 136,47, 136.22, 134.31, 133.91, 133.84, 133.47, 131.74, 131.56, 130.66, 130.62, 130.43, 130.08, 130.00, 129.99, 129.24, 129.17, 128.95, 128.38, 127.98, 127.28, 127.17, 127.07, 127.03, 126.86, 126.28, 125.37, 125.02, 124.92, 124.86, 124.66, 124.12, 122.94, 122.79, 122.58, 122.16, 94.82, 87.39, 57.38, 44.80, 44.37, 35.95, 34.53, 32.66, 32.25, 31.57, 30.65, 29.93, 29.85, 29.80, 29.71, 29.66, 27.28, 22.90, 13.73. MS (MALDI-TOF, Matrix DCTB): calcd for $C_{101}H_{96}N_4O_8$ $[M]^-$ 1493.726; found 1493.728 (Monomer), 2987.809 (Dimer) (Due to its bad solubility in acetonitrile, no ESI-HRMS could be acquired).

PBI Dyad 9: It was prepared by general procedure 5, using *N*-(3-iodobenzyl)-*N'*-(2,5-di-*tert*-butylphenyl)-perylene-3,4:9,10-tetracarboxylic acid bisimide **13** (7.9 mg, 10 μmol) and *N*-(2-ethynylbenzyl)-*N'*-(12-tricosanyl)perylene-3,4:9,10-tetracarboxylic acid bisimide **6** (8.7 mg, 10.5 μmol). Yield: 7.4 mg (4.9 μmol, 49%) as a deep-red solid. M.p. 360–361 °C. ^{1}H NMR (600 MHz, $CDCl_3/CF_3COOD$ (v:v = 1:1)): δ 8.82–8.98 (m, 16H, perylene protons), 7.69 (d, J = 8.4 Hz, 1H, ph-*H*), 7.65 (s, 1H, ph-*H*), 7.58–7.61 (m, 2H, ph-*H*), 7.47 (d, J = 8.4 Hz, 1H, ph-*H*), 7.42 (d, J = 8.4 Hz, 1H, ph-*H*), 7.30 (t, J = 8.4 Hz, 1H, ph-*H*), 7.27–7.29 (m, 2H, ph-*H*), 7.18–7.20 (m, 1H, ph-*H*), 7.10 (d, J = 2.4 Hz, 1H, ph-*H*), 5.79 (s, 2H, NCH_2), 5.52 (s, 2H, NCH_2), 5.25–5.30 (m, 1H, NCH(CH_2)$_2$), 2.23–2.30 (m, 2H, NCH(CH_2)$_2$), 1.94–2.00 (m, 2H, NCH(CH_2)$_2$), 1.32 (s, 9H, *t*-butyl-*H*), 1.30 (s, 9H, *t*-butyl-*H*), 1.23 (br-s, 36H, alkyl-*H*), 0.85 (t, J = 7.2 Hz, 6H, CH_2CH_3). ^{13}C NMR (150 MHz, $CDCl_3/CF_3COOD$ (v:v = 1:1)): δ 167.35, 166.12, 158.07, 157.78, 152.55, 150.82, 150.50, 150.18, 149.86, 144,28, 136.97, 136.67, 136,38, 136.23, 134.30, 133.86, 133.81, 133.44, 131.66, 131.50, 130.66, 130.60, 130.42, 130.02, 130.00, 129.94, 129.21, 129.15, 128.88, 128.36, 127.99, 127.27, 127.13, 127.03, 126.98, 126.82, 126.34, 124.98, 124.91, 124.82, 124.65, 124.08, 122.87, 122.77, 122.60, 122.21, 94.83, 87.39, 57.34, 44.75, 44.33, 35.94, 34.52, 32.64, 32.23, 31.57, 30.66, 29.91, 29.84, 29.79, 29.70, 29.64, 27.26, 22.89, 13.75. MS (MALDI-TOF, Matrix DCTB): calcd for $C_{101}H_{96}N_4O_8$ $[M]^-$ 1493.726; found 1493.739 (Monomer), 2987.492 (Dimer) (Due to its bad solubility in acetonitrile, no ESI-HRMS could be acquired).

***N*-(2-Ethynylbenzyl)-*N'*-(12-tricosanyl)perylene-3,4:9,10-tetracarboxylic acid bisimide (10):** It was prepared by general procedures 3 and 4, using *N*-(2-iodo-benzyl)-*N'*-(12-

tricosanyl)-perylene-3,4:9,10-tetracarboxylic acid bisimide **5** (93 mg, 0.10 mmol), trimethylsilylacetylene (14 mg, 0.14 mmol), $Pd(PPh_3)_2Cl_2$ (2 mg) and CuI (1 mg). The quantitative intermediate was subject to the desilylation procedure in the presence of 1.0 M TBAF (0.12 mL, 0.12 mmol). The crude product was purified by column chromatography on silica gel with CH_2Cl_2 as eluent. Yield: 64 mg (0.08 mmol, 77%) as a red solid. TLC (CH_2Cl_2) $R_f = 0.50$. M.p. 301–302 °C. ^{1}H NMR (400 MHz, $CDCl_3$): δ 8.57–8.68 (m, 8H, perylene protons), 7.54–7.56 (m, 1H, ph-*H*), 7.18–7.26 (m, 2H, ph-*H*), 7.12–7.14 (m, 1H, ph-*H*), 5.61 (s, 2H, NCH_2), 5.15–5.22 (m, 1H, $NCH(CH_2)_2$), 3.44 (s, 1H, CC*H*), 2.23–2.30 (m, 2H, $NCH(CH_2)_2$), 1.83–1.90 (m, 2H, $NCH(CH_2)_2$), 1.20 (br s, 36H, alkyl-*H*), 0.84 (t, $J = 7.0$ Hz, 6H, CH_2CH_3). ^{13}C NMR (150 MHz, $CDCl_3$): δ 164.55, 163.46, 163.33, 138.97, 134.92, 134.17, 133.09, 131.84, 131.79, 131.08, 129.50, 129.03, 126.95, 126.49, 126.29, 125.83, 124.13, 123.40, 123.20, 122.96, 122.88, 121.06, 82.60, 81.37, 54.82, 42.36, 32.35, 31.88, 29.60, 29.59, 29.57, 29.53, 29.31, 26.97, 22.65, 14.08. HRMS (ESI-TOF, pos. mode): calcd for $C_{56}H_{62}N_2O_4$ $[M+H]^+$ 827.47823; found 827.47826. Anal. calcd for $C_{56}H_{62}N_2O_4$: C, 81.32; H, 7.56; N, 3.39; found: C, 81.04; H, 7.65; N, 3.43.

***N*-(3-Iodo-benzyl)-*N'*-(2,5-di-*tert*-butylphenyl)-perylene-3,4:9,10-tetracarboxylic acid bisimide (12):** It was prepared by general procedure 2, using *N*-(2,5-di-*tert*-butylphenyl)perylene-3,4:9,10-tetracarboxy-3,4-anhydride-9,10-imide **11** (58 mg, 0.10 mmol), 3-iodobenzylamine **2** (35 mg, 0.15 mmol) and imidazole (10 g). The crude product was purified by column chromatography on silica gel with CH_2Cl_2 as eluent. Yield: 35 mg (0.04 mmol, 44%) as a red solid. TLC (CH_2Cl_2) $R_f = 0.50$. M.p. 283–284 °C. ^{1}H NMR (400 MHz, $CDCl_3$): δ 8.56–8.75 (m, 8H, perylene protons), 7.92 (t, $J = 2.4$ Hz, 1H, ph-*H*), 7.61 (dq, $J_1 = 8.0$ Hz, $J_2 = 2.4$ Hz, 1H, ph-*H*), 7.60 (d, $J = 8.8$ Hz, 1H, ph-*H*), 7.55 (dq, $J_1 = 8.0$ Hz, $J_2 = 2.4$ Hz, 1H, ph-*H*), 7.48 (dd, $J_1 = 8.8$ Hz, $J_2 = 2.4$ Hz, 1H, ph-*H*), 7.11 (d, $J = 2.4$ Hz, 1H, ph-*H*), 7.07 (t, $J = 8.0$ Hz, 1H, ph-*H*), 5.34 (s, 2H, NCH_2), 1.35 (s, 9H, *t*-butyl-*H*), 1.30 (s, 9H, *t*-butyl-*H*). ^{13}C NMR (100 MHz, $CDCl_3$): δ 164.1, 162.8, 150.4, 143.7, 139.3, 137.9, 136.9, 134.2, 134.1, 132.6, 131.5, 131.0, 130.2, 129.5, 128.8, 128.7, 128.0, 126.4, 126.1, 125.7, 123.7, 123.0, 122.8, 122.7, 94.3, 43.0, 35.5, 34.4, 31.7, 31.3. HRMS (ESI-TOF, pos. mode): calcd for $C_{45}H_{35}IN_2O_4$ $[M+H]^+$ 795.17143; found. 795.17111.

***N*-(2-Iodo-benzyl)-*N'*-(2,5-di-tert-butylphenyl)-perylene-3,4:9,10-tetracarboxylic acid bisimide (13):** It was prepared by general procedure 2, using *N*-(2,5-di-*tert*-butylphenyl)perylene-3,4:9,10-tetracarboxy-3,4-anhydride-9,10-imide **11** (58 mg, 0.10 mmol), 2-iodobenzylamine **3** (35 mg, 0.15 mmol) and imidazole (10 g). The crude product was purified by column chromatography on silica gel with CH_2Cl_2 as eluent. Yield: 37 mg (0.05 mmol, 47%) as a red solid. TLC (CH_2Cl_2) $R_f = 0.23$. M.p. 352–353 °C. ^{1}H NMR (400 MHz, $CDCl_3$): δ 8.70–8.79 (m, 8H, perylene protons), 7.91 (dd, $J_1 = 8.0$ Hz, $J_2 = 1.2$ Hz, 1H, ph-*H*), 7.61 (dd, $J = 8.4$ Hz, 1H, ph-*H*), 7.48 (dd, $J_1 = 8.4$ Hz, $J_2 = 2.4$ Hz, 1H, ph-*H*), 7.22 (td, $J_1 = 8.0$ Hz, $J_2 = 1.2$ Hz, 1H, ph-*H*), 7.02 (d, J= 2.4 Hz, 1H, ph-*H*), 7.01 (dd, $J_1 = 8.0$ Hz, $J_2 = 1.2$ Hz, 1H, ph-*H*), 6.95 (td, $J_1 = 8.0$ Hz, $J_2 = 1.2$ Hz, ph-*H*), 5.45 (s, 2H, NCH_2), 1.34 (s, 9H, *t*-butyl-*H*), 1.30 (s, 9H, *t*-butyl-*H*). ^{13}C NMR (150 MHz, $CDCl_3$): δ 164.4, 163.3, 150.2, 143.7, 139.7, 138.4, 135.2, 134.8, 132.5, 132.0, 131.9, 131.9, 129.9, 129.6, 128.8, 128.4, 127.7, 126.8, 126.7, 126.4, 126.1, 123.8, 123.4, 123.3, 123.0, 98.1, 49.2, 35.5, 34.3, 31.7, 31.2. HRMS (ESI-TOF, pos. mode): calcd for $C_{45}H_{35}N_2O_4I$ $[M+H]^+$ 795.17143; found. 795.17124.

4.6 References and Notes

[1] a) F. J. M. Hoeben, P. Jonkheijm, E. W. Meijer, A. P. H. J. Schenning, *Chem. Rev.* **2005**, *105*, 1491-1546; b) L. Brunsveld, B. J. B. Folmer, E. W. Meijer, R. P. Sijbesma, *Chem. Rev.* **2001**, *101*, 4071-4098; c) A. C. Grimsdale, K. Müllen, *Angew. Chem. Int. Ed.* **2005**, *44*, 5592-5629; d) F. Würthner, in *Supramolecular Dye Chemistry (Topics in Current Chemistry), Vol. 258*, Springer, Berlin, **2005**.

[2] a) T. Pullerits, V. Sundström, *Acc. Chem. Res.* **1996**, *29*, 381-389; b) X. Hu, T. Ritz, A. Damjanovic, F. Autenrieth, K. Schulten, *Q. Rev. Biophys.* **2002**, *35*, 1-62; c) T. S. Balaban, H. Tamiaki, A. R. Holzwarth, *Top. Curr. Chem.* **2005**, *258*, 1-38; d) G. McDermott, S. M. Prince, A. A. Freer, A. M. Hawthornthwaite-Lawless, M. Z. Papiz, R. J. Cogdell, N. W. Isaacs, *Nature* **1995**, *374*, 517-521.

[3] a) C. Wang, H. Dong, W. Hu, Y. Liu, D. Zhu, *Chem. Rev.* **2012**, DOI: 10.1021/cr100380z; b) A. Mishra, P. Bäuerle, *Angew. Chem. Int. Ed.* **2012**, *51*, 2020-2067; c) T. M. Clarke, J. R. Durrant, *Chem. Rev.* **2010**, *110*, 6736-6767.

[4] a) F. Wuerthner, *Chem. Commun.* **2004**, 1564-1579; b) M. R. Wasielewski, *Acc. Chem. Res.* **2009**, *42*, 1910-1921; c) F. Würthner, M. Stolte, *Chem. Commun.* **2011**, *47*, 5109-5115; d) J. E. Anthony, A. Facchetti, M. Heeney, S. R. Marder, X. Zhan, *Adv. Mater.*

2010, *22*, 3876-3892.

[5] Z. Chen, A. Lohr, C. R. Saha-Möller, F. Würthner, *Chem. Soc. Rev.* **2009**, *38*, 564-584.

[6] a) F. Würthner, Z. Chen, V. Dehm, V. Stepanenko, *Chem. Commun.* **2006**, 1188-1190; b) Z. Chen, V. Stepanenko, V. Dehm, P. Prins, L. D. A. Siebbeles, J. Seibt, P. Marquetand, V. Engel, F. Würthner, *Chem.-Eur. J.* **2007**, *13*, 436-449; c) V. Dehm, Z. Chen, U. Baumeister, P. Prins, L. D. A. Siebbeles, F. Würthner, *Org. Lett.* **2007**, *9*, 1085-1088.

[7] R. F. Fink, J. Seibt, V. Engel, M. Renz, M. Kaupp, S. Lochbrunner, H.-M. Zhao, J. Pfister, F. Würthner, B. Engels, *J. Am. Chem. Soc.* **2008**, *130*, 12858-12859.

[8] a) J. M. Giaimo, J. V. Lockard, L. E. Sinks, A. M. Scott, T. M. Wilson, M. R. Wasielewski, *J. Phys. Chem. A* **2008**, *112*, 2322-2330; b) C. Hippius, I. H. M. van Stokkum, E. Zangrando, R. M. Williams, M. Wykes, D. Beljonne, F. Würthner, *J. Phys. Chem. C* **2008**, *112*, 14626-14638; c) A. Syamakumari, A. P. H. J. Schenning, E. W. Meijer, *Chem. Eur. J.* **2002**, *8*, 3353-3361; d) V. Dehm, M. Buchner, J. Seibt, V. Engel, F. Würthner, *Chem. Sci.* **2011**, *2*, 2094-2100; e) W. Wang, J. J. Han, L.-Q. Wang, L.-S. Li, W. J. Shaw, A. D. Q. Li, *Nano Lett.* **2003**, *3*, 455-458; f) W. Wang, L. Wang, B. J. Palmer, G. J. Exarhos, A. D. Q. Li, *J. Am. Chem. Soc.* **2006**, *128*, 11150-11159.

[9] J. K. Klosterman, Y. Yamauchi, M. Fujita, *Chem. Soc. Rev.* **2009**, *38*, 1714-1725.

[10] a) Y. Li, J. Zhao, X. Yin, H. Liu, G. Yin, *Phys. Chem. Chem. Phys.* **2007**, *9*, 1186-1193; b) J. M. Seminario, A. G. Zacarias, J. M. Tour, *J. Am. Chem. Soc.* **1998**, *120*, 3970-3974.

[11] *Maestro, version 9.1, MacroModel, version 9.8,* Schrödinger, LLC, New York, NY, **2011**.

[12] a) F. Graser, E. Hädicke, *Liebigs Ann. Chem.* **1980**, 1994-2011; b) F. Graser, E. Hädicke, *Liebigs Ann. Chem.* **1984**, 483-494; c) E. Hädicke, F. Graser, *Acta Crystallogr., Sect. C* **1986**, *42*, 189-195; d) E. Hädicke, F. Graser, *Acta Crystallogr., Sect. C* **1986**, *42*, 195-198; e) G. Klebe, F. Graser, E. Hädicke, J. Berndt, *Acta Crystallogr., Sect. B* **1989**, *45*, 69-77.

[13] a) J. A. A. W. Elemans, A. E. Rowan, R. J. M. Nolte, *J. Am. Chem. Soc.* **2002**, *124*, 1532-1540; b) L. Isaacs, D. Witt, *Angew. Chem. Int. Ed.* **2002**, *41*, 1905-1907; c) F.-G. Klärner, B. Kahlert, A. Nellesen, J. Zienau, C. Ochsenfeld, T. Schrader, *J. Am. Chem. Soc.* **2006**, *128*, 4831-4841; d) A. Lohr, M. Grüne, F. Würthner, *Chem. Eur. J.* **2009**, *15*, 3691-3705; e) A. Wu, A. Chakraborty, J. C. Fettinger, R. A. Flowers Ii, L. Isaacs, *Angew. Chem. Int. Ed.* **2002**, *41*, 4028-4031; f) A. Wu, P. Mukhopadhyay, A. Chakraborty, J. C. Fettinger, L. Isaacs, *J. Am. Chem. Soc.* **2004**, *126*, 10035-10043.

[14] a) R. Bhosale, A. Perez-Velasco, V. Ravikumar, R. S. K. Kishore, O. Kel, A. Gomez-Casado, P. Jonkheijm, J. Huskens, P. Maroni, M. Borkovec, T. Sawada, E. Vauthey, N.

Sakai, S. Matile, *Angew. Chem. Int. Ed.* **2009**, *48*, 6461-6464; b) S. Maity, R. Bhosale, N. Banerji, E. Vauthey, N. Sakai, S. Matile, *Org. Biomol. Chem.* **2010**, *8*, 1052-1057.

[15] a) H. Kaiser, J. Lindner, H. Langhals, *Chem. Ber.* **1991**, *124*, 529-535; b) M. J. Tauber, R. F. Kelley, J. M. Giaimo, B. Rybtchinski, M. R. Wasielewski, *J. Am. Chem. Soc.* **2006**, *128*, 1782-1783.

[16] S. Takahashi, Y. Kuroyama, K. Sonogashira, N. Hagihara, *Synthesis* **1980**, *8*, 627-630.

[17] K. Sonogashira, Y. Tohda, N. Hagihara, *Tetrahedron Lett.* **1975**, *16*, 4467-4470.

[18] S. Demmig, H. Langhals, *Chem. Ber.* **1988**, *121*, 225-230.

[19] C. Shao, M. Grüne, M. Stolte, F. Würthner, *Chem. Eur. J.* **2012**, DOI: 10.1002/chem.201201661.

[20] H. Langhals, *Chem. Ber.* **1985**, *118*, 4641-4645.

[21] U. H. F. Bunz, *Chem. Rev.* **2000**, *100*, 1605-1644.

[22] a) B. Baytekin, H. T. Baytekin, C. A. Schalley, *Org. Biomol. Chem.* **2006**, *4*, 2825-2841; b) C. A. Schalley, *Int. J. Mass. Spectrom.* **2000**, *194*, 11-39.

[23] a) G. Fernández, E. M. Pérez, L. Sánchez, N. Martín, *J. Am. Chem. Soc.* **2008**, *130*, 2410-2411; b) G. Fernández, L. Sánchez, E. M. Pérez, N. Martín, *J. Am. Chem. Soc.* **2008**, *130*, 10674-10683; c) P. D. Frischmann, S. Guieu, R. Tabeshi, M. J. MacLachlan, *J. Am. Chem. Soc.* **2010**, *132*, 7668-7675; d) K. A. Jolliffe, M. C. Calama, R. Fokkens, N. M. M. Nibbering, P. Timmerman, D. N. Reinhoudt, *Angew. Chem. Int. Ed.* **1998**, *37*, 1247-1251; e) A. Lohr, S. Uemura, F. Würthner, *Angew. Chem. Int. Ed.* **2009**, *48*, 6165-6168; f) A. n. Molina-Ontoria, G. Fernández, M. Wielopolski, C. Atienza, L. Sánchez, A. Gouloumis, T. Clark, N. Martín, D. M. Guldi, *J. Am. Chem. Soc.* **2009**, *131*, 12218-12229; g) T. van der Boom, R. T. Hayes, Y. Zhao, P. J. Bushard, E. A. Weiss, M. R. Wasielewski, *J. Am. Chem. Soc.* **2002**, *124*, 9582-9590.

[24] See the mass spectrum schown in *Chapter 5* for a direct comparison. When kinetically stable large aggregates are formed, peaks for trimer, tetramer and so on should also be detectable in the MALDI-TOF mass spectrum.

[25] a) J. Wu, A. Fechtenkötter, J. Gauss, M. D. Watson, M. Kastler, C. Fechtenkötter, M. Wagner, K. Müllen, *J. Am. Chem. Soc.* **2004**, *126*, 11311-11321; b) B. Rybtchinski, L. E. Sinks, M. R. Wasielewski, *J. Phys. Chem. A* **2004**, *108*, 7497-7505; c) M. J. Ahrens, L. E. Sinks, B. Rybtchinski, W. Liu, B. A. Jones, J. M. Giaimo, A. V. Gusev, A. J. Goshe, D. M. Tiede, M. R. Wasielewski, *J. Am. Chem. Soc.* **2004**, *126*, 8284-8294.

[26] M. J. Ahrens, R. F. Kelley, Z. E. X. Dance, M. R. Wasielewski, *Phys. Chem. Chem. Phys.* **2007**, *9*.

[27] L. D. Wescott, D. L. Mattern, *J. Org. Chem.* **2003**, *68*, 10058-10066.

[28] a) C. A. Hunter, *Angew. Chem. Int. Ed.* **1993**, *32*, 1584-1586; b) C. A. Hunter, *Chem. Soc. Rev.* **1994**, *23*, 101-109; c) C. A. Hunter, K. R. Lawson, J. Perkins, C. J. Urch, *J.*

Chem. Soc., Perkin Trans. 2 **2001**, 651-669; d) C. A. Hunter, J. K. M. Sanders, *J. Am. Chem. Soc.* **1990**, *112*, 5525-5534.

[29] M. R. Hansen, T. Schnitzler, W. Pisula, R. Graf, K. Müllen, H. W. Spiess, *Angew. Chem. Int. Ed.* **2009**, *48*, 4621-4624.

[30] a) J. J. Han, W. Wang, A. D. Q. Li, *J. Am. Chem. Soc.* **2006**, *128*, 672-673; b) J. J. Han, A. D. Shaller, W. Wang, A. D. Q. Li, *J. Am. Chem. Soc.* **2008**, *130*, 6974-6982.

[31] a) H. Yoo, J. Yang, A. Yousef, M. R. Wasielewski, D. Kim, *J. Am. Chem. Soc.* **2010**, *132*, 3939-3944; b) D. Veldman, S. p. M. A. Chopin, S. C. J. Meskers, M. M. Groeneveld, R. M. Williams, R. A. J. Janssen, *J. Phys. Chem. A* **2008**, *112*, 5846-5857.

[32] J. Seibt, T. Winkler, K. Renziehausen, V. Dehm, F. Würthner, H. D. Meyer, V. Engel, *J. Phys. Chem. A* **2009**, *113*, 13475-13482.

[33] a) J. Seibt, P. Marquetand, V. Engel, Z. Chen, V. Dehm, F. Würthner, *Chem. Phys.* **2006**, *328*, 354-362; b) H.-M. Zhao, J. Pfister, V. Settels, M. Renz, M. Kaupp, V. C. Dehm, F. Würthner, R. F. Fink, B. Engels, *J. Am. Chem. Soc.* **2009**, *131*, 15660-15668; c) A. E. Clark, C. Qin, A. D. Q. Li, *J. Am. Chem. Soc.* **2007**, *129*, 7586-7595; d) F. Gao, Y. Zhao, W. Liang, *J. Phys. Chem. B* **2011**, *115*, 2699-2708.

[34] a) M. Kasha, *Radiat. Res.* **1963**, *20*, 55-70; b) M. Kasha, H. R. Rawls, M. A. El-Bayoumi, *Pure Appl. Chem.* **1965**, *11*, 371-392.

[35] a) Y. Hirata, T. Okada, T. Nomoto, *Chem. Phys. Lett.* **1998**, *293*, 371-377; b) Y. Hirata, T. Okada, N. Mataga, T. Nomoto, *J. Phys. Chem.* **1992**, *96*, 6559-6563; c) S. Anand, O. Varnavski, J. A. Marsden, M. M. Haley, H. B. Schlegel, T. Goodson, *J. Phys. Chem. A* **2006**, *110*, 1305-1318.

[36] The absorption band of PBI $S_0 \rightarrow S_2$ transition resides below 270 nm and therefore, is not overlapped with DPA absorption between 275 and 320 nm.

[37] A. D. Q. Li, W. Wang, L.-Q. Wang, *Chem. Eur. J.* **2003**, *9*, 4594-4601.

[38] Z. Chen, B. Fimmel, F. Würthner, *Org. Biomol. Chem.* **2012**, *10*, 5845–5855.

[39] This apparent decrease is, however, mostly related to a broadening of the band due to excitonic couplings. Thus, the transition dipole moments calculated by integration of the $S_0 \rightarrow S_1$ band from 400 to 650 nm are 11.89 D for non-aggregated dyads (in $CHCl_3$) and 8.60 D for aggregated dyads (in CCl_4).

[40] a) G. Brizius, K. Billingsley, M. D. Smith, U. H. F. Bunz, *Org. Lett.* **2003**, *5*, 3951-3954; b) K. Okuyama, T. Hasegawa, M. Ito, N. Mikami, *J. Phys. Chem.* **1984**, *88*, 1711-1716.

[41] Even though the high activation energy of dissociation of dyad **7** dimers, the acivation energy of self-assembly of dyad **7** monomers into dimers seems quite low. After concentrating the solution of dyad **7** in chloroform, the color turns red immediately and no absorption spectral changes can be detected on the convensional time scale.

[42] P. A. Korevaar, S. J. George, A. J. Markvoort, M. M. J. Smulders, P. A. J. Hilbers, A.

P. H. J. Schenning, T. F. A. De Greef, E. W. Meijer, *Nature* **2012**, *481*, 492-496.

[43] S. H. M. Söntjens, R. P. Sijbesma, M. H. P. van Genderen, E. W. Meijer, *J. Am. Chem. Soc.* **2000**, *122*, 7487-7493.

[44] a) L. J. Prins, D. N. Reinhoudt, P. Timmerman, *Angew. Chem. Int. Ed.* **2001**, *40*, 2382-2426; b) L. J. Prins, F. De Jong, P. Timmerman, D. N. Reinhoudt, *Nature* **2000**, *408*, 181-184; c) L. J. Prins, E. E. Neuteboom, V. Paraschiv, M. Crego-Calama, P. Timmerman, D. N. Reinhoudt, *J. Org. Chem.* **2002**, *67*, 4808-4820.

[45] D. D. Perrin, W. L. F. Armarego, *Purification of Laboratory Chemicals*, Pergamon Press: Oxford, 1980.

[46] H. Langhals, G. Range, E. Wistuba, C. Rüchardt, *Chem. Ber.* **1981**, *114*, 3813-3830.

[47] a) G. A. Crosby, J. N. Demas, *J. Phys. Chem.* **1971**, *75*, 991-1024; b) N. Vân Anh, F. Schlosser, M. M. Groeneveld, I. H. M. van Stokkum, F. Würthner, R. M. Williams, *J. Phys. Chem. C* **2009**, *113*, 18358-18368.

4.7 Supporting Information

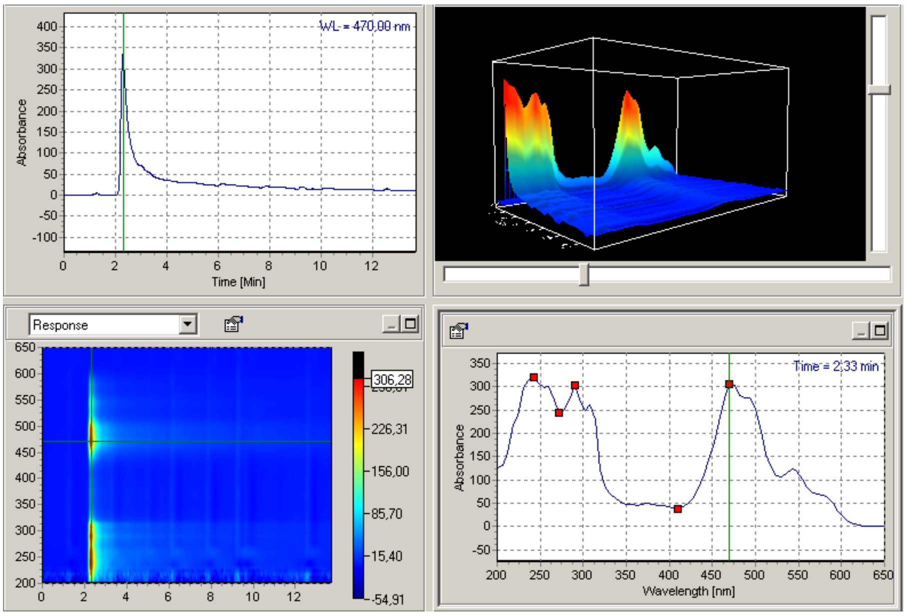

Figure S1. Screenshot from analytical HPLC for purified dyad **7** sample injected from concentrated chloroform solution. The in-situ absorption spectrum of the fraction band is shown on the right side. Analytical HPLC column was used und the eluent is a solvent mixture of $CHCl_3$/MeOH (*v*:*v* = 100:1).

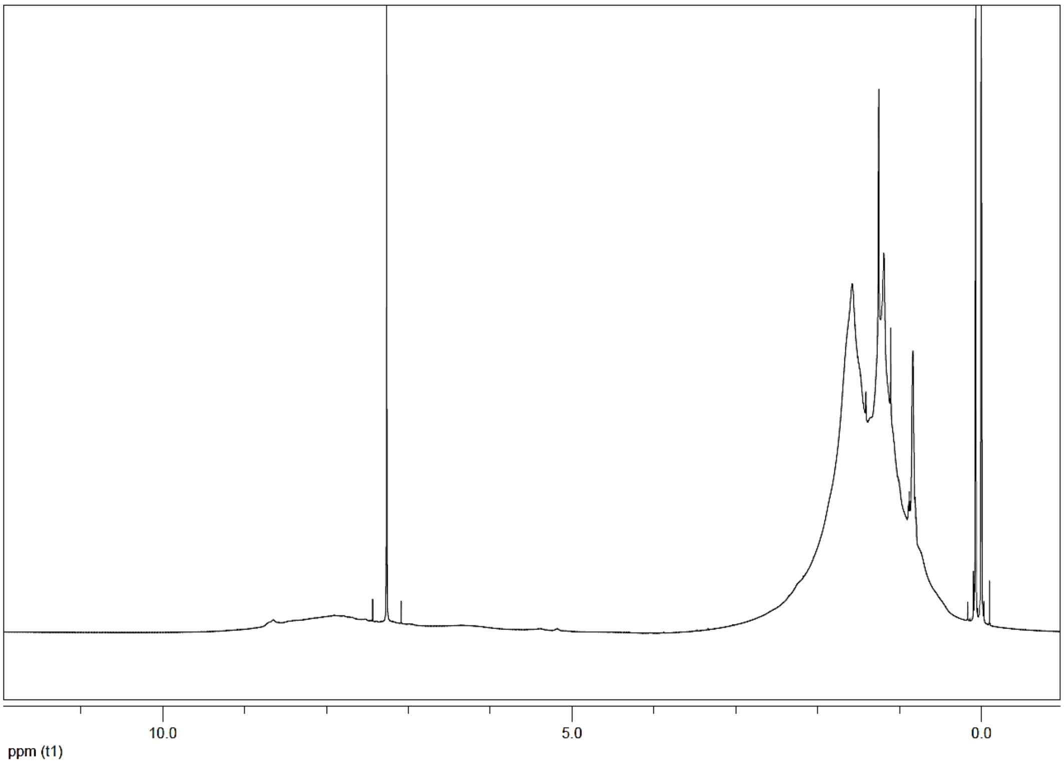

Figure S2. ^{1}H NMR spectrum of dyad **7** at a concentration of 10^{-2} M in $CDCl_3$ recorded with 600 MHz NMR at 293 K.

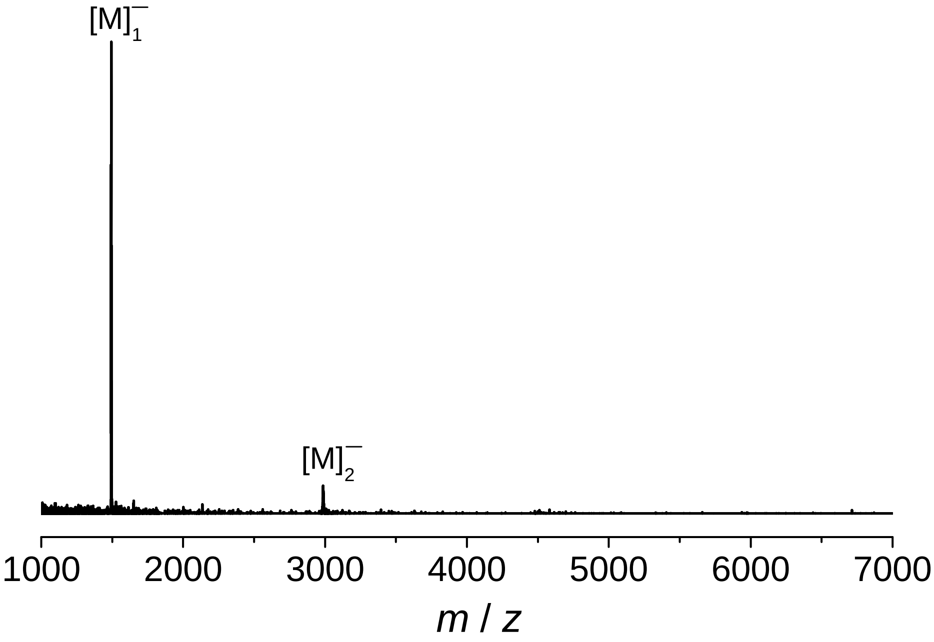

Figure S3. MALDI-TOF mass spectrum (linear mode) of PBI dyad **8**. The peaks corresponding to monomer and dimer species are marked with $[M]_1^-$ and $[M]_2^-$, respectively. 2-[(2E)-3-(4-*tert*-butylphenyl)-2-methylprop-2-enylidene]malononitrile (DCTB) was used as the matrix.

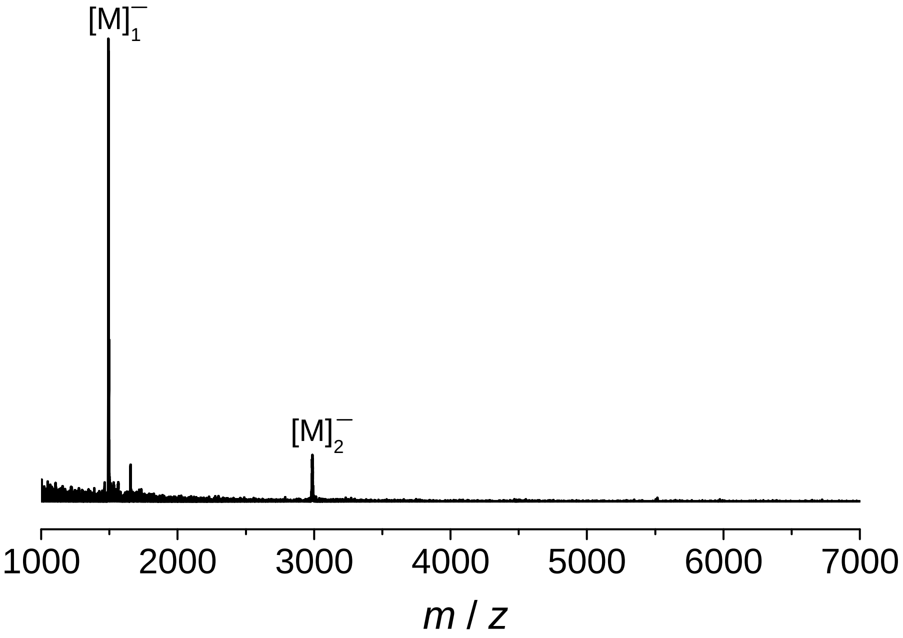

Figure S4. MALDI-TOF mass spectrum (linear mode) of PBI dyad **9**. The peaks corresponding to monomer and dimer species are marked with $[M]_1^-$ and $[M]_2^-$, respectively. 2-[(2E)-3-(4-*tert*-butylphenyl)-2-methylprop-2-enylidene]malononitrile (DCTB) was used as the matrix.

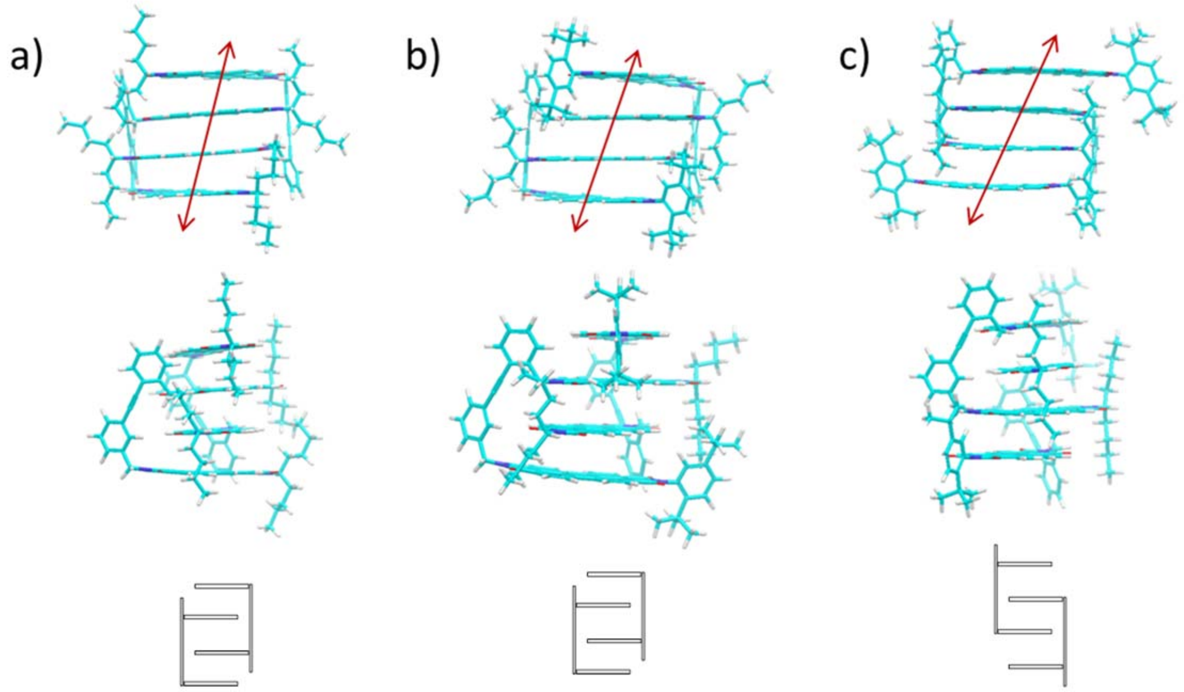

Figure S5. MM3+ calculated dimer structure of the PBI dyads a) **7**, b) **8** and c) **9**.

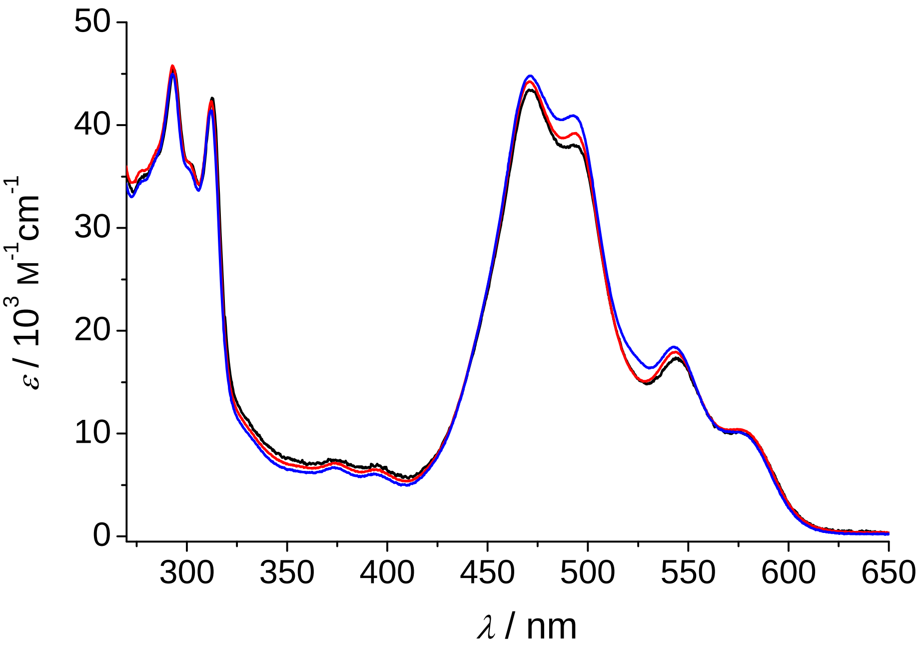

Figure S6. Concentration-dependent absorption spectra of dyad **7** for 10^{-3} (black), 10^{-4} (red) to 10^{-5} M (blue) in CCl_4 recorded at 293 K. Each sample was kept at the given concentration for one week to reach the thermodynamic equilibrium.

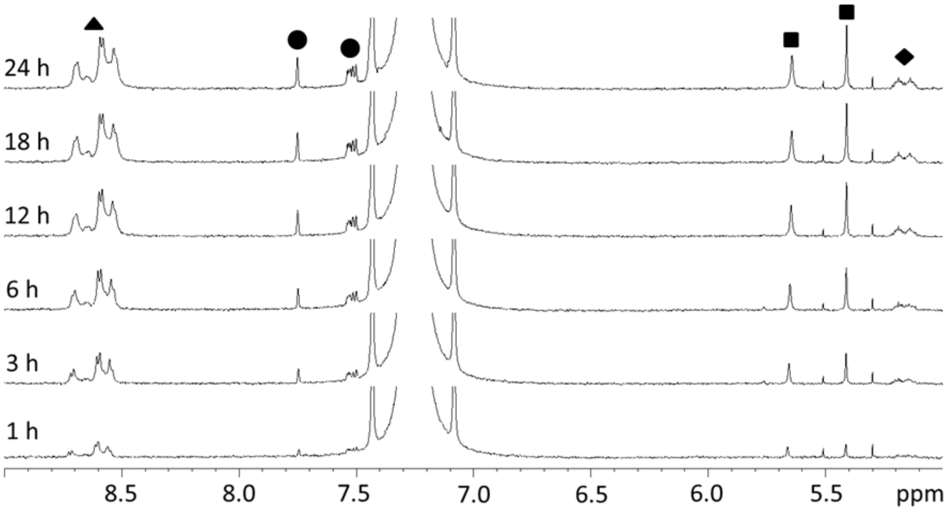

Figure S7. ^{1}H NMR spectra of dyad **7** recorded with 600 MHz NMR at 1, 3, 6, 12, 18, 24 hours after 3 μL of 10^{-2} M dyad **7** in $CDCl_3$ was added into 3.0 mL of $CDCl_3$ at 293 K. Triangle: perylene protons; cycle: DPA backbone protons; square: methylene protons; rhombus: N*H*$(CH_2)_2$ protons.

Wavelength (nm)	ε_M ($M^{-1}cm^{-1}$)	C ($M^{-1}cm^{-1}$)	k_1 (h^{-1})	correlation coefficient
576	655	9407	0.159	0.9996
528	157626	–141502	0.164	0.9997
491	104320	–64362	0.161	0.9997
470	32091	12117	0.158	0.9995
312	11891	29551	0.164	0.9995
293	26968	17857	0.161	0.9995
261	73552	–29572	0.166	0.9997
Average:	----	----	0.162	0.9996

Table S1. List of monomer absorption coefficient ε_M, constant C and disassembly rate constant k_1 extracted from the fitting curves of absorption changes at different wavelengths into a single exponential curve in terms of equation (6).

Temperature (°C)	$k_{1(470)}$ (h^{-1})	$k_{1(528)}$ (h^{-1})	k_{average} (h^{-1})	$t_{1/2}$ (h)	ln (k_{average}/T)
25	0.158	0.164	0.161	4.308	−7.525
30	0.262	0.280	0.271	2.555	−7.019
35	0.482	0.484	0.483	1.435	−6.458
40	0.815	0.850	0.832	0.833	−5.931
45	1.247	1.403	1.325	0.523	−5.481
50	2.055	2.308	2.181	0.318	−4.998

Table S2. List of the disassembly rate constant k_1 at different temperatures acquired at a wavelength of 470 and 528 nm according to the process shown in Figure 10 and Table S1. k_{average} is the averaged value of $k_{1(470)}$ and $k_{1(528)}$. The half time of the disassembly process was calculated with the formula $t_{1/2}$ = ln2 / k_{average} for the first order reaction.

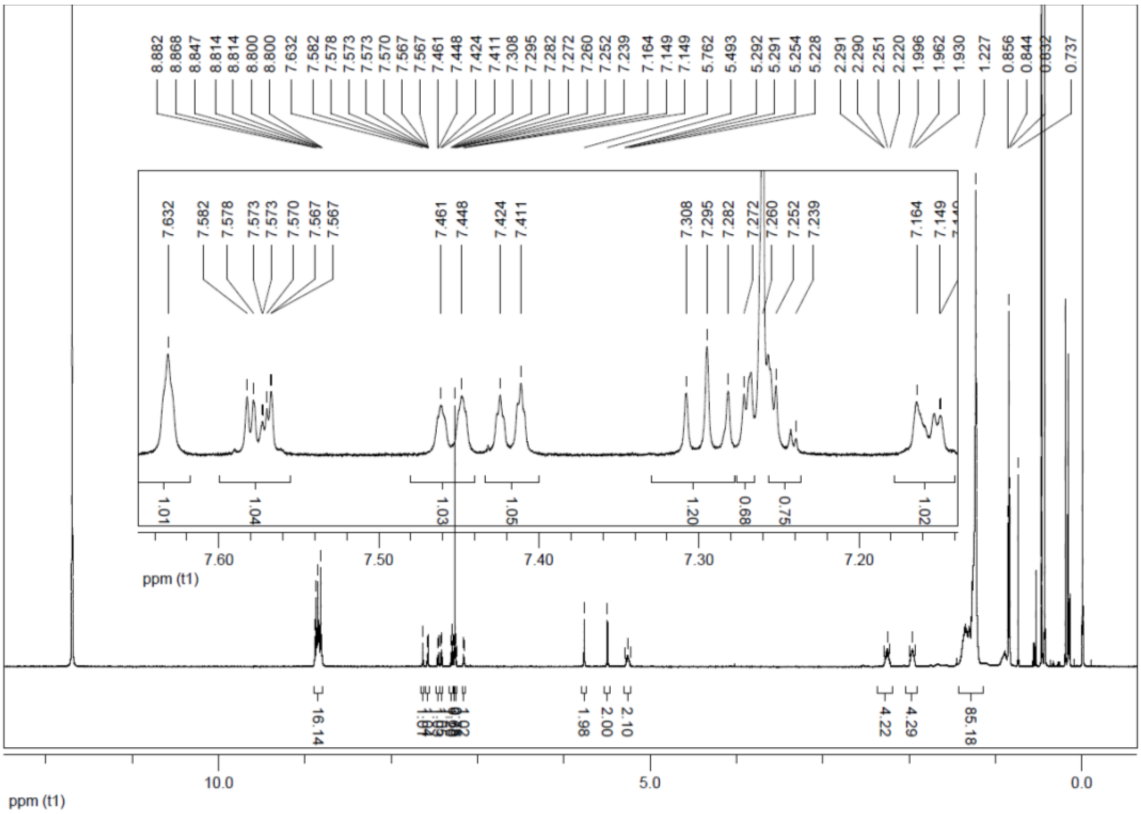

Figure S8. ^{1}H NMR spectrum of PBI dyad **7** in a solvent mixture of $CDCl_3/CF_3COOD$ (*v*:*v* = 4:3) recorded with 600 MHz NMR at 293 K.

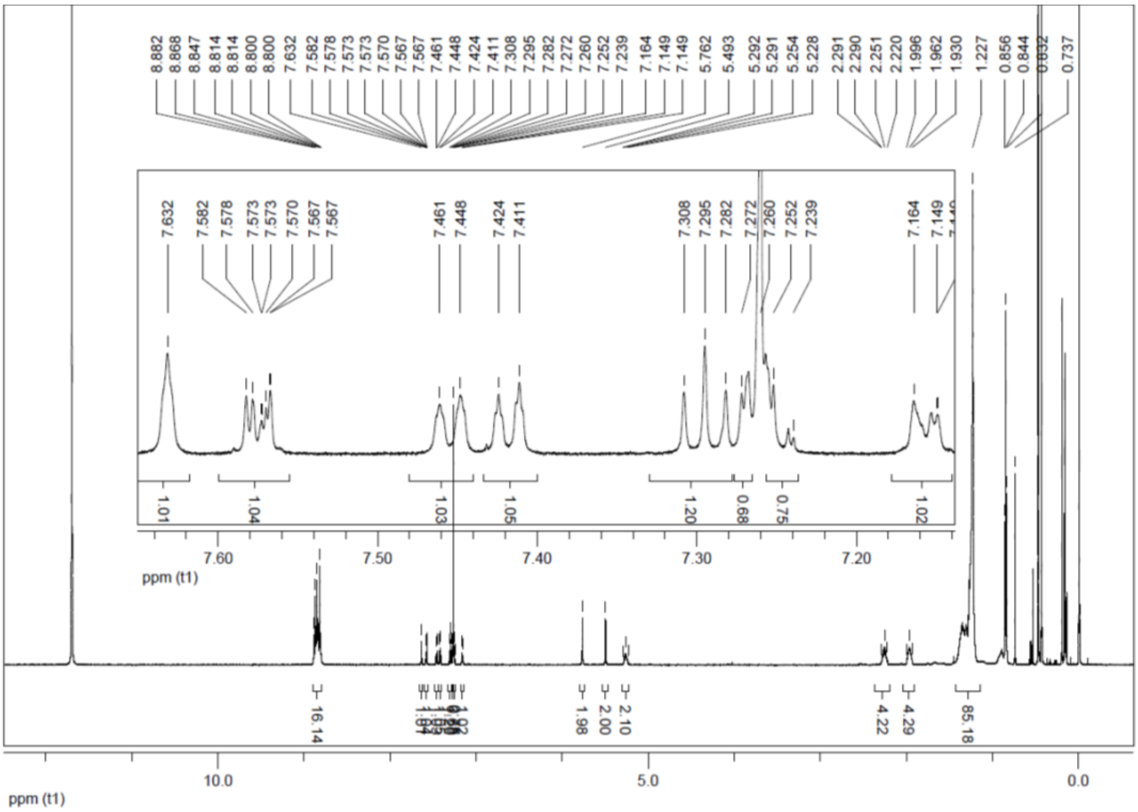

Figure S9. ^{1}H NMR spectrum of PBI dyad **8** in a solvent mixture of $CDCl_3/CF_3COOD$ (*v*:*v* = 1:1) recorded with 600 MHz NMR at 293 K.

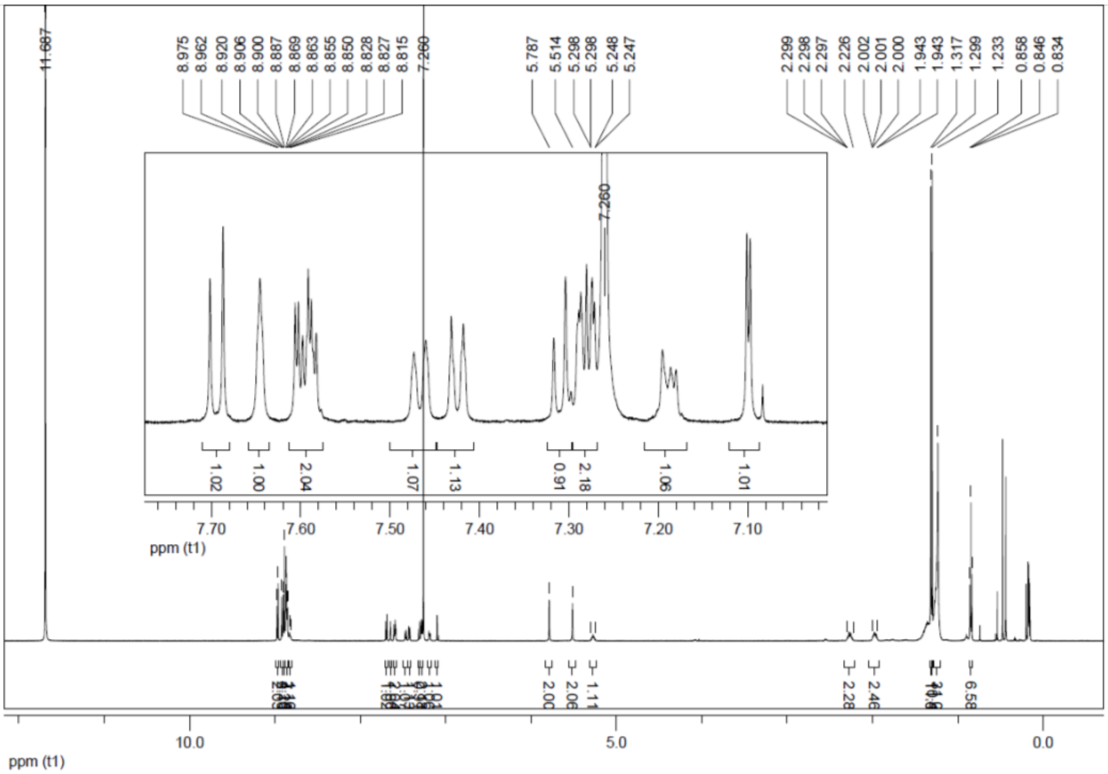

Figure S10. ^{1}H NMR spectrum of PBI dyad **9** in a solvent mixture of $CDCl_3/CF_3COOD$ (*v*:*v* = 1:1) recorded with 600 MHz NMR at 293 K.

Chapter 5

Perylene Bisimide Oligomer Stacks:

In-depth Understanding of the Backbone-directed PBI Self-assembly

Abstract: A perylene bisimide (PBI) dyad compound with two PBI units appended at the *m*-position of a diphenylbutadiyne (DPB) backbone was synthesized and characterized. The DPB backbone provides sufficient intramolecular space between the two PBI units to accommodate another two PBI units in between. Therefore, interdigitated oligomer formation with one-dimensional H-type PBI stacking can be envisioned. The formation of extended oligomer stacks for this PBI dyad was confirmed by MALDI-TOF mass spectrometry and DOSY NMR spectroscopy. From the concentration-dependent NMR experiments, the aggregation motif of PBI π-π-interactions and the backbone function of DPB moiety could be recognized. The UV/Vis and fluorescence studies indicated H-coupled columnar PBI π-stacks in the oligomer aggregates. Furthermore, by analyzing the whole range of concentration-dependent UV/Vis absorption changes using non-linear least-square analysis, cooperative aggregation behavior of this PBI dyad was elucidated. In addition, the activation energy of oligomer disassembly was determined by time-dependent absorption measurements at different temperatures. Thus, the energy diagram of the self-assembly-disassembly process of this PBI dyad is fully depicted.

5.1 Introduction

Backbone-supported self-assembly is a widely used method in supramolecular chemistry.[1] In nature, DNA strands self-order into the double helical structure supported by the backbone made of sugars and phosphate groups.[2] Similarly, foldable protein backbones organize chlorophyll dyes into efficient light harvesting complexes of purple bacteria.[3] To mimic and analyze the aggregate structure and functionalities of peptides, proteins and other natural biomacromolecules, researchers have synthesized and explored artificial foldamers,[4] helical polymers[5] and DNA-multichromophore systems[6]. However, the production of high-molecular-weight polymers that mimic the sophisticated aggregation of biomacromolecules in function remains far away to date. One difficulty is to understand the thermodynamics and kinetics of complex aggregation processes, which need the troublesome determination of energy levels of self-assembled products, intermediates and/or transition states. [4-5, 7]

In Chapter 4, we introduced PBI dyad **1** in which the two PBI units are appended at a diphenylacetylene (DPA) backbone to afford a intramolecular distance of 6.9 Å, exactly twice the space of PBI π-π-interaction. Consequently, the tweezer-like PBI dyad **1** is apt to self-assemble into interdigitated dimers. In a similar manner, by extending the intramolecular distance in a PBI dyad molecule to be triple the space for PBI π-π-interaction, "arm-in-arm" aggregation into extended PBI π-stacks can be anticipated.[8] According to molecular modeling studies, the spatial control for triple π-π-interactions can be achieved by attaching two PBI units at the *m*-positions of a diphenylbutadiyne (DPB) backbone (Figure 1).

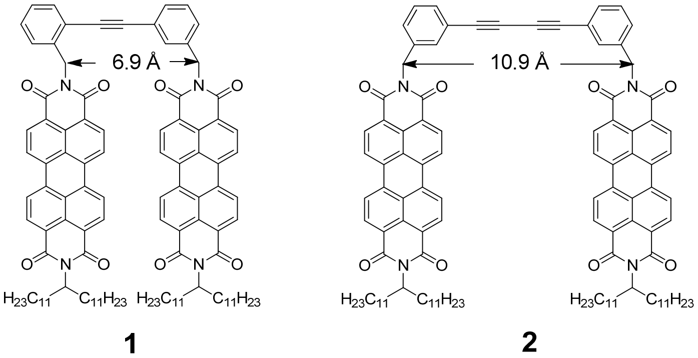

1 **2**

Figure 1. Molecular structure of PBI dyad **1** and **2**.

The oligomer formation of dyad **2** via PBI π-π-interactions into extended H-type columnar PBI π-stacks was elucidated by means of MALDI-TOF mass spectrometry, NMR, UV/Vis and fluorescence spectroscopic studies. Unlike the isodesmic aggregation of large π-conjugated dyes,[9] it was found that the backbone-directed PBI stacking exhibits cooperative aggregation behavior, leading to π-stacks of high kinetic stability. With great efforts, we have performed both thermodynamic and kinetic investigations to describe the full energy landscape of the cooperative self-assembly process of PBI dyad **2**.

5.2 Results and Discussion

5.2.1 Synthesis

The desired PBI dyad building block **2** was obtained according to the synthetic route outlined in Scheme 1. PBI **3**[10] was treated with trimethylsilylacetylene (TMSA) in the presence of Pd and Cu catalysts to quantitatively yield PBI **4**. After isolation by column chromatography to remove the inorganic catalyst, PBI **4** was subsequently converted into PBI **5** by desilylation with tetra-*n*-butylammonium fluoride (TBAF).[10] Cu-catalyzed Glaser homo-coupling of PBI **5** afforded the target PBI dyad **2** in high yield (90%).

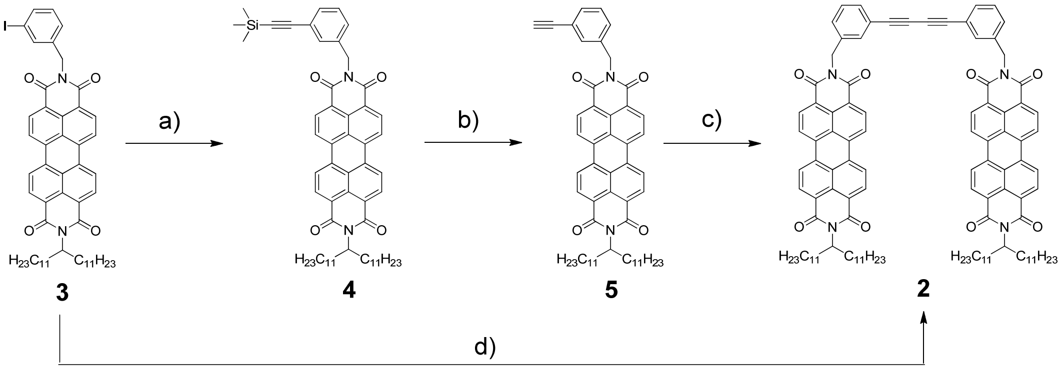

Scheme 1. Synthesis of dyad **2**: a) Trimethylsilylacetylene, $Pd(PPh_3)_2Cl_2$, CuI, CH_2Cl_2/NEt_3 (*v*:*v* = 3:1), 40 °C, 3 h, 100%. b) Tetra-*n*-butylammonium fluoride, THF, r.t., 10 min, 89%. c) $Pd(PPh_3)_2Cl_2$, CuI, THF/NH(*i*Pr)$_2$ (*v*:*v* = 5:1), 40 °C, 18 h, 90%. d) Trimethylsilylacetylene, $Pd(PPh_3)_2Cl_2$, CuI, CH_2Cl_2/NEt_3 (*v*:*v* = 3:1), 40 °C, 3 h; tetra-*n*-butylammonium fluoride, THF, r.t., 18 h, 70% over two steps.

This synthetic route was further improved by using a one-pot procedure, taking benefit of the similar conditions used for Sonogashira and Glaser couplings. After the reaction of PBI **3** with one equivalent of TMSA, TBAF was directly added into the reaction mixture under an air atmosphere. It was found that the main product purified from the reaction mixture by silica gel column is dyad **2** rather than PBI **5**. This fact indicates that the in-situ produced PBI **5** was instantaneously coupled to furnish dyad **2** owing to the presence of Cu catalyst in the reaction system.

PBI dyad **2** was purified by using recycling HPLC and fully characterized by ^{1}H and ^{13}C NMR spectroscopy, MALDI-TOF mass spectrometry and elemental analysis. The long swallow-tail-like long alkyl chains at imide positions provide good solubility of dyad **2** in chloroaliphatic solvents of intermediate polarity such as chloroform.[11] Despite the similar components and structure, dyad **2** shows better solubility than dyad **1** and can even achieve a certain solubility (less than 1 mM) in non-polar methylcyclohexane (MCH) that is known to facilitate aggregation.[12]

5.2.2 Determination of the Aggregate Size

First evidence for the self-assembly of PBI dyad **2** into oligomers was provided by MALDI-TOF mass spectrometry.[13] The sample used for mass spectrometry measurement was prepared by solvent evaporation from the solution of PBI dyad **2** (0.5 mM in MCH) using 2-[(2*E*)-3-(4-*tert*-butylphenyl)-2-methylprop-2-enylidene]malononitrile (DCTB) as a matrix. Besides the monomer peaks at an m/z value of 1652 confirming the molecular mass of dyad **2**, a series of signals spaced by the same molecular mass of 1652 can be clearly observed as shown in Figure 2.[14] Moreover, a careful analysis of the MALDI-TOF spectrum brings as many as 21 peaks to light, which can be ascribed to the formation of aggregates as large as 21-mer. Since the absorption and fluorescence spectra suggest that the existence of dyad **2** monomer in the applied sample solution is negligible (*vide infra*), the monomers, as well as small aggregates, detected by mass spectrometry should result from the partial fragmentation of large aggregates in the ion source on account of the laser energy and the weak π-π-interaction for dyad **2** aggregates.[15] In addition, high-mass ions are usually underestimated from MALDI spectra because of the mass-dependent desorption and detection characteristics of the mass spectrometry experiment.[16] These may be the reasons why exponentially decreasing signal intensities for larger species are detected in the mass spectrum, although large aggregates are the more abundant species in the sample solution.[16c]

In comparison, the MALDI-TOF mass spectrum of PBI dyad **1** showed only monomer and dimer peaks.[10] This can be attributed to the simple interdigitated dimer formation of PBI dyad **1** as the backbone-controlled intramolecular space can only accommodate one PBI unit. In contrast, two PBI units can insert into the extended intramolecular space in PBI dyad **2** and "arm-in-arm-like" aggregation of dyad **2** can therefore be expected.

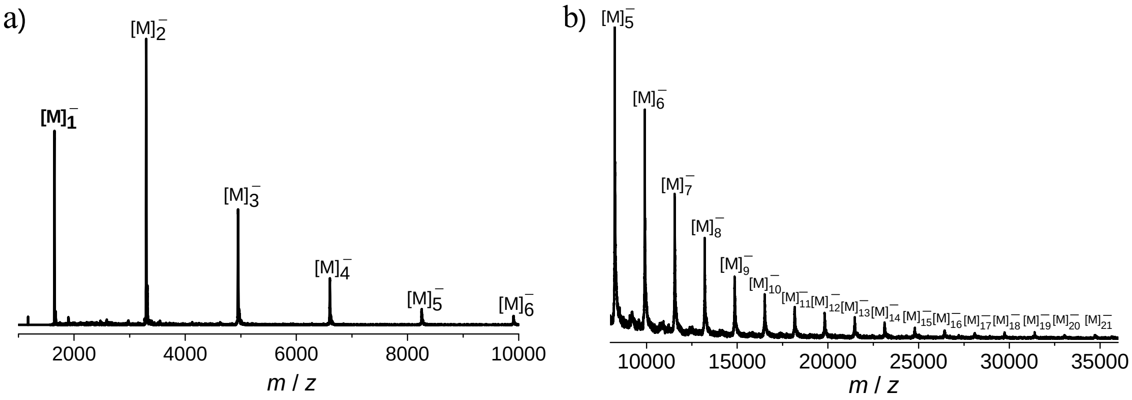

Figure 2. MALDI-TOF mass spectrum (linear mode) of PBI dyad **2**. The peaks corresponding to monomer and aggregate species are marked with $[M]_n^-$ ($n \geq 1$). a) and b) result from the same mass measurement. While a) shows the m/z range from 1000 to 10000, b) exhibits the m/z range from 10000 to 35000 with enlarged signal intensities.

To get first information on the aggregate size in solution, a diffusion ordered spectroscopy (DOSY) NMR experiment[17] was performed with the sample of PBI dyad **2** at a concentration of 0.5 mM in D_{14}-MCH. As demonstrated in Figure 3, the proton NMR spectrum has a complex resonance pattern and the corresponding translational diffusion coefficient D value is recorded to be 1.26×10^{-10} m^2 s^{-1}. Both findings are indicative for extended oligomer formation of dyad **2**.[18] Simplistically assuming all oligomers to be hydrodynamically spherical, the cube root of molecular weight of the aggregates is suggested to be proportional to D^{-1}.[19] Thus, with a reference compound which possesses a similar molecular mass and does not aggregate,[20] the average aggregate size can be estimated according to the equation $N_{\text{DOSY}} \approx (D_{\text{ref}} / D)^3$. By this method, the average aggregate size of dyad **2** in solution is calculated to be 20-mer, in good agreement with the mass spectrometric result.

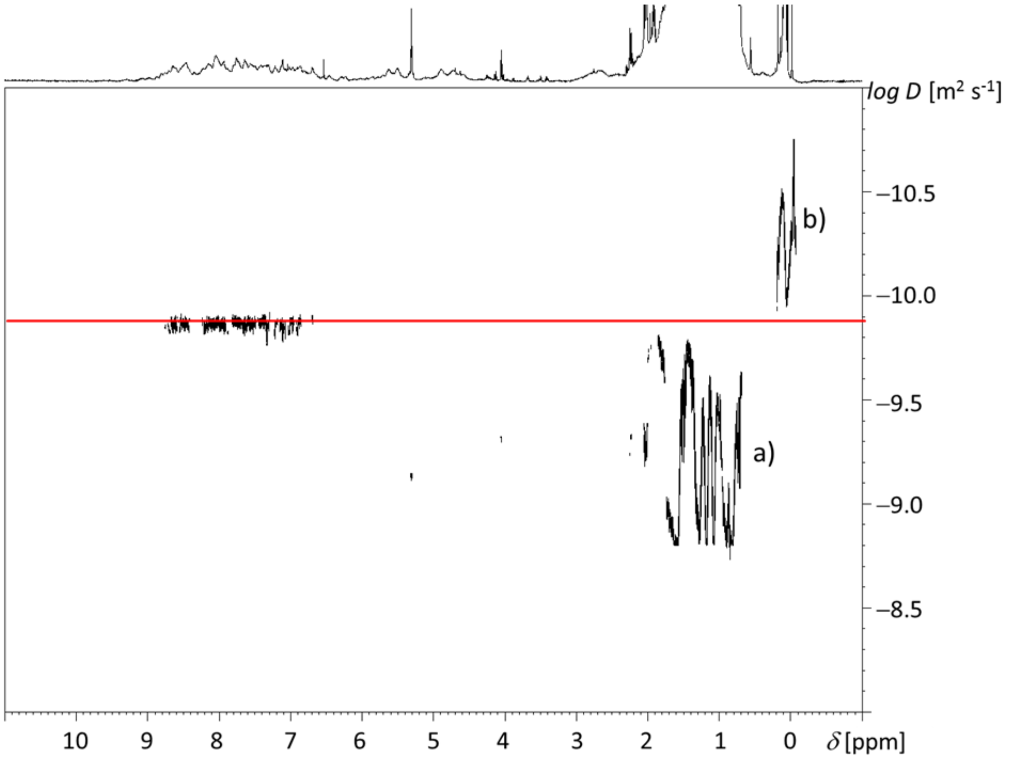

Figure 3. DOSY NMR spectrum of dyad **2** (0.5 mM in D_{14}-MCH, 600 MHz NMR, at 293 K). The diffusion coefficients D [m^2 s^{-1}] are plotted in a logarithmic scale against chemical shift δ [ppm]. Note: a) the signals for residual not deuterated solvent MCH and b) the signals for silicon grease.

5.2.3 Determination of the Aggregation Thermodynamics

The aggregation of PBI dyad **2** was firstly investigated by means of concentration-dependent ^{1}H NMR experiments in $CDCl_3$, in which case a single pattern of proton resonances is observed in terms of fast exchange between monomer and aggregate of dyad **2** on the NMR time scale. Figure 4 displays the distinct chemical shifts of protons of perylene core and DPB moiety. Upon increasing concentration, the resonances of perylene protons undergo a pronounced up-field shift, reflecting the π-π-interaction of PBI chromophores.[21] On the contrary, the chemical shifts of DPB moiety remain almost unaltered between 7.25 and 7.75 ppm. Accordingly, the DPB chromophores are not involved in π-stacking but reside on the periphery of PBI π-stacks, revealing the backbone function of DPB moiety upon the aggregation of PBI dyad **2**.

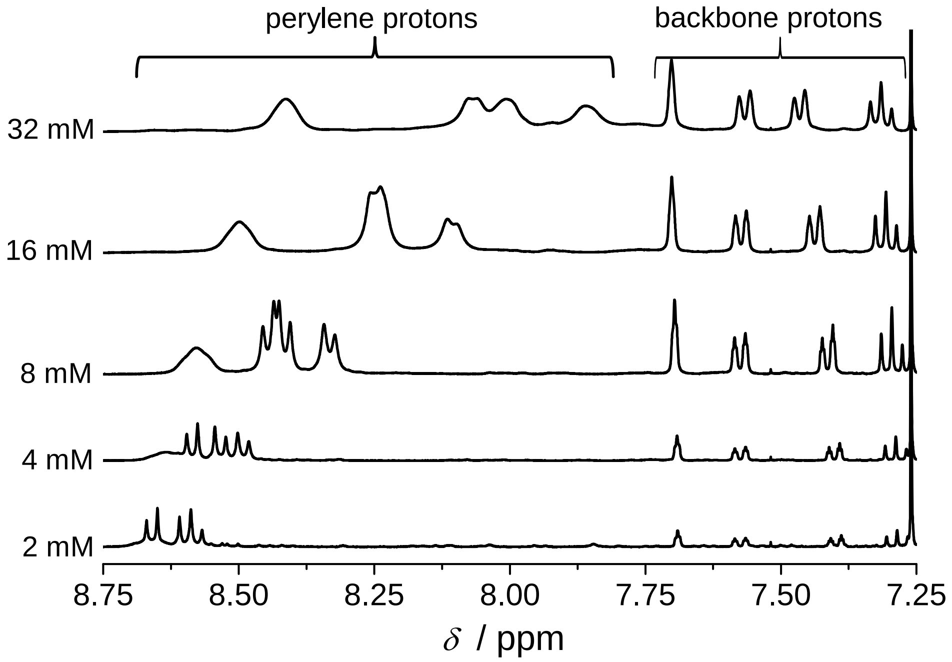

Figure 4. Aromatic part of concentration-dependent ^{1}H NMR spectra of PBI dyad **2** from 2 to 32 mM in $CDCl_3$ conducted with 400 MHz NMR at 293 K. The ppm ranges for perylene and DPB protons are marked on top.

Since the NMR experiments of PBI π-stacking suffer from either significant broadening or complex pattern of resonance signals, we have further studied the thermodynamics of aggregation behavior of dyad **2** by using concentration-dependent UV/Vis spectroscopy.[22] By modulating the binding strength in a suitable solvent mixture of "good" chloroform and "bad" MCH,[12] the whole aggregation process of dyad **2** from molecularly dissolved to fully stacked species was recorded in the concentration range from 5×10^{-7} to 2×10^{-4} M as shown in Figure 5. Herein, we chose the solvent mixture of $CHCl_3$/MCH (*v*:*v* = 3:7) as the best-suited solvent system for both the thermodynamic and kinetic studies (*vide infra*).[22]

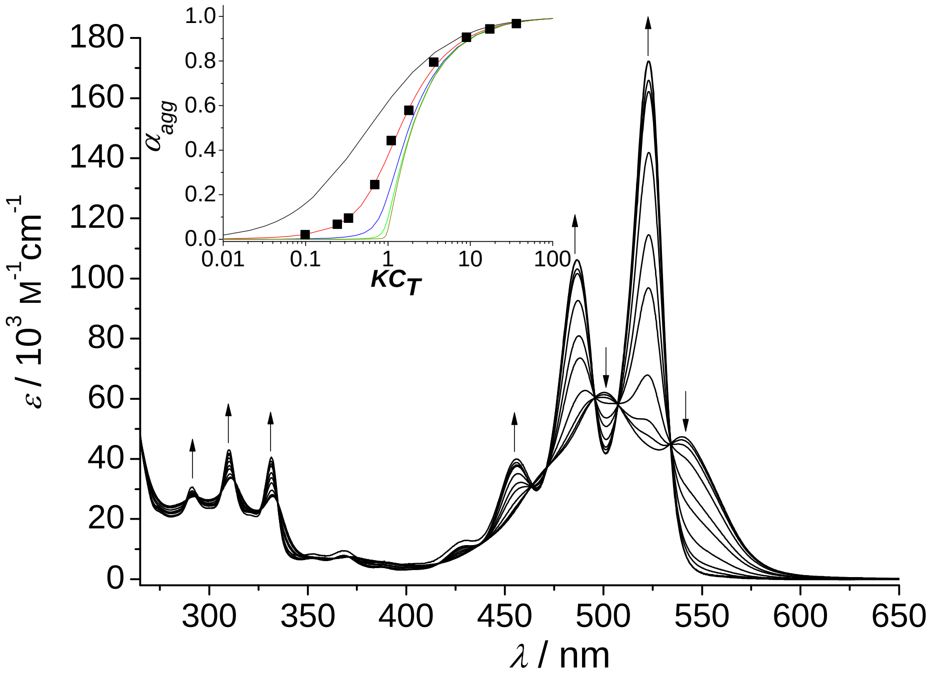

Figure 5. Concentration-dependent absorption spectra of dyad **2** from 5×10^{-7} to 2×10^{-4} M in $CHCl_3$/MCH (*v*:*v* = 3:7) recorded at 298 K. Each sample was kept at the given concentration for one week to reach the thermodynamic equilibrium (*vide infra*). Arrows indicate the spectral changes upon decreasing concentration. Inset: Fraction of aggregated molecules α_{agg} plotted as a function of Kc_T with different $\sigma = K_2/K$ values according to the cooperative model (lines from left to right: σ = 1 (black), 0.1 (red), 0.01 (blue), 0.001 (green) and 0.0001 (brown)), and plot of experimental absorption data of dyad **2** in $CHCl_3$/MCH (*v*:*v* = 3:7) at 528 nm.

In general, for the formation of extended PBI stacks from simple PBI monomers the isodesmic model can be applied.[9, 18] The concentration-dependent UV/Vis data for the self-assembly of dyad **2** suggest, however, the involvement of some cooperativity.[23] By employing the cooperative K_2–K model,[24] equilibrium constants of K_2 = 18000 M^{-1} for dimerization and K = 180000 M^{-1} for subsequent growth were evaluated (inset of Figure 5). According to the equation of $\Delta G° = -RT\ln K$, the Gibbs free energy of dyad **2** dimer and oligomer can be deduced from the corresponding binding constants to be $\Delta_D G° = -23.9$ kJ mol^{-1} and $\Delta G° = -29.5$ kJ mol^{-1}, respectively. In comparison, single PBI **5** shows only weak aggregation behavior in the solvent mixture of $CHCl_3$/MCH (*v*:*v* = 3:7) with a binding constant of 127 M^{-1} calculated in terms of the isodesmic model (Figure S1). Thus, at the highest concentration applied for PBI **2** (2×10^{-4} M), the aggregation degree of PBI **5** is only less than 5%, while dyad **2** prevails in a fully aggregated state (less than 4% of monomers).

Accordingly, based on the ^{1}H NMR and UV/Vis dilution experiments we can derive a conclusive picture for the aggregation process of dyad **2** as illustrated in Figure 6. The first step can be attributed to the formation of interdigitated dyad **2** dimers, analogous to the self-assembly of dyad **1**. Because of the improper intramolecular spacing in dyad **2**, however, these dimers are not as stable as those of dyad **1** and experience fast exchange with dyad **2** monomers in solution. Once the dimers of dyad **2** interlock with each other in an “arm-in-arm” way to give extended aggregates (on average as large as 20-mers in the given concentration range evidenced by DOSY NMR), the constructed oligomers exhibit considerable thermodynamic stability on account of the structural integration.

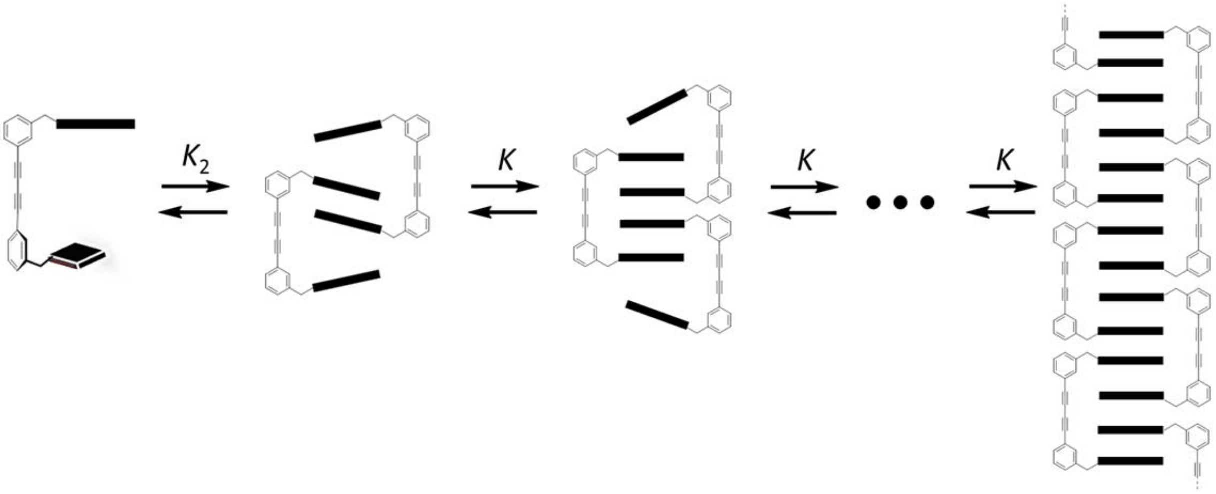

Figure 6. Schematic representation of the proposed aggregation behavior of PBI dyad **2**.

5.2.4 UV/Vis and Fluorescence Spectroscopic Studies

The optical properties of the aggregate were elucidated by absorption and emission spectroscopy at the demanded low concentrations in two extreme situations. Whereas dyad **2** is molecularly dissolved in ‘‘good’’ solvent chloroform at a low concentration, it forms stable aggregates in non-polar MCH even at a low concentration of 5.0×10^{-6} M (Figure 7 and Figure S2).

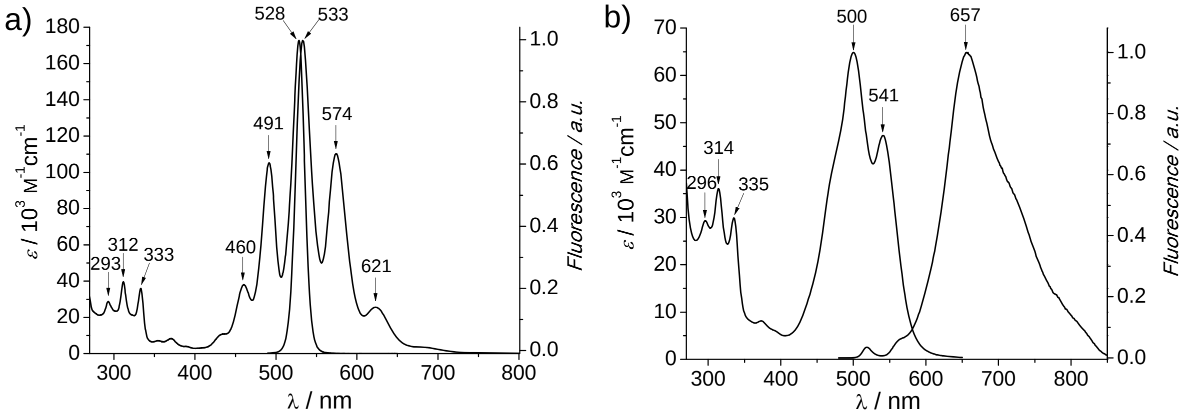

Figure 7. The UV/Vis absorption and normalized fluorescence (excited at 460 nm) spectra of a) dyad **2** monomer (at 1.0×10^{-6} M in $CHCl_3$) and b) dyad **2** aggregate (at 5.0×10^{-5} M in MCH) recorded at 298 K.

In the molecularly dissolved state at 10^{-6} M in $CHCl_3$, the UV/Vis und fluorescence spectra of dyad **2** display the characteristic well-resolved vibronic structure of a single PBI chromophore, which have a mirror-image relationship (Figure 7a). The vibronic 0→0 and 0→1 intensity ratio of $A^{0\rightarrow0}/A^{0\rightarrow1}$ is larger than 1.6, indicating the absence of either inter- or intramolecular excitonic coupling of PBI chromophores in dyad **2**.[16c, 25] This result confirms that the two PBI units within dyad **2** are fixed at large distance by the rigid DPB backbone. The three weak bands between 280 and 350 nm can be assigned to the absorption of the DPB chromophore,[26] which has no electronic communication with the PBI units owing to the interruption of conjugation by the methylene linkers.

In strong contrast, the PBI absorption maximum is hypsochromically shifted to 500 nm in the aggregate state of dyad **2**, accompanied with a weaker bathochromically shifted band at 541 nm and a shoulder around 470 nm (Figure 7b). Such a spectral profile results from the strong excitonic coupling of PBI chromophores and is typical for H-type columnar PBI stacking.[18, 27] However, unlike the broad emission observed for simple H-type columnar PBI stacks due to excimer formation,[18] dyad **2** aggregates show a relatively sharp fluorescence band with the maximum at 657 nm. Meanwhile, the monomer emission between 500 and 600 nm has almost vanished, pinpointing the almost complete aggregation of dyad **2** even at these low concentrations in MCH solvent. The emission profile resembles that of the dimer of dyad **1**, but the maximum is at longer wavelengths relative to the value of 602 nm for PBI **1** quadruple stacks.[10] Considering the large Stokes shift from 541 nm (lowest energy transition of absorption) to 657 nm (emission maximum) as well as the long fluorescence lifetime of 42.7 nm for dyad **2** aggregates (Figure 8) compared to PBI monomers (~ 3 ns),[18] a pronounced geometrical and energetic relaxation process into an excimer-type state appears to originals in photoexcited aggregates of dyad **2**.[16c, 28]

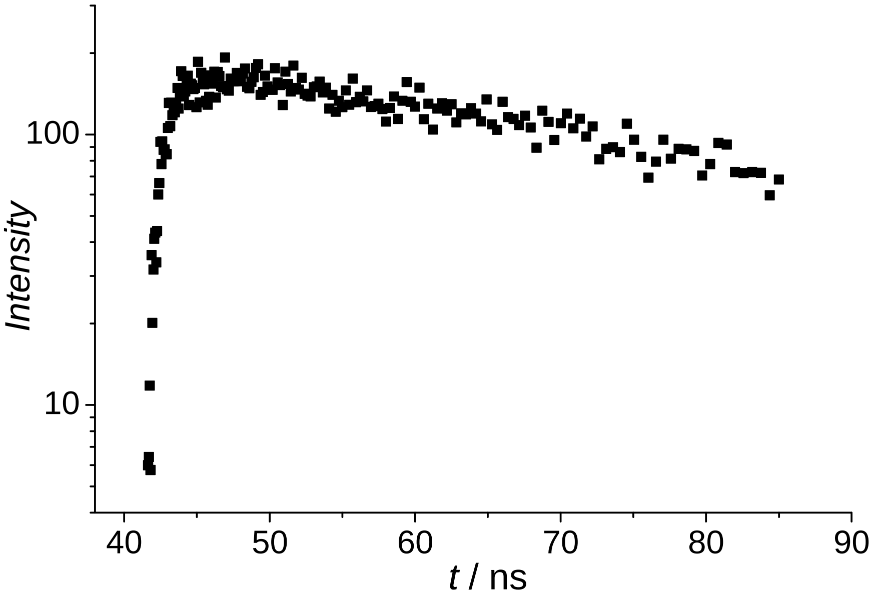

Figure 8. Fluorescence decay curve for dyad **2** aggregate band (detected at 660 nm) at a concentration of 5×10^{-6} M in MCH recorded at 298 K (one exponential, life time of 42.7 ns).

5.2.5 Kinetic Studies

During our studies on PBI dyad **2** self-assembly (*vide supra*), we noted increasing equilibration times with increasing MCH content. To quantify the activation energy of dyad **2** self-assembly/disassembly we carried out kinetic studies by means of time-dependent UV/Vis measurements.[10] Figure 9 shows the absorption variations with time upon dilution of a solution of dyad **2** aggregates[29] in the solvent mixture of $CHCl_3$/MCH (*v*:*v* = 3:7) by a factor of 400. In this solvent mixture, the time-dependent absorption changes can be conveniently recorded on conventional time scale and for suitable temperatures.[30]

In these experiments, the stock solution of dyad **2** in $CHCl_3$/MCH (*v*:*v* = 3:7) is 2×10^{-4} M, while after dilution the final solution of dyad **2** in $CHCl_3$/MCH (*v*:*v* = 3:7) is 5×10^{-7} M. At this dilution the thermodynamically equilibrated state for dyad **2** is the molecularly dissolved molecules as shown before. The disassembly process can be appreciated from the gradual absorption transition from aggregate to monomer of dyad **2**. Even though the thermodynamic studies demonstrated the cooperative self-assembly of dyad **2** over dimer formation, the occurrence of the dimers and/or other intermediates should be negligible in our kinetic measurements since there are several well-defined isosbestic points during the entire absorption changes. This indicates only two species are involved, namely the large oligomer and monomer of dyad **2**.

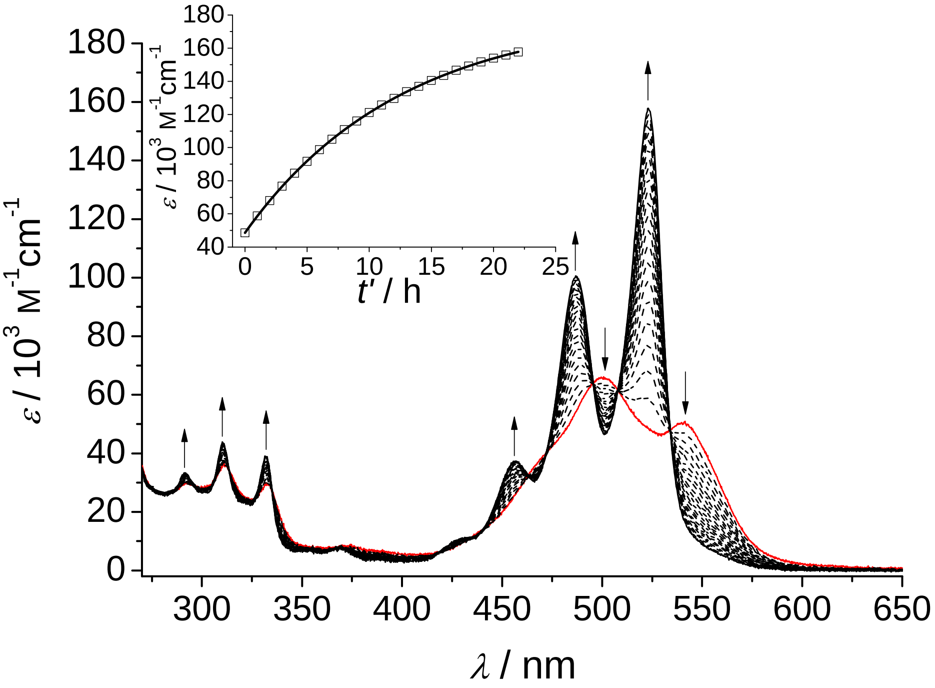

Figure 9. Absorption spectral variations recorded at a time interval of 60 min for 22 h when 7.5 μL of dyad **2** stock solution at 2×10^{-4} M in $CHCl_3$/MCH (*v*:*v* = 3:7) was added into 3 mL of $CHCl_3$/MCH (*v*:*v* = 3:7) solvent at 298 K. The initial aggregate spectrum is highlighted in red color. Arrows indicate the absorption changes with time. Inset: a plot of the absorbance at 523 nm versus time and the best fitting to a simple exponential equation.

Assuming the concentration of dyad **2** is a and dyad **2** forms uniform n-mers in the system, the n-mer concentration $c_{\mathrm{M_n}}(0)$ at time t = 0 hours is equal to a/n. After a time interval of t hours, the n-mer concentration $c_{\mathrm{M_n}}(t)$ changes to $(a/n - x)$ and the monomer concentration is accordingly $c_{\mathrm{M}}(t) = nx$.

$$\mathrm{M_n} \xrightarrow{k_1} \mathrm{nM}$$

$$t = 0 \qquad c_{\mathrm{M_n}}(0) = a/n \qquad c_{\mathrm{M}}(0) = 0$$

$$t = t \qquad c_{\mathrm{M_n}}(t) = a/n - x \qquad c_{\mathrm{M}}(t) = nx$$

During this set of absorption experiments, the ensemble absorption $A(t)$ measured at time t is the summation of the n-mer and monomer absorption of dyad **2** in the system and can therefore be expressed as a single function of the x value, where the ε_{M_n} and ε_M are the extinction coefficients of n-mer and monomer of dyad **2**, d is the cuvette length of 1 cm.

$$A(t) = \varepsilon_{M_n} \cdot d \cdot (a/n - x) + \varepsilon_M \cdot d \cdot nx \qquad (1)$$

Consequently, the ensemble extinction coefficient $\varepsilon(t)$ can be written as

$$\varepsilon(t) = \frac{A(t)}{d \cdot a} = \varepsilon_{M_n} \cdot (1/n - x/a) + \varepsilon_M nx/a \qquad (2)$$

Providing that the disassembly of dyad **2** is regarded as a first-order reaction, the concentration variation x can be expressed as an exponential function of time t, where k_1 is the disassembly rate constant from dyad **2** n-mers to monomers.

$$x = a/n - ae^{-k_1 t}/n \qquad (3)$$

Taking equation (3) into equation (2), the ensemble extinction coefficient $\varepsilon(t)$ can be rewritten as an exponential function of time t:

$$\varepsilon(t) = \varepsilon_{M_n} e^{-k_1 t}/n + \varepsilon_M(1 - e^{-k_1 t}) = \varepsilon_M + \left(\frac{\varepsilon_{M_n}}{n} - \varepsilon_M\right) e^{-k_1 t} \qquad (4)$$

Considering a dead time of $t^0 = t - t'$ between the ideal time t and recorded time t' and set a constant value $C = \left(\frac{\varepsilon_{M_n}}{n} - \varepsilon_M\right) e^{-k_1 t^0}$, we can get:

$$\varepsilon(t') = \varepsilon_M + \left(\frac{\varepsilon_{M_n}}{n} - \varepsilon_M\right) e^{-k_1 t^0} \cdot e^{-k_1 t'} = \varepsilon_M + C \cdot e^{-k_1 t'} \qquad (5)$$

Fitting the measured absorption coefficient $\varepsilon(t')$ values at 523 nm against the measured time t' gives exactly an exponential function (inset of Figure 9), confirming the assumption of first-order disassembly of dyad **2** oligomers into monomers. The rate constant k_1 of the disassembly process is deduced to be 0.08 h^{-1}, giving rise to a corresponding half time of $t_{1/2}$ = 8.66 h at the given temperature of 25 °C.

At different temperatures, the same kinetic experiments were repeated. As expected the rate constant of the disassembly process increases with temperature. According to the Eyring-Polanyi equation that gives a quantitative dependence of the rate constant k on the absolute temperature T:

$$\ln\frac{k}{T} = -\frac{\Delta H^{\neq}}{R} \cdot \frac{1}{T} + (\ln\frac{k_B}{h} + \frac{\Delta S^{\neq}}{R}) \qquad (6)$$

where R is gas constant, k_B is Boltzmann constant and h is Planck's constant, the $\ln(k_1/T)$ values against $1/T$ were fitted to give a linear relationship (Figure 10). Thus, for the disassembly process a Gibbs energy of activation $\Delta G^{\neq}$ = 79.2±2.3 kJ mol^{-1} and an activation energy Ea = 97.9±2.3 kJ mol^{-1} of dyad **2** oligomer in CHCl$_3$/MCH (v:v = 3:7) at room temperature were calculated in terms of the equations (7) and (8), respectively.

$$\Delta G^{\neq} = \Delta H^{\neq} - T\Delta S^{\neq} \qquad (7)$$

$$E_a = \Delta H^{\neq} + RT \qquad (8)$$

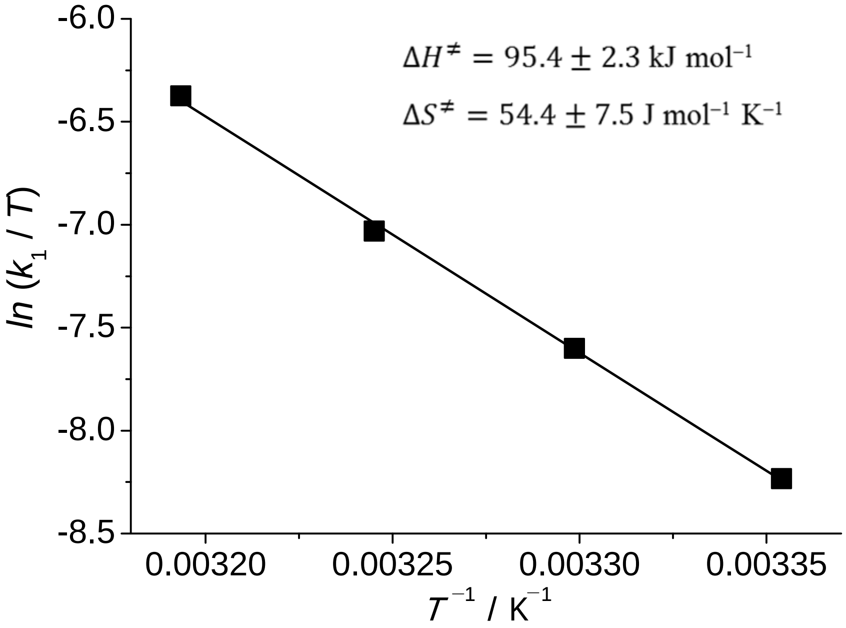

Figure 10. Eyring plot for the temperature dependence of the disassembly rate constant k_1 of dyad **2** oligomers in CHCl$_3$/MCH (v:v = 3:7).

From both thermodynamic and kinetic studies we can now describe the full energy landscape of the self-assembly-disassembly process of dyad **2** in a solvent mixture of CHCl$_3$/MCH (v:v = 3:7) (Figure 11). In the former thermodynamic studies, the Gibbs dimerization energy $\Delta_D G°$ and the Gibbs free energy $\Delta G°$ for further aggregation of dyad **2** were deduced from the corresponding binding constants K_2 and K to be –23.9 kJ mol^{-1} and –29.5 kJ mol^{-1}, respectively. In the kinetic studies, the dissociation of dyad **2** aggregates has been accomplished only by dilution. Thus, the gain in entropy upon dilution afforded the required thermodynamic driving force for a reaction that would be strongly endothermic at standard conditions (i.e. 1 M concentration). To reach the new state of equilibrium, however, dyad **2** aggregates had to overcome an energy barrier $\Delta G^{\neq}$ of ~ 80 kJ mol^{-1} for disassembly at room temperature. In similarity to the cooperative aggregate growth revealed by thermodynamic studies, the dissociation of dyad **2** aggregates are also "cooperative" since the disassembly follows a first-order kinetics and no intermediates such as dyad **2** dimers can be detected. Thus, the Gibbs activation energy $\Delta_{\mathrm{D}}G^{\neq}$ for dimer dissociation should be much smaller than the energy barrier $\Delta_{\mathrm{D}}G^{\neq}$ for disassembly of larger aggregates of dyad **2**. This finding can be attributed to the tight (≈ 3.5 Å) tweezer-type PBI stacking within dyad **2** aggregates larger than dimers. Obviously this tight π-π-stacking imposes some sterical constraints that need to be overcome in the dissociation process, leading to a substantial Gibbs activation energy.

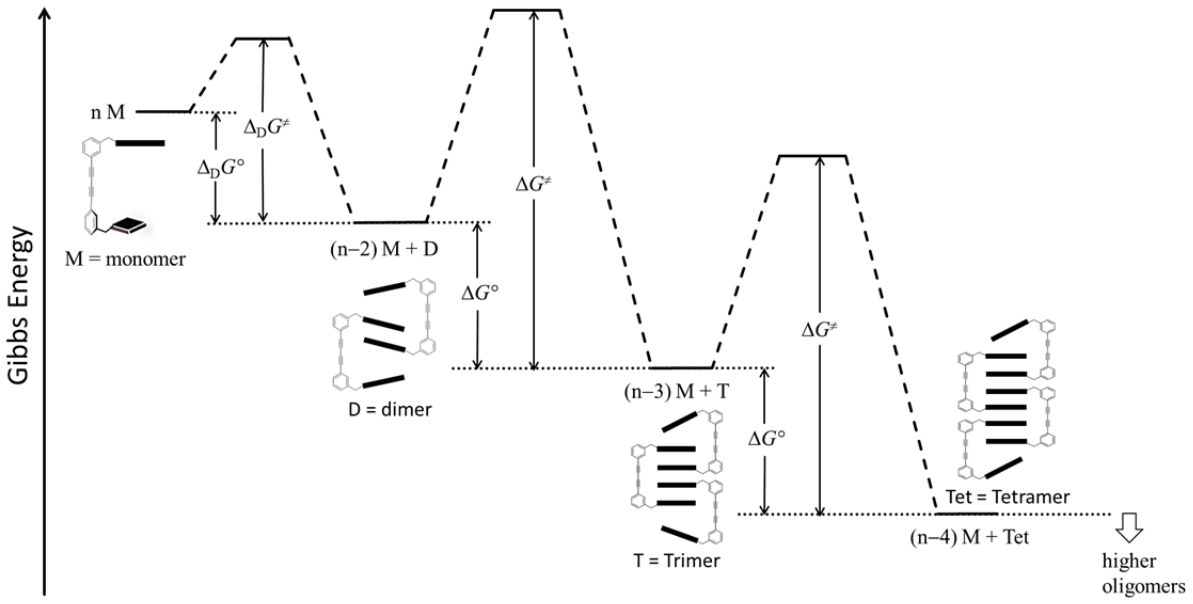

Figure 11. Energy landscape of self-assembly-disassembly process of dyad **2** in a solvent mixture of $CHCl_3$/MCH (v:v = 3:7) at room temperature. $\Delta_{\mathrm{D}}G°$ and $\Delta G°$ were deduced from the corresponding binding constants K_2 and K to be –23.9 kJ mol^{-1} and –29.5 kJ mol^{-1}, respectively. $\Delta G^{\neq}$ of 79.2 kJ mol^{-1} was determined in terms of the Eyring-Polanyi equation. M, D, T and Tet are the abbreviation of monomer, dimer, trimer and tetramer, respectively.

Most likely, the self-assembly-disassembly process takes place stepwise via the two terminal sides of dyad **2** aggregates on account of the less tightly bound outer PBI tweezer unit. According to this model the even less tightly bound dimer nucleus may be considered as being formed in a pre-equilibrium process that is characterized by a smaller Gibbs activation energy. In this regard the kinetic model for the formation of extended PBI stacks closely resembles to established models in covalent organic chemistry. The most notable difference is the very large entropic contribution $\Delta S^{\neq}$ (+54 J mol^{-1} K^{-1}) owing to the pronounced increase of particle number upon disassembly.

5.3 Conclusions

In this chapter, we described the formation of extended PBI oligomer π-stacks by DPB backbone-directed aggregation of PBI dyad **2**. MALDI-TOF mass spectrometry provided first evidence for stable π-aggregates up to 21-mers, however, with exponentially decreased signal intensities. The concentration-dependent ^{1}H NMR verified the aggregation motif of dyad **2** is based on the interdigitated PBI π-π-stacking. The oligomer stacks of PBI dyad **2** exhibits not only high thermodynamic but also high kinetic stability. The activation energy for the disassembly of PBI dyad **2** oligomer in a solvent mixture of $CHCl_3$/MCH (v:v = 3:7) was determined to be 97.9±2.3 kJ mol^{-1}. Accordingly, the energy landscape of self-assembly-disassembly process of dyad **2** can be described which provides in-depth understanding of backbone-directed PBI self-assembly process. By considering the kinetic stability and long fluorescence lifetime, the backbone-directed PBI π-stacks should possess improved mechanical and energy transfer properties compared to PBI π-stacks composed of simple PBIs,[18] which deserves further investigation for light-harvesting and charge transport applications.

5.4 Experimental Section

All solvents and reagents were purchased from commercial sources and used as received without further purification, unless otherwise stated. Dry solvents were purified according to literature procedures.[31] PBI **3** and PBI **5** were synthesized as described in Chapter 4. Thin layer chromatography (TLC) was conducted on aluminum plates coated with silica gel (60 F_{254}, Merck). Column chromatography was performed using silica gel (Geduran Si 60 from Merck, particle size 0.040–0.063 mm) as stationary phase. Recycling preparative HPLC was performed on a system (JAI LC-9105) equipped with a photodiode array UV/Vis detector (JAI 3702) and an RI detector (JAI RI-7s) by use of a semi-preparative NUCLEOSIL 100−5 NO_2 column (Macherey&Nagel). For HPLC separation, HPLC grade solvents ($CHCl_3$ and MeOH) from VWR (Darmstadt, Germany) were used. MALDI-TOF measurements were carried out on a Bruker Autoflex II by using a nitrogen laser (337.1 nm). The melting points were measured by using Olympus BX-41 polarization microscope equipped with a Linkam THMS 600 hot stage and a temperature controller unit.

UV/Vis and Fuorescence Studies. The UV/Vis absorption measurements were performed on a Perkin Elmer Lambda 40 spectrometer making use of conventional quartz cells with 0.01−100 mm path length to cover a large concentration range. The slit width and the scan speed were set to be 1.0 nm and 240 nm/min, respectively. The temperature was controlled with a PTP-1+1 Peltier Temperature Programmer (PerkinElmer). The fluorescence studies were conducted on a PTI QM-4/2003 spectrofluorometer. The fluorescence spectra were corrected against photomultiplier and lamp intensity. The solvents for absorption and fluorescence measurements were of spectroscopic grade und used as received. The fluorescence yield was measured according to the literature procedure with the *N*,*N'*-bis(2,5-di-*tert*-butylphenyl)-3,4:9,10- tetracarboxylic acid bisimide (Φ_{fl} = 0.99 in chloroform) as standard.[32]

NMR Spectroscopic Studies. ^1H and ^{13}C NMR spectra were recorded in standard 5 mm NMR tubes on a Bruker Avance 400 and/or a Bruker DMX 600 spectrometer with TMS or residual undeuterated solvents as internal standard (7.26 ppm for $C\mathit{H}Cl_3$ and 77.00 ppm for $\mathit{C}DCl_3$). The 2D DOSY data were acquired with the 600 MHz instrument which is equipped with a 5 mm $^{13}C/^1H$ cryoprobe with z axis gradient coil capable of producing pulsed magnetic field gradients of 55 G/cm. In the DOSY experiments, the suppression of flow effects owing to temperature gradients in the coil of the cryoprobe was achieved in two different ways: (i) using the stimulated echo BPP-LED pulse sequence[33] (longitudinal eddy current delay sequence with bipolar gradient pulse pairs for diffusion and additional spoil gradients after the second and fourth 90° pulse) in which convection in the z direction was suppressed by sample rotation[34] and (ii) by the corresponding double stimulated echo pulse sequence[35] (without sample rotation and with spoil gradients after the second, fourth and sixth 90° pulse) in which the double stimulated echo results in a compensation of the flow effects. The following acquisition parameters were used for both methods: duration δ of a bipolar gradient pulse 10.8 ms, diffusion time Δ 50 ms, eddy current delay 5 ms. The diffusion time Δ was kept constant in each DOSY experiment while the sinusoidal diffusion gradients were incremented from 2% to 95% of maximum gradient strength in 32 linear steps. The DOSY spectra were calculated using the Bruker software Topspin. For this purpose, a Levenberg-Marquardt algorithm was used for one-component fittings of the dependence of the signal intensities on the gradient strength for each data point in the ^{1}H spectrum according to standard equations.[36] In addition, identical fittings for the individual ^{1}H signals were performed to judge the quality of the DOSY spectrum.

PBI Dyad 2:

Method 1: A mixture of *N*-(3-ethynylbenzyl)-*N*'-(12-tricosanyl)perylene-3,4:9,10-tetracarboxylic acid bisimide **5** (21 mg, 25 μmol), bis(triphenylphosphine)palladium(II) dichloride (4 mg), copper iodide (4 mg) in THF/NH(*i*Pr)$_2$ (*v*:*v* = 5:1, 4 mL) was stirred at 40 °C under an air atmosphere for 18 h. The reaction was then quenched with MeOH (20 mL). The precipitate was filtered and washed sequentially with 2.0 M HCl, H_2O and MeOH (3×20 mL). The crude product was dried in vacuum overnight and purified by column chromatography on silica gel with CH_2Cl_2 as eluent. Yield: 18 mg (11 μmol, 90%) as a red solid.

Method 2: To a mixture of *N*-(3-Iodobenzyl)-*N'*-(12-tricosanyl)perylene-3,4:9,10-tetracarboxylic acid bisimide **3** (93 mg, 0.1 mmol), bis(triphenylphosphine)palladium(II) dichloride (4 mg) and copper iodide (2 mg) in degassed CH_2Cl_2/NEt_3 (*v*:*v* = 3:1, 10 mL), trimethylsilylacetylene (10 mg, 0.1 mmol) was added under an argon atmosphere. The successful start of the reaction can be monitored by the increase of turbidity of the reaction mixture, which was stirred at 40 ^{o}C for 3 h. After that, 0.2 mL of tetra-*n*-butylammonium fluoride solution (1.0 M in THF) was added into the reaction vessel and stirred under an air atmosphere for 18 h. The reaction was then quenched with 20 mL of MeOH and the resulting precipitate was separated by filtration. After drying in vacuum, the crude product was firstly purified by silica gel chromatography with CH_2Cl_2 as eluent, followed by means of recycling preparative HPLC with $CHCl_3$ as eluent. Finally, the product was concentrated in $CHCl_3$ and precipitated by adding MeOH solvent. Yield: 58 mg (0.04 mmol, 70%) as a red solid.

TLC ($CHCl_3$) $R_f = 0.20$. M.p. 192−193 °C. ^{1}H NMR (400 MHz, $CDCl_3$): δ 8.26−8.56 (m, 16H, perylene protons), 7.70 (s, 2H, ph-*H*), 7.58 (d, *J* = 8.0 Hz, 2H, ph-*H*), 7.42 (d, *J* = 8.0 Hz, 2H, ph-*H*), 7.30 (t, *J* = 8.0 Hz, 2H, ph-*H*), 5.29 (s, 4H, NCH_2), 5.14−5.21 (m, 2H, $NCH(CH_2)_2$), 2.20−2.28 (m, 4H, $NCH(CH_2)_2$), 1.85−1.94 (m, 4H, $NCH(CH_2)_2$), 1.19 (br s, 72H, alkyl-*H*), 0.83 (t, *J* = 7.0 Hz, 12H, CH_2CH_3). ^{13}C NMR (100 MHz, $CDCl_3$): δ 162.99, 137.47, 134.55, 133.89, 133.03, 131.77, 131.33, 130.91, 130.29, 129.32, 129.09, 128.65, 126.07, 126.02, 122.99, 122.70, 121.95, 81.62, 74.18, 54.86, 43.17, 32.37, 31.89, 29.61, 29.60, 29.56, 29.31, 27.02, 22.65, 14.08. MS (MALDI-TOF, Matrix DCTB): calcd for $C_{112}H_{122}N_4O_8$ $[M]^-$ 1651.930; found 1651.923 (Due to the bad solubility in acetonitrile, no ESI-HRMS could be recorded). Anal. calcd for $C_{112}H_{122}N_4O_8$: C, 81.42; H, 7.44; N, 3.39; found: C, 81.15; H, 7.60; N, 3.62.

5.5 References and Notes

[1] a) L. Brunsveld, B. J. B. Folmer, E. W. Meijer, R. P. Sijbesma, *Chem. Rev.* **2001**, *101*, 4071-4098; b) F. J. M. Hoeben, P. Jonkheijm, E. W. Meijer, A. P. H. J. Schenning, *Chem. Rev.* **2005**, *105*, 1491-1546; c) J. K. Klosterman, Y. Yamauchi, M. Fujita, *Chem. Soc. Rev.* **2009**, *38*, 1714-1725.

[2] J. D. Watson, F. H. C. Crick, *Nature* **1953**, *171*, 737-738.

[3] a) G. McDermott, S. M. Prince, A. A. Freer, A. M. Hawthornthwaite-Lawless, M. Z. Papiz, R. J. Cogdell, N. W. Isaacs, *Nature* **1995**, *374*, 517-521; b) T. Pullerits, V. Sundström, *Acc. Chem. Res.* **1996**, *29*, 381-389; c) X. Hu, T. Ritz, A. Damjanovic, F. Autenrieth, K. Schulten, *Q. Rev. Biophys.* **2002**, *35*, 1-62

[4] D. J. Hill, M. J. Mio, R. B. Prince, T. S. Hughes, J. S. Moore, *Chem. Rev.* **2001**, *101*, 3893-4012.

[5] E. Yashima, K. Maeda, H. Iida, Y. Furusho, K. Nagai, *Chem. Rev.* **2009**, *109*, 6102-6211.

[6] Y. N. Teo, E. T. Kool, *Chem. Rev.* **2012**, DOI: 10.1021/cr100351g.

[7] a) D. Thirumalai, G. Reddy, *Nat. Chem.* **2011**, *3*, 910-911; b) P. A. Korevaar, S. J. George, A. J. Markvoort, M. M. J. Smulders, P. A. J. Hilbers, A. P. H. J. Schenning, T. F. A. De Greef, E. W. Meijer, *Nature* **2012**, *481*, 492-496; c) T. F. A. de Greef, G. B.

W. L. Ligthart, M. Lutz, A. L. Spek, E. W. Meijer, R. P. Sijbesma, *J. Am. Chem. Soc.* **2008**, *130*, 5479-5486.

[8] a) M. Yoshizawa, J. Nakagawa, K. Kumazawa, M. Nagao, M. Kawano, T. Ozeki, M. Fujita, *Angew. Chem. Int. Ed.* **2005**, *44*, 1810-1813; b) T. Murase, K. Otsuka, M. Fujita, *J. Am. Chem. Soc.* **2010**, *132*, 7864-7865.

[9] Z. Chen, A. Lohr, C. R. Saha-Möller, F. Würthner, *Chem. Soc. Rev.* **2009**, *38*, 564-584.

[10] *See Chapter 4*.

[11] S. Demmig, H. Langhals, *Chem. Ber.* **1988**, *121*, 225-230.

[12] Z. Chen, B. Fimmel, F. Würthner, *Org. Biomol. Chem.* **2012**, *10*, 5845–5855.

[13] For the application of mass spectrometer in supramelcular chemistry, see: a) B. Baytekin, H. T. Baytekin, C. A. Schalley, *Org. Biomol. Chem.* **2006**, *4*, 2825-2841; b) C. A. Schalley, *Int. J. Mass. Spectrom.* **2000**, *194*, 11-39.

[14] For the application of MALDI-TOF mass spectrometer to determine the pi-stacked aggregate formation, see: a) G. Fernández, E. M. Pérez, L. Sánchez, N. Martín, *J. Am. Chem. Soc.* **2008**, *130*, 2410-2411; b) G. Fernández, L. Sánchez, E. M. Pérez, N. Martín, *J. Am. Chem. Soc.* **2008**, *130*, 10674-10683; c) P. D. Frischmann, S. Guieu, R. Tabeshi, M. J. MacLachlan, *J. Am. Chem. Soc.* **2010**, *132*, 7668-7675; d) K. A. Jolliffe, M. C. Calama, R. Fokkens, N. M. M. Nibbering, P. Timmerman, D. N. Reinhoudt, *Angew. Chem. Int. Ed.* **1998**, *37*, 1247-1251; e) A. Lohr, S. Uemura, F. Würthner, *Angew. Chem. Int. Ed.* **2009**, *48*, 6165-6168; f) A. n. Molina-Ontoria, G. Fernández, M. Wielopolski, C. Atienza, L. Sánchez, A. Gouloumis, T. Clark, N. Martín, D. M. Guldi, *J. Am. Chem. Soc.* **2009**, *131*, 12218-12229; g) T. van der Boom, R. T. Hayes, Y. Zhao, P. J. Bushard, E. A. Weiss, M. R. Wasielewski, *J. Am. Chem. Soc.* **2002**, *124*, 9582-9590.

[15] a) K. Dreisewerd, S. Berkenkamp, A. Leisner, A. Rohlfing, C. Menzel, *Int. J. Mass. Spectrom.* **2003**, *226*, 189-209; b) R. Zenobi, R. Knochenmuss, *Mass. Spectrom. Rev.* **1998**, *17*, 337-366.

[16] a) R. Arakawa, S. Watanabe, T. Fukuo, *Rapid Commun. Mass. Spectrom.* **1999**, *13*, 1059-1062; b) M. W. F. Nielen, S. Malucha, *Rapid Commun. Mass. Spectrom.* **1997**, *11*, 1194-1204; c) V. Dehm, M. Buchner, J. Seibt, V. Engel, F. Würthner, *Chem. Sci.* **2011**, *2*, 2094-2100.

[17] Y. Cohen, L. Avram, L. Frish, *Angew. Chem. Int. Ed.* **2005**, *44*, 520-554.

[18] Z. Chen, V. Stepanenko, V. Dehm, P. Prins, L. D. A. Siebbeles, J. Seibt, P. Marquetand, V. Engel, F. Würthner, *Chem. Eur. J.* **2007**, *13*, 436-449.

[19] B. C. Burdett, Studies in Physical and Theoretical Chemistry, 1983, 26, 241-270.

[20] The reference compound used is *N*,*N'*-di(2,6-bis(1-methylethyl)phenyl)-1,6,7,12-tetra(4-(1,1,3,3-tetramethylbutyl)phenoxy)perylene-3,4:9,10-tetracarboxylic acid bisimide (see reference 18).

[21] a) J. Wu, A. Fechtenkötter, J. Gauss, M. D. Watson, M. Kastler, C. Fechtenkötter, M.

Wagner, K. Müllen, *J. Am. Chem. Soc.* **2004**, *126*, 11311-11321; b) J. A. A. W. Elemans, A. E. Rowan, R. J. M. Nolte, *J. Am. Chem. Soc.* **2002**, *124*, 1532-1540; c) D. Zhao, J. S. Moore, *J. Org. Chem.* **2002**, *67*, 3548-3554.

[22] C. Shao, M. Grüne, M. Stolte, F. Würthner, *Chem. Eur. J.* **2012**, DOI: 10.1002/chem.201201661.

[23] C. A. Hunter, H. L. Anderson, *Angew. Chem. Int. Ed.* **2009**, *48*, 7488-7499.

[24] T. E. Kaiser, V. Stepanenko, F. Würthner, *J. Am. Chem. Soc.* **2009**, *131*, 6719-6732.

[25] A. D. Q. Li, W. Wang, L.-Q. Wang, *Chem. Eur. J.* **2003**, *9*, 4594-4601.

[26] a) S. Anand, O. Varnavski, J. A. Marsden, M. M. Haley, H. B. Schlegel, T. Goodson, *J. Phys. Chem. A* **2005**, *110*, 1305-1318; b) Y. Hirata, T. Okada, T. Nomoto, *Chem. Phys. Lett.* **1998**, *293*, 371-377; c) T. Hoshi, J. Okubo, M. Kobayashi, Y. Tanizaki, *J. Am. Chem. Soc.* **1986**, *108*, 3867-3872.

[27] a) V. Dehm, Z. Chen, U. Baumeister, P. Prins, L. D. A. Siebbeles, F. Würthner, *Org. Lett.* **2007**, *9*, 1085-1088; b) F. Würthner, Z. Chen, V. Dehm, V. Stepanenko, *Chem. Commun.* **2006**, 1188-1190.

[28] a) J. Seibt, P. Marquetand, V. Engel, Z. Chen, V. Dehm, F. Würthner, *Chem. Phys.* **2006**, *328*, 354-362; b) R. F. Fink, J. Seibt, V. Engel, M. Renz, M. Kaupp, S. Lochbrunner, H.-M. Zhao, J. Pfister, F. Würthner, B. Engels, *J. Am. Chem. Soc.* **2008**, *130*, 12858-12859; c) H.-M. Zhao, J. Pfister, V. Settels, M. Renz, M. Kaupp, V. C. Dehm, F. Würthner, R. F. Fink, B. Engels, *J. Am. Chem. Soc.* **2009**, *131*, 15660-15668.

[29] Even though the high activation energy for the dissociation of dyad **2** oligomers, the acivation energy for the self-assembly of dyad **2** monomers into oligomers seems quite low. After concentrating the solution of dyad **2** in chloroform in the synthetic procedure, the color turned red immediately and no absorption spectral changes could be detected on the conventional time scale. Upon addition of MeOH into the concentrated aggregate solution, immediate precipitation was observed.

[30] A. Lohr, M. Lysetska, F. Würthner, *Angew. Chem. Int. Ed.* **2005**, *44*, 5071-5074.

[31] D. D. Perrin, W. L. F. Armarego, *Purification of Laboratory Chemicals*, Pergamon Press: Oxford, 1980.

[32] a) G. A. Crosby, J. N. Demas, *J. Phys. Chem.* **1971**, *75*, 991-1024; b) N. Vân Anh, F. Schlosser, M. M. Groeneveld, I. H. M. van Stokkum, F. Würthner, R. M. Williams, *J. Phys. Chem. C* **2009**, *113*, 18358-18368.

[33] D. H. Wu, A. D. Chen, C. S. Johnson, *J. Magn. Reson. A* **1995**, *115*, 260-264.

[34] a) J. Lounila, K. Oikarinen, P. Ingman, J. Jokisaari, *J. Magn. Reson. A* **1996**, *118*, 50-54; b) N. Esturau, F. Sánchez-Ferrando, J. A. Gavin, C. Roumestand, M.-A. Delsuc, T. Parella, *J. Magn. Reson.* **2001**, *153*, 48-55.

[35] A. Jerschow, N. Müller, *J. Magn. Reson.* **1997**, *125*, 372-375.

[36] C. S. Johnson Jr, *Prog. Nucl. Mag. Res. Sp* **1999**, *34*, 203-256.

5.6 Supporting Information

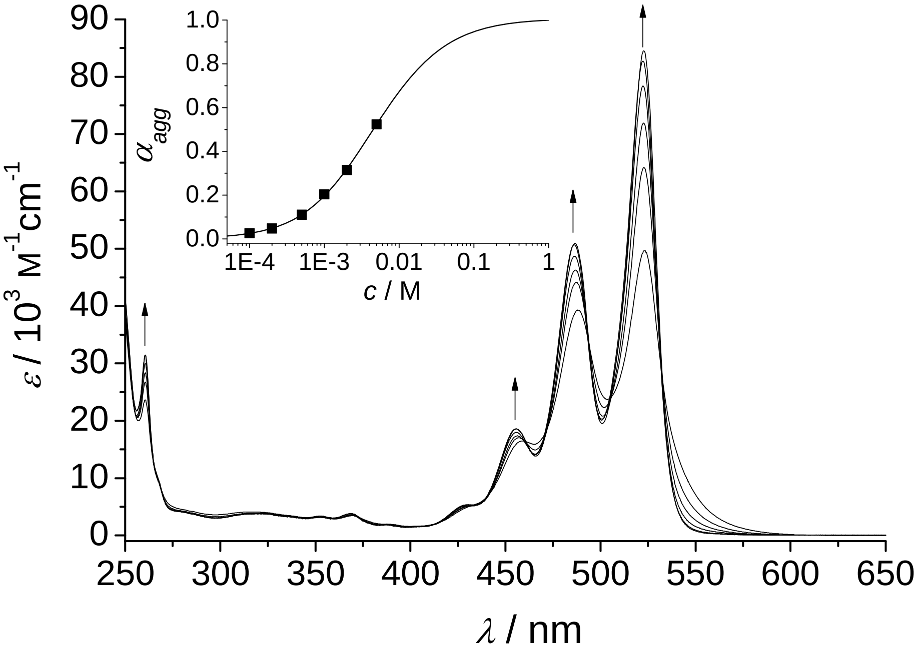

Figure S1. Concentration-dependent absorption spectra of PBI **5** from 1.0×10^{-4} to 5.0×10^{-3} M in $CHCl_3$/MCH (*v*:*v* = 3:7) recorded at 298 K. Inset: Fitting of the concentration-dependent absorbance at 522 nm to the isodesmic model by means of nonlinear least-squares analysis.

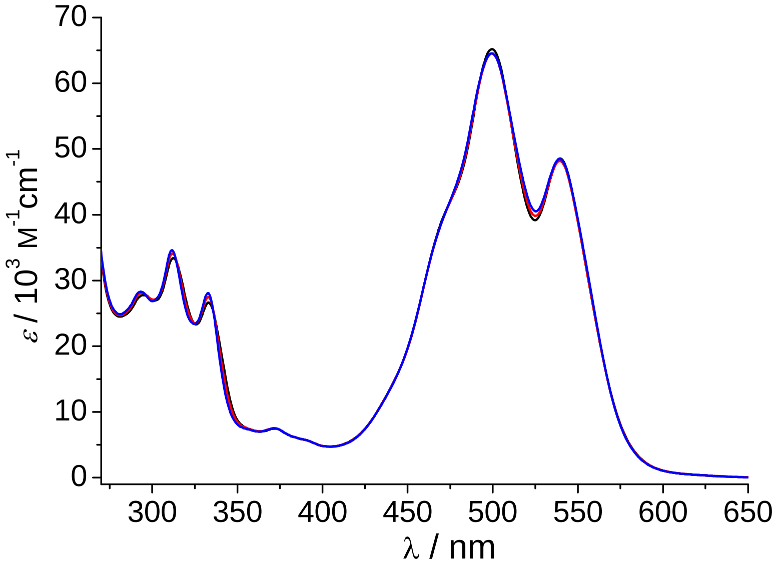

Figure S2. Concentration-dependent absorption spectra of PBI dyad **2** from 5.0×10^{-4} (black), 5.0×10^{-5} (red) to 5.0×10^{-6} M (blue) in MCH recorded at 298 K. Each sample was kept at the given concentration for one week to reach the thermodynamic equilibrium.

Chapter 6

Summary

Self-assembled π-conjugated systems featuring charge and energy transport properties are of great interest in biological and materials sciences. As an important class of industrial dyes and pigments, perylene bisimides have found applications as versatile and promising functional materials for organic electronics. Because the aggregation behavior strongly influences the properties of the material and device performance, it is crucial to control the self-assembly of PBIs. Thus, extensive investigation of the structure-property relationships of PBI self-assembly is necessary to tune the aggregate properties for maximum device performance. Due to the large flat aromatic surface, PBIs have a high propensity to form infinite one-dimensional aggregates. Until now, most studies on controlling PBI aggregation have focused on either preventing aggregation or promoting the formation of soluble infinite linear assemblies. The ability to tailor PBI aggregates of intermediate size has posed a greater challenge. The formation of discrete aggregates has applications as supramolecular building blocks and is meaningful to understand the structural and functional properties of PBIs.

The objective of this thesis focuses on the development of strategies for precise control of PBI self-assembly and the in-depth elucidation of structural and optical features of discrete PBI aggregates by means of NMR and UV/Vis spectroscopy. With regard to the formation of kinetically stable discrete PBI aggregates, a literature overview on the kinetic studies of self-assembly is given in **Chapter 2** that includes the introduction to experimental methods, thermodynamic versus kinetic control and mechanistic investigations of complex self-assembly processes.

The strategy for discrete dimer formation of PBIs is based on delicate steric control that distinguishes the two facets of the central perylene surface. **Chapter 3** describes the design, synthesis and characterization of a novel PBI dye that features both rigid and flexible substituents at each imide position (Figure 1). The aggregation behavior of this PBI dye was analyzed in various chloroform/methylcyclohexane (MCH) solvent mixtures. In the presence of no less than 10 vol% chloroform, exclusive self-assembly into π-stacked dimers was illustrated by means of both concentration-dependent ^{1}H NMR and UV/Vis spectroscopic experiments. Furthermore, DOSY NMR precluded large aggregate formation beyond dimers. On the basis of ROESY NMR, a well-defined π-stacked dimer structure was determined and further depicted by molecular modeling studies. In addition, solvent effects on the Gibbs free energy of PBI dimerization were investigated by altering the solvent composition of chloroform and MCH. These studies showed a pronounced nonlinearity between lower and higher MCH contents. This observation could be related to a further growth process of dimers into larger aggregates that occurs in the absence of chloroform, the solvent that is required to solvate the aromatic π-surfaces of PBIs. With the assistance of a single crystal structure analysis of a related PBI derivative, a structural model could be derived for the unusual stacking that are still composed of defined π-π-stacked PBI dimer entities.

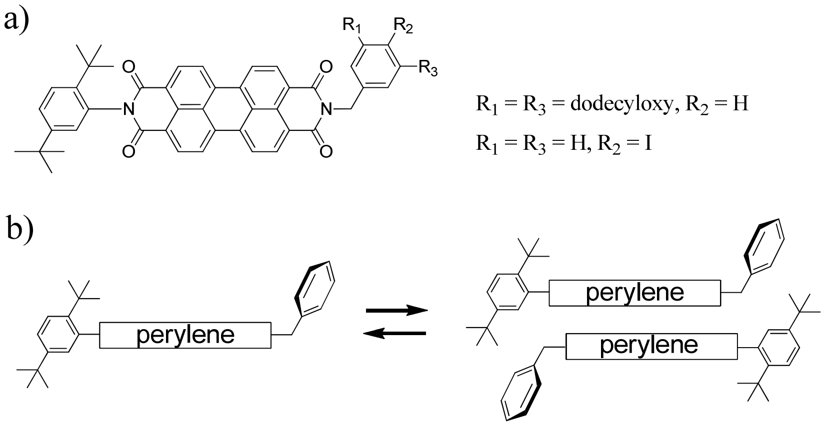

Figure 1. a) Chemical structures of the designed PBI dyes investigated in **Chapter 3** and b) the dimerization process of these PBI derivatives.

The strategy applied in this thesis for accessing discrete PBI quadruple and further oligomeric stacks relies on backbone-directed PBI self-assembly. For this purpose, two tweezer-like PBI dyads bearing the respective rigid backbones, diphenylacetylene (DPA) and diphenylbutydiyne (DPB), were synthesized (Figure 2). The distinct aggregation behavior of these structurally similar PBI dyads can be ascribed to the intramolecular distance between the two PBI chromophores imparted by the DPA and DPB spacers.

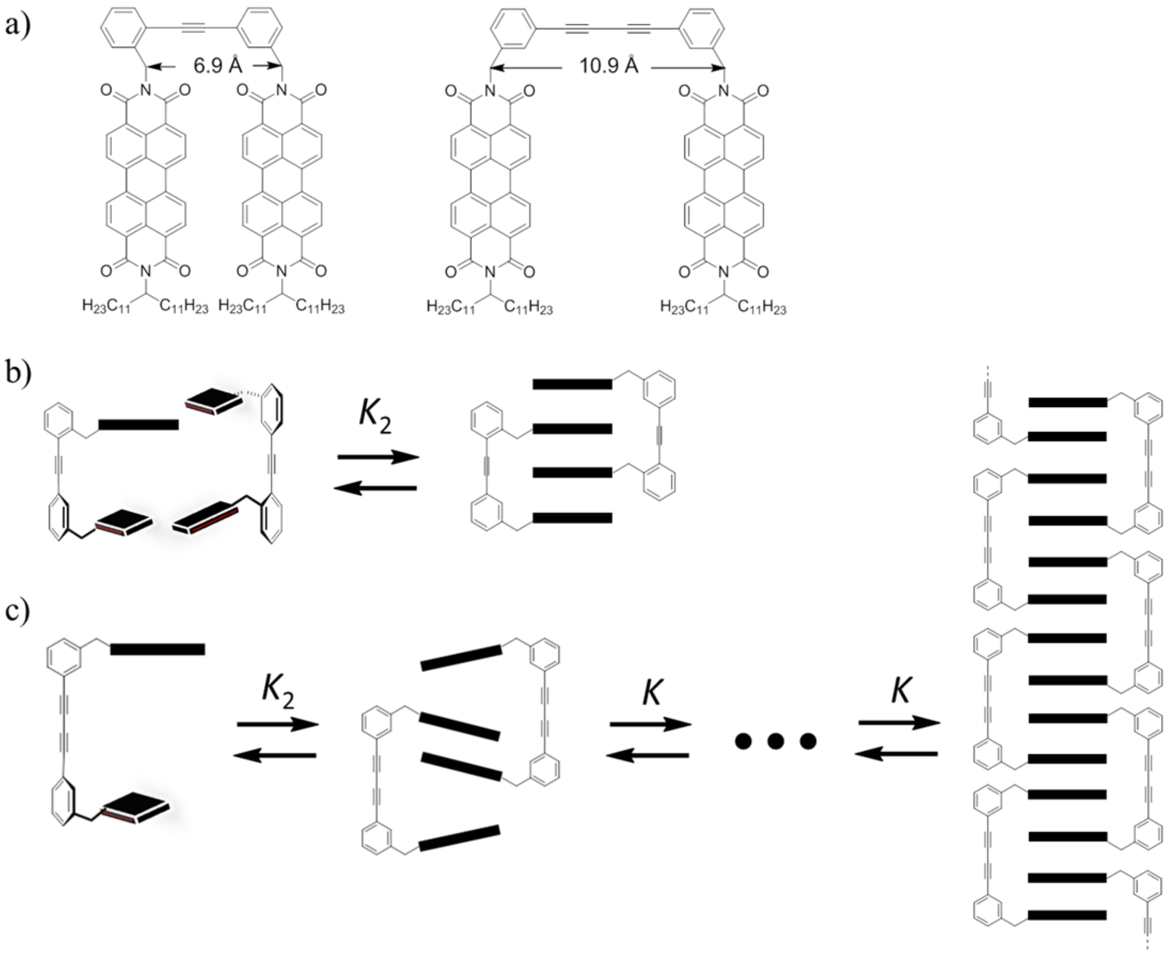

Figure 2. a) Chemical structures of the designed PBI dyad compounds investigated in **Chapter 4** and **5**, respectively; b) dimerization process of DPA-supported PBI dyad and c) oligomer stacking of DPB-supported PBI dyad.

With the two PBI units tethered at the respective *o*- and *m*'-position of DPA, the interplanar space of PBI units is around 6.9 Å, exactly twice the π-π-spacing of PBIs. Thus, this PBI dyad compound has a strong tendency to form interdigitated dimer aggregates with PBI quadruple stacks. In **Chapter 4**, the dimer aggregates of DPA-supported PBI dyads were verified by MALDI-TOF mass spectrometry and dynamic light scattering (DLS). Such dimer aggregates showed high kinetic stability, thus facilitating direct observation of optical properties of PBI quadruple stacks. The structural feature of the PBI quadruple stacking was elucidated by a comparison study with reference PBI dyad compounds and the analysis of absorption spectra in both aggregated and non-aggregated states. Time-dependent ^{1}H NMR and UV/Vis measurements revealed first-order kinetics for disassembly of the dimer aggregates and an activation energy of 83.8±0.8 kJ mol^{-1} in chloroform. The high activation energy of disassembly might originate from the multiple cooperative π-π-interactions, a concept analogous to the multiple cooperative hydrogen bonds that was applied for non-covalent synthesis of kinetically stable hydrogen-bonded complex assemblies.

By extending the backbone length and appending the two PBI chromophores at *m*- and *m*'-positions, DPB-supported PBI dyads can accommodate two PBI units within the tweezer scaffold upon aggregation. In this way, the formation of extended PBI oligomeric aggregates can be realized. In **Chapter 5**, the oligomer formation of DPB-supported PBI dyads was confirmed by MALDI-TOF mass spectrometry and DOSY NMR to extend up to 20-mers (including 40 PBI units). From the concentration-dependent NMR experiments in chloroform, the aggregation motif of PBI π-π-interactions and the backbone function of DPB moiety could be recognized. By analyzing the whole range of concentration-dependent UV/Vis absorption changes in a solvent mixture of $CHCl_3$/MCH (v:v = 3:7), cooperative aggregation behavior of this PBI dyad compound was elucidated. Furthermore, the activation energy of disassembly of the oligomer aggregates in the same solvent mixture was determined by time-dependent absorption monitoring at different temperatures. Accordingly, the energy diagram of the (dis)aggregation process of this PBI dyad could be fully depicted, providing the mechanistic interpretation of backbone-directed PBI self-assembly process (Figure 3). In this mechanistic picture the formation of the dimer nucleus can be interpreted as a pre-equilibrium process whilst the measured Gibbs activation energies $\Delta G^{\neq}$ obtained for the disassembly process relate to the dissociation of PBI tweezers located at the terminal positions of the columnar ladder-type π-π-stacks.

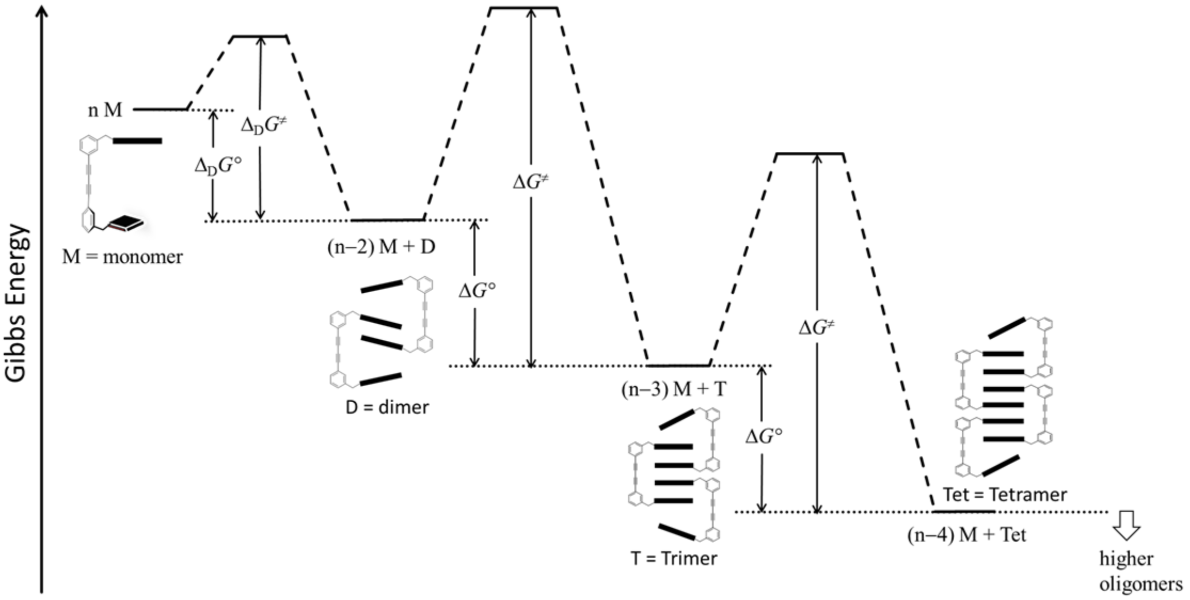

Figure 3. Energy landscape of self-assembly-disassembly process of dyad **2** in a solvent mixture of $CHCl_3$/MCH (*v*:*v* = 3:7) at room temperature.

The discrete PBI aggregates described in this thesis exhibit distinct optical properties, which have not been observed before. For instance, mathematical analysis of the monomer-dimer equilibrium reveals the presence of two allowed optical transitions in the dimer spectrum that are displaced to longer and shorter wavelengths with regard to the main transition of the monomer. In the case of kinetically stable PBI quadruple stacking, a structured absorption spectrum bearing four optical transitions is observed, in good agreement with the prediction of Kasha's exciton theory. Unlike the broadened fluorescence observed for infinite PBI aggregates, PBI quadruple and oligomeric stacks display relatively sharp fluorescence bands, with the emission maximum located at 602 nm and 657 nm, respectively. Thus, discrete PBI aggregates provide new insights into the optical features of PBI self-assembly, which surely deserve more theoretical interpretations and perspectives for applications in (opto)electronic devices.

Zusammenfassung

Selbstorganisierende π-konjugierte Systeme mit Ladungs- und Energietransporteigenschaften besitzen große Bedeutung in der Biologie und in den Materialwissenschaften. Perylenbisimide (PBIs) stellen eine wichtige Klasse industrieller Farbstoffe und Pigmente dar und weisen vielfältige und vielversprechende Anwendungsmöglichkeiten als funktionelle Materialien in der organischen Elektronik auf. Sowohl die Eigenschaften der PBI-Materialien als auch die Effizienz der darauf aufbauenden Bauteile werden stark vom Aggregationsverhalten beeinflusst, sodass die Kontrolle der PBI-Selbstorganisation eine entscheidende Rolle spielt. Deshalb sind umfassende Untersuchungen der Beziehungen zwischen Struktur und Eigenschaften des Selbstassemblierungsprozesses von PBIs notwendig, um die Eigenschaften der Aggregate für eine maximale Bauteileffizienz zu optimieren. PBIs tendieren aufgrund der großen aromatischen π-Flächen zur Ausbildung ausgedehnter eindimensionaler Aggregate. Bisher haben sich die meisten Studien zur Steuerung der PBI-Aggregation darauf konzentriert, Aggregation zu verhindern oder die Bildung von löslichen ausgedehnten linearen Anordnungen zu fördern. Weitaus schwieriger gestaltete sich der gezielte Aufbau von PBI-Aggregaten mittlerer Größe. Die Bildung diskreter Aggregate findet Anwendung in supramolekularen Bausteinen und ist für das Verständnis der strukturellen und funktionellen Eigenschaften von PBIs bedeutend.

Das Ziel dieser Arbeit ist die Entwicklung von Strategien für die präzise Steuerung der PBI-Selbstorganisation sowie die gründliche Aufklärung der strukturellen und optischen Eigenschaften von diskreten PBI-Aggregaten mittels NMR- und UV/Vis-Spektroskopie. Im Hinblick auf die Bildung von kinetisch stabilen und diskreten PBI-Aggregaten findet sich in **Kapitel 2** eine Literaturübersicht der kinetischen Untersuchungen von Selbstorganisationsprozessen, welches eine Einführung in die experimentellen Methoden, die thermodynamische und kinetische Kontrolle sowie mechanistische Untersuchungen von komplexen Selbstorganisationsprozessen umfasst.

Die Strategie der diskreten Dimerbildung von PBIs ist auf der empfindlichen sterischen

Kontrolle begründet, die eine Differenzierung der beiden Facetten der zentralen Perylenoberfläche ermöglicht. **Kapitel 3** beschreibt das Design, die Synthese und die Charakterisierung eines neuen PBI-Farbstoffs, der sowohl einen starren als auch einen flexiblen Substituent an den Imidpositionen trägt (Abbildung 1). Das Aggregationsverhalten dieses PBI-Farbstoffs wurde für verschiedene Chloroform/Methylcyclohexan (MCH) Mischungsverhältnisse untersucht. In Lösungsmittelgemischen mit einem Chloroformanteil von nicht weniger als 10% konnte mittels konzentrationsabhängigen ^{1}H NMR und UV/Vis-spektroskopischen Experimenten gezeigt werden, dass ausschließlich Selbstorganisation zu π-gestapelten Dimeraggregaten stattfindet. Die Ausbildung von über Dimeren hinausgehenden, größeren Aggregaten konnte mit Hilfe von DOSY NMR-Messungen ausgeschlossen werden. Mittels ROESY NMR-Experimenten wurde eine wohldefinierte π-gestapelte Dimerstruktur bestimmt, welche ferner durch Molecular-Modelling-Studien veranschaulicht wurde. Darüber hinaus wurde der Einfluss des Lösungsmittels auf die freie Gibbssche Energie für die PBI-Dimerisierung untersucht, wozu das Mischungsverhältnis von Chloroform und MCH variiert wurde. Diese Studien zeigten eine ausgeprägte Nichtlinearität für sowohl niedrige als auch hohe MCH-Anteile. Diese Beobachtung wurde durch ein fortgesetztes Wachstum von Dimeren zu größeren Aggregaten erklärt. Dieser Prozess ist nur in Abwesenheit von Chloroform zu beobachten, da dieses für die Solvatisierung der aromatischen π-Oberflächen des PBIs erforderlich ist. Mit Hilfe der Kristallstrukturanalyse eines verwandten PBI-Derivats konnte ein Strukturmodell für die ungewöhnliche Anordnung abgeleitet werden, die sich aus definierten π-gestapelten PBI-Dimereinheiten zusammensetzt.

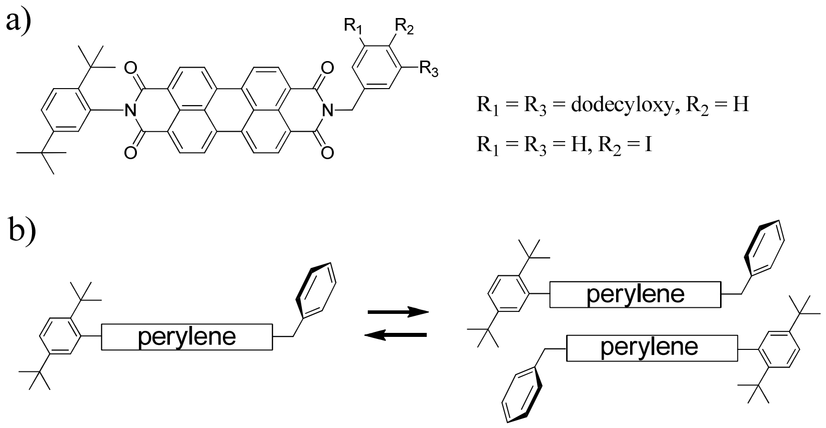

Abbildung 1. a) Chemische Strukturen der in **Kapitel 3** synthetisierten PBI-Farbstoffe und b) der Dimerisierung dieser PBI-Derivate.

Um diskrete vierfache und höhere oligomere PBI-Stapel zu erhalten, behilft sich die vorliegende Arbeit der PBI-Selbstorganisation, die durch ein Rückgrat vermittelt wird. Zu diesem Zweck wurden zwei pinzettenartige PBI-Dyaden synthetisiert, die die starren Rückgrate Diphenylacetylen (DPA) bzw. Diphenylbutydiyn (DPB) tragen (Abbildung 2). Das unterschiedliche Aggregationsverhalten dieser strukturell ähnlichen PBI-Dyaden kann den verschiedenen intramolekularen Abständen der beiden PBI-Chromophore zugeschrieben werden, die durch DPA bzw. DPB als Abstandshalter vorgegeben werden.

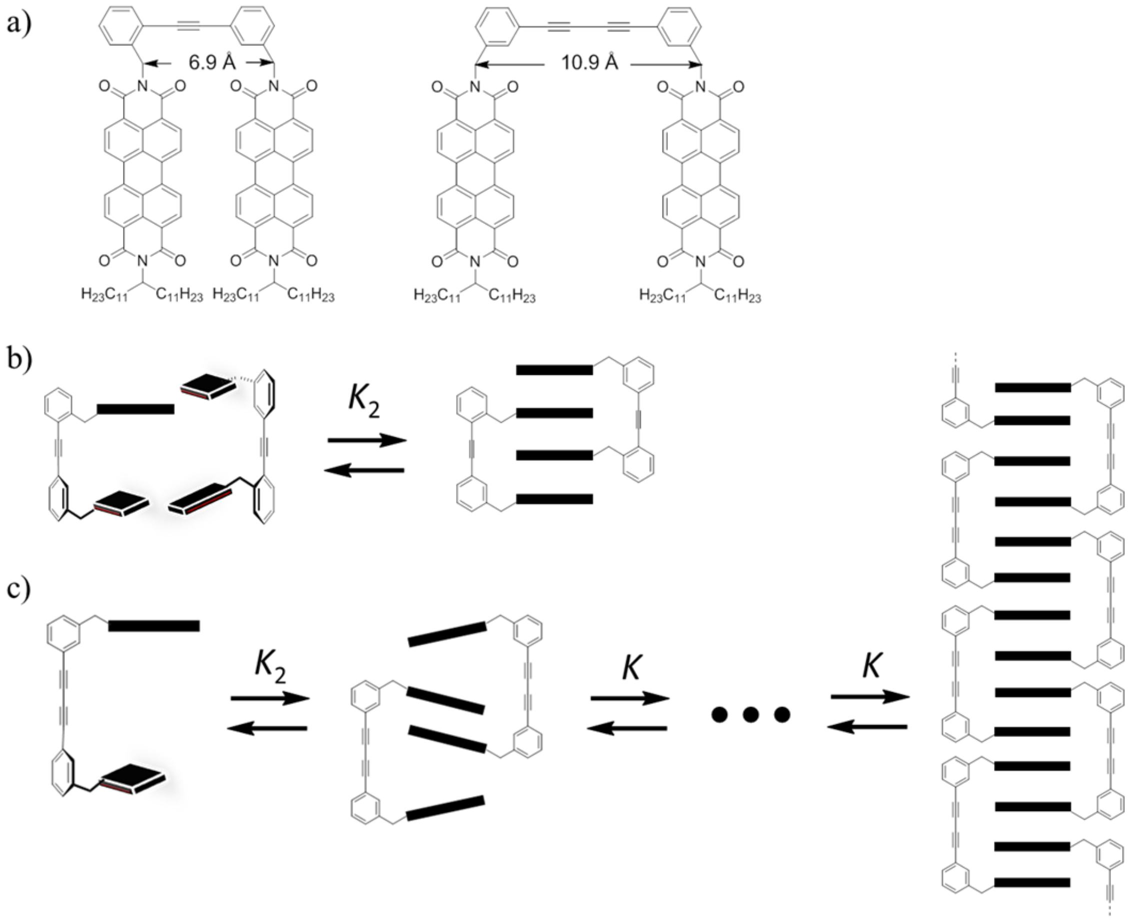

Abbildung 2. a) Chemische Strukturen der synthetisierten PBI-Dyadenverbindungen, die jeweils in **Kapitel 4** und **5** untersucht wurden, b) Dimerisierung der DPA-gestützten PBI-Dyade und c) Oligomere Stapel von DPB-gestützten PBI-Dyaden.

Die Verknüpfung der beiden PBI-Einheiten über die jeweiligen *o*- und *m'*-Positionen des DPA bedingt einen Ebenenabstand der zwei PBI-Einheiten von 6,9 Å, was genau dem doppelten π-π-Abstand von PBIs entspricht. Folglich weist diese PBI-Dyadenverbindung eine starke Tendenz zur ineinandergreifenden Dimerbildung mit vierfachen PBI-Stapeln auf. In

Kapitel 4 wurden die Dimeraggregate von DPA-gestützten PBI-Dyaden durch MALDI-TOF-Massenspektrometrie und Dynamische Lichtstreuung (DLS) nachgewiesen. Diese Dimeraggregate zeigten hohe kinetische Stabilität. Das Strukturmerkmal der vierfachen PBI-Stapeln konnte mit Hilfe einer Vergleichsstudie von relevanten PBI-Dyadenverbindungen und der Analyse von Absorptionsspektren sowohl im aggregierten als auch im nicht aggregierten Zustand aufgeklärt werden. Zeitabhängige ^{1}H NMR und UV/Vis-Messungen förderten für die Dissoziation der Dimeraggregate eine Kinetik erster Ordnung zu Tage, wobei sich für die Aktivierungsenergie ein Wert von 83,8±0,8 kJ mol^{-1} in Chloroform ergab. Die hohe Aktivierungsenergie der Disaggregation könnte durch die multiplen kooperativen π-π-Interaktionen bedingt sein. Dieses Konzept kann in Analogie zu den multiplen kooperativen Wasserstoffbrücken gesehen werden, die zur nicht-kovalenten Synthese von kinetisch stabilen Wasserstoff-verbrückten komplexen Aggregaten verwendet wurde.

Eine Erweiterung der Rückgrat-Länge und die Anordnung der zwei PBI-Chromophore in den *m*- und *m'*-Positionen ermöglicht DPB-gestützte PBI-Dyaden, die bei der Aggregation zwei PBI Einheiten innerhalb der Pinzette aufnehmen können. Auf diese Weise kann die Bildung von ineinandergreifenden oligomeren PBI-Aggregaten realisiert werden. In **Kapitel 5** wurde die Oligomerbildung von solchen DPB-gestützten PBI Dyaden bis zu 20-meren (mit bis zu 40 PBI-Einheiten) durch MALDI-TOF-Massenspektrometrie und DOSY NMR nachgewiesen. Die konzentrationsabhängigen NMR-Experimente in Chloroform erlaubten den Schluss auf ein Aggregationsmotiv mit PBI-π-π-Interaktionen und auf die Funktion der DPB-Einheit als Rückgrat. Durch die Analyse der Veränderungen der konzentrationsabhängigen UV/Vis-Absorptionsspektren in einem Lösungsmittelgemisch von $CHCl_3$/MCH (*v*:*v* = 3:7) konnte für diese PBI-Dyadenverbindung ein kooperatives Aggregationsverhalten gefunden werden. Weiterhin konnte die Aktivierungsenergie der Dissoziation der Oligomeraggregate im gleichen Lösungsmittelgemisch durch zeitabhängige Absorptionsmessungen bei verschiedenen Temperaturen bestimmt werden. Somit war es möglich, das Energiediagramm des Dissoziationsprozesses dieser PBI Dyade vollständig darzustellen, was die mechanistische Interpretation von Rückgrat-gestützter PBI Selbstorganisation möglich machte (Abbildung 3). Nach dieser mechanistischen Vorstellung kann das Entstehen des dimeren Nukleus als Vorgleichgewicht verstanden werden, wohingegen die gemessene freie Aktivierungsenthalpie $\Delta G^{\neq}$ für den Dissoziationsprozess der Ablösung von PBI Pinzettenmolekülen von den Endpositionen der kolumnaren leiterartigen π-π-Stapeln zugeordnet werden kann.

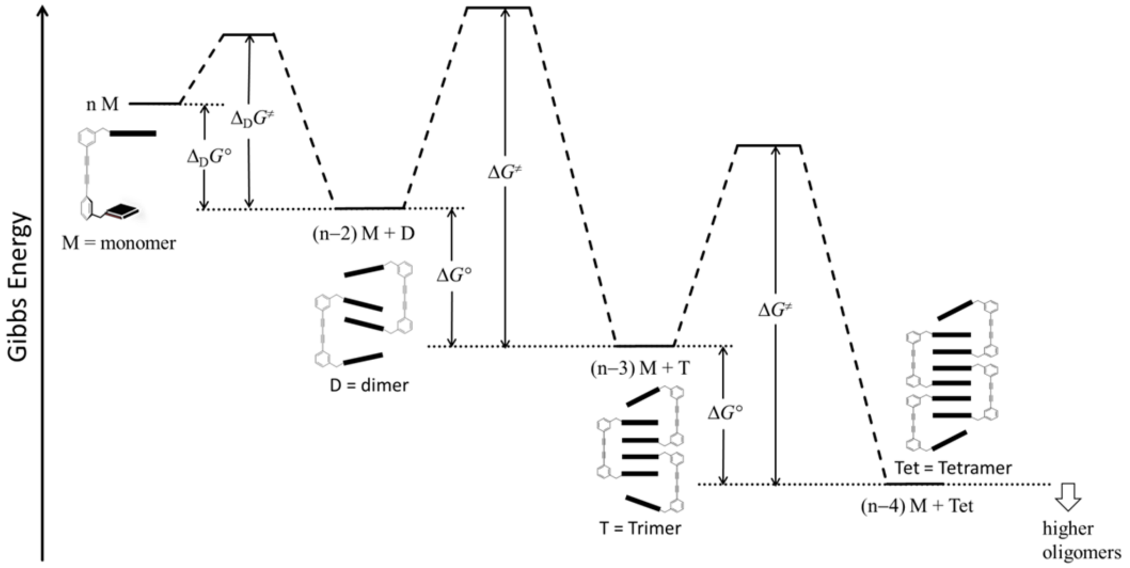

Abbildung 3. Energiediagramm für den Selbstassemblierungs- und Disassemblierungsprozess aus DPB-gestützten PBI-Dyaden in einem Lösungsmittelgemisch von $CHCl_3$/MCH (*v*:*v* = 3:7) bei Raumtemperatur.

Die diskreten PBI-Aggregate weisen ausgeprägte exzitonische Wechselwirkungen auf. Die mathematische Analyse des Monomer-Dimer-Gleichgewichts, zeigt die Anwesenheit von zwei optisch-erlaubten Übergängen im Spektrum des Dimers, die jeweils zu längeren und kürzeren Wellenlängen im Vergleich zum Hauptübergang des Monomerspektrums verschoben sind. Im Falle der kinetisch stabilen vierfachen PBI-Stapel wurde ein strukturiertes Absorptionsspektrum mit vier optischen Übergängen beobachtet, die in guter Übereinstimmung mit der Vorhersage von Kashas Exzitonentheorie stehen. Im Gegensatz zur breiten Fluoreszenz von einfachen ausgedehnten PBI-Aggregaten zeigen vierfache sowie oligomere PBI-Stapel relativ scharfe Fluoreszenzbanden, wobei das Emissionsmaximum jeweils bei 602 nm und 657 nm zu finden ist. Demnach bieten diskrete PBI-Aggregate neue Einblicke in die optischen Eigenschaften der PBI-Selbstassemblierung, die sicherlich weitere theoretische Interpretationen und Perspektiven für die Anwendung in (opto-)elektronischen Bauteilen verdienen.

List of Publications

- *High photocatalytic activity and selectivity for nitrogen in nitrate reduction on Ag/TiO_2 catalyst with fine silver clusters*

  F. Zhang, R. Jin, C. Shao, W. Gao, N. Guan, *J. Catal.* **2005**, *232*, 424–431.

- *Perylene Bisimide Dimer Aggregates: Fundamental Insights into Self-assembly by NMR and UV/Vis Spectroscopy*

  C. Shao, M. Grüne, M. Stolte, F. Würthner, *Chem. Eur. J.* **2012**, DOI: 10.1002/chem.201201661 (ranked as "VIP").

- *Kinetically Stable Dimer Aggregates of a Tweezer-Type Perylene Bisimide Dyad by Quadruple Stacking*

  C. Shao, M. Stolte, F. Würthner, *manuscript in preparation*.

Acknowledgement

I would like to express my sincere gratitude to the following persons who gave me their kind support and help to complete this thesis:

First and foremost, my supervisor Prof. Dr. F. Würthner for giving me the chance to pursue my Ph.D study in this fascinating research area. I am very grateful for his valuable motivations and constructive suggestions which provide a good basis for the present thesis.

Dr. M. Stolte for his wide concerns and encouragement in my last two Ph.D years.

Dr. C. Saha-Möller for his careful correction in manuscript preparation.

Dr. M. Grüne and Ms. E. Ruckdeschel for the numerous 600 MHz NMR measurements.

Dr. M. Büchner for the MALDI-TOF mass measurements.

Dr. X. Zhang for his help with fluorescence and DLS measurements.

D. Phil. K. Thorley and Dr. P. Frischmann for the kind discussion and language correction of this thesis.

Ms. A-M. Krause for the polarization microscope measurements and the single crystal analysis.

Dipl.-Chem. M. Gsänger for the German language correction of the summary part of this thesis and also for the single crystal analysis.

Last but not the least, all other colleagues in the research group for their warm-hearted help and the pleasant activities that we spent together. Personally, loves and thanks to my wife and parents for their steadfast support throughout the past years.